## **Lehigh University Lehigh Preserve**

Theses and Dissertations

2014

# The Study of Biomolecule-Substrate Interactions by Single Molecule Force Spectroscopy and Brownian Dynamics Simulations

Sara Iliafar Cook Lehigh University

Follow this and additional works at: http://preserve.lehigh.edu/etd



**Part** of the <u>Chemical Engineering Commons</u>

### Recommended Citation

Cook, Sara Iliafar, "The Study of Biomolecule-Substrate Interactions by Single Molecule Force Spectroscopy and Brownian Dynamics Simulations" (2014). Theses and Dissertations. Paper 1461.

This Dissertation is brought to you for free and open access by Lehigh Preserve. It has been accepted for inclusion in Theses and Dissertations by an authorized administrator of Lehigh Preserve. For more information, please contact preserve@lehigh.edu.

## The Study of Biomolecule-Substrate Interactions by Single Molecule Force Spectroscopy and Brownian Dynamics Simulations

by

Sara Iliafar Cook

A Dissertation

Presented to the Graduate and Research Committee of Lehigh University in Candidacy for the Degree of Doctor of Philosophy

in Chemical Engineering

Lehigh University January 2014

Copyright by Sara Iliafar Cook

January 2014

Approved and recommended for acceptance as a dissertation in partial fulfillment of the requirements for the degree of Doctor of Philosophy in Chemical Engineering.

"The Study of Biomolecule-Su Spectroscopy and Brownian Dy	bstrate Interactions by Single Molecule Force ynamics Simulations"
Sara Iliafar Cook	
Date	
	Anand Jagota, Ph.D., Dissertation Adviser
Accepted Date	
	Dmitri Vezenov, Ph.D., Dissertation Co-Adviser
	Jeetain Mittal, Ph.D., Committee Member
	Bryan W. Berger, Ph.D., Committee Member
	Dimitrios Vavylonis, Ph.D., Committee Member

## **Copyright Permissions**

The material contained in Chapters 2 and 4 has been published prior to submittal of this dissertation. The proper copyright permission was obtained from each journal prior to submittal of this document, with the publication cited at the beginning of each chapter.

### Acknowledgments

I wish to thank many people for their unconditional love and support throughout my Ph.D. studies. First and foremost, I would like to express my most sincere gratitude and appreciation to my adviser, Professor Anand Jagota, whose support, patience and guidance has made this thesis possible. Professor Jagota's contagious passion and curiosity for true science and his confidence in his students' capability to contribute to scientific advancements has made my graduate work a pleasure and a success. Being mentored by Professor Jagota is a privilege – one that has greatly impacted my professional and personal life in the best way possible. He has taught me to undertake problems with patience, persistence, and an open mind to a wide range of possible causes and solutions. I have become a better team player and independent professional researcher, a more effective mentor and leader, and a more reliable friend by having Professor Jagota as my adviser, professor, and role model.

I would also like to thank my co-adviser, Professor Dmitri Vezenov, for his invaluable guidance, mentorship, and creative ideas. By expecting perfection from his students, Professor Vezenov has taught me to constantly aim for perfection in my performance and take advantage of my capabilities to their maximum potential. He has shown me that it is possible for chemical engineers to have a deep understanding of materials chemistry. Similar to Professor Jagota, I am grateful to Professor Vezenov for teaching me the importance of research quality. I am thankful to my dissertation committee, Prof. Jeetain Mittal, Prof. Bryan Berger, and Prof. Dimitrios Vavylonis for their time, interest, and help during this process. I also thank our collaborators Dr. Ming

Zheng and Dr. Constantine Khripin from National Institute for Stanadards and Technology (NIST) for sharing their helpful ideas and techniques with us. Additionally, I would like to thank Lehigh University and National Science Foundation (NSF) for their financial support during my time at Lehigh University.

I thank my colleagues Shilpi Vajpayee, Suresh Manohar, Daniel Roxbury, Arun Singh, Nichole Nadermann, Ying Bai, Walter Jokiel, Akshaya Shankar, Nicole Fortoul, Dadhichi Paretkar, Xun Gong, and Xuejuan Xu for their good company and making my experience enjoyable at Lehigh. I am grateful to the Chemical Engineering faculty for their support throughout my courses. I would like to thank the department secretaries Elaine, Ruth, Tracey, Janine, and especially Barbara for always making sure that my paperwork was processed quickly.

I greatly appreciate the endless support and encouragement of my family and friends throughout my education. I am thankful to my husband, Kevin, for his dedication to making this process easier for me. By watching our puppies, Selma and Walter, and taking care of as many things as possible, he has given me the time and the space I needed to work. I truly appreciate this support and his confidence in my achievements. I am very grateful to my mother, Tahereh Moghadasi, and my father, Ahmad Iliafar, for raising me, and for their never ending love, encouragement, and believing in me since the day I was born. I am privileged to have you as my parents and would have never made it this far without you. I would like to thank my brother, Siavash, and my sister, Soha, for their constant care, love, and support. Despite not having the opportunity to visit my

siblings for longer than a decade now, I have always felt their strong presence in my life. I thank my aunt, Monir Iliafar, for facilitating my education in England and enabling the advances in my life that have followed. I appreciate all the help and encouragement that Farah and Ali Houshmand have provided me since my first day in the U.S., as though I was one of their own. I thank my friend, Sarah Cohen, and her parents for their support and treating me like family. Finally, I am grateful to my extended family – Kevin's mother and family – for their continuous support and help.

Thank you!

Sara Iliafar Cook

## **Table of Contents**

List o	f Figures	xii
List o	f Tables	XX
Abstra	act	1
	Chapter 1 Introduction to Carbon Surfaces, Single Stranded DNA, Force Spectroscopy, and Brownian Dynamics Simulations	3
1.1	Introduction	3
1.2 1.2.1 1.2.2	Carbon Nanotubes and Their Applications Carbon Nanotubes Carbon Nanotube Applications	4 4 6
1.3 Stranc	Hybrids of Single Walled Carbon Nanotubes and Single led DNA	9
1.4 1.4.1 1.4.2	Single Molecule Force Experiments The Atomic Force Microscope Dynamic Force Spectroscopy	13 14 19
1.5 and So	Modeling the Interactions between Single Stranded DNA olid Surfaces	22
1.6	Scope of the Dissertation	25
1.7	References	27
	Chapter 2 Quantifying Interactions between DNA Oligomers and Graphite Surface Using Single Molecule Force Spectroscopy	39
2.1	Introduction	40
2.2 2.2.1 2.2.2 2.2.3	Experimental Section Materials Probe Functionalization Preparation of a Hydrophobic Methyl-terminated	43 43 43
Mono	layer	44
2.2.4	Force Calibration and Force Curve Capture	45
2.3	Results and Discussion	46
2.4	Conclusions	62
2.5 2.5.1 2.5.2 2.5.3	Appendix Effect of oligomer attachment direction on peeling forces Effect of oligomer chain length on peeling forces Peeling forces of polyadenine	65 65 66 67

2.5.4	Peeling of polythymine from hydrophobic and hydrophilic	
surfac	es	68
	Pull-off forces for polyguanine observed in the course of	
	ning behavior	69 <b>7</b> 0
	Initial pull-off forces for polyguanine modified probes Relating peeling force to adhesion free energy for a worm-	70
like ch		71
2.5.8	Correlation between binding free energy per base and non-	, -
polar i	molecular area	75
2.6	References	76
	Chapter 3 Interaction of Single-Stranded DNA with Curved	
	Carbon Nanotube is Much Stronger than with Flat Graphite	81
3.1 In	ntroduction	82
3.2	Experimental Section	83
3.2.1	Uniform Dispersions of 5'-(GT) <sub>3</sub> -3'/(6,5) SWCNTs	83
3.2.2	Formation of Hydrophobic Methyl-Terminated Self-	0.4
	nbled Monolayers (SAM) on Silicon Wafers	84
	Deposition of SWCNTs on Hydrophobic SAM	85
3.2.4 SWC	Displacement of 5'-(GT) <sub>3</sub> -3' from the Surfaces of NTs Using Sodium Dodecyl Benzene Sulfonate (SDBS)	85
3.2.5		63
	(6,5) SWCNTs	87
3.3	RESULTS AND DISCUSSION	89
3.3.1	Bare Carbon-Nanotubes on a Hydrophobic Self-Assembled	0)
Mono	· · · · · · · · · · · · · · · · · · ·	89
3.3.2	Peeling of Homopolymer ssDNA from Bare Single Walled	
Carbo	n Nanotubes	97
3.4	Conclusions	109
3.5	References	110
	Chapter 4 Brownian Dynamics Simulation of Peeling a	
	Strongly-Adsorbed Polymer Molecule from a Frictionless	
	Substrate	116
4.1	Introduction	117
4.2	Methods	120
4.3	Results and Discussion	127
4.3.1	Equilibrium peeling of a freely jointed chain from a	
	nless surface under force control	129
	Peeling of a freely jointed chain from a frictionless surface displacement control	135
under	distriguement control	1.45

4.3.3 4.3.4	Departure from equilibrium Effect of AFM probe fluctuations	137 150
4.4	Conclusions	152
4.5	Appendix	154
4.5.1	Brownian Dynamics	154
4.5.2	Relating the Variance of Random Force to the Viscous	
	156	
4.5.3	Potential between a monomer in the FJC and the surface	163
4.5.4	The desorption energy barrier of a freely jointed chain that	
	to be overcome for peeling from a surface	167
	Derivation of the Force Required for Equilibrium Peeling	169
	Estimate of Attempt Frequency	174
	Number of Links Going In and Out of Contact with a	171
	e in Equilibrium	176
	Derivation of peeling force at finite forcing rates	187
	Conformation of a FJC as a Function of Forcing Rate	189
	Reducing noise from the simulations by means of	10)
averag	•	191
_	Effect of Removal Rate on Force Spikes in Displacement	171
Contro		194
	Effect of chain length on force spikes of block-co-polymers	174
	lacement control	195
		193
	Testing Thermal Fluctuation Effects of an Added AFM	196
	to the System  Pate Dependence of Pacling Forces under Dignlessment	190
	Rate Dependence of Peeling Forces under Displacement	100
Contro	OI	199
4.6	References	200
	Chapter 5 In-plane force-extension response of a polymer	
	confined to a surface	205
5 1 Int	roduction	206
5.2 htt	Methods	208
3.2	Methods	200
5.3	Results and Discussions	209
5.3.1	Force-displacement response of a freely jointed chain in 2D	209
5.3.2	Approximations to Explicit Force-Extension Relationships	224
5.4	Conclusions	228
5.5	References	230
	Chapter 6 Future Work: Exploratory Studies on the Effect	
	of Surface Friction on the Removal Dynamics of a	
	Polymeric Chain from a Graphitic Surface	235
	- 01,1110110 CHARLE HOLLE A CHAPILLE NOLLAND	

6.1	Introduction	235
6.2	Methods	237
6.3	Results and Discussions	244
6.4	Conclusions	254
6.5	References	255
	Curriculum Vitae	259

## **List of Figures**

Figure	1.1. (a) The structure of SWNT is as a cylinder formed by one wrapped
	graphene sheet. (b) The roll-up vector, $\vec{C}$ , is used to produce CNTs of different chirality and diameter. Figure 1.1.b. was published by Belin and Epron, <sup>24</sup> and the proper copyright permission was obtained from Elsevier prior to submittal of this document
	1.2. (a) Double stranded DNA (dsDNA) comprises two hydrogen bonded single stranded DNA (ssDNA) molecules. (b) Single stranded DNA is a biopolymer in which the monomeric unit is a nucleotide. (c) Each nucleotide is composed of a DNA nucleobase, a 5-membered sugar ring and a phosphate group. (d) DNA bases are classified as purines and pyrimidines. Adenine (A) and Guanine (G) are purines while Cytosine (C) and Thymine (T) are pyrimidines.
	1.3. (a) Schematic picture of an atomic force microscope. (b) Pictorial representation of the direction of laser path reflected from the back of the AFM cantilever as it changes with the upward and downward movements of the probe. (c) Schematic of the movements of the laser spot position on the quadrant photodiode detector with changes in the cantilever deflection.
_	1.4. Pictorial illustration of changes in deflection of an AFM cantilever as the tip is brought in and out of contact with the hard surface
	1.5. The freely jointed chain consists of identical segments of length b, joined together by freely rotating hinges
	2.1. (A) Idealized cartoon (not drawn to scale) of frictionless peeling of a ssDNA homopolymer, attached to a gold coated force probe, from a graphite surface. Due to the frictionless nature of the substrate, the adsorbed bases slide freely on the surface and ssDNA detachment occurs perpendicular to the surface. (B) Typical force-distance curves for peeling 5'-poly(dT <sub>100</sub> ) ssDNA from the surface of graphite obtained at a tip velocity of 200 nm/s in 10 mM phosphate buffer solution containing 100 mM NaCl. Red curve is approach, blue is retraction
	2.2. Typical force-distance curves obtained for probes functionalized with 5'-poly( $dG_{100}$ ) (200 nm/s retraction velocity, 10 mM phosphate buffer with 100 mM NaCl) showing peeling (A) and stretching (B)
	2.3. Proposed mechanisms to describe the possible reasons for observing: (A) force curves with small forces at separations larger than the ssDNA's contour length, (B) large forces at short separations, (C) and (D) both peeling and stretching. This figure was created by Dr. Kyle Wagner 60

Figure	2.4. Histogram of 5'-poly( $dG_{100}$ ) peeling forces showing two distinct peaks at $66.4 \pm 13.7$ pN and $121.4 \pm 14.4$ pN (mean $\pm$ standard deviation derived form a fit to a Gaussian distribution)
Figure	2.5. Typical force-distance curve for peeling 5'-poly(dT <sub>100</sub> ) ssDNA from the surface of a methyl terminated self-assembled monolayer on silicon obtained at a tip velocity of 200 nm/s in 10 mM phosphate buffer solution containing 100 mM NaCl
Figure	2.6. Typical force-distance curve for interaction between 5'-poly( $dT_{100}$ ) ssDNA and clean silicon surface obtained at a tip velocity of 200 nm/s in 10 mM phosphate buffer solution containing 100 mM NaCl
Figure	2.7. Histogram of pull off force for 5'-poly(dG <sub>100</sub> ) showing single molecule stretching behavior
Figure	2.8. Typical force-distance curve for peeling 5'-poly(dG <sub>100</sub> ) ssDNA from the surface of graphite obtained at a tip velocity of 200 nm/s in 10 mM phosphate buffer solution containing 100 mM NaCl
Figure	2.9. Dependence of dimensionless adhesion free energy,
	$\Gamma' = \frac{2p}{k_B T} \gamma - \Delta \ln[w]$ , on dimensionless force, $F = fb/k_B T$ , for WLC and FJC
	models of a polymer molecule. 74
Figure	2.10. Dependence of binding free energy per nucleotide on non-polar molecular area of a nucleobase. The dotted line is a linear fit to the data to guide the eye
Figure	3.1. Typical force—distance curve for peeling 5′- T <sub>100</sub> ssDNA from SWCNTs deposited on a methyl-terminated SAM on a silicon wafer. The force curves were obtained at a tip velocity of 200 nm/s in 10 mM phosphate buffer containing 100 mM NaCl. The red curve is for the tip approaching the surface, blue curve represents tip retraction
Figure	3.2. The peak position of the NIR absorbance spectrum of the SWCNT dispersion shifts from 990 nm (DNA-coated) to 978 nm (SDBS-coated) immediately upon addition of the SDBS solution. Subsequent scans obtained 10 minutes after the addition of SDBS to the 5'-(GT) <sub>3</sub> -3'/SWCNT dispersion showed no further change. This experiment was repeated three times to ensure reproducibility of the results90
Figure	3.3. Surface topography of SAM-coated silicon wafers obtained in air for (A) a control sample exposed to phosphate buffer only, and (B) a sample exposed for 10 minutes to a droplet of 90 µg/ml dispersion of 5'-(GT) <sub>3</sub> -3'-coated SWCNTs and then rinsed by SDBS (2 minutes) and DI water. The sample in (B) had undergone three CNT-deposition-surfactant/water-rinse cycles. (C) Using the depth analysis tool, the diameter of the SWCNTs

	was obtained from the peak-to-peak difference in depth and averaged ove multiple areas and samples
Figure	3.4. Analysis of the average height of the nanotubes after each step of 5' $(GT)_3$ -3'/SWCNT deposition and SDBS/DI water rinse showed a gradual decrease in the apparent mean diameter of the CNTs. After the third rinsing step, the mean diameter of $0.85\pm0.06$ nm (35 separate measurements) is well within the diameter range (0.7-0.9 nm) of bard SWCNTs reported by the manufacturer
Figure	3.5. (A) High resolution XPS spectra of the N 1s region obtained for three samples with the following variations in the preparation: i) a sample exposed to buffer (no DNA) without the rinse step, ii) a dispersion of 5' (GT) <sub>3</sub> -3'/SWCNT deposited without the rinse step, and iii) a dispersion o 5'-(GT) <sub>3</sub> -3'/SWCNT deposited, followed by the SDBS/DI water rinse The SAM-coated silicon wafer on which a dispersion of 5'-(GT) <sub>3</sub> 3'/SWCNT was deposited without the rinse step displayed a peak located at 401.2 eV with FWHM of 2.02 eV. (B) The N 1s peak from sample (i in (A) can be represented by the superposition of two Gaussian components
Figure	3.6. Force histograms for peeling ssDNA homopolymers from SWCNT dispersed on a methyl-terminated SAM showing two distinct peaks (peal positions and errors of the mean are derived from the Gaussian fits to the experimental data). The distributions of peeling forces were centered a 78.4 $\pm$ 0.8 pN (total of n=1673 force curves) and 172.0 $\pm$ 1.6 pN (n= 714 in 4 independent experiments for 5'-T <sub>100</sub> (A), 130.0 $\pm$ 1.5 pN (n= 1948 and 265.4 $\pm$ 2.2 pN (n=890) in 3 independent experiments for 5'-A <sub>100</sub> (B) 72.5 $\pm$ 0.9 pN (n= 1863) and 131.2 $\pm$ 1.1 pN (n=1114) in 3 independent experiments for 5'-C <sub>100</sub> (C), and 80.1 $\pm$ 1.2 pN (n=1879) and 239.8 $\pm$ 1.5 pN (n=1339) from 3 independent experiments for 5'-G <sub>100</sub> (D)
Figure	3.7. Superposition of the sample topography and locations of the gridpoints where individual force-distance curves were acquired from SWCNTs and a methyl terminated SAM. Placement on the sample of valid force curves with the peeling force of less than 127 pN is shown by red squares and placement of force curves higher than 127 pN is shown in blue. Despite some mismatch, there is a clear correlation between the location of the SWCNTs and the high peeling forces, and between the location of regions presenting methyl-terminated SAM and low peeling forces.
Figure	3.8. Pictorial representation of proposed mechanisms to explain the enhanced interaction between ssDNA and SWCNTs, compared to ssDNA with graphite. (A) ssDNA has a natural curvature that prefers to adsorb on the curved surface of an SWCNT. (B) ssDNA intercalates between the SWCNT and the hydrophobic substrate.

- Figure 4.2. Clusters of two, 21-node, freely jointed chains with two different binding energies are shown as the applied force in the z-direction increases. Each cluster contains forty conformations. Within one cluster each conformation has been shifted in the x-y plane such that all 21<sup>st</sup> nodes coincide. (Left) At the beginning of the simulation (t = 0.09 ps), the force is too small to peel the chain off the substrate. Not all nodes of Chain B (moderate binding energy) are adsorbed on the surface, whereas all nodes of chain A (strong surface adhesion) are bound to the surface. (Middle) The physical state of the FJCs when the end-to-end distance of the chains is slightly higher than half their contour length (t = 5.3 μs). (Right) Final conformation obtained near the end of the simulations (t = 9.0 μs) when the FJCs are nearly fully stretched to their contour length.
- (A) Effect of dimensionless adhesion,  $\Gamma = \gamma b/(k_B T)$ , on the Figure 4.3. equilibrium force-displacement relationship in force-controlled peeling. The simulations are shown as thick dashed or solid lines. The equilibrium model is shown by thin solid lines. (B) The conformational free energy required to desorb a link from a 2D-FJC-state on a surface into a 3D-FJCstate in solution,  $\ln(w_{3D}/w_{2D})$ , as a function of adhesion free energy. This quantity was determined by finding the value of  $\ln(w_{3D}/w_{2D})$  that minimizes the normalized root-mean squared difference between the simulated and theoretical force. The normalized root mean squared errors of  $\ln(w_{3D}/w_{2D})$  are comparable to the size of the symbols. relationship between  $\ln(w_{3D}/w_{2D})$  and  $\Gamma$  is captured, empirically, by as  $\ln(w_{3D}/w_{2D}) = a(1 - \exp(-b\Gamma)) + c$ fitting the with a = 1.8, b = 0.19, c = 0.75. This fit correctly extrapolates to a value close to  $\ln(w_{3D}/w_{2D}) = \ln(2)$ , as expected, in the absence of adhesion (magenta
- Figure 4.4. Effects of surface adhesion on the force-displacement of an FJC under displacement control (solid lines) compared with the theoretical results obtained for the equilibrium rates under force control (dashed lines). The magnitude of the force spikes is represented reasonably well

	values of $\ln(w_{3D}/w_{2D})$ plotted in Figure 4.3B
Figure	4.5. Comparison of the potential energy of a chain interacting with an ideal surface when the applied force is much smaller than, equal to, and much larger than the force needed to obtain a steady state peeling plateau. Shown in the lower inset, the behavior of the potential energy of the chain (solid blue) is reproduced by a simple periodic function (dotted pink) as described in Equation 4.28.
Figure	4.6. (A) Stretching of an FJC with 20 Kuhn links and no binding energy peeled at different forcing rates. The dimensionless forcing rates (D.F.R.) were calculated using Equation 4.26. The chain's stretching follows the Langevin function ( $F_{theoretical}$ ) at slow rates as the chain is stretched nearly in equilibrium. As the rates of removal increase, force increases linearly with end-to-end distance, which is captured well by Equations 4.24 and 4.25 and is labeled " $F_{Stokes}$ " in the figure. (B) Effect of forcing rate on force-displacement curve of an FJC with binding energy per Kuhn segment of 11.5 $k_B$ T under force control
Figure	4.7. The relationship between the dimensionless force, $F = f b/(k_B T)$ , and the dimensionless forcing rate, $\dot{F} = \frac{\sqrt{6\pi \eta a \dot{f} b^3}}{k_B T}$ , captured at $R_z = L_c/2$
	for removing an FJC with 20 Kuhn links with different surface adhesion. The lines are predicted by Equation 4.34 for $\Gamma=14~k_BT$ (solid) and $\Gamma=2~k_BT$ (dashed). The height of the reduced energy barrier, $a$ , for the chains with free energy of binding of 14 $k_BT$ and 2 $k_BT$ per Kuhn segment were numerically found to be 4.0 $k_BT$ and 0.6 $k_BT$ using the potential energy profile of these chains as they are being removed at equilibrium peeling as plotted in Figure 4.5. The unknown parameters $J_{0,14~k_BT}=1.0\cdot10^9~{\rm s}^{-1}$ , $J_{0,2k_BT}=1.2\cdot10^{10}~{\rm s}^{-1}$ and $q=1.1\cdot10^{10}~{\rm s}^{-1}$ were estimated using
	Equation 4.31.a. with frequency $q = \frac{6D}{b^2}$ obtained using the diffusion
ъ.	coefficient. 149
Figure	4.8. Effect of thermal fluctuations of a force probe on peeling forces in block-co-polymer poly(dT) <sub>10</sub> poly(dC <sub>10</sub> ) with adhesion energy of 11.5 k <sub>B</sub> T and 8.3 k <sub>B</sub> T per link corresponding to poly(dT) and poly(dC). <sup>25</sup> Despite the added noise from the AFM probe, the force plateaus associated with block-co-polymers remain distinguishable. Varying the AFM tip spring constant has a minor effects of the peeling forces although it smoothes out the sudden jump between the force plateaus (from one monomer unit to 2.5 bases monomeric units)

Figure	4.9. Schematic of the domain over which the Lennrad Jones potential was integrated. The distance between the monomer and the half-space is denoted by $z_n$
Figure	4.10. A schematic diagram of step-wise removal of a FJC from a surface, where $R_z$ represents the displacement and $F_z$ represents the applied force in the z-direction.
Figure	4.11. A schematic diagram of the potential energy profile for removing of a FJC from a surface
Figure	4.12. The energy barrier for removing an individual monomer from an ideal surface is obtainable from the Kuhn segment length, $b=0.65$ nm, of the freely jointed chain and the slope was of potential energy profile for peeling a chain ( $z_{\min} = 0.5$ nm, $\phi_{\min} = \gamma b$ ).
Figure	4.13. A schematic diagram of FJC removal under displacement control176
Figure	4.14. Comparison of the potential energy of a freely jointed chain interacting with an ideal surface when peeling of the chain is not in equilibrium (black line) against the equilibrium entropic stretching of the chain obtained from the Langevin function
Figure	4.15. Snapshots of a freely jointed chain with 20 Kuhn links is shown as the applied force in z-direction increases at different forcing rates. (Left) At the beginning of the simulation, the force is too small to uncoil the chain. (Middle) The second set of conformations illustrates the effect of forcing rate and chain equilibration on the physical state of the FJC when the end-to-end distance of the chain is slightly higher than half of its contour length. (Right) Final conformation was obtained at the very end of the simulations when the FJC is fully stretched to its contour length. 190
Figure	4.16. Comparison between results for a chain with adhesion energy of $14  k_B T$ per base under force control with and without averaging
Figure	4.17. Pulling a free chain with 20 Kuhn links at different forcing rates in fluid. The dimensionless forcing rates were obtained using $\dot{F} = \frac{\sqrt{6\pi \eta a  \dot{f}  b^3}}{k_B T} \ $
Figure	4.18. The effect of rate on the force-displacement relationship for a 20-mer FJC with surface adhesion of 11.5 k <sub>B</sub> T per link under displacement control. Similar to the force control results, moving away from the equilibrium rate results in deviations from the equilibrium force until the plateau is no longer recognizable
Figure	4.19. The effect of the length of homopolymer sequence in block-co-polymers on peeling of the FJC with stiff probes ( $k_{probe} = 5.2 \text{ N/m}$ ) and in the presence of compliant probes ( $k_{probe} = 0.2 \text{ N/m}$ )

riguie	(log-log plot). The green line shows the diffusive limit of true evolution of mean square displacement (Equation 4.153), and the red lines are the equilibrium limit for springs of different stiffness described by Equation 4.154
Figure	4.21. Cumulative distribution of mean square displacement for $k_{sp}=1$ mN/m after 0.72 $\mu s$ compared to the exact results given by Equation 4.155
Figure	5.1. A schematic diagram of the freely jointed chain adsorbed on a solid substrate. The polymer chain is fixed to a point on the surface at one end (red node) and force is applied to the opposite end (A) or uniformly to each node (B). The molecule is represented by identical nodes, connected by freely jointed links.
Figure	5.2. The force-displacement relationship for a freely jointed chain in 3D, 2D, and 1D under a point force. The solid curves represent the equilibrium results (equations 5.6, 5.13, and 5.14 for 3D, 2D, and 1D, respectively). The dashed lines are results obtained via Brownian dynamics simulations carried out without (A) and with (B) self-avoidance and at slow-enough rates to occur in equilibrium.
Figure	5.3. The force-displacement relationship for a non-self-avoiding freely jointed chain presenting the elastic response of the chain when it is stretched in 2D due to i) force applied to one end of the chain, <i>i.e.</i> point force (dashed blue line), and ii) a force field applied to the entire chain (dashed magenta line). The total force is the same in both cases. The stretching behavior of the chain is correctly predicted by $L_{pf,2D} = \frac{I_1(F)}{I_o(F)}$
	and $L_{ff,2D} = \frac{1}{N} \sum_{i=1}^{N} \frac{I_1(iF/N)}{I_o(iF/N)}$ as shown by the solid black and red lines,
	respectively. 219
Figure	5.4. The elastic response of a long freely jointed chain when it is stretched in 2D due to i) a force field applied to the entire chain e.g. under an $\frac{1}{2} \left( \frac{1}{2} \left( \frac{1}{2} \right) \right)$
	electric field (solid line) predicted by $L_{ff,2D} = \frac{\ln (I_o(F))}{F}$ , and ii) force
	applied to one end of the chain, i.e. point force (dashed line) predicted by
	$L_{pf,2D} = \frac{I_1(F)}{I_o(F)}$ . The experimental data <sup>36</sup> (squares) for stretching $\lambda$ -DNA
	confined to a surface and under an electric field closely follow the predicted results for the distributed force mode of stretching

Figure	5.5. The force-displacement relationship for 3D and 2D elastic responses of a freely jointed chain. The solid curves represent the exact results; the dashed lines show the approximate inverse functions
Figure	6.1. Pictorial presentation of a graphene-like surface, divided into subunits to create two new frames of reference, labeled in subscripts $g$ and $b$ 238
Figure	6.2. The normalized corrugated surface potential of a graphitic surface, with hexagonal repeating unit cells, over the planar surface (in the x-y directions) viewed from an angle (a) and directly from the top (b). A Carbon-Carbon bond length of 1.42 Å was used
Figure	6.3. The total surface energy potential for a bead interacting with a corrugated surface such as graphene shown as a function of x- and z In this schematic presentation of the surface potential energy, $\alpha$ was set to 1, $\phi_{\min}$ to 12 k <sub>B</sub> T, and $z_{\min}$ to 0.25 nm
Figure	6.4. (a-b) Molecular conformation of a 20-mer long FJC, interacting with a flat surface with a binding strength of 2 kBT per Kuhn link, equilibrated for 0.903 microseconds shown from above as well as the side. (c) The dimensionless average end-to-end distance, $R_{ee}/b$ , of this molecule over
	time shows that equilibrium was reached quickly
Figure	6.5. Effect of surface undulations, $\alpha$ , on the equilibrium force-displacement relationship in force-controlled peeling. Simulations at $\phi_{\min} = 12 \; k_B T$ are shown as dashed lines lines, and the analytically predicated result for a flat surface $(\alpha = 0)$ as a solid black line
Figure	6.6. Effect of surface adhesion, $\Gamma$ , on the equilibrium force–displacement relationship in force-controlled peeling in the presence of maximum surface undulations (dotted lines) compared to those from a flat surface (solid lines)
Figure	6.7. Effect of peeling rate on the force—displacement curve of an FJC with binding energy per Kuhn segment of 12 $k_BT$ under force control, when surface undulations are maximized ( $\alpha = 1$ ) (dashed lines) vs. absent (solid lines)
Figure	6.8. The equilibrium lateral peeling behavior of 20-mer FJC with binding energy per Kuhn segment of 12 $k_BT$ under force control from a highly undulated surface ( $\alpha = 1$ ).

### **List of Tables**

Table 2.1. Summary of all SMFS measurements of binding affinity between DNA homopolymers and graphite (errors are 95% confidence limit) 63
Table 2.2. Peeling forces for 5'-poly(dT <sub>50</sub> )
Table 2.3. Peeling forces for 5'-poly(dT <sub>100</sub> )
Table 2.4. Peeling forces for 3'-poly(dA <sub>50</sub> )
Table 2.5. Peeling forces for 5'-poly(dT <sub>100</sub> ) from methyl terminated self-assembled monolayer on silicon
Table 2.6. Initial tip adhesion for 3'-poly(dG <sub>100</sub> )
Table 3.1. Summary of the peeling forces and the free energy of binding per nucleotide for all ssDNA homopolymers interacting with methyl terminated SAM or SWCNT.
Table 4.1. Summary of characteristic length scales and peeling velocities associated with processes involving a freely jointed chain interacting with a substrate in fluid. The numbers in parentheses in the third column refer to equation numbers in the text
Table 5.1. Exact extension-force relations and approximations for inverse force-extension relations for a freely jointed chain in 2D & 3D, under point or distributed force.

### **Abstract**

Hybrids of biomolecules and nanomaterials have been identified as promising candidates in the development of novel therapeutics and electronic devices. Single stranded DNA (ssDNA)-bound Single-walled carbon nanotubes (SWCNTs) are of particular interest as they may be the key to solving the challenges that face the carbon nanotube separation technology and because of their potential application in bionanomedicine. The ability of ssDNA to form a stable hybrid with CNTs has been attributed to the structure and amphiphilic nature of this macromolecule, enabling the dispersion, sorting and patterned placement of nanotubes. Considering the significant role of ssDNA-CNTs in future technologies and the potential toxicity of such nanomaterials in biological systems, it is essential to gain a quantitative and fundamental understanding on the interactions that allow, weaken or prevent the formation of these hybrids. In this dissertation, we use both experimental and theoretical methods to systematically investigate the major characteristics of these interactions.

The free energy of binding of ssDNA homopolymers to solvated carbon nanotubes is one of the key characteristics that determine the stability of such dispersions. We used single molecule force spectroscopy (SMFS), first on graphite and next on single walled carbon nanotubes, to probe and directly quantify the binding strength of ssDNA homopolymer oligomers to these substrates. The force resisting removal of DNA molecules from these surfaces shows characteristic steady-state force plateaus which were distinguishable for each DNA sequence. The free energy of binding per nucleotide for these oligomers on graphite were ranked as  $T \ge A > G \ge C$  (11.3  $\pm$  0.8 k<sub>B</sub>T, 9.9  $\pm$  0.4

 $k_BT$ ,  $8.3 \pm 0.2$   $k_BT$ , and  $7.5 \pm 0.8$   $k_BT$ , respectively). On SWCNTs, these interactions decreased in the following order: A > G > T > C, and their magnitude was much larger than on graphite (38.1  $\pm$  0.2; 33.9  $\pm$  0.1; 23.3  $\pm$  0.1; 17.1  $\pm$  0.1  $k_BT$ , respectively).

In addition to the binding strength of ssDNA nucleotide to surfaces, it is equally as important to understand the dynamics of these interactions. The force response of a simple chain-like polymeric molecule (representative of single stranded DNA) was studied using Brownian dynamics to shed light on these dynamics and the features that may be masked in SMFS experiments. Through simulations at slow peeling rates, our Brownian dynamics model confirmed the predictions of an equilibrium statistical thermodynamic model. Faster removal rates resulted in deviations from equilibrium which were dominated by a combination of Stokes (viscous) drag and a finite desorption rate of the monomeric units. Furthermore, the force probe's thermal fluctuations were shown to be affected by the spring constant of the contact mode AFM cantilever Consequently, this effect provided evidence on the source of disappearance for certain key features such as force spikes, associated with the desorption of individual links and predicted by the statistical thermodynamic model under displacement control, from SMFS experiments. In studying the elastic response of a freely jointed chain stretched in 2D and 3D, we obtained analytical expressions for two modes of stretching: i) when force is applied only to one end of the chain, and ii) when the applied force is distributed uniformly throughout the chain. By comparing, we confirmed that these expressions correctly predict the results obtained from our Brownian dynamics simulations as well as experimental results from the literature.

# Chapter 1 Introduction to Carbon Surfaces, Single Stranded DNA, Force Spectroscopy, and Brownian Dynamics Simulations

#### 1.1 Introduction

Graphene and carbon nanotubes (CNTs), which effectively are rolled up graphene sheets, are low-dimensional sp<sup>2</sup> hybridized carbon nanomaterials with many unique physical and chemical characteristics. Their high aspect ratios, mechanical strength, and surface areas, their excellent chemical and thermal stability, and their rich electronic and optical properties make carbon nanotubes promising candidates for a wide range of applications.<sup>1</sup> Examples of these technologies include nanomedicine, sensors, transparent thin film conductors, transistors, photovoltaics, fuel cell electrodes, etc.

Most of the potential applications of single-walled carbon nanotubes (SWCNTs) require a population that is purified with identical chirality, which in itself is one of the major challenges facing the carbon nanotube technology.<sup>2</sup> The current methods of CNT production often result in inherent heterogeneities that are not desirable. Additionally, the strong van der Waals interactions between individual CNTs result in formation of nanotube aggregates, making it difficult to use these nanomaterials in potential applications. To advance nanotube separation technology, intense efforts have been made to separate identical chiral SWCNTs from their synthetic mixture.<sup>3</sup> Examples of these methods include ultracentrifugation,<sup>4</sup> dielectrophoresis,<sup>5</sup> electrical breakdown,<sup>6</sup> selective oxidation,<sup>7</sup> and the use of noncovalent adsorbing amphiphilic molecules, such as surfactants,<sup>8</sup> peptides,<sup>9,10</sup> and lipids.<sup>11,12</sup> Specifically, chromatography of

deoxyribonucleic acid (DNA)-wrapped-nanotubes has been identified as one of the more promising techniques. 13, 14

By taking advantage of the noncovalent attachment of single stranded (ssDNA) oligomers on the hydrophobic nanotube sidewall, these nanomaterials can be made into stable dispersants that are soluble in aqueous medium. Scientists have used this technique to accomplish CNT solution-based tasks such as sorting by diameter, <sup>15</sup> length, <sup>16</sup> and species <sup>17, 18</sup> as well as deposition of aligned tubes on surfaces. <sup>19</sup> These polyelectrolytic, anisotropic hybrids have not only been employed in creating nanostructured constructs, <sup>20, 21</sup> but also they have been highly sought after for the fields of nanomedicine and nanotechnology. Understanding the properties of the ssDNA-SWCNTs complexes allows one to predict their behavior at macroscopic scales, establish new concepts for controlling their performance, and facilitate the design and optimization of devices that are based on these materials. For these reasons, it is imperative to explore the interaction of ssDNA oligomers with SWCNTs on a molecular level. Through experimental and theoretical methods, we address questions about the binding dynamics of ssDNA to carbon surfaces such as graphite and carbon nanotubes in this dissertation.

### 1.2 Carbon Nanotubes and Their Applications

### 1.2.1 Carbon Nanotubes

First discovered by Iijima in 1991, carbon nanotubes are thin sheets of sp<sup>2</sup> carbon, also known as graphene, that are rolled up into a tubular structure.<sup>22</sup> Generalized into two major categories, single-walled nanotubes (SWNTs) consist of a single layer of

cylinder graphene, while multi-walled tubes (MWNTs) contain several concentric graphene sheets.<sup>2</sup> With diameters ranging from 0.4 nm to 2 nm in SWCNTs and 2 nm to 100 nm in MWCNTs, and lengths of hundreds of nanometers to several millimeters, these novel fullerenes possess extremely high aspect ratios. They are the third allotropic form of carbon next to graphite and diamond. The optical, mechanical and electronic properties of these structures are affected by their chirality defined as the angle,  $\Theta$ , at which the graphene sheets are roll up, and graphene's p orbitals aligned (Figure 1.1). Three major techniques have generally been used to synthesize CNTs: i) electric arc discharge, ii) laser ablation, and iii) thermal or plasma enhanced chemical vapor deposition (CVD).<sup>23</sup>

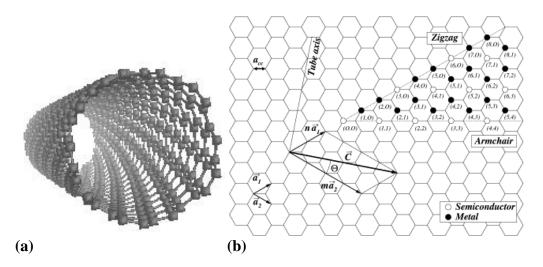


**Figure 1.1.** (a) The structure of SWNT is as a cylinder formed by one wrapped graphene sheet. (b) The roll-up vector,  $\vec{C}$ , is used to produce CNTs of different chirality and diameter. Figure 1.1.b. was published by Belin and Epron,<sup>24</sup> and the proper copyright permission was obtained from Elsevier prior to submittal of this document.

As shown in Fig. 1.1. (b), two atoms in a planar graphene sheet are chosen, and one of them is set as the origin. The chiral vector  $\vec{C}$  is then pointed from the first atom toward the second one. Described by  $\vec{C} = n\vec{a}_1 + m\vec{a}_2$ , this single vector completely describes the chirality of a nanotube through the values of (n, m). In this definition, n and m are integers and  $\vec{a}_1$  and  $\vec{a}_2$  are the unit cell vectors of the two-dimensional lattice formed by the graphene sheet. The direction of the nanotube axis is perpendicular to the chiral vector. While MWNTs are found to be metallic conductors, the SWCNTs are metallic if |n-m| = 3q, and semiconducting if  $|n-m| = 3q\pm 1$ , with q being an integer.  $^{25,26}$ 

### 1.2.2 Carbon Nanotube Applications

Carbon nanotubes have been found to show significantly higher carrier mobility and reduced trap density compared to organic electronic materials. These organic materials can be processed at low temperatures and used in fabrication of mechanically flexible solar devices for large areas. Carbon nanotube films with densities close to the percolation threshold show semiconducting behavior, and can be used as an active layer in thin film transistors in electrodes for solar cell, photo detectors or organic transistors.<sup>27, 28</sup> For these reasons as well as their high optical transparency and chemical stability, organic photovoltaics is an emerging area for carbon nanomaterials especially in photoelectrochemical or dye sensitized solar cells (DSSCs).<sup>29</sup> Assemblies of several layers of CNTs have also been pursued as an ideal candidate to replace the relatively expensive Indium tin oxide (ITO).<sup>30, 31</sup> The polydispersity of as-grown nanotube films, however, compromises their performance in electronics and photovoltaics as the contact

resistance between CNTs of different electronic types has been found to be 100 times higher than that of tubes with the same electronic characteristics.<sup>32, 33</sup>

In electrocatalysis, the high costs, susceptibility to time-dependent drift,<sup>34</sup> and CO poisoning<sup>35</sup> of the traditional catalysts such as platinum and its alloy<sup>36, 37</sup> have resulted in an intensive search to reduce reliance on or replace these electrodes. Meanwhile, the high aspect ratio, high conductivity and corrosion resistant properties of CNTs make them ideal for use as catalyst supports especially in fuel cells. Recent studies using vertically aligned nitrogen-containing carbon nanotubes<sup>38</sup> and nitrogen-containing graphene sheets show a much better electrocatalytic activity, long-term operation stability, and a high tolerance to crossover and poison effects in comparison to platinum electrodes for the oxygen reduction reaction.<sup>39</sup>

Carbon nanotubes' excellent conductivity, good electrochemical properties, and nanometer dimensions have also enabled many advances in highly sensitive, nanoscale electrochemical, electrical, and optical biosensors that could be used inside cells or dispersed through a system.<sup>40</sup> As electrochemical biosensors, CNTs can directly be plugged into individual redox enzymes for better transduction.<sup>41, 42</sup> In nanoscale FETs, these electrical biosensors can detect single molecule events or biological targets.<sup>43</sup>

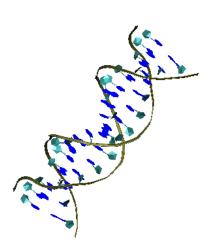
In addition to novel biosensing platforms, CNTs are a promising tool in cancer detection and therapy. Once functionalized with biomolecules, these nanomaterials can cross the mammalian cell membranes by endocytosis and other mechanisms, <sup>2, 44, 45</sup> and become targeted drug delivery carriers. <sup>44, 46</sup> Since drug delivery is one of the most extensively explored applications of CNTs in bio-nanomedicine, different strategies have been investigated so far. For example, covalently conjugated drug molecules can be

linked, via cleavable bonds, to the functional groups on the CNT surface or to the polymeric molecules coating them.<sup>47</sup> Besides covalent linkage, aromatic molecules with a flat structure can be adsorbed on the surface of CNTs via non-covalent  $\pi$ - $\pi$  stacking. An example of this method is a study in which doxorubicin, a commonly used cancer chemotherapy drug, was stacked on the surface of PEGylated SWNTs; the results showed a remarkably high loading capacity (up to 4 grams of drug per 1 gram of nanotubes), which was attributed to the ultrahigh surface area of the tubes.<sup>48</sup>

Functionalized-SWCNTs, and in particular single stranded sDNA (ssDNA)functionalized SWCNTs, have been identified as one of the most promising complexes of
carbon nanotubes. Fabricated ssDNA-coated SWCNT may serve as a conducting
channel for a field-effect transistor (FET) whose transport properties can be controlled by
the encapsulation of a ssDNA molecule. For example, it has been shown that singlestranded polyguanine can change the characteristic of pristine SWCNTs from p-type into
n-type, while single-stranded polycytosine enhances its p-type character. These
experiments suggest that one can use DNA-CNT hybrid systems as building blocks to
form p-n junctions for nanoelectronic devices. Furthermore, the highly sensitive band
gap photoluminescence in DNA-SWCNT hybrids, strongly dependent on their local
environment, has shown capability of molecular detection. Despite the successful
fabrication of the ssDNA-SWCNT hybrid system, its fundamental characteristics are still
far from being fully understood.

### 1.3 Hybrids of Single Walled Carbon Nanotubes and Single Stranded DNA

DNA is a flexible, amphiphilic, and genetic material,  $^{52}$  whose electronic nature can be easily tuned by changing its nucleobase sequences. Double stranded DNA (dsDNA) is comprised of two hydrogen bonded single stranded DNA molecules. A monomeric unit of DNA is a nucleotide. Nucleotides are composed of three units: a nucleobase, a 5-membered sugar ring, and a phosphate group. The DNA nucleobases are heterocycles categorized into two general groups: pyrimidines and purines. Adenine (A) and guanine (G) are classified as purines, while cytosine (C) and thymine (T) are classified as pyrimidines (Figure 1.2). In a ssDNA homopolymer, the end of the strand that is terminated in a free phosphate group is known as the  $5^{\circ}$  end, while the other end terminated with a free hydroxyl group is referred to as the  $3^{\circ}$  end in accordance with proximity to  $5^{\circ}$  or  $3^{\circ}$  carbons of the ribose. The persistence length,  $l_p$ , of ssDNA and dsDNA are about 0.8 nm and 50 nm, respectively.



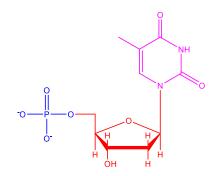
(a) Double stranded DNA

5' end
$$O = P - O - CH_2$$

$$O =$$

3' end

# (b) Single Stranded DNA: polyadenine



Phosphate Sugar Base

# (c) Thymine nucleotide

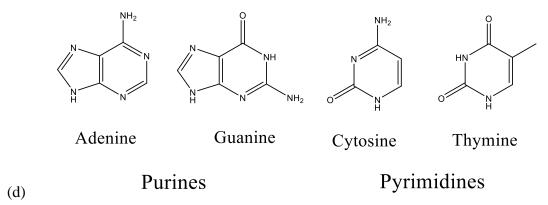


**Figure 1.2.** (a) Double stranded DNA (dsDNA) comprises two hydrogen bonded single stranded DNA (ssDNA) molecules. (b) Single stranded DNA is a biopolymer in which the monomeric unit is a nucleotide. (c) Each nucleotide is composed of a DNA nucleobase, a 5-membered sugar ring and a phosphate group. (d) DNA bases are classified as purines and pyrimidines. Adenine (A) and Guanine (G) are purines while Cytosine (C) and Thymine (T) are pyrimidines.

In comparison to dsDNA, ssDNA is a much more powerful and effective candidate for wrapping the surface of carbon nanotubes. These hybrids are usually prepared via an exfoliation process, where a mixture of DNA and CNTs is sonicated to form an aqueous dispersion. The DNA-CNT hybridization has been attributed to the amphiphilic nature of ssDNA, that is, the hydrophobic nucleobases and the hydrophilic or charged phosphate backbone. Many theoretical send experimental studies have been devoted to gain a better understanding of the interactions that occur between the ssDNA biopolymer and the organic SWCNT. These studies have concluded that  $\pi$ -stacking and some van der Waals (vdW) interactions are the driving force for the hybridization mechanism.

Certain short strands of ssDNA are referred to as "recognition sequences" due to their ability to recognize specific chiralities of SWCNTs. These highly sequence-specific oligomers are typically 8–20 nucleotides in length, and have been used to sort chirality-diverse mixtures of SWCNTs.<sup>3,62</sup> In addition to this technological application, ssDNA-covered CNT dispersions are useful in other potential applications such as bionanomedicine. The ability to sort these tubes and the stability of DNA-CNT dispersions in the cellular environment are highly dependent on the mechanism and strength of interactions between the two materials.<sup>63</sup> For this reason, the interactions between a few chiral SWCNT and ssDNA sequences were studied experimentally to elucidate the origin of their selectivity.<sup>17,59,61</sup> Interestingly, it was found that there is a direct correlation between the recognition ability of a DNA strand for a particular target SWCNT and its experimentally measured bulk binding affinity.<sup>57</sup>

The high selectivity of these recognition sequences is strongly suggestive of the formation of ordered structures by these molecules around a particular SWCNT. This hypothesis has been tested and confirmed by capillary electrophoresis measurements of well-defined charge densities for  $(GT)_{30}$ -CNT hybrids.<sup>62</sup> Additionally, the role of hydrogen bonding and base stacking in the putative formation of  $\beta$ -sheet and  $\beta$ -barrel secondary structures of DNA onto the substrate has been studied.<sup>3, 16, 64</sup> A recent theoretical study demonstrated that while a combination of intrastrand self-stitching and interstrand hydrogen bonds stabilizes the ordered, right-handed, helically wrapped barrel of  $(TAT)_4$  on its recognition partner, the (6,5) SWCNT,<sup>65</sup> a different sequence such as

(T)<sub>12</sub>, forms a distinctly left-handed wrap with weaker tendency for intrastrand hydrogen bonding on the same tube.<sup>66</sup>

Although theoretical studies have shed light on the dynamics of interactions between ssDNA molecules and CNTs, very little quantitative information is yet available on their binding strength. Previously, Manohar et al. used single molecule force spectroscopy (SMFS) to measure the force required to remove single-stranded DNA molecules from single-crystal graphite, an analogue to the surface of carbon nanotubes.<sup>54</sup> The SMFS technique proved to be sensitive enough to differentiate between pyrimidine bases and quantify the peeling forces of polythymine (poly-T) and polycytosine (poly-C) from graphite to be  $85.3 \pm 4.7$  pN and  $60.8 \pm 5.5$  pN, respectively. These forces correspond to the average binding energy per nucleotide of  $11.5 \pm 0.6$  k<sub>B</sub>T for poly-T and  $8.3 \pm 0.7$  k<sub>B</sub>T for poly-C, and were found to be independent of salt concentration and detachment rate.<sup>54</sup> In comparing MD simulations to these experimental results, the binding energies were found to be greater than experimental values, probably due to the nonequilibrium nature of the modeled process. The robustness and reproducibility of the SMFS method in directly quantifying the interactions between DNA homopolymers and a flat substrate motivated us to use this technique in our studies of DNA-CNT binding as discussed in this dissertation.

### 1.4 Single Molecule Force Experiments

Single-molecule methods have been developed to i) accurately measure and analyze the interactions between molecules and surfaces, and ii) facilitate the

investigation of the complex relationship between force, lifetime, and chemistry of even low-affinity interactions. In addition to optical tweezers<sup>67</sup> and magnetic tweezers,<sup>68</sup> atomic force microscopy (AFM) is the most prominent single molecule spectroscopy approach. Atomic force microscope, evolved from the scanning tunneling microscope (STM),<sup>69</sup> was invented by Binnig *et al.* in 1986 to enable researchers to study nonconducting samples, such as biological samples, with atomic and molecular resolution.<sup>70</sup>

### 1.4.1 The Atomic Force Microscope

The main components of the AFM are a probe scanner, probe displacement detector, electronics connected to a computer and a system of isolation from vibrations. The central part of an AFM is its force sensor, or the cantilever tip assembly, composed of a sharp pyramidal tip attached to the end of a typically hundred-micrometer-long flexible cantilever beam. Either the force probe or the surface underneath the tip can be moved very accurately with a piezoelectric 3D-scanner. The tip-sample adhesion and repulsion at the atomic level result in the cantilever deflection, and this information is converted into a height value for each position on the x,y plan to reconstitute a pseudo-three-dimensional (3D) image of the sample surface. Any cantilever displacement is usually detected by an optical lever scheme in which i) a laser beam is directed to and reflected from the backside of the cantilever at its free end, and ii) a four-segmented photodiode detector captures this reflected light and transmits information regarding changes in the laser beam position (lateral or normal) to the signal processing electronics and a computer.

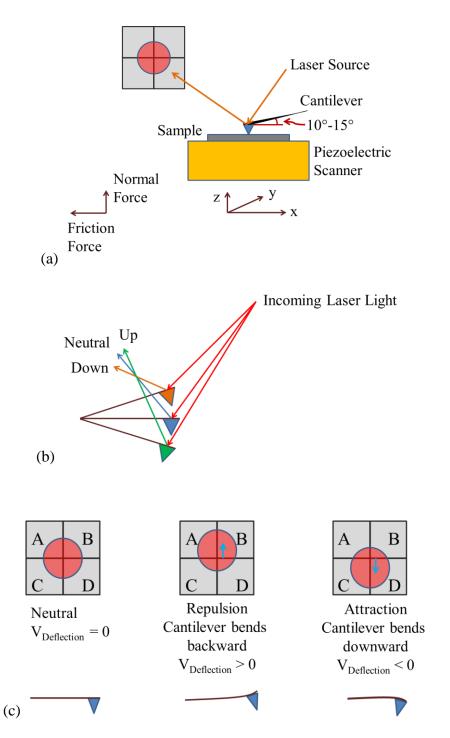


**Figure 1.3.** (a) Schematic picture of an atomic force microscope. (b) Pictorial representation of the direction of laser path reflected from the back of the AFM cantilever as it changes with the upward and downward movements of the probe. (c) Schematic of the movements of the laser spot position on the quadrant photodiode detector with changes in the cantilever deflection.

As shown in Figure 1.3 a-b, the tip-surface interactions result in changes in the AFM probe deflection, in turn resulting in the movement of the laser spot on the quadrant photodiode. Changes in the location of the laser spot are analyzed with respect to a reference position set at zero force. To detect normal deflection of the probe, the difference between the voltages detected in the top half quadrants (A and B) and bottom half quadrants (C and D) of the photodiode detector are considered, i.e.  $(V_A+V_B) - (V_C+V_D)$ . Similarly, the torsional deflections are obtained by taking the difference between the two left (A and C) and right (B and D) halves of the quadrant photodetector, i.e.  $(V_A+V_C) - (V_B+V_D)$ .

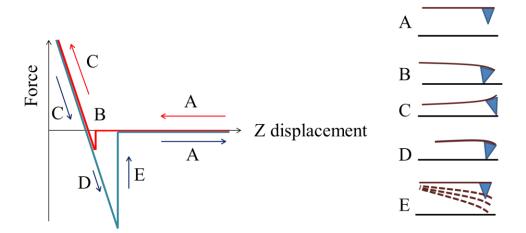


**Figure 1.4.** Pictorial illustration of changes in deflection of an AFM cantilever as the tip is brought in and out of contact with the hard surface.

The probe distance from the sample strongly influences the tip-surface interactions (Figure 1.4). As shown schematically in region A, the zero deflection of an

AFM probe corresponds to the absence of long range forces in the course of approaching (i.e. moving toward) and retracting (i.e. moving away) from the surface. In approaching the surface, the attractive van der Waals and capillary forces deflect the cantilever towards the surface. Eventually, the force gradient exceeds the cantilever spring constant resulting in abrupt snapping of the AFM tip into contact with the surface (region B). Additional external forces applied after this stage, translate into compressive loading on the sample, and both the deflection of the cantilever as well as the repulsive contact force increase (region C). The slope of the force-distance curve in region C is referred to as the response of the optical detector or the optical lever sensitivity (OLS), and has units of V/nm. Upon retraction of the cantilever, large adhesive forces often maintain the force probe in contact with the sample (region D) until at an appropriate critical pulling force, this contact is broken, releasing the tip away from the surface (region E). The difference between the minimum deflection and the zero deflection (scaled by cantilever spring constant) is referred to as adhesion or pull off force. In addition to the tip-sample distance, the force-distance relationship is strongly influenced by the tip, sample, and medium composition. 72,73 To convert cantilever deflection versus piezoscanner displacement into a force– distance curve, Hookes's law of elasticity:  $F = -k \Delta z$  is applied, where F is the applied force, k is the cantilever spring constant, and  $\Delta z$  is the normal deflection of the cantilever (i.e. deflection (V) / OLS (V/nm)). As a result, real force acting on the cantilever's tip can be calculated.

AFM has the capacity to image nonconductive and conductive surfaces in air or in liquid with the resolution beyond the diffraction limit of light microscopy. Depending on

the XYZ scanner stage, the AFM can scan areas up to around  $100 \times 100 \ \mu m^2$  in a line by line fashion <sup>74</sup> with sub-nanometer lateral resolutions and subatomic (< 1 A°) vertical resolutions. <sup>75</sup> In addition to imaging, the AFM's pico-newton force sensitivity makes this technique ideal for quantifying the inter- and intramolecular interaction forces required to separate surfaces at the single molecule level. This approach is usually termed single molecule "force spectroscopy" even though it is not based on the interaction of radiation with matter. In single molecule force spectroscopy, one can record the force-distance curves either for single well-defined points on the x-y plane or for multiple locations, generating a "force–volume" image.

In single-molecule force spectroscopy (SMFS) studies of molecular recognition, tips are generally functionalized with probe molecules, capable of recognizing a specific target molecule on the sample surface. Since the cantilever can be vertically brought in-and out- of contact with the surface, this technique does not require the entire sample surface to be scanned. As mentioned earlier, the cantilever deflection needs to be converted into force. To determine the cantilever spring constant, several calibration techniques are in common use, the inaccuracy of all of which is about 10%. Some of these methods require knowledge of the precise geometrical parameters for the cantilever, 71, 76, 77 making this approach problematic for non-rectangular tips.

Furthermore, calibration results can dramatically be skewed due to the large sensitivity of these methods to small errors in thickness and the use of inexact estimates for the cantilever's Young's modulus and Poisson's ratio. An alternative, robust, method has been established based on the treatment of the cantilever as a harmonic oscillator. In this

technique, either the added mass procedure, <sup>78</sup> Sader method, <sup>71</sup> or the equipartition theorem are applied to analyze the power spectrum and estimate the cantilever spring constant. <sup>79</sup> This method is advantageous to use due to its non-destructive nature and applicability to modified cantilevers.

## 1.4.2 Dynamic Force Spectroscopy

The majority of equations discussed in this section were published in a review journal article by Ritzefeld, et al., <sup>80</sup> and the proper copyright permission was obtained from Springer prior to submittal of this document.

So far, we have established that the accurate piconewton-resolution measurements in force spectroscopy are only possible with a properly calibrated system. The next crucial step is to extract information regarding the strength of the interactions for the purpose of data analysis. In SMFS, the commonly used and basic framework to bridge nanoscopic force data to macroscopic parameters was worked out by Evans and Ritchie, which was built upon the work published by Bell and Kramers. The Kramers-Bell-Evans model is based on the interaction between a receptor (*R*) and a ligand (*L*), forming a complex (*RL*). At thermal equilibrium, the association and dissociation rates are constant:

$$L + R \xleftarrow{k_{on}^0} RL \tag{1.1}$$

where  $k_{on}^0$  and  $k_{off}^0$  are the corresponding rate constants. Applying an external force, f, to this complex is expected to lower the free activation barrier ( $\Delta G^{\neq}$ ) of the interactions by the quantity  $f x_{\beta}$ :

$$\Delta G^{\neq}(f) = \Delta G^{\neq} - f x_{\beta} \tag{1.2}$$

with  $x_{\beta}$  being the distance between the potential minimum and the maximum. In the absence of force, the dissociation rate constant depends on  $\Delta G^{\neq}$  as:

$$k_{off}^{0} \propto \exp\left(-\frac{\Delta G^{\neq}}{k_{B}T}\right) \tag{1.3}$$

where  $k_B$  is the Boltzmann constant and T is the temperature. The force dependent offrate, also known as Bell rate, then becomes:<sup>83</sup>

$$k_{off}(f) = k_{off}^{0} \exp\left(-\frac{fx_{\beta}}{k_{B}T}\right)$$
 (1.4)

The dissociation of *RL* complex, considered as a thermally activated decay process, is governed by the first-order reaction kinetics:

$$\frac{dp(t)}{dt} = -k_{off}(f(t))p(t) \tag{1.5}$$

Here, p(t) is the probability that the bond is intact at time t, and re-association of R and L is neglected. Due to fast molecular relaxation times in comparison to the temporal evolution of the force, the dissociation of the complex is only governed by the force currently applied. Furthermore, since in SMFS experiments, the AFM cantilever is typically retracted at a constant velocity (v), the cantilever displacement (z) can be written as:

$$z = vt \tag{1.6}$$

Therefore, the force (f(t)) is only affected by the current displacement (z(t)) of the cantilever and not its velocity (v):

$$f(t) = f(vt) = f(z(t))$$
(1.7)

Since the cantilever deflection is easily convertible to force in SMFS experiments, time is substituted by force ( $dt \rightarrow df$ ) to solve Eq. (1.5):

$$df = \frac{df}{dz}\frac{dz}{dt}dt = k_{eff}vdt \tag{1.8}$$

 $k_{eff}$  and v are the effective spring constant and the pull-off velocity, the product of which is known as the loading rate, r. Solving Eq. (1.5) results in:

$$p(f) = \exp\left\{-\frac{k_{off}}{r} \frac{\exp\left(\frac{x_{\beta}f}{k_{B}T}\right) - \exp\left(\frac{x_{\beta}f_{\min}}{k_{B}T}\right)}{\frac{x_{\beta}f}{k_{B}T}}\right\}$$
(1.9)

The theoretical probability distribution of the dissociation forces is the negative derivative of Eq. (1.9) with respect to force, i.e.  $-\frac{dp(f)}{df}$ . By finding the peak of the predicted force distribution, the most probable dissociation force,  $F_{max}$ , can be expressed in terms of the dissociation rate constant  $k_{off}^0$ . To derive this expression, Strunz et al. evaluated the second derivative of Eq. (1.9) with respect to force and set it to zero:

$$F_{\text{max}} = \frac{k_B T}{x_\beta} \ln \left( \frac{x_\beta r}{k_{off}^0 k_B T} \right)$$
 (1.10)

The result shown by Eq. (1.10) is significant as it demonstrates that the most probable dissociation forces increase with pulling velocities as  $\ln(r)$ . Consequently, it is essential to repeat the experiments at numerous pulling velocities, spanning several orders of magnitude, in order to make a good estimate for  $k_{off}^0$  and  $x_\beta$ . The magnitude of  $x_\beta$  and  $k_{off}^0$  can be determined from a semi-logarithmical plot of the most probable dissociation forces versus the loading rate. 85

As we discuss later in this thesis, our single-stranded DNA peeling experiments and model are quite different than the Bell model discussed in this introduction section. For example, instead of having a single dissociation event, we find that desorption of individual monomers result in a multi-well energy landscape when peeling ssDNA from a surface. To calculate the binding energy per base of ssDNA, we use a statistical-mechanical model.<sup>86</sup> This model assumes that the peeling is an equilibrium process in which the individual bases have sufficient time to sample all conformations when they are in or out of contact with the surface. In contrast, we consider a complete detachment or the removal of the final few bases in these experiments, which appear as an abrupt jump from a constant force plateau to zero force, to be a non-equilibrium process.

# 1.5 Modeling the Interactions between Single Stranded DNA and Solid Surfaces

Understanding ssDNA interactions with graphitic carbon surfaces is important in developing technologies that are based on these bio-nanomaterial hybrids. Computational approaches to study such interactions often involve large-scale data driven

analysis and dynamic simulations that are based on experimental knowledge of identified interactions. Theoretical predictions for these systems are typically based on studies that use density functional theory, <sup>83, 86, 87</sup> Monte Carlo, or molecular dynamics (MD) simulations. <sup>84, 85</sup>

In calculating the time dependent behavior of a molecular system using all-atom MD simulations, the large-scale atomic/molecular massively parallel simulator (LAMMPS)<sup>81</sup> and the chemistry at Harvard molecular mechanics (CHARMM)<sup>82</sup> programs are the most prominent computational methods used. The popularity of MD simulation stems from their ability to generate microscopic information on the atomic positions and velocities. This information is then convertible into macroscopic observables such as pressure, energy, heat capacities, etc. through statistical mechanics. As a result, scientists have obtained detailed information on not only the structure and fluctuations of proteins and nucleic acids, but also the conformational changes, dynamics and thermodynamics of biological molecules and their complexes.

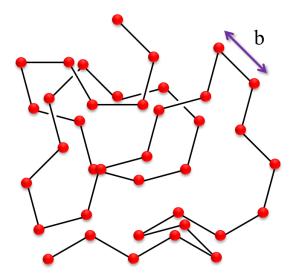


**Figure 1.5.** The freely jointed chain consists of identical segments of length b, joined together by freely rotating hinges.

The all atom computational study of such complex system, although successful, can be quite expensive (in terms of time and computational resources). An alternative method for modeling our ssDNA-CNT system is to describe the three main components (i.e. the molecule, the substrate, and the surrounding environment) by using approximations. The idealized polymer models, commonly used to describe molecules are the freely jointed chain (FJC) the wormlike chain (WLC), and the rotational isomeric state model (RIS). Of these three models, the FJC is the most suitable starting point for a single stranded DNA, in which the molecule is defined as a connection of n rigid subunits of (Kuhn) length b. The elasticity of this chain is entropic. Furthermore, the average end-to-end distance  $\langle R_z \rangle$  of this chain under an external force, f, is described by the Langevin equation:

$$\langle R_z \rangle = b \, n \left( \coth \frac{f \, b}{k_B T} - \frac{k_B T}{f \, b} \right)$$
 (1.1)

To describe the substrates used in SMFS experiments, an appropriate representation of their surface energy potentials is needed. For example, a graphite surface can be modeled as an ideal, frictionless, flat surface to which the ssDNA nucleobases are strongly adsorbed. The experimentally determined adsorption energies of the FJC to the surface can then be implemented into the Lennard Jones (9,3) potential <sup>90, 91</sup> to describe the strength of these interactions (the details of our derivations are discussed in Chapter 4).

Lastly, collisions of macromolecules with themselves and/or those in their surrounding environment can be represented through a simple heat bath as described by

Langevin or Brownian dynamics. In these models, the explicit solvent molecules in the system are replaced with a stochastic force and a viscous drag. 92-94 In Langevin dynamics, the relative strength in the inertial forces with respect to random forces is determined from the magnitude of the frictional forces. In other words, the system is best described by the inertial regime when the frictional contributions are small, while it eventually becomes governed by the diffusive or Brownian regime at large enough frictional forces. To determine whether the frictional forces are high enough to operate in the Brownian regime, one must first confirm that the momentum relaxation is much faster than the position relaxation. In the high friction Brownian limit, the solvent effects are large, the inertial term is ignored, and larger time steps can be used than for molecular and Langevin dynamics simulations. Furthermore, friction is related to fluctuations of the random force through the fluctuation dissipation theorem, which assumes that the Brownian particle is randomly moving about thermal equilibrium. In Chapter 4, the procedure for implementation of this theory to simulate our peeling experiments is discussed in detail.

## 1.6 Scope of the Dissertation

The topic of interest discussed in this dissertation concerns the interactions between single stranded DNA and single walled carbon nanotubes. The major components of this research topic are addressed individually in each chapter. The second chapter describes our single molecule force spectroscopy studies used to directly quantify the binding strength of ssDNA homopolymers to a flat graphite surface. To investigate the interaction of these biopolymers with SWCNTs, we modified silicon wafers with self-

assembled monolayers on which pristine nanotubes were deposited. Upon characterization of these substrates, we performed SMFS experiments to measure the ssDNA nucleotide interactions with SWCNTs and SAM surfaces, described in Chapter 3. In Chapter 4, we developed a Brownian dynamics model to describe the elastic response of a polymeric chain that is under an externally applied force and strongly adsorbed to a flat surface. To extract information on the dynamics of ssDNA-graphite interactions, we used values for the free energy of binding that were comparable to those previously obtained from our SMFS experiments. Chapter 5 focuses on developing our Brownian dynamics model further to study the effect of i) dimensionality, and ii) modes of applying force (i.e. point force vs. distributed force) on the chain's stretching response. As our future work, in Chapter 6, we discuss our theoretical and exploratory studies, so far, of the effect of surface friction on the dynamics of removal of a polymeric chain from a graphitic surface.

## 1.7 References

- (1) Ajayan, P. M., Nanotubes from Carbon. *Chem. Rev.* **1999**, *99*, 1787-1799.
- (2) Sinha, N.; Yeow, J. T. W., Carbon nanotubes for biomedical applications. *IEEE Trans Nanobioscience* **2005**, *4*, 180-95.
- (3) Tu, X.; Manohar, S.; Jagota, A.; Zheng, M., DNA sequence motifs for structure-specific recognition and separation of carbon nanotubes. *Nature* **2009**, *460*, 250-253.
- (4) Arnold, M. S.; Green, A. A.; Hulvat, J. F.; Stupp, S. I.; Hersam, M. C., Sorting carbon nanotubes by electronic structure using density differentiation. *Nat. Nanotechnol.* **2006**, *1*, 60-65.
- (5) Krupke, R.; Hennrich, F.; Loehneysen, H. V.; Kappes, M. M., Separation of metallic from semiconducting single-walled carbon nanotubes. *Science* **2003**, *301*, 344-347.
- (6) Collins, P. G.; Arnold, M. S.; Avouris, P., Engineering carbon nanotubes and nanotube circuits using electrical breakdown. *Science* **2001**, *292*, 706-709.
- (7) Miyata, Y.; Kawai, T.; Miyamoto, Y.; Yanagi, K.; Maniwa, Y.; Kataura, H., Chirality-Dependent Combustion of Single-Walled Carbon Nanotubes. *J. Phys. Chem. C* **2007**, *111*, 9671-9677.
- (8) Bonaccorso, F.; Hasan, T.; Tan, P. H.; Sciascia, C.; Privitera, G.; Di, M. G.; Gucciardi, P. G.; Ferrari, A. C., Density Gradient Ultracentrifugation of Nanotubes: Interplay of Bundling and Surfactants Encapsulation. *J. Phys. Chem. C* **2010**, *114*, 17267-17285.

- (9) Battigelli, A.; Russier, J.; Venturelli, E.; Fabbro, C.; Petronilli, V.; Bernardi, P.; Da, R. T.; Prato, M.; Bianco, A., Peptide-based carbon nanotubes for mitochondrial targeting. *Nanoscale* **2013**, *5*, 9110-9117.
- (10) Huang, X. H.; Johnson, R. P.; Song, S. I.; Kim, I., Noncovalent functionalization of carbon nanotubes by fluorescent polypeptides: supramolecular conjugates with pH-dependent absorbance and fluorescence. *J. Nanosci. Nanotechnol.* **2013**, *13*, 7406-7412.
- (11) Dayani, Y.; Malmstadt, N., Lipid bilayers covalently anchored to carbon nanotubes. *Langmuir* **2012**, *28*, 8174-8182.
- (12) Skandani, A. A.; Zeineldin, R.; Al-Haik, M., Effect of Chirality and Length on the Penetrability of Single-Walled Carbon Nanotubes into Lipid Bilayer Cell Membranes.

  Langmuir 2012, 28, 7872-7879.
- (13) Zheng, M.; Jagota, A.; Semke, E. D.; Diner, B. A.; McLean, R. S.; Lustig, S. R.; Richardson, R. E.; Tassi, N. G., DNA-assisted dispersion and separation of carbon nanotubes. *Nat. Mater.* **2003**, *2*, 338-342.
- (14) Zheng, M.; Semke, E. D., Enrichment of Single Chirality Carbon Nanotubes. *J. Am. Chem. Soc.* **2007**, *129*, 6084-6085.
- (15) Zheng, M.; Jagota, A.; Strano, M. S.; Santos, A. P.; Barone, P.; Chou, S. G.; Diner, B. A.; Dresselhaus, M. S.; McLean, R. S.; Onoa, G. B.; Samsonidze, G. G.; Semke, E. D.; Usrey, M.; Walls, D. J., Structure-Based Carbon Nanotube Sorting by Sequence-Dependent DNA Assembly. *Science* **2003**, *302*, 1545-1548.
- (16) Huang, X.; McLean, R. S.; Zheng, M., High-Resolution Length Sorting and Purification of DNA-Wrapped Carbon Nanotubes by Size-Exclusion Chromatography. *Anal. Chem.* **2005**, *77*, 6225-6228.

- (17) Kim, S. N.; Kuang, Z.; Grote, J. G.; Farmer, B. L.; Naik, R. R., Enrichment of (6,5) Single Wall Carbon Nanotubes Using Genomic DNA. *Nano Lett.* **2008**, 8, 4415-4420.
- (18) Tu, X.-M.; Hight, W. A. R.; Khripin, C. Y.; Zheng, M., Evolution of DNA Sequences Toward Recognition of Metallic Armchair Carbon Nanotubes. *J. Am. Chem. Soc.* **2011**, *133*, 12998-13001.
- (19) Khripin, C. Y.; Zheng, M.; Jagota, A., Deposition and meniscus alignment of DNA-CNT on a substrate. *J. Colloid Interface Sci.* **2009**, *330*, 255-265.
- (20) Muller, K.; Malik, S.; Richert, C., Sequence-Specifically Addressable Hairpin DNA-Single-Walled Carbon Nanotube Complexes for Nanoconstruction. *ACS Nano* **2010**, *4*, 649-656.
- (21) Han, S.-p.; Maune, H. T.; Barish, R. D.; Bockrath, M.; Goddard, W. A., DNA-Linker-Induced Surface Assembly of Ultra Dense Parallel Single Walled Carbon Nanotube Arrays. *Nano Lett.* **2012**, *12*, 1129-1135.
- (22) Iijima, S., Helical microtubules of graphitic carbon. *Nature* **1991**, *354*, 56-8.
- (23) Yan, Y.; Chan-Park, M. B.; Zhang, Q., Advances in carbon-nanotube assembly. *Small* **2007**, *3*, 24-42.
- (24) Belin, T.; Epron, F., Characterization methods of carbon nanotubes: a review. *Mater. Sci. Eng.*, *B* **2005**, *B119*, 105-118.
- (25) Odom, T. W.; Huang, J.-L.; Kim, P.; Lieber, C. M., Atomic structure and electronic properties of single-walled carbon nanotubes. *Nature* **1998**, *391*, 62-64.
- (26) Odom, T. W.; Huang, J.-L.; Kim, P.; Lieber, C. M., Structure and Electronic Properties of Carbon Nanotubes. *J. Phys. Chem. B* **2000**, *104*, 2794-2809.

- (27) Javey, A.; Guo, J.; Farmer, D. B.; Wang, Q.; Wang, D.; Gordon, R. G.; Lundstrom, M.; Dai, H., Carbon nanotube field-effect transistors with integrated Ohmic contacts and high-k gate dielectrics. *Nano Lett.* **2004**, *4*, 447-450.
- (28) Hu, L.; Hecht, D. S.; Gruener, G., Carbon Nanotube Thin Films: Fabrication, Properties, and Applications. *Chem. Rev.* **2010**, *110*, 5790-5844.
- (29) O'Regan, B.; Graetzel, M., A low-cost, high-efficiency solar cell based on dye-sensitized colloidal titanium dioxide films. *Nature* **1991**, *353*, 737-40.
- (30) Chien, Y.-M.; Lefevre, F.; Shih, I.; Izquierdo, R., A solution processed top emission OLED with transparent carbon nanotube electrodes. *Nanotechnology* **2010**, *21*, 134020/1-134020/5.
- (31) Scardaci, V.; Coull, R.; Coleman, J. N., Very thin transparent, conductive carbon nanotube films on flexible substrates. *Appl. Phys. Lett.* **2010,** *97*, 023114/1-023114/3.
- (32) Fuhrer, M. S.; Nygard, J.; Shih, L.; Forero, M.; Yoon, Y.-G.; Mazzoni, M. S. C.; Choi, H. J.; Ihm, J.; Louie, S. G.; Zettl, A.; McEuen, P. L., Crossed nanotube junctions. *Science* **2000**, 288, 494-497.
- (33) Gao, B.; Chen, Y. F.; Fuhrer, M. S.; Glattli, D. C.; Bachtold, A., Four-point resistance of individual single-wall carbon nanotubes. *Phys Rev Lett* **2005**, *95*, 196802.
- (34) Yu, X.; Ye, S., Recent advances in activity and durability enhancement of Pt/C catalytic cathode in PEMFC. *J. Power Sources* **2007**, *172*, 145-154.
- (35) Winter, M.; Brodd, R. J., What are batteries, fuel cells, and supercapacitors? *Chem. Rev.* **2004**, *104*, 4245-4269.

- (36) Neergat, M.; Shukla, A. K.; Gandhi, K. S., Platinum-based alloys as oxygen-reduction catalysts for solid-polymer-electrolyte direct methanol fuel cells. *J. Appl. Electrochem.* **2001**, *31*, 373-378.
- (37) Ji, X.; Lee, K. T.; Holden, R.; Zhang, L.; Zhang, J.; Botton, G. A.; Couillard, M.; Nazar, L. F., Nanocrystalline intermetallics on mesoporous carbon for direct formic acid fuel cell anodes. *Nat. Chem.* **2010**, *2*, 286-293.
- (38) Gong, K.; Du, F.; Xia, Z.; Durstock, M.; Dai, L., Nitrogen-Doped Carbon Nanotube Arrays with High Electrocatalytic Activity for Oxygen Reduction. *Science* **2009**, *323*, 760-764.
- (39) Qu, L.; Liu, Y.; Baek, J.-B.; Dai, L., Nitrogen-Doped Graphene as Efficient Metal-Free Electrocatalyst for Oxygen Reduction in Fuel Cells. *ACS Nano* **2010**, *4*, 1321-1326.
- (40) Heller, D. A.; Jin, H.; Martinez, B. M.; Patel, D.; Miller, B. M.; Yeung, T.-K.; Jena, P. V.; Hoebartner, C.; Ha, T.; Silverman, S. K.; Strano, M. S., Multimodal optical sensing and analyte specificity using single-walled carbon nanotubes. *Nat. Nanotechnol.* **2009**, *4*, 114-120.
- (41) Guiseppi-Elie, A.; Lei, C.; Baughman, R. H., Direct electron transfer of glucose oxidase on carbon nanotubes. *Nanotechnology* **2002**, *13*, 559-564.
- (42) Gooding, J. J.; Wibowo, R.; Liu, J.; Yang, W.; Losic, D.; Orbons, S.; Mearns, F. J.; Shapter, J. G.; Hibbert, D. B., Protein electrochemistry using aligned carbon nanotube arrays. *J. Am. Chem. Soc.* **2003**, *125*, 9006-9007.

- (43) Goldsmith, B. R.; Coroneus, J. G.; Khalap, V. R.; Kane, A. A.; Weiss, G. A.; Collins, P. G., Conductance-Controlled Point Functionalization of Single-Walled Carbon Nanotubes. *Science* **2007**, *315*, 77-81.
- (44) Bhirde, A. A.; Patel, V.; Gavard, J.; Zhang, G.; Sousa, A. A.; Masedunskas, A.; Leapman, R. D.; Weigert, R.; Gutkind, J. S.; Rusling, J. F., Targeted Killing of Cancer Cells in Vivo and in Vitro with EGF-Directed Carbon Nanotube-Based Drug Delivery. *ACS Nano* **2009**, *3*, 307-316.
- (45) Liu, G.; Shen, H.; Mao, J.; Zhang, L.; Jiang, Z.; Sun, T.; Lan, Q.; Zhang, Z., Transferrin Modified Graphene Oxide for Glioma-Targeted Drug Delivery: In Vitro and in Vivo Evaluations. *ACS Appl. Mater. Interfaces* **2013**, *5*, 6909-6914.
- (46) Kavitha, T.; Haider, A. S. I.; Park, S.-Y., pH-Sensitive nanocargo based on smart polymer functionalized graphene oxide for site-specific drug delivery. *Phys. Chem. Chem. Phys.* **2013**, *15*, 5176-5185.
- (47) Wu, W.; Wieckowski, S.; Pastorin, G.; Benincasa, M.; Klumpp, C.; Briand, J.-P.; Gennaro, R.; Prato, M.; Bianco, A., Targeted delivery of amphotericin B to cells by using functionalized carbon nanotubes. *Angew. Chem., Int. Ed.* **2005**, *44*, 6358-6362.
- (48) Liu, Z.; Sun, X.; Nakayama-Ratchford, N.; Dai, H., Supramolecular Chemistry on Water-Soluble Carbon Nanotubes for Drug Loading and Delivery. *ACS Nano* **2007**, *1*, 50-56.
- (49) Choi, J. H.; Strano, M. S., Solvatochromism in single-walled carbon nanotubes. *Applied Physics Letters* **2007**, *90*, 223114.
- (50) Barone, P. W.; Baik, S.; Heller, D. A.; Strano, M. S., Near-infrared optical sensors based on single-walled carbon nanotubes. *Nat. Mater.* **2005**, *4*, 86-92.

- (51) Heller, D. A.; Jeng, E. S.; Yeung, T.-K.; Martinez, B. M.; Moll, A. E.; Gastala, J.
  B.; Strano, M. S., Optical Detection of DNA Conformational Polymorphism on Single-Walled Carbon Nanotubes. *Science* 2006, *311*, 508-511.
- (52) Saenger, W., *Principles of Nucleicd Acid Structure*. SpringerVerlag: New York, 1984.
- (53) Senthilkumar, K.; Grozema, F. C.; Guerra, C. F.; Bickelhaupt, F. M.; Lewis, F. D.; Berlin, Y. A.; Ratner, M. A.; Siebbeles, L. D. A., Absolute Rates of Hole Transfer in DNA. *J. Am. Chem. Soc.* **2005**, *127*, 14894-14903.
- (54) Manohar, S.; Mantz, A. R.; Bancroft, K. E.; Hui, C.-Y.; Jagota, A.; Vezenov, D. V., Peeling Single-Stranded DNA from Graphite Surface to Determine Oligonucleotide Binding Energy by Force Spectroscopy. *Nano Lett.* **2008**, *8*, 4365-4372.
- (55) Cathcart, H.; Nicolosi, V.; Hughes, J. M.; Blau, W. J.; Kelly, J. M.; Quinn, S. J.; Coleman, J. N., Ordered DNA Wrapping Switches on Luminescence in Single-Walled Nanotube Dispersions. *J. Am. Chem. Soc.* **2008**, *130*, 12734-12744.
- (56) Zhao, X., Self-Assembly of DNA Segments on Graphene and Carbon Nanotube Arrays in Aqueous Solution: A Molecular Simulation Study. *J. Phys. Chem. C* **2011**, *115*, 6181-6189.
- (57) Roxbury, D.; Tu, X.; Zheng, M.; Jagota, A., Recognition Ability of DNA for Carbon Nanotubes Correlates with Their Binding Affinity. *Langmuir* **2011**, *27*, 8282-8293.
- (58) Johnson, R. R.; Johnson, A. T. C.; Klein, M. L., The Nature of DNA-Base-Carbon-Nanotube Interactions. *Small* **2010**, *6*, 31-34.

- (59) Gigliotti, B.; Sakizzie, B.; Bethune, D. S.; Shelby, R. M.; Cha, J. N., Sequence-Independent Helical Wrapping of Single-Walled Carbon Nanotubes by Long Genomic DNA. *Nano Lett.* **2006**, *6*, 159-164.
- (60) Singh, P.; Kumar, J.; Toma, F. M.; Raya, J.; Prato, M.; Fabre, B.; Verma, S.; Bianco, A., Synthesis and Characterization of Nucleobase-Carbon Nanotube Hybrids. *J. Am. Chem. Soc.* **2009**, *131*, 13555-13562.
- (61) Chen, Y.; Liu, H.; Ye, T.; Kim, J.; Mao, C., DNA-Directed Assembly of Single-Wall Carbon Nanotubes. *J. Am. Chem. Soc.* **2007**, *129*, 8696-8697.
- (62) Khripin, C. Y.; Manohar, S.; Zheng, M.; Jagota, A., Measurement of Electrostatic Properties of DNA-Carbon Nanotube Hybrids by Capillary Electrophoresis. *J. Phys. Chem. C* **2009**, *113*, 13616-13621.
- (63) Lustig, S. R.; Jagota, A.; Khripin, C.; Zheng, M., Theory of structure-based carbon nanotube separations by ion-exchange chromatography of DNA/CNT hybrids. *J. Phys. Chem. B* **2005**, *109*, 2559-2566.
- (64) Roxbury, D.; Manohar, S.; Jagota, A., Molecular Simulation of DNA β-Sheet and β-Barrel Structures on Graphite and Carbon Nanotubes. *J. Phys. Chem. C* **2010**, *114*, 13267-13276.
- (65) Roxbury, D.; Jagota, A.; Mittal, J., Sequence-Specific Self-Stitching Motif of Short Single-Stranded DNA on a Single-Walled Carbon Nanotube. *J. Am. Chem. Soc.* **2011**, *133*, 13545-13550.
- (66) Roxbury, D.; Mittal, J.; Jagota, A., Molecular-Basis of Single-Walled Carbon Nanotube Recognition by Single-Stranded DNA. *Nano Lett.* **2012**, *12*, 1464-1469.

- (67) Ashkin, A.; Dziedzic, J. M., Optical trapping and manipulation of viruses and bacteria. *Science* **1987**, *235*, 1517-20.
- (68) Gosse, C.; Croquette, V., Magnetic tweezers: micromanipulation and force measurement at the molecular level. *Biophys. J.* **2002**, *82*, 3314-3329.
- (69) Binning, G.; Rohrer, H.; Gerber, C.; Weibel, E., Surface studies by scanning tunneling microscopy. *Phys. Rev. Lett.* **1982**, *49*, 57-61.
- (70) Binnig, G.; Gerber, C.; Stoll, E.; Albrecht, T. R.; Quate, C. F., Atomic resolution with atomic force microscope. *Europhys. Lett.* **1987**, *3*, 1281-6.
- (71) Sader, J. E.; Chon, J. W. M.; Mulvaney, P., Calibration of rectangular atomic force microscope cantilevers. *Rev. Sci. Instrum.* **1999**, *70*, 3967-3969.
- (72) Heinz, W. F.; Hoh, J. H., Spatially resolved force spectroscopy of biological surfaces using the atomic force microscope. *Trends Biotechnol.* **1999**, *17*, 143-150.
- (73) Zlatanova, J.; Lindsay, S. M.; Leuba, S. H., Single molecule force spectroscopy in biology using the atomic force microscope. *Prog. Biophys. Mol. Biol.* **2000**, *74*, 37-61.
- (74) Santos, N. C.; Castanho, M. A. R. B., An overview of the biophysical applications of atomic force microscopy. *Biophys. Chem.* **2004**, *107*, 133-149.
- (75) Parot, P.; Dufrene, Y. F.; Hinterdorfer, P.; Le, G. C.; Navajas, D.; Pellequer, J.-L.; Scheuring, S., Past, present and future of atomic force microscopy in life sciences and medicine. *J. Mol. Recognit.* **2007**, *20*, 418-431.
- (76) Poggi, M. A.; McFarland, A. W.; Colton, J. S.; Bottomley, L. A., A method for calculating the spring constant of atomic force microscopy cantilevers with a nonrectangular cross section. *Anal. Chem.* **2005**, *77*, 1192-1195.

- (77) Burnham, N. A.; Chen, X.; Hodges, C. S.; Matei, G. A.; Thoreson, E. J.; Roberts, C. J.; Davies, M. C.; Tendler, S. J. B., Comparison of calibration methods for atomic-force microscopy cantilevers. *Nanotechnology* **2003**, *14*, 1-6.
- (78) Cleveland, J. P.; Manne, S.; Bocek, D.; Hansma, P. K., A nondestructive method for determining the spring constant of cantilevers for scanning force microscopy. *Rev. Sci. Instrum.* **1993**, *64*, 403-5.
- (79) Hutter, J. L.; Bechhoefer, J., Calibration of atomic-force microscope tips. *Rev. Sci. Instrum.* **1993**, *64*, 1868-73.
- (80) Ritzefeld, M.; Walhorn, V.; Anselmetti, D.; Sewald, N., Analysis of DNA interactions using single-molecule force spectroscopy. *Amino Acids* **2013**, *44*, 1457-1475.
- (81) Ralston, J.; Larson, I.; Rutland, M. W.; Feiler, A. A.; Kleijn, M., Atomic force microscopy and direct surface force measurements. *Pure Appl. Chem.* **2005**, *77*, 2149-2170.
- (82) Evans, E.; Ritchie, K., Dynamic strength of molecular adhesion bonds. *Biophys*. *J.* **1997**, 72, 1541-1555.
- (83) Bell, G. I., Models for the specific adhesion of cells to cells. *Science* **1978**, *200*, 618-27.
- (84) Kramers, H. A., Brownian motion in a field of force and the diffusion model of chemical reactions. *Physica* **1940**, *7*, 284-304.
- (85) Strunz, T.; Oroszlan, K.; Schumakovitch, I.; Guntherodt, H. J.; Hegner, M., Model energy landscapes and the force-induced dissociation of ligand-receptor bonds. *Biophys. J.* **2000**, *79*, 1206-1212.

- (86) Manohar, S.; Jagota, A., Sequence-dependent force response during peeling of single-stranded DNA from graphite. *Phys Rev E Stat Nonlin Soft Matter Phys* **2010**, *81*, 021805.
- (87) Iliafar, S.; Vezenov, D.; Jagota, A., Brownian Dynamics Simulation of Peeling a Strongly-Adsorbed Polymer Molecule from a Frictionless Substrate. *Langmuir* **2013**, 29, 1435-1445.
- (88) Mate, C. M.; McClelland, G. M.; Erlandsson, R.; Chiang, S., Atomic-scale friction of a tungsten tip on a graphite surface. *Phys. Rev. Lett.* **1987**, *59*, 1942-5.
- (89) Krim, J.; Solina, D. H.; Chiarello, R., Nanotribology of a krypton monolayer: a quartz-crystal microbalance study of atomic-scale friction. *Phys. Rev. Lett.* **1991,** *66*, 181-4.
- (90) Morita, S.; Fujisawa, S.; Sugawara, Y., Spatially quantized friction with a lattice periodicity. *Surf. Sci. Rep.* **1996**, *23*, 1-41.
- (91) Kerssemakers, J.; De, H. J. T. M., Atomic force microscopy imaging of transition metal layered compounds: a two-dimensional stick-slip system. *Appl. Phys. Lett.* **1995**, 67, 347-9.
- (92) Holscher, H.; Schwarz, U. D.; Zworner, O.; Wiesendanger, R., Consequences of the stick-slip movement for the scanning force microscopy imaging of graphite. *Phys. Rev. B: Condens. Matter Mater. Phys.* **1998**, *57*, 2477-2481.
- (93) Socoliuc, A.; Bennewitz, R.; Gnecco, E.; Meyer, E., Transition from stick-slip to continuous sliding in atomic friction: entering a new regime of ultralow friction. *Phys Rev Lett* **2004**, *92*, 134301.

(94) Sung, I.-H.; Lee, H.-S.; Kim, D.-E., Effect of surface topography on the frictional behavior at the micro/nano-scale. *Wear* **2003**, *254*, 1019-1031.

# **Chapter 2 Quantifying Interactions between DNA Oligomers and Graphite Surface Using Single Molecule Force Spectroscopy**

The work described in this chapter has been published in "Quantifying Interactions between DNA Oligomers and Graphite Surface Using Single Molecule Force Spectroscopy" by Sara Iliafar, Kyle Wagner, Suresh Manohar, Anand Jagota, and Dmitri Vezenov, *The Journal of Physical Chemistry C* **2012** 116 (26), 13896-13903.

In single molecule force spectroscopy experiments, force probes chemically modified with synthetic, single-stranded DNA oligomers produced characteristic steadystate forces connected by abrupt steps between plateaus, as the probes moved away from a graphite substrate. The force plateaus represent peeling of a small number of polymer molecules from the flat surface. The final force jump in the retraction region of the forcedistance curves can be attributed to a single DNA molecule detaching from the graphite surface. Previously, Manohar et. al (Nano Letters, 2008, 8, 4365) reported the peeling forces of the pyrimidine oligomers as  $85.3 \pm 4.7$  pN and  $60.8 \pm 5.5$  pN for polythymine and polycytosine, respectively. We measured the force-distance curves for purine oligomers on a graphite surface and found the peeling forces to be 78.5 ± 5.0 pN and  $66.4 \pm 1.4$  pN for polyadenine and polyguanine, respectively. Using a refined model for peeling a single freely jointed polymer chain from a frictionless substrate, we determined a ranking of the effective average binding energy per nucleotide for all four bases as  $T \ge A > G \ge C (11.3 \pm 0.8 \ k_B T, 9.9 \pm 0.4 \ k_B T, 8.3 \pm 0.2 \ k_B T, and 7.5 \pm 0.8 \ k_B T, respectively).$ The binding energy determined from the peeling force data did not scale with the size of the base. The distribution of peeling forces of polyguanine from the graphite surface was

unusually broad in comparison to the other homopolymers, and often with inconsistent chain extensions, possibly indicating the presence of secondary structures (intra- or inter-molecular) for this sequence.

# 2.1 Introduction

The interaction between biological molecules and nano- or macro-sized surfaces is a dynamic and commonly occurring process in nature, and if well understood, it can be used to develop novel biosensing technologies and therapeutics. The attachment of biomolecules to nanomaterial substrates such as gold nanoparticles and single walled carbon nanotubes (SWCNTs) greatly enhances their structural functionality, making it possible for these hybrids to be used in biological processes. The formation of stable dispersions of SWCNTs formed by helical wrapping of single-stranded DNA (ssDNA) around the tubes<sup>1</sup> makes SWCNTs highly compatible for in vivo systems and also provides a means for tube sorting and positioning<sup>2, 3</sup>. CNT-DNA complexes have potential applications of broad biomedical impact, such as, transport of biomolecular agents into cells, 4-6 optical sensing for biological systems, 7 rapid DNA sequencing, 8 and diagnosis and therapeutic treatment of diseases, such as cancer, through imaging and targeted drug delivery. 4, 5, 9-14 Rational development of these applications will greatly benefit from quantitative understanding of the interactions that occur between the CNT and biomolecules.

It has previously been shown that single molecule force spectroscopy (SMFS) is an appropriate method to directly measure the force required to overcome the binding free energy between peptides and DNA oligomers and a solid substrate as the molecule is separated from a surface e.g. graphite. These single molecule experiments are analogous to a classical macroscopic peeling test, including their conceptual interpretation. The SMFS experiments, we assumed that the graphite substrate serves as an appropriate analog for SWCNTs used in bulk dispersion experiments. Within the pyrimidine family, using SMFS, we were previously able to differentiate between 3'-poly(dT50) and 3'-poly(dC50) – with peeling forces of 85.3  $\pm$  4.7 pN and 60.8  $\pm$  5.5 pN, respectively, which we interpreted as corresponding to the binding free energies per base of 11.5  $\pm$  0.6 k<sub>B</sub>T and 8.3  $\pm$  0.7 k<sub>B</sub>T. As a shorthand notation in this chapter, we will use an oligomer naming convention where the point of attachment to the force probe is listed first and the number of bases in the oligomer chain is signified by a subscript.

Simulations have shown that the binding strength of homopolymers to graphite follow a different sequence: T>A>C, 1, 26 than that of individual nucleotides obtained from solution studies: G>A>T>C, 27-30 or of nucleobases and nucleosides determined by isothermal titration calorimetry: G>A>C>T. 31 Furthermore, guanine-rich DNA sequences are known to form G-quartets and, in some cases, they form quadruplex structures by the vertical stacking of G-quartets. 32 Since purines are larger and chemically different from pyrimidines, it is interesting to use the SMFS technique to compare the interaction between homopolymer purines (polyadenine and polyguanine) and graphite with reported observations for homopolymer pyrimidines and graphite in order to understand differences between observed trends for monomers and predict the behavior for DNA oligomers in complexation with CNT.

By its nature, single-molecule force spectroscopy provides properties of the system from measurements performed on individual molecules and is thus complementary to bulk solution techniques that yield averages over a population. In the context of adsorption of oligomers and polymers, force spectroscopy allows measurements where solution techniques might be limited. For example, solution techniques work better for shorter oligomers (i.e. <20 bases) or single bases, whereas SMFS can be used effectively to peel long macromolecules that may require untenably long time to achieve equilibrium in bulk samples.

Many studies using high resolution scanning tunneling microscopy and atomic force microscopy (AFM) show that when bases are adsorbed on atomically flat hydrophobic surfaces (e.g. graphite or  $MoS_2$ ), they interact with each other to form dimers, which in turn can form highly ordered monolayers. <sup>1, 15, 16, 25-29, 33-36</sup> However, not much is known about the base-base interaction with surfaces when they are attached to a phosphate backbone. Higher order hydrogen bonded and stacked structures are known for polyguanine and hypothesized for special sequences. <sup>30, 37</sup> Therefore, it is interesting to see whether such structural features will be reflected in the SMFS measurements as they are the likely reason for sequence dependence of the binding strengths. In this chapter, we report on the use of SMFS to measure the peeling forces of the purine homopolymers, 3'-poly( $dA_{50}$ ) and 5'-poly( $dG_{100}$ ), in order to complete a full ranking of the four homopolymer chains.

# 2.2 Experimental Section

## 2.2.1 Materials

Grade 2 highly ordered pyrolytic graphite was purchased from Structure Probe, Inc. (West Chester, PA). Disulfide-protected thiol-modified DNA was resuspended in Milli-Q deionized (DI) water upon receipt from Integrated DNA Technologies, Inc. (Coralville, IA), aliquoted and stored at -20°C. DNA molecules studied in this work were: 5'-poly(dT<sub>50</sub>), 5'-poly(dT<sub>100</sub>), 3'-poly(dA<sub>50</sub>), and 5'-poly(dG<sub>100</sub>). Tris(2-carboxyethyl)phosphine hydrochloride (TCEP), 98% purity, was used as-received from TCI America (Portland, OR). Mercaptohexanoic acid (MHA), 90% purity, was used as received from Sigma Aldrich (St. Louis, MO) and stored at -4° C. Mono- and di-basic sodium phosphate and sodium chloride in ultra-pure bio-grade were purchased from J.T. Baker (Phillipsburg, NJ).

## 2.2.2 Probe Functionalization

AFM probes (ContGB gold coated AFM probes with normal spring constant ~0.3 N/m from Budget Sensors, Inc., Sofia, Bulgaria) were cleaned by exposure to air plasma (using room air as source) for 1 minute on high power (PDC-001 plasma cleaner from Harrick Plasma, Ithaca, NY). After cleaning, gold coated tips were immediately immersed in ethanol to reduce any Au-oxides formed during cleaning. The terminal thiol group in the modified ssDNA was deprotected with 6 mM TCEP in the solution containing the DNA for 30 minutes. To attach thiol modified ssDNA to the Au coated AFM tips, the chip was placed in a 0.1-1 nM solution of ssDNA in a 10 mM phosphate buffer and 1 M ionic strength NaCl (pH ~7) for 1 hour. In order to fill in the remaining

Au sites on the surface of the tip, the cantilever chip was then submerged in a 3-15 mM solution of MHA in ethanol for 1 hour. Each functionalization step was followed by washing with ethanol and drying with nitrogen gas. Empirically, optimized density of the DNA molecules on the AFM tip is a compromise between the needs of 1) having a high number of attached ssDNA molecules to increase the yield of tips displaying peeling and 2) ensuring low enough contact adhesion so that initial adhesive pull-off of the tip from the surface does not mask the peeling process that follows.

# 2.2.3 Preparation of a Hydrophobic Methyl-terminated Monolayer

The surface of a polished silicon wafer was functionalized via methyl-terminated self-assembled monolayer following a previously described procedure.  $^{37,38}$  Several 1 cm  $\times$  1 cm pieces of silicon wafer (500  $\mu$ m thick, <100> orientation, obtained from Silicon Quest International, Santa Clara, CA) were cleaned in piranha solution (70 % H<sub>2</sub>SO<sub>4</sub> and 30 % H<sub>2</sub>O<sub>2</sub> by volume) for 30 min. The sample was then rinsed with DI water and placed into a 300 mL Pyrex crystallization dish containing 9 % (vol.) solution of octyldimethyl-chlorosilane in heptane and 1% (vol.) butylamine (catalyst). The dish was covered with a watch glass containing a small amount of methanol to control cooling of the watch glass surface. The reaction mixture was placed on a hotplate set at 60-65° C and stirred gently for 3 h. The samples were rinsed with isopropanol and placed for 2 h into an oven at 110° C under nitrogen atmosphere to complete the condensation reaction. The advancing and receding angles of water were 94±3° and 89±4°, respectively. For comparison, the advancing and receding angles of water on graphite were 85±4° and 47±6°. The thickness

of the monolayer was  $6.6\pm0.3$  Å as measured by the ellipsometry (VASE, J.A. Woollam Co).

## 2.2.4 Force Calibration and Force Curve Capture

Force spectroscopy measurements were performed using an MFP-3D atomic force microscope (Asylum Research, Santa Barbara, CA). The graphite surface was freshly cleaved with Scotch tape prior to each experiment and immediately placed in a fluid cell, which was then filled with approximately 3 mL of 10 mM phosphate buffer containing 100 mM NaCl. Probes were calibrated at the end of each experiment to avoid damaging the DNA or the gold coating under heavy compressive loading. The deflection sensitivity for each AFM cantilever in fluid was calibrated by determining the slope of the linear compliance region of the force-distance curves taken with the graphite sample. The most accurate calibration of the spring constant, however, is found in air, where the thermal spectrum of the cantilever is robustly represented by a simple harmonic oscillator model.<sup>38</sup> Therefore, the spring constant of the cantilever was determined at the end of each experiment in air by the thermal calibration method using the deflection sensitivity measured against glass in air.<sup>38</sup>

DNA peeling forces were measured using a force-volume map over a 5  $\mu$ m  $\times$  5  $\mu$ m area (with a 16×16 grid of force-distance curves) or by collecting individual force curves at several different locations on the sample. The force-volume map provides a fast, representative view of the interactions between DNA and graphite surface – accounting for any surface defects or steps between layers. Most force curves were recorded at a scan rate of 200 nm/s using a maximum compressive force of less than 1

nN. The maximum applied force was limited in order to protect the DNA from damage at high compressive loads. Analysis of the force-distance curves was performed using a custom code written in IGOR Pro (Wavemetrics, Eugene, OR). This code averages the force measured over a distance of at least 2 nm on both sides of the molecule detachment step and determines the peeling force by taking the difference.

In analyzing the force-displacement curves obtained from these force spectroscopy experiments, the force curves were only considered to be valid and suitable for further measurements if they possessed all of the following characteristics: 1) the approach and retraction retraces overlapped for the non-contact region, 2) the separation distance of the last peeling step is smaller than that of the sequence's contour length unless the formation of secondary structures is possible, 3) the tip-surface adhesion is small enough that the peeling steps are not masked by initial pull-off force, and 4) the peeling region displays a flat plateau for at least 10 nm of separation to present a steady state peeling process. All forces are reported as mean values  $\pm$  95 % confidence limit, resulting from averaging mean peeling forces from multiple experiments on a given sequence. The number of experiments used in this analysis is specified individually in each case.

#### 2.3 Results and Discussion

In the course of the tip retraction from the surface, force versus distance traces for tips modified with oligonucleotides displayed characteristic plateaus with abrupt force jumps to a progressively lower adhesive force. We interpreted this retraction behavior as steady state peeling that is occasionally interrupted by complete detachment of one or more molecules form the surface of graphite. Figure 2.1.A shows an idealized example of such a peeling of a single DNA oligomer from a graphite surface. In this setup, the detachment of the oligomer is depicted as perpendicular with respect to the substrate surface – a situation that occurs when the adsorbed bases slide freely on the graphite surface.<sup>39</sup> Figure 2.1.B, displays a characteristic force-distance curve of the steady-state peeling process. Our previous SMFS studies of the pyrimidine homopolymer-graphite system have shown that the peeling force is independent of the detachment rate (in the range of 100 to 1000 nm/s). Therefore, single molecule peeling proceeds in a quasi-equilibrium manner.<sup>25, 40</sup>

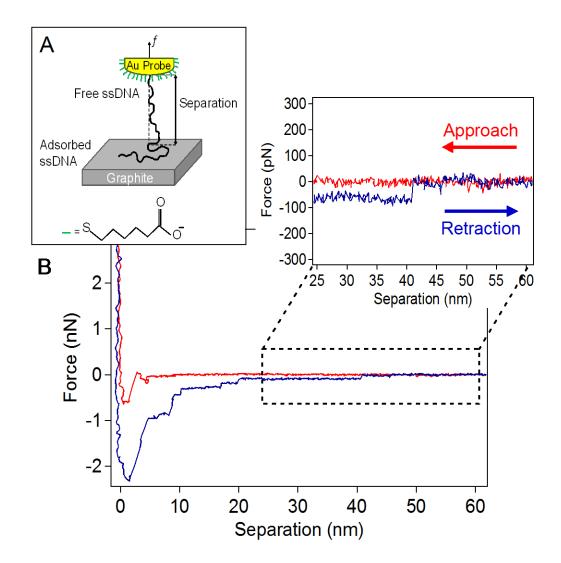


**Figure 2.1.** (A) Idealized cartoon (not drawn to scale) of frictionless peeling of a ssDNA homopolymer, attached to a gold coated force probe, from a graphite surface. Due to the frictionless nature of the substrate, the adsorbed bases slide freely on the surface and ssDNA detachment occurs perpendicular to the surface. (B) Typical force-distance curves for peeling 5'-poly(dT<sub>100</sub>) ssDNA from the surface of graphite obtained at a tip velocity of 200 nm/s in 10 mM phosphate buffer solution containing 100 mM NaCl. Red curve is approach, blue is retraction.

An equilibrium model for detachment of a laterally mobile freely jointed chain (FJC) from a flat surface gives the relationship between peeling force, f, and adhesion per unit length,  $\gamma$ , presented by Equation 2.1:<sup>25</sup>

$$\Gamma = \ln \left[ 4\pi \frac{\sinh(F)}{F} \right] \tag{2.1}$$

where  $F=fb/k_BT$  and  $\Gamma=\gamma b/k_BT$  are the dimensionless force and the dimensionless free energy of adhesion per Kuhn segment of length b, respectively. Given the known Kuhn length for single-stranded DNA (ssDNA) and its contour length per base (0.56 nm), one can calculate the binding energy per monomer from the experimentally measured peeling forces. A correction to the model accounting for enthalpic stretching of the backbone at high loads (>10 pN) can be made by using a Kuhn length elongated by a small fraction,  $f/\kappa$ , where  $\kappa$  is segment elasticity of ssDNA:

$$F = \frac{fb\left(1 + \frac{f}{\kappa}\right)}{k_{R}T} \tag{2.2}$$

For the purpose of calculation of the average binding energies, we set the size of the monomer to the distance between phosphorus atoms in the phosphodiester backbone (taken to be 0.56 nm), and used the same Kuhn length and the same segment elasticity for all DNA oligomer compositions.<sup>25</sup> Therefore, using SMFS, the forces needed to peel an ssDNA molecule can be quantified for a variety of sequences and the corresponding average binding energies per base can be compared.

In Equation 2.1, the reference states for determining adhesion have some arbitrary characteristics. We effectively assumed a density of states of one per steradian with the normalization constant. The corresponding term for the adsorbed state was incorporated

into the value of the free energy of adhesion per link. We briefly revisit the derivation of Equation 2.1 and refine the analysis to define the free energy of adhesion in a slightly different manner that, we believe, is directly relevant to our experiemnts and to the thermodynamic quantity one would obtain in an analogous, thermally-driven process.

In solution, the free energy of an FJC of n segments having end-to-end distance L under fixed load f, can be calculated from the conformational partition function  $Z_C$ :

$$G_{FJC}\Big|_{3D} = -k_B T \ln Z_C$$
, where  $Z_C = \sum \exp(fL/k_B T)$  (2.3)

where the summation is over all conformations that the FJC can access and L is the end-to-end distance for any given conformation. It is convenient to account for all of the conformations by realizing that each link samples all orientations in 3D (defined by the polar angle  $\vartheta$  and azimuthal angle  $\varphi$ ) uniformly and independently of all other links in the chain (and makes a projection l on the force axis). Therefore, the total conformational partition function,  $Z_c = z^n$ , where z is the partition function of a single link is:

$$Z_C = z^n = \left(\sum_{\text{orientations}} \exp\left(\frac{fl}{k_B T}\right)\right)^n \tag{2.4}$$

The sum can be converted into an integral using the density of states (per solid angle) for a single segment,  $\rho_{3D} = w_{3D}/4\pi$ , where  $w_{3D}$  represents the total number of microstates for a single link:

$$z = \int_{\theta=0}^{\pi} \int_{\varphi=0}^{2\pi} \exp\left(\frac{fl}{kT}\right) w_{3D} \frac{\sin\theta d\theta d\varphi}{4\pi}$$
 (2.5)

Since  $l = b\cos\theta$ , Equation 2.5 becomes:

$$z = \int_{\theta=0}^{\pi} \int_{\varphi=0}^{2\pi} \exp\left(\frac{fb\cos\theta}{k_B T}\right) w_{3D} \frac{\sin\theta d\theta d\varphi}{4\pi} = -w_{3D} \int_{\theta=0}^{\pi} \exp\left(\frac{fb\cos\theta}{k_B T}\right) \frac{d(\cos\theta)}{2}$$

$$= w_{3D} \frac{\sinh(F)}{F}$$
(2.6)

with the free energy given by:

$$G_{FJC}(F)\Big|_{3D} = -nk_B T \ln \left[ w_{3D} \frac{\sinh(F)}{F} \right]$$
 (2.7)

As expected, in the absence of force, the free energy per link is (in units of  $k_BT$ ) just the logarithm of the total number of microstates of a single link due to its orientation in space. In the adsorbed state, similar arguments lead one to conclude that, for a freely-jointed chain on a surface having (N-n) links, the free energy in the absense of force is given by:

$$G_{FJC}(F=0)\Big|_{2D} = -(N-n)k_B T \ln[w_{2D}]$$
 (2.8)

The equilibrium condition is obtained by the minimization of the total free energy under fixed force and fixed adhesion free energy per unit length,  $\gamma$ , *i.e.*:

$$\frac{\partial G_{total}}{\partial n} = \frac{\partial}{\partial n} \left( G_{adh} + G_{FJC} \Big|_{3D} + G_{FJC} \Big|_{2D} \right) = 0$$
 (2.9)

The parameter  $\gamma$  is properly understood here as adhesion free energy per unit length of an isolated (i.e. not part of the chain) segment. Using:

$$G_{adh} = -b(N-n)\gamma = -k_B T(N-n)\Gamma$$
(2.10)

and Equations 2.7 and 2.8, the condition for equilibrium (Eq. 2.9) results in the relationship between the dimensionless force F and the dimensionless free energy of adhesion per Kuhn segment  $\Gamma$ :

$$\Gamma = \ln \left[ \frac{w_{3D}}{w_{2D}} \right] + \ln \left[ \frac{\sinh(F)}{F} \right]$$
 (2.11)

The first term in Equation 2.11 gives the minimum adhesion required to hold the chain adsorbed on the surface – a non-zero contribution, because there is an overall gain in the number of microstates (i.e. an increase in entropy) when the link goes from a 2D (adsorbed) to a 3D (in solution) state. Since the first term in Equation 2.11 is system (model) dependent and only the second term is determined in our experiments, it is convenient to redefine the adhesion quantity of interest as  $\Gamma'$  – the free energy required to desorb a link in a 2D-FJC-state from the surface into a 3D-FJC-state in solution:

$$\Gamma' = \Gamma - \ln\left[\frac{w_{3D}}{w_{2D}}\right] = \Gamma - \Delta \ln\left[w\right] = \ln\left[\frac{\sinh(F)}{F}\right]$$
 (2.12)

The adhesion free energy per base,  $k_BT\Gamma'(b_{mono}/b)$  ( $b_{mono}$  is the polymer contour length per monomer), is then obtained directly from the force peeling data and is the desired property that also determines the thermally-established equilibria between the adsorbed and desorbed homopolymers with no externally applied force.

Alternatively, the relation between force and adhesion free energy can be derived from a worm like chain (WLC) model of a stretched DNA molecule.<sup>41</sup> In the worm like chain model of a polymer having contour length  $L_c$ , the force f is given in terms of extension, L, as

$$f = \frac{k_B T}{p} \left( \frac{L}{L_c} - \frac{1}{4} + \frac{1}{4 \left( 1 - L/L_c \right)^2} \right)$$
 (2.13)

where p is the persistence length (half of the Kuhn length, or b=2 p). Using Equation 2.13 to estimate fractional extension  $\lambda = L/L_c$ , given measured force f, the adhesion free energy (per unit length) can then be expressed as (see SI, section S5 for derivation):

$$\frac{\gamma p}{k_B T} - \frac{1}{2} \ln \left[ \frac{w_{3D}}{w_{2D}} \right] = \frac{\lambda^2}{4} \frac{\left( 3 - 4 \lambda + 2 \lambda^2 \right)}{\left( I - \lambda \right)^2}; \quad \lambda = \frac{L}{L_c}$$
 (2.14)

In the worm like chain model, the steady state peeling force and adhesion are given parametrically as  $f(\lambda)$  and  $\gamma(\lambda)$  with fractional extension  $\lambda$  as a common parameter, thus allowing us to produce explicit numerical  $\gamma$  versus f dependence. A plot of dimensionless adhesion versus peeling force ( $\Gamma'$  versus F) combining both FJC and WLC models (setting p=b/2) indicates that adhesion per unit length for WLC polymer is lower by ~15% than adhesion for FJC polymer, in the range of peeling forces observed in our experiments (Figure 2.9). For consistency with previous work and since FJC model should describe single stranded DNA better than WLC model, which is more appropriate for double stranded form, we will continue to use FJC model here in the interpretation of our force spectroscopy data. In our analysis, we will calculate adhesion free energy in the sense defined by Equation 2.12 and reinterpret our previously published peeling force data accordingly.

The Kuhn length for single stranded DNA (or RNA) is in the range of 0.5 to 3.5 nm depending on the ionic strength of the solution, sequence, and methods used 15, 23, 25, 42-45 thus, we expect the behavior of the DNA strands longer than 30 nm (~50 bases) to be well represented by a freely jointed chain model. Indeed, the exact statistical mechanical treatment of the single-molecule peeling of a freely jointed chain under force control

results in the appearance of a well-developed force plateau for molecules having 15-20 Kuhn segments or longer. The plateau force does not depend on the number of segments according to the model. Our model is only modestly sensitive to the exact value of the Kuhn's length, since it appears in both dimensionless quantities ( $\Gamma$  and F). We will use a mid-range value of 1.5 nm with a segment elasticity of 0.8 nN, as determined in the initial work that applied extensible FJC model to describe stretching of a long (e.g. kbase) ssDNA in 150 mM NaCl with optical tweezers. We note that use of b=0.5 nm and  $\kappa$ =2.4 nN found in our own experiments on short DNA<sup>25</sup> will result in reduction of binding energy values (per base) reported in Table 2.1 by 2.0-2.5 k<sub>B</sub>T, while use of the WLC model with reported value of persistence length of 1.5 nm (100 mM NaCl) will reduce these values by 0.9-1.8 k<sub>B</sub>T.

The presence of salt decreases the repulsive forces between the negatively charged phosphate groups of the DNA backbone and results in coiling of the chain, improving validity of the freely joined chain approximation for our short (50-100 bases) DNA oligomers. In our previous experiments on pyrimidines, in the absence of NaCl in dilute buffer solutions (ionic strength of 1 to 10 mM phosphate buffer), long range electrostatic repulsion was readily observed as the tip approached the surface, and the effective range of the repulsive forces could be reduced at higher salt concentrations. However, despite the changes in salt concentration, we still observed that the magnitude of the average peeling forces remain virtually unchanged. This observation is consistent with a notion that the peeling forces are due to dominance of non-electrostatic interactions, such as van der Waals forces and hydrophobic interaction between the bases

and graphite, over the contributions resulting from the electrostatic/double layer interactions between the charged DNA backbone and the graphite surface.<sup>25</sup>

To complete our previous description of factors affecting the binding strength of homopolymers, we carried out additional experiments for polythymine using 5'-thiol modified DNA as opposed to 3'-modified DNA in order to study the effect of direction of ssDNA binding to the gold tip and corresponding direction of detachment from the solid surface (Table 2.2). The peeling force for 5'-poly( $dT_{50}$ ) was found to be 73.4  $\pm$  5.5 pN (3 experiments with a total of 132 force curves), which is similar to forces previously observed using 3'-poly( $dT_{50}$ ) functionalized tips (85.3 ± 4.7 pN).<sup>25</sup> Further experiments were completed on 5'-poly( $dT_{100}$ ) and yielded 78.5  $\pm$  5.0 pN average peeling force (17 experiments with a total of 884 force curves), very similar to those obtained for 5' $poly(dT_{50})$  and 3'- $poly(dT_{50})$ . Figure 2.1.B shows a typical force-distance curve obtained for polythymine under our standard experimental conditions (200 nm/s, 100 mM NaCl, pH 7 phosphate buffer). The only readily detected difference was that the length of the peeling steps sometimes could be as long as 45 nm for the case of the 100-mer, as expected for a ssDNA molecule having a contour length of about 55 nm. The 5'-poly(dT) chains do display a peeling force that is lower than previously reported for 3'-poly(dT<sub>50</sub>) by Manohar et al. 25 The observed difference of 6.8±6.7 pN for peeling DNA in 3'-5' versus 5'-3' directions, however, appears minor compared to the overall binding force (<10%) and, given experimental errors, it may not be possible to make a distinction between any two specific peeling experiments. The small effect of the directionality and the polymer chain length on average peeling force supports our use of the freely jointed chain model to extract the binding energy values per monomer in this system.

To support our interpretation of the dominant role of hydrophobic interactions between the DNA bases and the surface of graphite to peeling forces, we also carried out single molecule peeling experiments using 5'-poly( $dT_{100}$ ) and model surfaces at extreme ends of the hydrophobicity scale - hydrophobic methyl-terminated self assembled monolayers on silicon<sup>46, 47</sup> and hydrophilic surface of silicon dioxide (produced by exposing silicon wafer to piranha solution). When SMFS experiments were carried out on the hydrophilic substrate using either DNA-modified or MHA-modified AFM probes, the force-disrtance curves obtained from the interactions between probes with silicone dioxide looked indentical to those derived from SMFS experiments that used MHAmodified probes on graphite.<sup>25</sup> The resulting force-distance curves, obtained from over 3800 force curves corresponding to 6 experiments, were completely reversible on retraction and showed no adhesion. On the contrary, when the same DNA-modified AFM probes were used on methyl functionalized surfaces, a strong tip-sample intial adhesion of 3-15 nN resulted and long steady-state peeling plateaus with an average peeling force of  $77.5 \pm 8.3$  pN were produced (5 experiments with a total of 207 force curves).

For the study of purine homopolymers, we investigated peeling forces for 3'-poly( $dA_{50}$ ) and 5'-poly( $dG_{100}$ ). We decided to use longer chains for polyguanine since a longer contour length increases the success rate of obtaining force curves that show critical characteristics described in the experimental section. We found that using a longer chain (100mer versus 50mer) diminishes the effect of strong tip-surface contact adhesion, and makes identification and interpretation of plateaus due to DNA peeling a more robust process. In the case of polyguanine, we observed that the initial tip-graphite adhesion was much higher than the measured adhesion for the other three homopolymers

(up to 15 nN versus 1-2 nN) and the success rate of our experiments improved dramatically by using a longer chain length for polyguanine.

The average plateau force for peeling 3'-poly( $dA_{50}$ ) from graphite was determined to be  $76.6 \pm 3.2$  pN (mean  $\pm 95$  % confidence limit, 25 experiments with a total of 1185 force curves). Using Equations 2.1 and 2.2, the average binding energy per monomer was calculated to be  $9.9 \pm 0.4$  k<sub>B</sub>T. From comparison of the average binding energy per base of 3'-poly( $dT_{50}$ ) with that of 3'-poly( $dA_{50}$ ) – 11.3 k<sub>B</sub>T<sup>25</sup> versus 9.9 k<sub>B</sub>T, it is clear that the effective strength of interactions with graphite fall within the same range for the two sequences. Given the accuracy of cantilever spring constants obtained from the thermal calibration method (~10-20% error)<sup>48, 49</sup> and the typical width of the peeling force distribution in a given experiment (5-15 % of the mean), the binding energy of poly(dT) and poly(dA) cannot be distinguished from one another.

If one accepts the view of the dominant contribution of hydrophobic forces to the binding affinity between the bases and graphite, the closeness of the two values is surprising, since the maximum contact area between adenine and graphite is higher than between thymine and graphite. Indeed, affinity to graphite of individual bases scales according to the size of the respective heterocycles.<sup>24</sup> This discrepancy in binding between free and constrained bases is an indication of the possible influence of the DNA backbone on the conformation that an absorbed base can adopt on a graphite surface. Constraints imposed by the backbone of purine homopolymers prevent conformational changes that would result in maximum contact areas and highest interaction energies between the bases and graphite surface.<sup>50</sup>

Force-distance curves for peeling 5'-poly(dG<sub>100</sub>) from graphite consistently showed behavior different from what we observed for the other three homopolymers (Figure 2.2). In general, the peeling steps for polyguanine could be categorized by the following characteristics: 1) the force curves either displayed large separations (greater than the contour length of the strand) with small peeling forces (<60 pN), or small separation of the last peeling step (less than half the contour length) with large peeling forces (>100 pN), 2) most of the results showed initial adhesion forces that were much larger than those observed from any of the other homopolymers investigated (4-15 nN versus 1-3 nN), and 3) about half of the experiments showed behavior characteristic of stretching a molecule in addition to the force plateaus representative of peeling of the homopolymer from the graphite surface. Since polyguanine has a propensity to form secondary structures,<sup>32</sup> we suggest that these features are caused by different modes of peeling or states of adsorbed polyguanine, leading to the variability in peeling force magnitude and the shape of force-distance curves.

To summarize the differences in behavior that we observed between the forcedistance curves obtained from polythymine and polyguanine, the following statistics are considered. In our SMFS studies of polythymine, more than 10000 force curves were analyzed. Among those, 16 % displayed valid peeling steps, the rest either not having peeling steps at all (due to low density of the DNA attachment or loss of the molecule in the course of the experiment) or resulting in a large initial adhesion possibly hiding peeling of the individual molecules. In all of the valid peeling force curves, the tipsample separation at the last detachment step was smaller than the contour length of the molecule. In contrast, the SMFS studies using tips functionalized with 5'-poly( $dG_{100}$ ) showed a great deal of variability of responses. Here, over 6500 force curves were analyzed, with 12 % of all force curves showing valid peeling steps. In almost a third of all

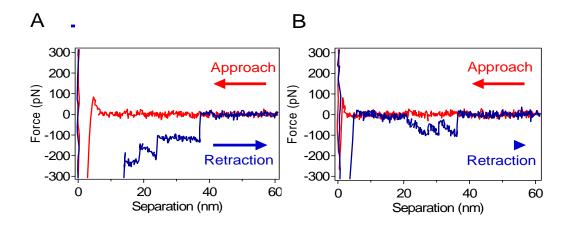


**Figure 2.2.** Typical force-distance curves obtained for probes functionalized with 5'-poly( $dG_{100}$ ) (200 nm/s retraction velocity, 10 mM phosphate buffer with 100 mM NaCl) showing peeling (A) and stretching (B).

valid force curves, the terminal separation was at a distance from the surface that exceeded the contour length of the homopolymer. Furthermore, 40% of all force curves showed stretching of a ssDNA molecule in addition to or instead of peeling upon tip retraction from the substrate, indicating the presence of pinning points for this sequence.

We envision several modes of peeling for 5'-poly( $dG_{100}$ ) that are consistent with our observations and imply formation of stable secondary structures as outlined in Figure 2.3. For example, Figure 2.3.A shows that formation of a stable dimer molecule would result in the final separation step being larger than the contour length of the individual homopolymer molecule. Strands with stable intrastrand secondary structure adsorbed

onto the surface (Figure 2.3.B) could explain observation of large peeling forces at much smaller separation distances. Furthermore, since most of the force curves showed both peeling and stretching, it is proposed that the formation of secondary structures at random locations along the chain led to strong adsorption of

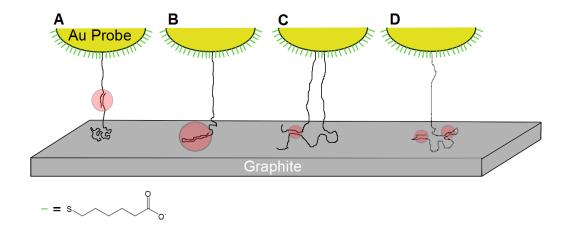


**Figure 2.3.** Proposed mechanisms to describe the possible reasons for observing: (A) force curves with small forces at separations larger than the ssDNA's contour length, (B) large forces at short separations, (C) and (D) both peeling and stretching. This figure was created by Dr. Kyle Wagner.

the polymer at these locations and formation of pinning points resulting in characteristic stretching behavior (Figure 2.3.C and D).

Simply averaging all the force steps obtained from the 5'-poly(d $G_{100}$ ) results in a large variation in peeling forces:  $80.8 \pm 14.3$  pN (9 experiments with a total of 490 force curves). However, compiling all results obtained from the analysis of the plateau forces for 5'-poly(d $G_{100}$ ) into a histogram (Figure 2.4.), reveals two distinct peaks at  $66.4 \pm 1.4$  pN and  $121.4 \pm 2.4$  pN (corresponding to mean  $\pm$  95 % confidence limit from the

combined dataset containing 355 force curves in the first peak and 135 curves in the second peak). The histogram's most prominent peak had the lowest value of the two peaks, and it was interpreted as the peeling force of 5'-poly( $dG_{100}$ ) absent of secondary structures, while the latter peak is interpreted to have resulted from the contributions of the secondary (intra- or intermolecular) structures and could be assigned to forced desorption of two monomers simultaneously (in the same strand or two different strands). In the case of force-distance curves characteristic of the single molecule stretching behavior, total of 280 force curves were analyzed. The cumulative histogram of pull-off forces at which detachment occurred also featured a bimodal distribution, with the two peaks centered at approximately  $70 \pm 3.2$  pN and  $112 \pm 4.4$  pN (corresponding to mean  $\pm$  95 % confidence limit from the combined dataset containing 153 force curves in the first peak and 127 curves in the second peak) (Figure 2.7).

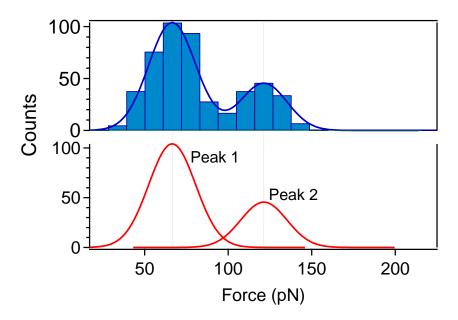


**Figure 2.4.** Histogram of 5'-poly( $dG_{100}$ ) peeling forces showing two distinct peaks at  $66.4 \pm 13.7$  pN and  $121.4 \pm 14.4$  pN (mean  $\pm$  standard deviation derived form a fit to a Gaussian distribution).

Using Equations 2.1 and 2.2, the average binding energy per monomer of polyguanine was calculated to be  $8.3 \pm 0.2$  k<sub>B</sub>T. As with the interaction strength between graphite and polythymine and polyadenine oligomers, the average per base binding energies in 5'-poly(dG<sub>100</sub>)and 3'-poly(dC<sub>50</sub>) fall within the same range and are indistinguishable from each other within our experimental error. On the other hand, it is clear that the binding force of polythymine and polyadenine is larger than that of both polyguanine and polycytosine. This finding is in agreement with reports on the dispersion efficiency of CNT by these homopolymer DNA sequences, where poly(dT) is clearly more effective than poly(dG).<sup>1</sup>

### 2.4 Conclusions

In this chapter, we report direct measurements, using single molecule force spectroscopy, for a complete set of interaction forces between DNA and graphite surface for all four homopolymer sequences (Table 2.1). Herein, we found that the DNA chain length and its direction of attachment to a gold coated AFM tip have negligible effects on the peeling forces of homopolymers. The force required to detach 3'-poly(dA<sub>50</sub>) from graphite surface was measured to be  $76.6 \pm 3.0$  pN, while that of 5'-poly(dG<sub>100</sub>) was found to be  $66.4 \pm 1.4$  pN; these force measurements correspond to the average binding energy per monomer of  $9.9 \pm 0.4$  k<sub>B</sub>T and  $8.3 \pm 0.2$  k<sub>B</sub>T, respectively. Moreover, the experiments with 5'-poly(dG<sub>100</sub>)/MHA functionalized gold tips showed stretching behavior suggestive of the formation of secondary structures as the reason for obtaining a complex set of force curves for this homopolymer. Overall, the binding energies for all

four bases are in the range of  $8-11~k_BT$ . With these results, it is clear that polythymine and polyadenine fall within the same range in terms of their binding strength, while polycytosine and polyguanine can also be coupled into a single group in terms of their binding affinity to graphite.

**Table 2.1.** Summary of all SMFS measurements of binding affinity between DNA homopolymers and graphite (errors are 95% confidence limit).

Sequence	Peeling force (pN)	Binding energy per nucleotide (k <sub>B</sub> T)			
Pyrimidines					
<b>3'-poly(dT</b> <sub>50</sub> ) (Ref. <sup>25</sup> )	$85.3 \pm 4.7$	$11.3 \pm 0.8$			
<b>3'-poly</b> ( <b>dC</b> <sub>50</sub> ) (Ref. <sup>25</sup> )	$60.8 \pm 5.5$	$7.5 \pm 0.8$			
$5'$ -poly( $dT_{50}$ )	$73.4 \pm 5.5$	$9.4 \pm 0.9$			
$5$ '-poly( $dT_{100}$ )	$78.5 \pm 5.0$	$10.2 \pm 0.8$			
Purines					
3'-poly(dA <sub>50</sub> )	$76.6 \pm 3.0$	$9.9 \pm 0.5$			
5'-poly(dG <sub>100</sub> )	$66.4 \pm 1.4$	$8.3 \pm 0.2$			

The force measurements reported in this table were obtained collectively by Sara I. Cook, Dr. Kyle Wagner, and Dr. Suresh Manohar.

The binding energy does not scale with the size of the base as in the case of individual nucleobases or nucleosides, possibly indicating an important role of the restrictions placed by the phosphodiester backbone on conformations of the DNA bases on graphite. While there is a correlation between binding energy and non-polar molecular area (see SI, section S8), we believe that this trend is likely coincidental given that for single bases both experiment and theory show good scaling with the total area of the base. Since we are measuring the difference in free energy of the bound and unbound states, these arguments imply that we ignore stacking of bases to each other in the

unbound state (purine-purine stacking will be stronger than pyrimidine-pyrimidine stacking). No base stacking assumption in the desorbed state seems plausible given that the DNA backbone should be almost fully stretched under the high peeling forces (> 60 pN). Therefore, desorbed nucleobases cannot stack, because they will be too far apart. On the other hand, the stacking of the bases in the adsorbed state is plausible and would be consistent with the lower than expected binding energy for purines. To explore the possible contribution from this effect, one would likely have to rely on very detailed molecular mechanics calculations, but we note that simulations of ssDNA sequences on carbon nanotubes show very little propensity for base-base stacking.<sup>51</sup>

The SMFS studies described in this chapter, where ssDNA is adsorbed onto a two-dimensional substrate, used basic homopolymer sequences that are not capable of forming special recognition 3D-structures when wrapped around a SWCNT, such as poly(dTdAdTdT), poly(dGdT),<sup>52</sup> and others,<sup>3</sup> that are found to play a significant role in ssDNA/CNT interactions when placed in bulk dispersions. In order to overcome this shortcoming, future experiments should be conducted to assess the role of different bases within the same strand. Rational design of secondary structures to probe their effect on the magnitude of the interaction forces is fully compatible with single molecule force spectroscopy and can provide further quantification of the binding strength between various DNA motifs and solid surfaces. The potential drawback of using SMFS to uncover sequence dependent signatures due to recognition motifs is the relatively high (in the context of this system) variability of the typical force calibration methods employed with force microscopy. The problem may be alleviated by the design of the proper internal standard built into the oligomer sequence or by further improvements to force

probe calibration. The role of the high curvature of the CNT and size matching between CNT and nucleobases in determining the magnitude of the binding forces between DNA and CNT remains unknown and can only be assessed with experiments on actual nanotubes.

# 2.5 Appendix

### 2.5.1 Effect of oligomer attachment direction on peeling forces

We complemented our previous studies on the interaction of 3'-poly( $dT_{50}$ ) with graphite by investigating the effect of direction of the strand attachment on average pulling forces (Table 2.2). These results showed that the direction of peeling has a rather small effect on the peeling forces of this homopolymer. The mean peeling force measured from these experiments was  $73.4 \pm 5.5$  pN (mean  $\pm$  95 % confidence limit, 3 experiments with a total of 132 force curves).

**Table 2.2.** Peeling forces for 5'-poly( $dT_{50}$ ).

Experiment No.	No. of Curves	Mean Force (pN)	Standard Deviation (pN)
1	62	71.01	4.91
2	43	75.46	8.64
3	27	73.68	10.87

### 2.5.2 Effect of oligomer chain length on peeling forces

To overcome the problem of large initial adhesion observed in the case of AFM tips modified with 5'-poly(dG<sub>50</sub>)/MHA, ssDNA chain lengths larger than 50 bases were needed to enable consistent detection of peeling steps upon tip pull-off. Using polythymine as a control, we carried out experiments to show that the chain length has negligible effects on the peeling forces of DNA homopolymers. The average force measured from these experiments on a 100-mer (Table 2.3) was  $78.5 \pm 5.0$  pN (corresponding to mean  $\pm$  95 % confidence limit from 17 experiments with a total of 984 force curves), in close agreement with peeling forces of  $73.4 \pm 5.5$  pN for a corresponding 50-mer (Table 2.2).

**Table 2.3.** Peeling forces for 5'-poly( $dT_{100}$ ).

Experiment	No. of	Mean	Standard
No.	Curves	Force (pN)	<b>Deviation (pN)</b>
1	102	79.6	5.5
2	79	63.0	5.1
3	55	83.3	5.2
4	29	70.0	6.6
5	55	81.1	7.7
6	55	85.3	7.1
7	55	78.8	15.6
8	55	72.3	8.7
9	55	82.3	9.7
10	55	86.1	7.2
11	55	83.9	7.7
12	50	68.9	5.3
13	23	69.8	14.1
14	50	87.2	4.3
15	24	63.5	3.5
16	44	101.3	8.3
17	43	78.1	6.3

# 2.5.3 Peeling forces of polyadenine

The average peeling force observed for 3'-poly( $dA_{50}$ )/MHA functionalized tips (Table 2.4) under different conditions was  $76.6 \pm 3.2$  pN (mean  $\pm 95$  % confidence limit, 25 experiments with a total of 1185 force curves). These experiments were carried out at different peeling rates and salt concentrations to confirm that these two factors have no effect on the peeling forces of ssDNA as was the case for poly(dT) and poly(dC).

**Table 2.4.** Peeling forces for 3'-poly( $dA_{50}$ ).

Experiment	No. of	Peeling	NaCl	Mean	Standard
No.	Curves	Rate	Concentration	Force	Deviation
1,00	0 412 7 65	(nm/s)	(mM)	( <b>pN</b> )	( <b>pN</b> )
1	51	50	0	74.1	4.8
2	52	100	0	76.7	6.9
3	52	200	0	66.2	3.8
4	55	100	50	66.0	3.2
5	50	200	50	68.8	3.8
6	52	100	100	80.9	5.6
7	51	200	100	79.2	6.5
8	53	400	100	78.1	5.7
9	50	100	200	83.8	3.8
10	50	200	200	81.6	3.5
11	54	400	200	81.6	4.4
12	50	100	0	69.3	10.8
13	34	1000	0	63.6	6.4
14	50	100	50	79.4	5.7
15	39	600	50	81.2	7.8
16	40	800	50	80.8	7.9
17	41	1000	50	84.6	16.5
18	42	50	0	73.9	3.1
19	50	100	0	70.2	4.8
20	38	200	0	75.3	7.7
21	50	600	0	100.1	8.2
22	50	800	0	72.1	5.1
23	31	1000	0	71.6	7.4
24	50	100	100	78.4	9.6
25	50	400	100	77.9	8.3

### 2.5.4 Peeling of polythymine from hydrophobic and hydrophilic surfaces

Figure 2.5 shows force-distance curve derived in experiments on peeling of 5'poly( $dT_{100}$ ) from a methyl-terminated self-assembled monolayer on silicon. Table 2.5
presents a summary of force statistics from several such experiments using different
probes.

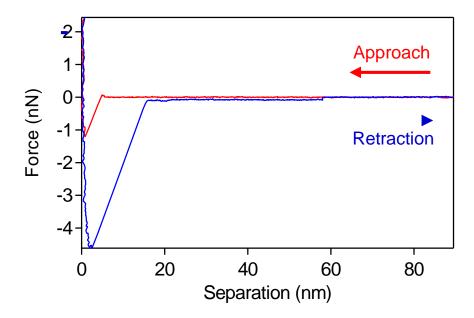


**Figure 2.5.** Typical force-distance curve for peeling 5'-poly( $dT_{100}$ ) ssDNA from the surface of a methyl terminated self-assembled monolayer on silicon obtained at a tip velocity of 200 nm/s in 10 mM phosphate buffer solution containing 100 mM NaCl.

**Table 2.5.** Peeling forces for 5'-poly( $dT_{100}$ ) from methyl terminated self-assembled monolayer on silicon.

Experiment	No. of	Peeling	NaCl	Mean	Standard	
No.	Curves	Rate (nm/s)	Concentration (mM)	Force (pN)	Deviation (pN)	
1	50	200	100	83.4	5.1	
2	50	200	100	71.3	7.6	
3	50	200	100	90.1	9.9	
4	50	200	100	66.2	5.5	
5	7	200	100	76.5	4.4	

Figure 2.6 displays a typical force-distance curve obtained when SMFS experiments were carried out on the hydrophilic substrate using either DNA-modified or MHA-modified AFM probes. Hydrophilic surface was created by cleaning silicon wafer in piranha solution.

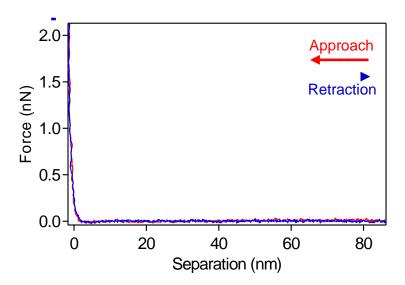


**Figure 2.6.** Typical force-distance curve for interaction between 5'-poly( $dT_{100}$ ) ssDNA and clean silicon surface obtained at a tip velocity of 200 nm/s in 10 mM phosphate buffer solution containing 100 mM NaCl.

2.5.5 Pull-off forces for polyguanine observed in the course of stretching behavior Figure 2.7 shows a histogram of forces (obtained from a total of 280 force curves characteristic of single molecule stretching rather than single molecule peeling), at which detachment of 5'-poly(d $G_{100}$ ) chains was observed. The histogram displays two peaks centered at  $70 \pm 3.2$  pN and  $112 \pm 4.4$  pN (corresponding to mean  $\pm 95$  % confidence

limit from the combined dataset containing 153 force curves in the first peak and 127 curves in the second peak), similar to a bimodal distribution of peeling forces observed for this sequence.

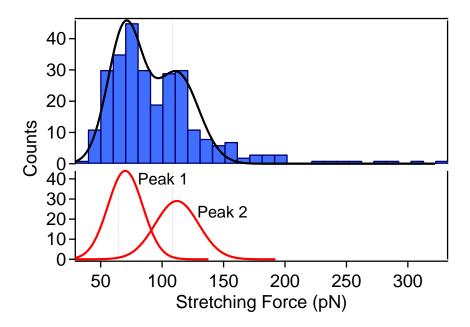


**Figure 2.7.** Histogram of pull off force for 5'-poly( $dG_{100}$ ) showing single molecule stretching behavior.

# 2.5.6 Initial pull-off forces for polyguanine modified probes

Figure 2.8 shows a typical force-distance curve for peeling 5'-poly( $dG_{100}$ ) ssDNA from graphite and indicates strong initial adhesion between the modified probe and the surface. Average adhesion force observed in multiple experiments is summarized in Table 2.6.

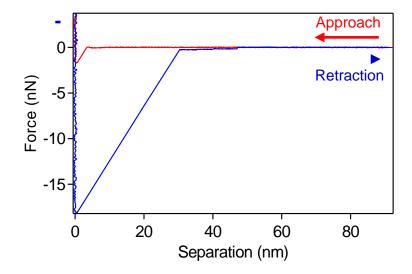


**Figure 2.8.** Typical force-distance curve for peeling 5'-poly( $dG_{100}$ ) ssDNA from the surface of graphite obtained at a tip velocity of 200 nm/s in 10 mM phosphate buffer solution containing 100 mM NaCl.

**Table 2.6.** Initial tip adhesion for 3'-poly( $dG_{100}$ ).

Experiment No.	1	2	3	4	5	6	7	8	9	10	11
Mean Force of Adhesion (nN)	7.0	12	3.3	5.5	15	7.7	7.6	4.6	4.7	3.5	1.4

### 2.5.7 Relating peeling force to adhesion free energy for a worm-like chain

In the worm-like chain model (WLC), the force f is given in terms of extension L as:

$$f = \frac{k_B T}{p} \left( \frac{L}{L_c} - \frac{1}{4} + \frac{1}{4(1 - L/L_c)^2} \right)$$
 (2.15)

where p is the persistence length (half of the Kuhn length, b) and  $L_c$  is the contour length of the desorbed part of the polymer. The corresponding free-energy of the WLC polymer is:

$$G_{WLC} = k_B TC(L=0) + \int_0^L f(L') dL' = \frac{k_B T}{4p} \frac{L^2}{L_c} \left( \frac{3 - 2L/L_c}{1 - L/L_c} \right) + k_B TC(L=0)$$
 (2.16a)

where  $k_BTC(L=0)$  is a constant of integration (free energy of unstressed polymer). The free energy of the freely joined chain with n Kuhn segments is:

$$G_{FJC} = -k_B T n \ln \left[ w_{3D} \frac{\sinh F}{F} \right] \tag{2.16b}$$

where  $F = \frac{fb}{k_B T}$  is a dimensionless force and w<sub>3D</sub> is the total numer of microstates per

Kunh length. By requiring the free energy of the WLC polymer under no external force (Gaussian chain) to be equal to the free energy of a freely jointed chain,

$$G_{FJC} = -k_B T n \ln[w_{3D}]$$
, we can set  $C(z=0) = -\frac{L}{2p} \ln[w_{3D}]$ .

Energy per unit length of the desorbed chain can be expressed as:

$$g_{WLC} = G_{WLC} / L = \frac{k_B T}{4p} \frac{L^2}{L_c^2} \left( \frac{3 - 2L/L_c}{1 - L/L_c} \right) - \frac{k_B T}{2p} \ln[w_{3D}] =$$

$$= \frac{k_B T}{4p} \left[ \lambda^2 \left( \frac{3 - 2\lambda}{1 - \lambda} \right) - 2\ln[w_{3D}] \right]; \lambda = L/L_c$$
(2.17)

where  $\lambda = L/L_c$  is the extension as a fraction of the full contour length of the molecule. Steady state peeling, i.e. a constant value of force, implies that the value of  $\lambda$  is some fixed, but as yet unknown, value in the desorbed part of the chain (Eq. 2.15). Then, in steady state, we can equate the work done by the external force to the work that goes into the free energy of adhesion (including the entropy term for adsorbed WLC) plus the work that goes into strain energy in the following way:

$$f(\lambda)dL = \gamma dL_c + \frac{k_B T}{2p} \ln[w_{2D}]dL_c + g_{WLC}(\lambda)dL_c$$
 or

$$f(\lambda)\lambda dL_c = \gamma dL_c + \frac{k_B T}{2p} \ln[w_{2D}] dL_c + g_{WLC}(\lambda) dL_c$$
 (2.18)

The quantity  $dL_c$  is the increase in the contour length of the desorbed part of the molecule. The first term on the left hand side of Eq. 2.18 is the work done by the external force. Note that this term has the form of a product of the force and the contour length increase times the extension fraction, since the chain need not be extended fully. The first term on the right hand side represents the free energy of desorption, and the second term accounts for loss in the entropy of the 2D WLC upon desorption, and the third term is the strain energy stored in the stretched chain in solution. From Eq. 2.18 it immediately follows that the steady-state value of  $\lambda$  is given by:

$$f(\lambda)\lambda - g_{WLC}(\lambda) - \frac{k_B T}{2p} \ln[w_{2D}] = \gamma$$
 (2.19)

Using Equations 2.15 and 2.17, we find that:

$$\frac{p}{k_B T} = \frac{\lambda^2}{4} \frac{\left(3 - 4\lambda + 2\lambda^2\right)}{\left(1 - \lambda\right)^2} + \frac{1}{2} \ln \left[\frac{w_{3D}}{w_{2D}}\right]$$
 (2.20)

In order words, to extract the adhesion free energy,  $\gamma$ , we would take the measured force and use Eq. 2.15 to find  $\lambda$ . Then, Eq. 2.20 can be used to find the adhesion free energy.

Unlike in the case of FJC model, where we obtained an explicit relationship between the peeling force and adhesion, for the WLC model, force and adhesion are given parametrically as  $f(\lambda)$  and  $\gamma(\lambda)$ . Setting dimensionless force to  $F = \frac{2p}{k_BT} f$  and dimensionless adhesion to  $\Gamma' = \frac{2p}{k_BT} \gamma - \Delta \ln[w]$  for consistency with the FJC model, we plotted adhesion versus steady-state peeling force in Figure 2.9. Estimates of adhesion is lower by ~15% for WLC model than for FJC model.

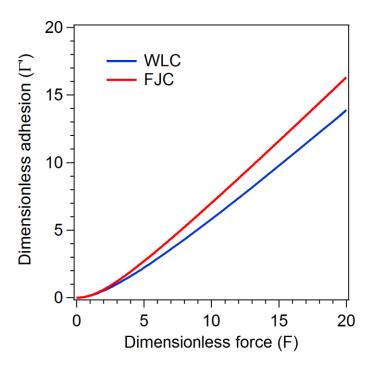


**Figure 2.9.** Dependence of dimensionless adhesion free energy,  $\Gamma' = \frac{2p}{k_B T} \gamma - \Delta \ln[w]$ , on dimensionless force,  $F = fb/k_B T$ , for WLC and FJC models of a polymer molecule.

2.5.8 Correlation between binding free energy per base and non-polar molecular area We used ChemBio3D Ultra 12.0 program (PerkinElmer Informatics) to calculate molecular (van der Waals) area and polar molecular area for each nucleobase. The non-polar molecular area is then found as the difference between the two calculated areas.

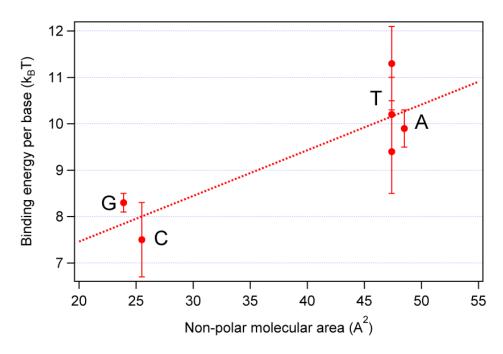


**Figure 2.10.** Dependence of binding free energy per nucleotide on non-polar molecular area of a nucleobase. The dotted line is a linear fit to the data to guide the eye.

### 2.6 References

- (1) Zheng, M.; Jagota, A.; Semke, E. D.; Diner, B. A.; Mclean, R. S.; Lustig, S. R.; Richardson, R. E.; Tassi, N. G., *Nature Materials* **2003**, *2*, 338-342.
- (2) Zheng, M.; Jagota, A.; Strano, M. S.; Santos, A. P.; Barone, P.; Grace Chou, S.; Diner, B. A.; Dresselhaus, M. S.; Mclean, R. S.; Onoa, G. B.; Samsonidze, G. G.; Semke, E. D.; Usrey, M.; Walls, D. J., *Science* **2003**, *302*, 1545-1548
- (3) Tu, X.; Manohar, S.; Jagota, A.; Zheng, M., *Nature* **2009**, *460*, 250-253.
- (4) Feazell, R. P.; Nakayama-Ratchford, N.; Dai, H.; Lippard, S. J., *Journal of the American Chemical Society* **2007**, *129*, 8438-8439.
- (5) Kam, N. W. S.; Dai, H., Journal of the American Chemical Society 2005, 127, 6021-6026.
- (6) Kam, N. W. S.; Jessop, T. C.; Wender, P. A.; Dai, H., *Journal of the American Chemical Society* **2004**, *126*, 6850-6851.
- (7) Heller, D. A.; Jeng, E. S.; Yeung, T. K.; Martinez, B. M.; Moll, A. E.; Gastala, J. B.; Strano, M. S., *Science* 2006, *311*, 508-511.
- (8) Meng, S.; Maragakis, P.; Papaloukas, C.; Kaxiras, E., *Nano Letters* **2007**, *7*, 45-50.
- (9) Prato, M.; Bianco, A., Advanced Materials 2003, 15, 1765-1768.
- (10) Kam, N. W. S.; Liu, Z.; Dai, H., *Journal of the American Chemical Society* **2005**, 127, 12492-12493
- (11) Kam, N. W. S.; O'Connell, M.; Wisdom, J. A.; Dai, H., Carbon nanotubes as multifunctional biological transporters and near-infrared agents for selective cancer cell

- destruction. Proceedings of the National Academy of Sciences of the United States of America 2005, 102, 11600-11605.
- (12) Liu, Z.; Li, X.; Tabakman, S. M.; Jiang, K.; Fan, S.; Dai, H., Journal of the American Chemical Society 2008, 130, 13540-13541
- (13) Liu, Z.; Winters, M.; Holodniy, M.; Dai, H., *Angew Chem Inter* **2007**, *Ed* 46, 2023–2027.
- (14) Prato, M.; Kostarelos, K.; Bianco, A., *Accounts of Chemical Research* **2008**, *41*, 60-68.
- (15) Noy, A., *Handbook of Molecular Force Spectroscopy*. Springer: New York: 2008.
- (16) Noy, A.; Vezenov, D. V.; Kayyem, J. F.; Meade, T. J.; Lieber, C. M., *Chemistry & Biology*. 1997; *Vol. 4*, p 519-527.
- (17) Krautbauer, R.; Rief, M.; Gaub, H. E., *Nano Letters* **2003**, *3*, 493-496
- (18) Ozkaya, B.; Ozcan, O.; Thissen, P.; Grundmeier, G., *Langmuir* **2010** *26*, 8155-8160.
- (19) Sonnenberg, L.; Billon, L.; Gaub, H. E., *Macromolecules* **2008**, *41*, 3688-3691
- (20) Scherer, A.; Zhou, C.; Michaelis, J.; Brauchle, C.; Zumbusch, A., *Macromolecules* **2005**, *38*, 9821-9825
- (21) Thyparambil, A. A. W., Y.; Latour, R. A.;, Determination of Peptide-Surface Adsorption Free Energy for Material Surfaces Not Conducive to SPR or QCM using AFM. *Langmuir* **2012** *28*, 5687-94.
- (22) Kendall, K., Journal of Physics D: Applied Physics **1971**, 4, 1186-1195.
- (23) Kendall, K., *Journal of Physics D: Applied Physics* **1975**, 8, 1449-1452.
- (24) Roxbury, D.; Tu, X.; Zheng, M.; Jagota, A., *Langmuir* **2011**, *27*, 8282-8293.

- (25) Manohar, S.; Mantz, A. R.; Bancroft, K. E.; Hui, C. Y.; Jagota, A.; Vezenov, D.V., Nano Letters 2008, 8, 4365-4372.
- (26) Manohar, S.; Tang, T.; Jagota, A., *Journal of Physical Chemistry C* **2007**, *111*, 17835-17845.
- (27) Ikeda, A.; Hamano, T.; Hayashi, K.; Kikuchi, J., *Organic Letters* **2006**, *8*, 1153-1156.
- (28) Sowerby, S. J.; Cohn, C. A.; Heckl, W. M.; Holm, N. G., *Proceedings of the National Academy of Sciences of the United States of America* **2001**, 98, 820-822.
- (29) Sowerby, S. J.; Morth, C. M.; Holm, N. G., *Astrobiology* **2001**, *1*, 481-487.
- (30) Saenger, W., Principles of nucleic acid structure Springer-Verlag: 1984.
- (31) Varghese, N.; Mogera, U.; Govindaraj, A.; Das, A.; Maiti, P. K.; Sood, A. K.; Rao, C. N., *Chemphyschem* **2009**, *10*, 206-10.
- (32) Szilagyi, A.; Bonn, G. K.; Guttman, A., *Journal of Chromatography, A* **2007**, *1161*, 15-21.
- (33) Edelwirth, M.; Freund, J.; Sowerby, S. J.; Heckl, W. M., *Surface Science* **1998**, 417, 201-209.
- (34) Tao, N. J.; Shi, Z., Journal of Physical Chemistry B **1994**, 98, 1464-1471.
- (35) Mamdouh, W.; Dong, M. D.; Xu, S. L.; Rauls, E.; Besenbacher, F., *Journal of the American Chemical Society* **2006**, *128*, 13305-13311.
- (36) Sowerby, S. J.; Stockwell, P. A.; Heckl, W. M., *Origins of Life and Evolution of the Biosphere* **2000**, *30*, 81-99.
- (37) Bloomfield, V. A.; Crothers, D. M.; Tinoco, I., *Nucleic Acids: Structures, Properties, and Functions*. University Science Books: 2000.

- (38) Hutter, J. L.; Bechhoefer, J., Review of Scientific Instruments 1993, 64, 1868
- (39) Kühner, F.; Erdmann, M.; Sonnenberg, L.; Serr, A.; Morfill, J.; Gaub, H. E., *Langmuir* **2006**, *22*, 11180-11186.
- (40) Staple, D. B. G., M.; Hugel, T.; Kreplak, L.; Kreuzer, H. J.;, Forced desorption of polymers from interfaces. *New Journal of Physics* **2011**, *13*, 013025.
- (41) Keten, S.; Buehler, M. J., *Physical Review Letters* **2008**, *100*, 198301.
- (42) Chen, H.; Meisburger, S. P.; Pabit, S. A.; Sutton, J. L.; Webb, W. W.; Pollack, L., *Proceedings of the National Academy of Sciences* **2012**, *109*, 799-804.
- (43) Seol, Y.; Skinner, G. M.; Visscher, K.; Buhot, A.; Halperin, A., Stretching of Homopolymeric RNA Reveals Single-Stranded Helices and Base-Stacking. *Physical Review Letters* **2007**, *98*, 158103.
- (44) Smith, S. B.; Cui, Y.; Bustamante, C., Science **1996**, 271, 795-799.
- (45) Rechendorff, K.; Witz, G.; Adamcik, J.; Dietler, G., Persistence length and scaling properties of single-stranded DNA adsorbed on modified graphite. *The Journal of Chemical Physics* **2009**, *131*, 095103.
- (46) Huang, X.; Kovaleski, J. M.; Wirth, M., *Journal of Analytical Chemistry* **1996**, 68 4119.
- (47) Khripin, C. Y.; Zheng, M.; Jagota, A., *Journal of Colloid and Interface Science* **2009**, *330*, 255-265.
- (48) Wagner, K.; Cheng, P.; Vezenov, D. V., *Langmuir* **2011**, *27*, 4635-4644
- (49) Kennedy, S. J.; Cole, D. G.; Clark, R. L., Review of Scientific Instruments 2009, 80, 125103.
- (50) Packer, M. J.; Hunter, C. A., Journal of Molecular Biology 1998, 280, 407-420.

- (51) Roxbury, D.; Mittal, J.; Jagota, A., Nano Letters 2012, 12, 1464-1469.
- (52) Roxbury, D.; Manohar, S.; Jagota, A., *The Journal of Physical Chemistry C* **2010**, *114*, 13267-13276.

# Chapter 3 Interaction of Single-Stranded DNA with Curved Carbon Nanotube is Much Stronger than with Flat Graphite

The work described in this chapter has been titled "Interaction of Single-Stranded DNA with Curved Carbon Nanotube is Much Stronger than with Flat Graphite" by Sara Iliafar, Dmitri Vezenov, and Anand Jagota, *submitted*.

We used single molecule force spectroscopy to measure the force required to remove single stranded DNA (ssDNA) homopolymers from single-walled carbon nanotubes (SWCNTs) deposited on methyl-terminated self-assembled monolayers (SAMs). The peeling forces obtained from these experiments are bimodal in distribution. The cluster of low forces corresponds to peeling from the SAM surface, while the cluster of high forces corresponds to peeling from the SWCNTs. Using a simple equilibrium model of the single molecule peeling process, we calculated the free energy of binding per nucleotide. We found that the free energy of ssDNA binding to hydrophobic SAMs decreases as  $poly(A) > poly(G) \approx poly(T) > poly(C)$  (16.9 ± 0.1; 9.7 ± 0.1; 9.5 ± 0.1; 8.7  $\pm$  0.1 k<sub>B</sub>T). The free energy of binding of SWCNT adsorbed on this SAM also decreases in the same order poly(A) > poly(G) > poly(T) > poly(C), but its magnitude is more than double that of DNA-SAM binding energy (38.1  $\pm$  0.2; 33.9  $\pm$  0.1; 23.3  $\pm$  0.1; 17.1  $\pm$  0.1  $k_BT$ ). An unexpected finding is that binding strength of ssDNA to the curved SWCNTs is much larger than to flat graphite, and has a different ranking. The enhancement in these surface interactions could be the result of intercalation of ssDNA bases between the hydrophobic SWCNT and SAM. It is also possible that the adsorption of the bases on the

nanotubes affects the structure of water inside the SWCNTs, resulting in stronger binding energies.

### 3.1 Introduction

The rich electrical, mechanical, and thermal properties of single walled carbon nanotubes (SWCNTs) have made them strong candidates for a number of applications. For biomedical applications such as sensing<sup>1</sup>, drug delivery,<sup>2</sup> and medical nanorobots<sup>3</sup>, as well as for solution-based sorting and purification<sup>4</sup>, SWCNTs are usually dispersed in water by covalent, non-covalent, ionic, and free-radical modification of the surface of the SWCNTs.<sup>5-7</sup> Non-covalent functionalization of SWCNTs by amphiphilic molecules such as surfactants<sup>8, 9</sup>, DNA<sup>4, 10, 11</sup>, and some peptides<sup>12-14</sup> has received significant attention because it permits ease of dispersion and processing without affecting significantly the intrinsic electronic structure of the SWCNTs.<sup>15</sup> Both for design of non-covalent functionalization strategies, and to establish a basis for understanding how nanomaterials such as SWCNTs interact with biological molecules, it is important to quantify the binding strength between SWCNTs and their dispersants.

Single molecule force spectroscopy (SMFS) has emerged as a powerful tool for the study of the mechanical behavior of individual entities. It has been used to characterize elasticity,  $^{16-18}$  DNA binding modes,  $^{19-22}$  cell adhesion,  $^{23-25}$  protein unfolding,  $^{26-29}$  and colloidal forces.  $^{30}$  It can also be used to measure the force required to remove an adsorbed molecule from a surface.  $^{19-22, 31}$  We have previously used SMFS to measure the interaction between ssDNA and graphite.  $^{22, 31}$  We found that binding strength between ssDNA homopolymers could be ranked as  $T \ge A > G \approx C$ , with

corresponding free energies of  $11.3 \pm 0.8$  k<sub>B</sub>T,  $9.9 \pm 0.4$  k<sub>B</sub>T,  $7.9 \pm 0.2$  k<sub>B</sub>T, and  $7.5 \pm 0.8$  k<sub>B</sub>T. Here, we report on work in which we applied SMFS to study the interaction of ssDNA homopolymers 5'-poly( $T_{100}$ ), 5'-poly( $G_{100}$ ), 5'-poly( $G_{100}$ ), and 5'-poly( $G_{100}$ ) (5'-terminus is attached to the force probe) with SWCNTs adsorbed onto a surface coated by a methyl-terminated SAM. We show that the force required to peel ssDNA off the SAM is distinctly different from that required to peel it off an SWCNT. Moreover, we report a surprising finding that binding strength of ssDNA to the curved SWCNTs is much larger than to flat graphite.

### 3.2 Experimental Section

In order to measure the force required to peel a molecule off the surface of an SWCNT we followed a multi-step experimental routine that consisted of (i) preparing samples with individually dispersed SWCNTs, (ii) depositing them on a methyl-terminated SAM on a silicon wafer, (iii) removing the dispersant molecule off the SWCNT surface, and (iv) carrying out peeling experiments on the exposed SWCNTs.

### 3.2.1 Uniform Dispersions of 5'- $(GT)_3$ -3'/(6,5) SWCNTs

Raw (6,5)-rich (>80%) semiconducting CoMoCAT carbon nanotubes (diameter of 0.7-0.9 nm) were obtained from South West NanoTechnologies (SWeNT). Single-stranded DNA 5'-(GT)<sub>3</sub>-3' was purchased from Integrated DNA Technologies, Inc. (Coralville, IA). Following a previously described procedure, <sup>11, 32</sup> SWCNTs were dispersed with 5'-(GT)<sub>3</sub>-3' in a 1:1.5 (mass) ratio in 10 mM phosphate buffer (pH 7) containing 0.3 mM EDTA. This ssDNA sequence was chosen to be long enough to

provide sufficient binding strength to disperse the SWCNTs effectively, but to be short enough to prevent DNA from wrapping around the SWCNTs. A sequence with the latter characteristic was selected in an effort to ease the post-dispersion removal of DNA from the SWCNTs. The mixture was sonicated for 90 minutes in an ice bath at 8W using a Branson probe sonicator (Sonifier 150, G. Heinemann, Germany). The dispersion was then centrifuged at 13,200 rpm for 90 minutes in order to separate the supernatant from residual undispersed SWCNTs (discarded as a pellet).

# 3.2.2 Formation of Hydrophobic Methyl-Terminated Self-Assembled Monolayers (SAM) on Silicon Wafers

Silicon wafers (500 µm thickness, 3 inch diameter, 1–20 ohm-cm resistivity, N-type phosphorus doped, <100> crystal orientation) were purchased from Silicon Quest International (Santa Clara, CA). Organic contaminants were removed from the surface of these wafers by placing them in piranha solution (70 % H<sub>2</sub>SO<sub>4</sub> and 30 % H<sub>2</sub>O<sub>2</sub> by volume) for 30 min. The surfaces were then immediately modified by forming a hydrophobic monolayer of octyldimethylchlorosilane (ODMCISi) following a previously described procedure.<sup>32, 33</sup> Briefly, the functionalization step was carried out by refluxing 9 % (vol.) ODMCISi in heptane and 1% (vol.) butylamine in a pyrex crystallization dish at 60-65° C for 3 hours. Upon the completion of the chemical modification process, the samples were rinsed with isopropanol and annealed at 110° C under nitrogen atmosphere for 2 hours. The SAM-coated silicon wafers were later cut into smaller pieces (1 cm × 1 cm) for handling purposes. The hydrophobicity of these surfaces was characterized by measurements of advancing and receding contact angles of water, which were found to be

 $94\pm3^{\circ}$  and  $89\pm4^{\circ}$ , respectively. The thickness of the SAM determined by ellipsometry (VASE, J.A. Woollam Co.) was  $6.6\pm0.3$  Å.

### 3.2.3 Deposition of SWCNTs on Hydrophobic SAM

A 150 μl droplet of 90 μg/ml sample of dispersed 5'-(GT)<sub>3</sub>-3'/(6,5) SWCNTs was deposited on SAM-coated silicon wafers, allowed to remain in contact with the substrate for a prescribed duration (typically 10 minutes), and removed by aspiration with a pipette. This procedure results in deposition of a sub-monolayer of individual SWCNTs on the substrate.<sup>32</sup> The topology of these surfaces was imaged using a Veeco Dimension V atomic force microscope (AFM) (Santa Barbara, CA).

# 3.2.4 Displacement of 5'-(GT)<sub>3</sub>-3' from the Surfaces of SWCNTs Using Sodium Dodecyl Benzene Sulfonate (SDBS)

We used a surfactant, SDBS, to remove the DNA from the SWCNTs adsorbed on the surface of hydrophobic silicon wafers. To establish that the SDBS indeed rapidly removes the DNA from SWCNTs, we conducted separate experiments in bulk solution phase. In this procedure, the absorbance spectrum of 100 µl of SWCNTs dispersed by ssDNA was measured using a UV/Vis/NIR spectrophotometer (Varian Cary 50). To displace the ssDNA molecules, 0.2% (wt.) solution of SDBS in 10 mM phosphate buffer (with 0.3 mM EDTA) was added to the ssDNA/SWCNT dispersion in a 1:1 ratio (vol.). To monitor the DNA-SDBS exchange, the shift in the position of the absorbance peak

from 990 nm to 978 nm was followed over time until SDBS had completely replaced ssDNA molecules from the SWCNTs.<sup>34</sup>

To remove DNA from the SWCNTs adsorbed on the solid surfaces, we immersed the samples into the same 0.2% (wt.) SDBS solution for 2 minutes followed by rinsing with DI water. The samples were then dried with nitrogen. To obtain both a high coverage of SWCNTs on the surface and to displace ssDNA completely, we repeated the 5'-(GT)<sub>3</sub>-3'/(6,5) SWCNTs deposition and SDBS/DI rinsing step three times. Control samples for analysis of surface chemical composition were prepared following the same procedure as described above except that, for the deposition step, we used a solution that contained no DNA-dispersed SWCNTs. For evidence of DNA removal by the SDBS solution, we carried out height analysis on AFM topography images of adsorbed SWCNTs captured between each step of the deposition and rinsing process.

We next used X-ray photoelectron spectroscopy (XPS) (Scienta ESCA-300) to scan for the presence of nitrogen on the substrate. The samples were positioned at a 20° take-off angle between the sample surface and the path to the analyzer. Spectra were analyzed using CASA XPS® software (version 2.3.15dev77). Survey spectra were taken at a 300-eV pass energy and with a step energy of 1 eV. The pass energy for high-resolution spectra in the N 1s region was 150 eV, and the step energy was 0.05 eV. Since, in our system, only ssDNA contains nitrogen, the existence or disappearance of this peak upon rinsing with SDBS indicates presence or absence, respectively, of DNA on the substrate.

# 3.2.5 Single Molecule Force Measurements on 5'- $T_{100}$ Peeling from (6,5) SWCNTs

Gold-coated NSC18 atomic force microscopy (AFM) probes with spring constant of  $3.5 \pm 1.5$  N/m were purchased from MikroMasch (San Jose, CA). The force probes were cleaned by exposure to a PDC-001 air plasma cleaner (Harrick Plasma, Ithaca, NY) for 1 minute on high power, and rinsed with ethanol. 5'-Thiol-modified  $T_{100}$  (purchased from Integrated DNA Technologies, Inc.) was dissolved at 0.1 nM concentration in a 10 mM phosphate buffer with 1 M ionic strength NaCl (pH ~7). To deprotect the thiol group, TCEP (tris(2-carboxyethyl)phosphine, 98% purity, purchased from Alfa Aesar, Ward Hill, MA) was added to the DNA solution (to obtain 6 mM concentration), and this solution was then left for 30 minutes to allow ample time to reduce the disulfide. Next, the Au-coated AFM tips were placed in the ssDNA solution for 1 hour. The chemically functionalized AFM probe was then placed in a 6 mM solution of mercaptohexanoic acid (MHA) in ethanol for 1 hour to space out the ssDNA molecules by filling the remaining sites on the surface of the gold-coated tip and to remove non-specifically adsorbed DNA. The probe was rinsed with ethanol and dried with nitrogen after each modification step.

Using an MFP-3D atomic force microscope (Asylum Research, Santa Barbara, CA), single molecule (SM) peeling experiments were carried out in approximately 3 mL of 10 mM phosphate buffer containing 100 mM NaCl. Following a previously established procedure,<sup>31</sup> the AFM cantilevers were calibrated in air after the completion of single molecule force spectroscopy (SMFS) experiments conducted in fluid. Because the surface consisted of SWCNTs adsorbed onto a methyl-terminated SAM, any particular experiment could represent peeling the molecule off an SWCNT or the SAM. To correlate a peeling experiment with the location off which the molecule was peeled,

we first imaged the surface under tapping mode in fluid immediately prior to the peeling experiments. Next, we acquired a force-volume map, i.e., force-distance measurements obtained in a 2-dimensional array from the same area of the sample for which the topography image was just obtained. As described later in the chapter, the distribution of peeling forces was found to be bimodal, with one cluster corresponding to peeling off the SAM and the other to peeling off SWCNTs. The peeling experiments were carried out at a scan rate of 200 nm/s. Maximum compressive force applied was less than 1 nN.

Figure 3.1 shows a typical force-distance relationship obtained for our steady state peeling process. In analyzing the force curves, we considered only the jump in the final peeling plateau, and used a custom code written in IGOR Pro (Wavemetrics, Eugene, OR) to obtain an average force measured over a distance of 2 nm on both sides of the molecule detachment step. We followed our previously established guidelines to identify valid force curves that were suitable for further analysis.<sup>31</sup> The peeling curves were considered to be valid if i) the approach and retraction retraces overlapped for the noncontact region, ii) the separation distance of the last peeling step was smaller than that of the DNA contour length, iii) the tip–surface adhesion was small enough that the peeling steps were not masked by the initial pull-off force, and iv) the peeling region displays a flat plateau for at least 10 nm of separation to present a steady-state peeling process.<sup>31</sup> All measurements reported in this chapter are mean values; errors indicate 95 % confidence limits obtained from averaging peeling forces from multiple experiments carried out under nominally identical conditions.

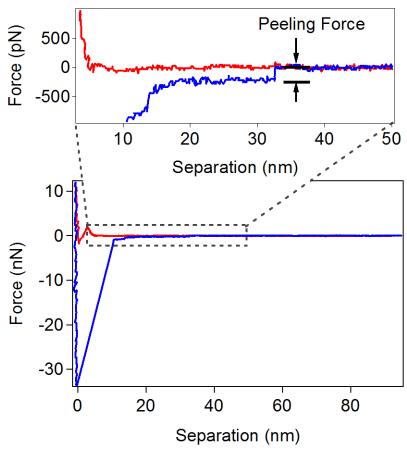


**Figure 3.1.** Typical force—distance curve for peeling 5'-  $T_{100}$  ssDNA from SWCNTs deposited on a methyl-terminated SAM on a silicon wafer. The force curves were obtained at a tip velocity of 200 nm/s in 10 mM phosphate buffer containing 100 mM NaCl. The red curve is for the tip approaching the surface, blue curve represents tip retraction.

## 3.3 RESULTS AND DISCUSSION

## 3.3.1 Bare Carbon-Nanotubes on a Hydrophobic Self-Assembled Monolayer

Prior to conducting force measurements, it is necessary to establish that the DNA has been removed from SWCNTs adsorbed on the silicon wafer. DNA was removed by rinsing samples with a solution of an ionic surfactant, SDBS. The surfactant, in turn, was

removed by rinsing with DI water. We first show that this surfactant is effective in removing DNA off the surface of dispersed SWCNTs. Figure 3.2 shows absorbance spectra of DNA-coated SWCNTs before and after addition of SDBS at ambient temperature. We have shown previously that DNA-coated SWCNTs have a characteristic absorbance peak at 990 nm, whereas SDBS-coated SWCNTs have a peak at 978 nm.<sup>34</sup> Figure 3.2 demonstrates that the displacement of 5'-(GT)<sub>3</sub>-3' by SDBS is very rapid at room temperature.

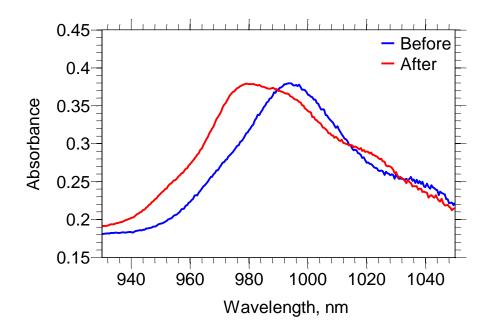


**Figure 3.2.** The peak position of the NIR absorbance spectrum of the SWCNT dispersion shifts from 990 nm (DNA-coated) to 978 nm (SDBS-coated) immediately upon addition of the SDBS solution. Subsequent scans obtained 10 minutes after the addition of SDBS to the 5'-(GT)<sub>3</sub>-3'/SWCNT dispersion showed no further change. This experiment was repeated three times to ensure reproducibility of the results.

To obtain bare SWCNTs, samples with adsorbed nanotubes were subjected to rinsing by SDBS solution followed by rinsing with DI water. We used several depositionrinse cycles to increase the density of the nanotubes on the surface. Between each step in the process, the topography of these samples was imaged in air. To obtain the average SWCNT diameters, we subtracted the baseline from the image, identified areas predominantly covered with individual SWCNTs rather than bundles (maximum height of less than 1.6 nm), zoomed into these areas (as shown in Figure 3.3), and used a depth analysis tool (Veeco) to determine the average diameter of the SWCNTs. This analysis tool builds a histogram of depth data within the specified area, applies a Gaussian lowpass filter to the data to remove noise, and compares the depths between two dominant features by automatically finding the mean of each distribution and calculating the peakto-peak distance, i.e. the difference in depth. In our studies, we obtained one depth distribution for the SAM-coated silicon wafer and another for the SWCNTs (Figure 3.3C). To measure the height of the SWCNTs, the difference between the depth of the background substrate and that of the SWCNTs was calculated. Furthermore, we independently checked and confirmed the values obtained via the depth analysis tool by manually measuring changes in height over the cross-section of SWCNTs deposited on the SAM for multiple samples. The average diameters (each obtained from over 300 or more image depth histograms) showed a gradual decrease from the first deposition of the nanotubes to the last DI water rinsing step (Figure 3.4). Quantitatively, the measured diameters decreased from  $1.4 \pm 0.20$  nm (19 samples) after the first SWCNT deposition to 0.85± 0.06 nm (35 samples) after the last rinsing step. Since the diameter of these SWCNTs as reported by the manufacturer (Sigma-Aldrich Corp) is 0.7-0.9 nm, our height analysis results evidently support the interpretation that SDBS rinsing replaces 5'- (GT)<sub>3</sub>-3' from the surface of SWCNTs, while the follow-up rinsing with DI water removes SDBS from the SWCNTs.

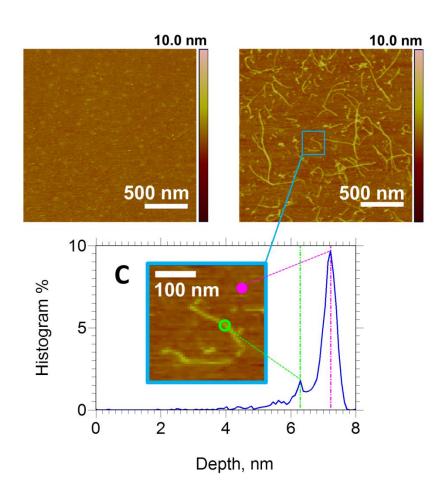


**Figure 3.3.** Surface topography of SAM-coated silicon wafers obtained in air for (A) a control sample exposed to phosphate buffer only, and (B) a sample exposed for 10 minutes to a droplet of 90  $\mu$ g/ml dispersion of 5'-(GT)<sub>3</sub>-3'-coated SWCNTs and then rinsed by SDBS (2 minutes) and DI water. The sample in (B) had undergone three CNT-deposition-surfactant/water-rinse cycles. (C) Using the depth analysis tool, the diameter of the SWCNTs was obtained from the peak-to-peak difference in depth and averaged over multiple areas and samples.

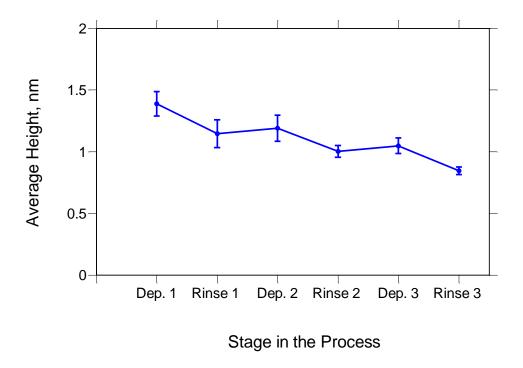


**Figure 3.4.** Analysis of the average height of the nanotubes after each step of 5'-(GT)<sub>3</sub>-3'/SWCNT deposition and SDBS/DI water rinse showed a gradual decrease in the apparent mean diameter of the CNTs. After the third rinsing step, the mean diameter of  $0.85 \pm 0.06$  nm (35 separate measurements) is well within the diameter range (0.7-0.9 nm) of bare SWCNTs reported by the manufacturer.

Figure 3.4 shows that each SDBS/water rinsing step reduces the average SWCNT height by 0.2-0.3 nm, consistent with the removal of DNA. Following the subsequent deposition step, the height increases only slightly. Khripin *et al.* have shown that the deposition of DNA-CNT on a SAM substrate is highly dependent on the density of previously deposited SWCNTs on that substrate. <sup>32</sup> In particular, they have reported that the random sequential adsorption approaches a saturation density, which likely limits how much the height can increase during subsequent depositions. Notice that average

SWCNT height after each SDBS/water rinse continues to decrease. This observation could be due to a number of reasons, e.g. i) because DNA is incompletely removed in a single rinse step and repeated rinsing is required to improve efficiency, ii) SDBS rinsing selectively removes larger diameter SWCNTs, or iii) rinsing breaks down small bundles of nanotubes or crossing nanotubes.

To investigate further whether the SDBS rinse fully removed the ssDNA from the surface of the previously deposited SWCNTs, we carried out an XPS study of the surface chemical composition. Following the same deposition-and-rinse procedure as described earlier, now with two cycles instead of three, we prepared the following three samples using SAM-coated silicon wafers: i) a control sample exposed to phosphate buffer (no rinse step), ii) a dispersion of 5'-(GT)<sub>3</sub>-3'-coated SWCNTs deposited without the rinse step, and iii) a dispersion of 5'-(GT)<sub>3</sub>-3'-coated SWCNTs deposited and rinsed with the SDBS/DI water. Since ssDNA is the only component in our system that contains nitrogen, we scanned for the presence of nitrogen in our samples.

Figure 3.5 shows a high-resolution XPS spectrum of N 1s region obtained from these three samples. The disappearance of the N 1s peak after the second SDBS/DI water rinse cycle observed here further supports our finding from the AFM height analysis that this rinsing step completely removes all ssDNA from the surface of carbon nanotubes deposited on the SAM substrate. Moreover, we found that this N 1s peak is best fitted with two Gaussian components, suggesting that the nitrogen has two distinct chemical environments, consistent with the ssDNA composition, 5'-(GT)<sub>3</sub>-3'. To obtain the fits, we restricted the full width at half maximum (FWHM) of the two peaks to be the same.

An XPS study conducted by Ptasinka et al. on DNA nucleobases deposited on untreated silicon wafers has shown that thymine's N 1s peak is best fitted with one Gaussian peak located slightly above 400 eV, while guanine's nitrogen peak is best fitted with two Gaussian components.<sup>35</sup> The first Gaussian component of guanine's N 1s peak is located at the same binding energy as that of thymine's N 1s peak, and its second component is positioned at a slightly lower energy, around 399 eV.<sup>35</sup> In their paper, Ptasinka et al. attributed the higher energy peak to amino (C-NH-C and C-NH<sub>2</sub>) sites, while they associated the lower energy peak with the imino (C-N=C) species.<sup>35</sup> Following Ptasinka's interpretation, we obtained a two-component Gaussian fit for our sample containing (GT)<sub>3</sub>. Here, we found that the ratio of the area for the high energy peak to that of the low energy one was, not surprisingly, 5:2, corresponding to five amino sites and two imino sites in the GT repeat unit. Since the complete removal of ssDNA from the substrate is evident from our XPS study, we attribute the small gradual decrease in SWCNT height with the number of SDBS rinsing steps to be due to the break-up of small bundles.

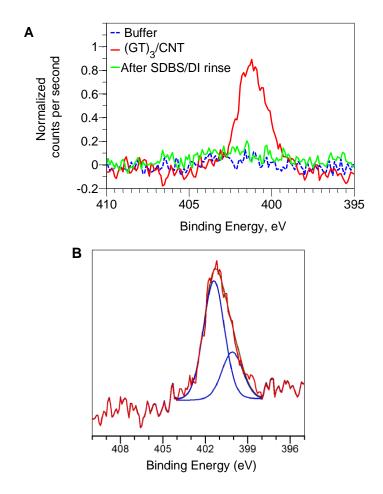


**Figure 3.5.** (A) High resolution XPS spectra of the N 1s region obtained for three samples with the following variations in the preparation: i) a sample exposed to buffer (no DNA) without the rinse step, ii) a dispersion of 5'-(GT)<sub>3</sub>-3'/SWCNT deposited without the rinse step, and iii) a dispersion of 5'-(GT)<sub>3</sub>-3'/SWCNT deposited, followed by the SDBS/DI water rinse. The SAM-coated silicon wafer on which a dispersion of 5'-(GT)<sub>3</sub>-3'/SWCNT was deposited without the rinse step displayed a peak located at 401.2 eV with FWHM of 2.02 eV. (B) The N 1s peak from sample (i) in (A) can be represented by the superposition of two Gaussian components.

### 3.3.2 Peeling of Homopolymer ssDNA from Bare Single Walled Carbon Nanotubes

To quantify the interaction between ssDNA homopolymers and SWCNTs,  $T_{100}$ /MHA functionalized gold-coated AFM force probes were first used to image a 3  $\mu$ m  $\times$  3  $\mu$ m area, where the SWCNTs were deposited on methyl-terminated SAM. The same force probe was then used to obtain a force map from the same region. The term force map refers to an array of force-distance measurements (Figure 3.1) obtained over a selected area with a specified number of gridpoints (40  $\times$  40 in our experiments).

The peeling forces measured from a typical force map acquired with a  $T_{100}$ modified probe were plotted as a histogram and revealed two distinct force peaks (similar to those shown in Figure 3.6A). Using Igor's multi-peak fitting package, we fitted two Gaussian distributions to our bimodal peeling force data and obtained mean peeling forces of  $78.4 \pm 0.8$  pN (total of n=1673 valid force curves) and  $172.0 \pm 1.6$  pN (n=714). We have previously reported that the peeling of polythymine from a methyl-terminated SAM prepared under the same conditions as used for this study results in 77.5 pN mean peeling force.<sup>31</sup> This comparison suggests that the first peak in the histogram corresponds to peeling ssDNA from the SAM, whereas the second peak should then correspond to peeling ssDNA from the SWCNT. Figures 3.6A-D show a compilation of the results from analysis of all our experiments conducted using the four ssDNA homopolymers on SAM surfaces with bare SWCNTs. All force histograms display two distinct clusters: i) low peeling forces with mean values similar across all sequences (70 to 130 pN), and ii) high peeling forces with mean values covering a broader range of forces (130 to 260 pN).

We associate the first peak in the force histograms with the DNA-SAM interactions and the second peak with the DNA-nanotube interactions on the basis of the following three pieces of evidence (discussed in more details below): i) high peeling forces are localized in the nanotubes occupied regions and low peeling forces are detected in the nanotube-free regions; ii) bare SAM surfaces lacking the CNTs show a single peak in force histograms whose position is identical to that of the first peak in the force histograms obtained from the SWCNT-on-SAM samples; iii) the relative frequency of low versus high forces (ratio of histogram peak areas) tracks the relative surface coverage of CNTs and SAM as sensed by the AFM probe.

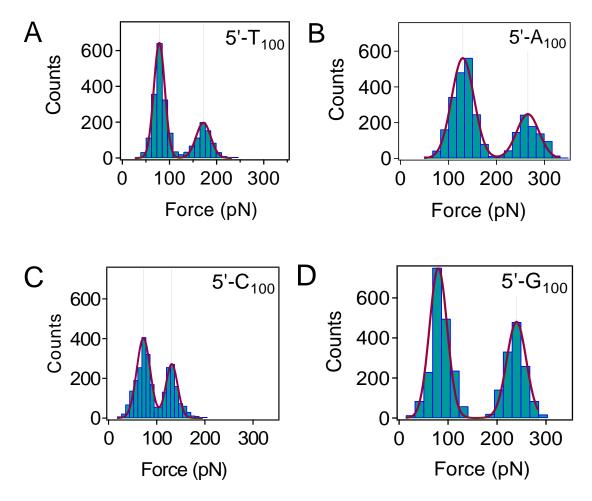


**Figure 3.6.** Force histograms for peeling ssDNA homopolymers from SWCNTs dispersed on a methyl-terminated SAM showing two distinct peaks (peak positions and errors of the mean are derived from the Gaussian fits to the experimental data). The distributions of peeling forces were centered at  $78.4 \pm 0.8$  pN (total of n=1673 force curves) and  $172.0 \pm 1.6$  pN (n=714) in 4 independent experiments for 5'-T<sub>100</sub> (A), 130.0  $\pm 1.5$  pN (n=1948) and  $265.4 \pm 2.2$  pN (n=890) in 3 independent experiments for 5'-A<sub>100</sub> (B),  $72.5 \pm 0.9$  pN (n=1863) and  $131.2 \pm 1.1$  pN (n=1114) in 3 independent experiments for 5'-C<sub>100</sub> (C), and  $80.1 \pm 1.2$  pN (n=1879) and  $239.8 \pm 1.5$  pN (n=1339) from 3 independent experiments for 5'-G<sub>100</sub> (D).

To confirm the assignment of the peaks, we correlated the spatial distribution of the high and low peeling forces with local sample composition. By considering the midpoint between peaks as a cut-off between the two force distributions, we assign a peeling force less than 127 pN to belong to the first peak in the histogram and a peeling force larger than 127 pN to belong to the second peak. We overlaid the locations of the sites where valid peeling force curves were obtained with the AFM height image (Figure 3.7). In Figure 3.7, we represent the location of a low force by a blue marker and the location of a high force by a red marker. It is clear that low forces identified as due to peeling from the SAM coated surface correspond well with regions of the image between SWCNTs. On the contrary, high forces identified as due to peeling from the SWCNT correlate well with regions of the image where the SWCNTs lie. This placement of high peeling forces in the vicinity of the nanotubes supports the interpretation that the high peeling forces are due to removal of  $T_{100}$  ssDNA from individual SWCNTs.

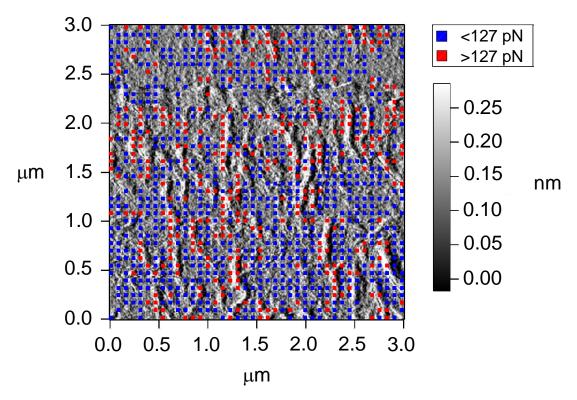


**Figure 3.7.** Superposition of the sample topography and locations of the gridpoints where individual force-distance curves were acquired from SWCNTs and a methyl terminated SAM. Placement on the sample of valid force curves with the peeling force of less than 127 pN is shown by red squares and placement of force curves higher than 127 pN is shown in blue. Despite some mismatch, there is a clear correlation between the location of the SWCNTs and the high peeling forces, and between the location of regions presenting methyl-terminated SAM and low peeling forces.

By carrying out experiments on peeling ssDNA from SAM-coated silicon wafers lacking the nanotubes, we observed a single-mode distribution of peeling forces:  $125.1 \pm 3.5 \text{ pN}$  for poly(A) (3 experiments with n=116 valid force curves),  $74.2 \pm 0.8 \text{ pN}$  for poly(C) (4 experiments, n=844), and  $77.0 \pm 1.9 \text{ pN}$  for poly(G) (3 experiments, n=316). Note that we previously reported 77.5 pN mean peeling force for poly(T), also producing

a single-mode force distribution. Since in the presence of deposited nanotubes a bimodal distribution of forces is observed reproducibly for all ssDNA homopolymers, and considering that the low-force mode was found to be similar to peeling from the bare SAM, we have interpreted the higher forces to be due to the interactions of the ssDNA with the carbon nanotubes.

Finally, we note that it is not surprising that the probability of the peeling force to fall into the distribution peak arising from the DNA-SWCNTs interaction is always lower than that associated with the SAM (compare peak heights in Figure 3.6A-D). corroborate this observation, we examined the surface coverage of SWCNTs on 34 independent SAM-coated silicon wafers with concentration of deposited SWCNTs typical of the sample preparation for the peeling experiments (i.e. deposition from 90 μg/ml solution). Since the radius of AFM probes is 1-2 orders of magnitude larger than the diameter of the SWCNTs, the surface fraction of CNTs and contact area available for ssDNA-CNT interactions are both effectively increased due to convolution with the tip shape (and multiple DNA molecules available for binding with CNT). The height image shows CNTs much wider than ~1 nm expected diameter. At the same time, long oligonucleotide (100-mers) at multiple attachment points near tip apex can interact with CNTs even when the probe is misaligned from the CNT axis. The ratio of SWCNTs to SAM on the substrates was found to be 1 to  $5.0 \pm 0.9$ . This finding indirectly supports our conclusion that high forces are due to peeling from SWCNTs, while the weak interactions are coming from ssDNA peeling from the SAM substrates.

The results shown in Figure 3.7 are summarized in Table-3.1. In our previous work, we demonstrated that a simple equilibrium model can relate the peeling force f of a freely jointed chain (FJC) to free energy required to desorb a link from its adsorbed state on the surface to its desorbed state in solution,  $\gamma'$ :<sup>31</sup>

$$\Gamma' = \ln \left\lceil \frac{\sinh(F)}{F} \right\rceil \tag{3.1}$$

where  $\Gamma' = \frac{\gamma' b}{k_B T}$  is the dimensionless free energy and  $F = \frac{f b}{k_B T}$  is the dimensionless force

per ssDNA Kuhn segment of length b (1.5 nm).<sup>36</sup> In this model, we assume that the part of the chain in the peeling junction (where the links switch between adsorbed and desorbed states) is in equilibrium. Given the contour length of ssDNA monomer, ( $b_{mono}$  = 0.56 nm),<sup>22</sup> one can calculate its free energy of binding per nucleotide,

 $\gamma' b_{mono} = \Gamma' k_B T \left( \frac{b_{mono}}{b} \right)$ , <sup>31</sup> by using the measured peeling forces, f. Furthermore, to account for the enthalpic stretching of the ssDNA, we used a corrected model (extendable FJC) to calculate the dimensionless peeling forces:<sup>22</sup>

$$F = \frac{f b \left(1 + \frac{f}{\kappa}\right)}{k_B T} \tag{3.2}$$

where,  $\kappa$  is the segment elasticity of ssDNA ( $\kappa = 2.4$  nN).

**Table 3.1.** Summary of the peeling forces and the free energy of binding per nucleotide for all ssDNA homopolymers interacting with methyl terminated SAM or SWCNT.

Sequence	SAM	SWCNT		
	Peeling	Binding	Peeling	Binding Energy
	Force (pN)	Energy	Force (pN)	per Nucleotide
		per		$(k_BT)$
		Nucleotide		
		$(k_BT)$		
	Substrate: SAM-coated silicon wafer			
Pyrimidines				
$5'$ - poly( $T_{100}$ )	$77.8 \pm 1.6$	$9.4 \pm 0.1$		
5'- $poly(C_{100})$	$74.2 \pm 0.8$	$8.9 \pm 0.1$		
Purines				
5'- $poly(A_{100})$	$125.1 \pm 3.5$	$16.2 \pm 0.3$		
5'- $poly(G_{100})$	$77.0 \pm 1.9$	$9.3 \pm 0.1$		
Substrate: SWCNT deposited on SAM-coated silicon wafer				
Pyrimidines				
5'- poly(T <sub>100</sub> )	$78.4 \pm 0.8$	$9.5 \pm 0.1$	$172.0 \pm 1.6$	$23.3 \pm 0.1$
5'- $poly(C_{100})$	$72.5 \pm 0.9$	$8.7 \pm 0.1$	$131.2 \pm 1.1$	$17.1 \pm 0.1$
Purines				
5'- $poly(A_{100})$	$130.0 \pm 1.5$	$16.9 \pm 0.1$	$265.4 \pm 2.2$	$38.1 \pm 0.2$
5'- poly(G <sub>100</sub> )	$80.1 \pm 1.2$	$9.7 \pm 0.1$	$239.8 \pm 1.5$	$33.9 \pm 0.1$

By comparing the mean free energy of binding per nucleotide required to remove ssDNA homopolymers, we rank the interaction of these sequences with SAM substrates in the following order:  $A > G \approx T > C$ , which is quite different from the interaction of the same molecules with HOPG:  $T \ge A > G \ge C$ .<sup>31</sup> On the other hand, with the exception of  $A_{100}$ , we have found that the peeling forces of ssDNA from the hydrophobic SAM surfaces are quite similar in magnitude (74-78 pN) to those we previously measured using HOPG as the solid substrate (65-80 pN). This similarity of peeling forces on the

two hydrophobic substrates points to the dominant nature of the hydrophobic interactions in this systems, as we have emphasized before. At the same time, the exact chemical nature of the substrate and effect of the phosphodiester backbone are reflected in the ranking of the strength of the DNA-surface interactions, which do not trace the trends expected on the basis of the size of the nucleobases (i.e. the forces do not scale with the footprint of the hydrophobic contact).

With the exception of adenine, interaction energy between SAM and all nucleotides is very similar. The unusually high binding energy between poly(A) and methyl SAM surface implies much greater hydrophobic character and base stacking energy for adenine than for other nucleobases, which is consistent with the propensity of poly(A) (unlike for the other homopolymers) to form stable helical secondary structure even in a single stranded form.<sup>37</sup>

The relative order of the DNA binding strength for SWCNT is the same as for SAM (A > G > T > C), however, the differences between different nucleotides are much more pronounced than in the case of flat surfaces (SAM and graphite). This ranking reflects the relative size of the nucleobases and agrees with the theoretical and experimental results on adsorption energies of monomeric nucleobases. <sup>22, 38-40</sup> Quantum mechanical studies on DNA nucleobases physisorbed on carbon surfaces have shown an inverse relationship between their free energy of binding and the curvature of the carbon nanotube. <sup>41</sup> This finding is consistent with the expectation that the  $\pi$ -stacking between the DNA's aromatic nucleobases and an aromatic surface should decrease with an increase in surface curvature, i.e. going from graphite to carbon nanotubes. However, our

experimental results are in stark contrast to this expectation, demonstrating that the interaction of the ssDNA with surface-adsorbed SWCNTs is much stronger than with flat graphite. Our results show that ssDNA binds to curved SWCNTs with strength roughly twice as great as that to flat graphite. As depicted in Figure 3.8A, one possibility is that this enhancement in interactions is indicative of a spontaneous or intrinsic curvature that the ssDNA backbone prefers to adopt. This natural curvature of the ssDNA matches the radius of the SWCNT. For example, Takahashi, et al, have shown that carbon nanotubes can disentangle the agglomerated structure that DNA takes in solution while HOPG cannot do so. The energy penalty for disrupting such molecular curvature of the DNA can then be estimated as a difference between the free energy of binding to SWCNT and graphite, i.e. will be in the range between 10 and 20 k<sub>B</sub>T per base. Given that the effective Kuhn length of ssDNA is generally greater than the distance between bases, and that the energy to straighten a freely jointed chain is on the order of k<sub>B</sub>T per Kuhn length, this value seems large.

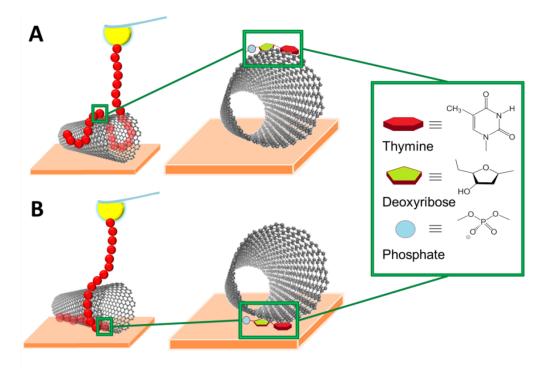


**Figure 3.8.** Pictorial representation of proposed mechanisms to explain the enhanced interaction between ssDNA and SWCNTs, compared to ssDNA with graphite. (A) ssDNA has a natural curvature that prefers to adsorb on the curved surface of an SWCNT. (B) ssDNA intercalates between the SWCNT and the hydrophobic substrate.

An alternative hypothesis is that the increase in the peeling forces of ssDNA homopolymers from SWCNTs (compared to graphite) is due to the preference of the hydrophobic bases to minimize their interactions with the surrounding aqueous buffer solution (Figure 3.8B).<sup>43</sup> In order to gain the most favorable interaction, these amphiphilic molecules may be repositioning themselves to insert the bases into the hydrophobic SAM-SWCNT interface, while keeping polar and charged backbone exposed to highly polar aqueous environment. Since free energy of binding to SAM and graphite are similar in magnitude, the intercalation of nucleobases between SWCNT and

SAM surface is consistent with approximately doubling of apparent free energy of binding when moving from flat surfaces of SAM or graphite to a sample of nanotubes residing on the methyl surface.

In principle, one should also consider the possibility that DNA stands can insert inside the nanotube. Experiments on pulling DNA from the nanotube pores demonstrate much higher steady state forces that what we typically observed for peeling ssDNA from graphite. However, several observations would contradict this interpretation. Many nanotubes shown in Figure 3.7 are 500 nm or greater in length. The length of the DNA used to produce this force-volume map is about 60 nm. In spite of this order of magnitude disparity in length, we observed high peeling forces along the entire axis of these long nanotubes and not only at the endpoints where DNA entry inside the nanotubes is possible. In addition, limiting presumed active sites for strong SWCNT-DNA interactions to nanotubes ends should greatly reduce the relative frequency of observing high forces. Thus, corresponding peak area would not reflect apparent surface coverage – an effect we do not observe.

Finally, it is possible that observed peeling forces reflect true difference in binding energy of nucleobases to nanotubes and graphite. For example, adsorption of the base could introduce significant structural changes to water adjacent to carbon layer inside the nanotube, interaction absent in the case of semi-infinite planar substrates such as SAM or graphite. The presence of the counter ions inside the nanotube could also affect the peeling process. To identify whether the enhancement in binding energy is from ssDNA base intercalation between SWCNT and SAM, or from structural changes to

the water inside the nanotube, one should repeat these experiments with suspended carbon nanotubes in a fluidic environment and ensure that the tubes do not come into contact with the supporting substrate that is below them.

#### 3.4 Conclusions

We have used single molecule force spectroscopy to measure the force required to remove each of the four ssDNA homopolymers from surface-adsorbed single-walled carbon nanotubes as well as from a methyl-terminated self-assembled monolayer. We have shown that free energy of binding of these ssDNA sequences to the SAM-modified substrate is quite similar to their free energy of binding to graphite. We discovered that, contrary to the expectation that the binding of ssDNA with carbon surfaces should decrease with surface curvature, the peeling forces in fact are greater by a factor of two to three in our measurements on SWCNTs. We interpret the enhancement in this binding either to represent an effect of spontaneous curvature of ssDNA, to result from intercalation of ssDNA bases between the SWCNT and the SAM surface, or to reflect complex contribution of water or counter ions inside the nanotube.

#### 3.5 References

- (1) Zhang, J.; Boghossian, A. A.; Barone, P. W.; Rwei, A.; Kim, J.-H.; Lin, D.; Heller, D. A.; Hilmer, A. J.; Nair, N.; Reuel, N. F.; Strano, M. S., Single Molecule Detection of Nitric Oxide Enabled by d(AT)15 DNA Adsorbed to Near Infrared Fluorescent Single-Walled Carbon Nanotubes. *Journal of the American Chemical Society* **2010**, *133*, 567-581.
- (2) Liu, Z.; Sun, X.; Nakayama-Ratchford, N.; Dai, H., Supramolecular Chemistry on Water-Soluble Carbon Nanotubes for Drug Loading and Delivery. *ACS Nano* **2007**, *1*, 50-56.
- (3) Popov, A. M.; Lozovik, Y. E.; Fiorito, S.; Yahia, L., Biocompatibility and applications of carbon nanotubes in medical nano robots. *International Journal of Nanomedicine* **2007**, *2*, 361-372.
- (4) Tu, X.; Manohar, S.; Jagota, A.; Zheng, M., DNA sequence motifs for structure-specific recognition and separation of carbon nanotubes. *Nature* **2009**, *460*, 250-253.
- (5) Tasis, D.; Tagmatarchis, N.; Georgakilas, V.; Prato, M., Soluble Carbon Nanotubes. *Chemistry A European Journal* **2003**, *9*, 4000-4008.
- (6) Balasubramanian, K.; Burghard, M., Chemically Functionalized Carbon Nanotubes. *Small* **2005**, *1*, 180-192.
- (7) Ghosh, S.; Rao, C., Separation of metallic and semiconducting single-walled carbon nanotubes through fluorous chemistry. *Nano Research* **2009**, *2*, 183-191.
- (8) Moore, V. C.; Strano, M. S.; Haroz, E. H.; Hauge, R. H.; Smalley, R. E.; Schmidt, J.; Talmon, Y., Individually suspended single-walled carbon nanotubes in various surfactants. *Nano Letters* **2003**, *3*, 1379-1382.

- (9) Arnold, M. S.; Green, A. A.; Hulvat, J. F.; Stupp, S. I.; Hersam, M. C., Sorting carbon nanotubes by electronic structure using density differentiation. *Nat. Nanotechnol.* **2006**, *1*, 60-65.
- (10) Zheng, M.; Jagota, A.; Semke, E. D.; Diner, B. A.; Mclean, R. S.; Lustig, S. R.; Richardson, R. E.; Tassi, N. G., DNA-assisted dispersion and separation of carbon nanotubes. *Nature Materials* **2003**, *2*, 338-342.
- (11) Zheng, M.; Jagota, A.; Strano, M. S.; Santos, A. P.; Barone, P.; Chou, S. G.; Diner, B. A.; Dresselhaus, M. S.; Mclean, R. S.; Onoa, G. B.; Samsonidze, G. G.; Semke, E. D.; Usrey, M.; Walls, D. J., Structure-Based Carbon Nanotube Sorting by Sequence-Dependent DNA Assembly. *Science* **2003**, *302*, 1545-1548.
- (12) Dieckmann, G. R.; Dalton, A. B.; Johnson, P. A.; Razal, J.; Chen, J.; Giordano, G. M.; Muñoz, E.; Musselman, I. H.; Baughman, R. H.; Draper, R. K., Controlled assembly of carbon nanotubes by designed amphiphilic peptide helices. *Journal of the American Chemical Society* **2003**, *125*, 1770-1777.
- (13) Grigoryan, G.; Kim, Y. H.; Acharya, R.; Axelrod, K.; Jain, R. M.; Willis, L.; Drndic, M.; Kikkawa, J. M.; DeGrado, W. F., Computational design of virus-like protein assemblies on carbon nanotube surfaces. *Science* **2011**, *332*, 1071-1076.
- (14) Zorbas, V.; Ortiz-Acevedo, A.; Dalton, A. B.; Yoshida, M. M.; Dieckmann, G. R.; Draper, R. K.; Baughman, R. H.; Jose-Yacaman, M.; Musselman, I. H., Preparation and characterization of individual peptide-wrapped single-walled carbon nanotubes. *Journal of the American Chemical Society* **2004**, *126*, 7222-7227.
- (15) Zhao, Y.-L.; Stoddart, J. F., Noncovalent Functionalization of Single-Walled Carbon Nanotubes. *Accounts of Chemical Research* **2009**, *42*, 1161-1171.

- (16) Li, H.; Cao, Y., Protein mechanics: from single molecules to functional biomaterials. *Acc Chem Res* **2010**, *43*, 1331-41.
- (17) Sbrana, F.; Lorusso, M.; Canale, C.; Bochicchio, B.; Vassalli, M., Effect of chemical cross-linking on the mechanical properties of elastomeric peptides studied by single molecule force spectroscopy. *J Biomech* **2011**, *44*, 2118-22.
- (18) Hugel, T.; Grosholz, M.; Clausen-Schaumann, H.; Pfau, A.; Gaub, H.; Seitz, M., Elasticity of Single Polyelectrolyte Chains and Their Desorption from Solid Supports Studied by AFM Based Single Molecule Force Spectroscopy. *Macromolecules* **2001**, *34*, 1039-1047.
- (19) Chaurasiya, K. R.; Paramanathan, T.; McCauley, M. J.; Williams, M. C., Biophysical characterization of DNA binding from single molecule force measurements. *Phys Life Rev* **2010**, *7*, 299-341.
- (20) Krautbauer, R.; Pope, L. H.; Schrader, T. E.; Allen, S.; Gaub, H. E., Discriminating small molecule DNA binding modes by single molecule force spectroscopy. *FEBS Lett.* **2002**, *510*, 154-158.
- (21) Paik, D. H.; Perkins, T. T., Dynamics and Multiple Stable Binding Modes of DNA Intercalators Revealed by Single-Molecule Force Spectroscopy. *Angew. Chem., Int. Ed.* **2012,** *51*, 1811-1815, S1811/1-S1811/9.
- (22) Manohar, S.; Mantz, A. R.; Bancroft, K. E.; Hui, C.-Y.; Jagota, A.; Vezenov, D. V., Peeling Single-Stranded DNA from Graphite Surface to Determine Oligonucleotide Binding Energy by Force Spectroscopy. *Nano Letters* **2008**, *8*, 4365-4372.

- (23) Martines, E.; Zhong, J.; Muzard, J.; Lee, A. C.; Akhremitchev, B. B.; Suter, D.
  M.; Lee, G. U., Single-Molecule Force Spectroscopy of the Aplysia Cell Adhesion
  Molecule Reveals Two Homophilic Bonds. *Biophys. J.* 2012, *103*, 649-657.
- (24) Notley, S. M.; Norgren, M., Study of thin films of kraft lignin and two DHPs by means of single-molecule force spectroscopy (SMFS). *Holzforschung* **2012**, *66*, 615-622.
- (25) Valle-Delgado, J. J.; Urban, P.; Fernandez-Busquets, X., Demonstration of specific binding of heparin to Plasmodium falciparum-infected vs. non-infected red blood cells by single-molecule force spectroscopy. *Nanoscale* **2013**, *5*, 3673-3680.
- (26) Bujalowski, P. J.; Oberhauser, A. F., Tracking unfolding and refolding reactions of single proteins using atomic force microscopy methods. *Methods (Amsterdam, Neth.)* **2013**, *60*, 151-160.
- (27) Stahl, S. W.; Puchner, E. M.; Alexandrovich, A.; Gautel, M.; Gaub, H. E., A Conditional Gating Mechanism Assures the Integrity of the Molecular Force-Sensor Titin Kinase. *Biophys. J.* **2011**, *101*, 1978-1986.
- (28) Puchner, E. M.; Franzen, G.; Gautel, M.; Gaub, H. E., Comparing proteins by their unfolding pattern. *Biophys. J.* **2008**, *95*, 426-434.
- (29) Puchner, E. M.; Gaub, H. E., Exploring the conformation-regulated function of titin kinase by mechanical pump and probe experiments with single molecules. *Angew*. *Chem., Int. Ed.* **2010**, *49*, 1147-1150, S1147/1-S1147/2.
- (30) Ducker, W. A.; Senden, T. J.; Pashley, R. M., Direct measurement of colloidal forces using an atomic force microscope. *Nature* **1991**, *353*, 239-241.

- (31) Iliafar, S.; Wagner, K.; Manohar, S.; Jagota, A.; Vezenov, D., Quantifying Interactions between DNA Oligomers and Graphite Surface Using Single Molecule Force Spectroscopy. *The Journal of Physical Chemistry C* **2012**, *116*, 13896-13903.
- (32) Khripin, C. Y.; Zheng, M.; Jagota, A., Deposition and meniscus alignment of DNA–CNT on a substrate. *Journal of Colloid and Interface Science* **2009**, *330*, 255-265.
- (33) Huang, X.; Kovaleski, J. M.; Wirth, M. J., Spectroscopic Probing of Mixed-Mode Adsorption of Ru(bpy)32+ to Silica. *Analytical Chemistry* **1996**, *68*, 4119-4123.
- (34) Roxbury, D.; Tu, X.; Zheng, M.; Jagota, A., Recognition Ability of DNA for Carbon Nanotubes Correlates with Their Binding Affinity. *Langmuir* **2011**, *27*, 8282-8293.
- (35) Ptasinska, S.; Stypczynska, A.; Nixon, T.; Mason, N. J.; Klyachko, D. V.; Sanche, L., X-ray induced damage in DNA monitored by X-ray photoelectron spectroscopy. *The Journal of Chemical Physics* **2008**, *129*, 065102-6.
- (36) Smith, S. B.; Cui, Y.; Bustamante, C., Overstretching B-DNA: The Elastic Response of Individual Double-Stranded and Single-Stranded DNA Molecules. *Science* **1996**, *271*, 795-799.
- (37) Ke, C.; Humeniuk, M.; S.-Gracz, H.; Marszalek, P. E., Direct Measurements of Base Stacking Interactions in DNA by Single-Molecule Atomic-Force Spectroscopy. *Phys. Rev. Lett.* **2007**, *99*, 018302/1-018302/4.
- (38) Sowerby, S. J.; Cohn, C. A.; Heckl, W. M.; Holm, N. G., Differential adsorption of nucleic acid bases: Relevance to the origin of life. *Proc. Natl. Acad. Sci. U. S. A.* **2001,** 98, 820-822.

- (39) Lee, J.-H.; Choi, Y.-K.; Kim, H.-J.; Scheicher, R. H.; Cho, J.-H., Physisorption of DNA Nucleobases on h-BN and Graphene: vdW-Corrected DFT Calculations. *J. Phys. Chem. C* **2013**, *117*, 13435-13441.
- (40) Shankar, A.; Jagota, A.; Mittal, J., DNA Base Dimers Are Stabilized by Hydrogen-Bonding Interactions Including Non-Watson-Crick Pairing Near Graphite Surfaces. *J. Phys. Chem. B* **2012**, *116*, 12088-12094.
- (41) Umadevi, D.; Sastry, G. N., Quantum mechanical study of physisorption of nucleobases on carbon materials. Graphene versus carbon nanotubes. *J. Phys. Chem. Lett.* **2011,** 2, 1572-1576.
- (42) Takahashi, H.; Numao, S.; Bandow, S.; Iijima, S., AFM imaging of wrapped multiwall carbon nanotube in DNA. *Chem. Phys. Lett.* **2006**, *418*, 535-539.
- (43) Lulevich, V.; Kim, S.; Grigoropoulos, C. P.; Noy, A., Frictionless Sliding of Single-Stranded DNA in a Carbon Nanotube Pore Observed by Single Molecule Force Spectroscopy. *Nano Lett.* **2011**, *11*, 1171-1176.

# Chapter 4 Brownian Dynamics Simulation of Peeling a Strongly-Adsorbed Polymer Molecule from a Frictionless Substrate

The work described in this chapter has been published in "Brownian Dynamics Simulation of Peeling a Strongly-Adsorbed Polymer Molecule from a Frictionless Substrate" by Sara Iliafar, Dmitri Vezenov, and Anand Jagota, *Langmuir* **2013** 29 (5), 1435-1445.

We used Brownian Dynamics to study the peeling of a polymer molecule, represented by a freely jointed chain, from a frictionless surface in an implicit solvent with parameters representative of single-stranded DNA adsorbed on graphite. For slow peeling rates, simulations match the predictions of an equilibrium statistical thermodynamic model. We show that deviations from equilibrium peeling forces are dominated by a combination of Stokes (viscous) drag forces acting on the desorbed section of the chain and finite rate of hopping over a desorption barrier. Characteristic velocities separating equilibrium and non-equilibrium regimes are many orders of magnitude higher than values accessible in force spectroscopy experiments. Finite probe stiffness resulted in disappearance of force spikes due to desorption of individual links predicted by the statistical thermodynamic model under displacement control. Probe fluctuations also masked sharp transitions in peeling force between blocks of distinct sequences, indicating limitation in the ability of single molecule force spectroscopy to distinguish small differences in homologous molecular structures.

#### 4.1 Introduction

Modern advancements in fields of bionanotechnology and biomedicine often involve developing and working with systems where biomolecules interact with inorganic materials at the nanoscale. Functionalized single-walled carbon nanotubes (SWCNTs) are a prime example when they are made into biocompatible structures through their functionalization by molecules such as proteins and nucleic acids. <sup>1</sup> Molecules can be attached to an SWCNT covalently or non-covalently; the latter of the two methods generally retains the SWCNT's optical integrity (NIR photoluminescence signals).<sup>2</sup> Cargo bound to SWCNTs have included antibodies, <sup>3</sup> chemotherapy drugs, <sup>4</sup> singlestranded DNA (ssDNA),<sup>5</sup> siRNA,<sup>6,7</sup> and short peptides.<sup>8</sup> Much effort has also been expended in developing conjugated SWCNTs as imaging and sensing entities in living organisms such as using fluorescence, 9-11 Raman, 3, 12, 13 and photoacoustic 14 techniques after substrate binding. In addition, there is considerable interest in understanding the potential health risks associated with carbon nanomaterials. The biocompatibility of functionalized SWCNTs is strongly correlated with the nature of the surface conjugation. For example, a well-coated biopolymer-conjugated SWCNT yields relatively low levels of toxicity. 6, 15, 16 To understand such heterogeneous materials at the fundamental level and to engineer new systems for bionanotechnology, it is important to understand and quantify the interactions of these nanomaterials with biological molecules.

Single molecule force spectroscopy (SMFS) has been used widely to study the interactions between individual molecules, and between polymers and solid surfaces. <sup>17-19</sup> We focus on constructs between biomolecules and nanomaterials, in particular, on the

characterization, formulation, and properties of stable DNA-SWCNT dispersions.<sup>20-24</sup> To quantify the strength of DNA-CNT interaction in these conjugates, we previously employed SMFS studies using graphite as a model system in place of the carbon nanotube surface.<sup>21, 25</sup> When detaching DNA from a graphite surface, we often observe steady state peeling in the force-displacement data<sup>14, 19, 28</sup> manifested as long regions of constant force punctuated by sudden jumps.<sup>19, 21, 26</sup>

We have proposed simple statistical-mechanical models to relate the peeling forces measured in these experiments to the effective binding energy per monomer. <sup>20, 21, 26</sup> In developing such equilibrium models for single molecule peeling, we assumed that the parts of the chain in proximity to the surface go in and out of contact with the surface and are at equilibrium. <sup>21</sup> The theoretical model predicted some ability to distinguish between different homopolymer blocks in a block-co-polymer sequence in both force and displacement control. The model also predicted decaying spikes in peeling forces associated with the removal of individual bases that can be highly specific to the sequence when an ssDNA molecule is peeled from a frictionless surface under displacement control. <sup>20</sup> These latter characteristics, however, are absent from the experimental force-displacement data we routinely generate. The limitations of the equilibrium models for this system are i) absence of an explicit account of rate effects; and ii) exclusion of the effects on force curves of the thermal noise of the force probe (i.e. cantilevers used in an atomic force microscope (AFM)).

Recent theoretical work on force-induced polymer desorption in constant force and constant height ensembles has used analytical solutions or Monte Carlo

simulations.<sup>27-29</sup> In these studies, the number of adsorbed monomers change steadily with displacement in constant-height ensemble, while they show abrupt jumps at particular force values in constant-force ensemble.<sup>27</sup> Furthermore, these studies have shown that the magnitude of applied pulling forces scales with the surface adhesion that is needed to maintain a chain on the surface.<sup>28, 29</sup> All of these findings are consistent with the results from our previously developed equilibrium model.<sup>20, 21</sup> Theoretical studies on peeling a polymer chain at different rates have shown that the chain length at the point of complete detachment and fluctuations in this distance increase with growing departure from equilibrium.<sup>30</sup>

In this manuscript, we report results of Brownian dynamics simulations to study the peeling of a single molecule, represented as a freely jointed chain (FJC), from a frictionless surface. Our goal was to obtain relevant time scales for all contributions responsible for observed phenomena of single molecule peeling using AFM probes and to be able to anticipate future experimental observations. Although the parameters used in this study are representative of an ssDNA molecule on graphite in water, the results apply to any molecule that can be modeled as an FJC. We investigated the conditions under which peeling of homopolymers and block-co-polymers occurs in equilibrium. We established key relationships between observed peeling force and i) the chain's free energy of binding per Kuhn length, and ii) different finite peeling rates. We have also examined the effect of having force sensors of different stiffness and AFM tip fluctuations on the measured response. We found that these fluctuations strongly affect the ability to make sequence-resolved force measurements.

#### 4.2 Methods

We used Brownian Dynamics to study the removal of a polymer molecule from a frictionless surface. Figure 4.1 depicts schematically the model analyzed in this work. It comprises a three-dimensional (3D) freely jointed chain (FJC) with N nodes (joints or beads) and N-1 links. All beads, except the two at the ends of the chain, are given identical properties. The main parameters controlling the simulation are the bead size, chain length, strength of interaction between the bead and the substrate, and the method by which the free end (AFM probe) is pulled away from the substrate. Since our particular interest was to simulate the conditions of our previous SMFS experiments, the parameters used in this study were chosen based on our experience of the system of ssDNA strongly adsorbed on a surface such as graphite.

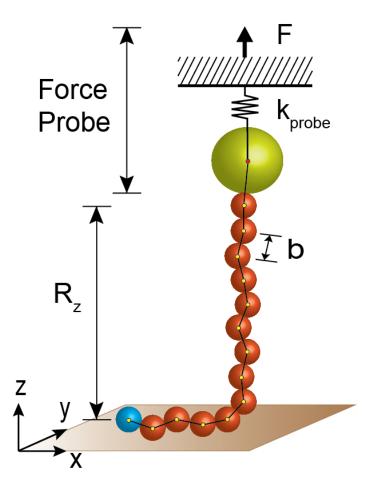


**Figure 4.1.** A schematic representation of the model for peeling a linear polymer molecule adsorbed on a solid substrate. A freely jointed chain is pulled away from a frictionless surface in either force or displacement control. The first bead (blue) is fixed on the surface in the z-direction and is allowed to move freely in the x-y directions. The AFM probe (green) applies either force or displacement and is represented by a bead much larger in comparison to the DNA beads in order to capture the effect of its thermal fluctuation that is present in experiments.

In Brownian dynamics, the effect of explicit solvent molecules on the polymer chain is represented by a stochastic force and viscous drag. This simplification reduces significantly the system size being modeled and enables one to use larger time steps than

in Langevin and molecular dynamics simulations. The equation of motion governing Brownian dynamics for the *n*-th bead at position  $\mathbf{r}_n = (x_n, y_n, z_n)$  in vector form is:

$$0 = -\xi_n \frac{d\mathbf{r}_n}{dt} + \mathbf{f}_n^r(t) - \nabla_n E$$
(4.1)

where  $\xi_n$  is the viscous damping constant (kg/s),  $\mathbf{f}_n^r(t)$  is a random force (N), E is the potential energy of the system as a function of coordinates of each link (J), and the gradient is with respect to coordinates of the n-th bead.<sup>31</sup> The random and frictional drag forces are related by the fluctuation-dissipation theorem:

$$\left\langle f_{n}^{r}(t) \cdot f_{n}^{r}(t') \right\rangle = 6 \xi_{n} k_{B} T \delta(t - t')$$
 (4.2)

where  $k_B$ , T,  $\delta(t-t')$ , and  $f_n^r(t)$  are the Boltzmann constant, temperature, Dirac delta function, and random force applied at time t, respectively. In the numerical modeling context, the standard deviation of the random force,  $\sigma_n^r$ , is derived from the Brownian motion of a single particle by applying the fluctuation-dissipation theorem in continuous contact (Eq. 4.2):<sup>31</sup>

$$\sigma_n^r = \left(\frac{6\xi_n k_B T}{\Delta t}\right)^{\frac{1}{2}} \tag{4.3}$$

This standard deviation is used to control the magnitude of random forces as they are generated using the standard normal distribution ( $\langle f_n^r(t) \rangle = 0$  and, which distributes the random variables around zero and, therefore, does not introduce bias to the system. It

is convenient to express  $\xi_n$  in terms of the diffusion coefficient,  $D_n$ , (m<sup>2</sup>/s) of each bead using the Stokes-Einstein relationship.<sup>31</sup> For simplicity, we used the same diffusion coefficient for all bases, except for the one representing the AFM probe. Its value was estimated using molecular dynamics simulations of a single nucleotide adsorbed on graphite in water.<sup>21</sup>

$$\xi_n = 6\pi \eta a = \frac{k_B T}{D_n} \tag{4.4}$$

Our model represents monomer units in the polymer chain by beads of identical hydrodynamic radius a (or identical diffusion coefficient  $D_n$ ). We assume that their interaction with a substrate can depend on their chemical identity. It was modeled using the Lennard-Jones potential, integrated over the half-space representing the substrate:

$$\phi_n = \frac{\phi_{\min}}{2} \left( \frac{z_{\min}^9}{z_n^9} - \frac{3z_{\min}^3}{z_n^3} \right)$$
 (4.5)

The parameters that describe the depth of the potential well,  $\phi_{\min}$ , and its location (the distance at which the inter-particle force is zero),  $z_{\min}$ , were chosen in a range typical for DNA nucleotides adsorbed on graphite. Considering the typical values reported in the literature for the distance at which the center of mass of a DNA base comes to rest if a nucleoside is released near the surface, the value for  $z_{\min}$  was set to be  $5\text{\AA}.^{23,\,24,\,32}$ 

The peeling process is accomplished by applying boundary conditions at the end of the chain connected to the AFM probe (Figure 4.1). Two limiting cases are peeling

under force or displacement control on the chain end. In the actual experimental situation, displacement is applied through an AFM force probe having a finite compliance. The ratio of the AFM probe size to the FJC bead size is very large in experiments. However, if a bead corresponding to the actual probe size is included in the simulation, to maintain the stability of the simulation, the time steps must be reduced significantly slowing down the simulations by orders of magnitude. In principle, it is unnecessary to represent the AFM probe by a bead with dimension comparable to its actual size. One only needs to make the "AFM bead" sufficiently large compared to DNA beads so that fluctuations of the force probe dominate (see Eq. 4.3 & 4.4).

In addition, the bandwidth ( $1/\Delta t$  in Eq. 4.3) in actual AFM experiments is on the order of 1 kHz, or about a factor of  $10^4$ - $10^6$  smaller that the bandwidth of the simulations. To reproduce the magnitude of the thermal noise seen in these experiments due to an AFM probe, one has to reduce accordingly the damping  $\xi$  of the cantilever or, equivalently, the diameter of the AFM bead. Using cantilever parameters quality factor Q, resonance frequency  $\omega_o$ , and spring constant  $k_{probe}$ , the effective friction coefficient of the AFM probe can be estimated as  $\xi_{probe} = \frac{k_{probe}}{Q\omega_o}$  and is in the range of  $10^{-5}$ - $10^{-4}$  kg/s for typical values in water ( $Q\sim2$ -5,  $k_{spring}\sim0.1$ -0.3 N/m,  $\omega_o\sim3$ -5 kHz). Thus, we selected the diameter of the bead representing the AFM probe to be 70 times larger than the diameter of beads representing each monomer unit. Specifically, the monomer beads each had a radius of 0.29 nm and friction coefficient of 5.5 x  $10^{-12}$  kg/s; the bead representing the AFM probe had a radius of 20.5 nm and friction coefficient of 3.9 x  $10^{-10}$ 

kg/s. This size ensured that the AFM probe fluctuations dominated the contributions from the smaller monomer beads and resulted in an appropriate magnitude of probe noise. In this manner, by adjusting the size of the AFM bead so that its fluctuations dominate over the smaller beads, while simultaneously accounting for the difference in bandwidth between experiment and simulation, we are able to run the simulations much faster than would be dictated by the dynamics of a physical-sized AFM bead to capture its influence on the molecule.

The chain is peeled by applying one of the following conditions to its desorbed end: (i) displacement control (stiffness of the probe is much larger than the stiffness of the molecule,  $k_{probe} >> k_{FJC}$ ), (ii) force control ( $k_{probe} << k_{FJC}$ ), or (iii) displacement control on a large fluctuating AFM bead through a spring corresponding to the cantilever stiffness ( $k_{probe} \approx k_{FJC}$ ). To peel the chain from the surface under force control, force is applied directly to the last bead at the desorbed end of the chain and is increased linearly in time. Under force control, the applied force was incremented at a specified rate and we report mean end-to-end displacement. To peel the chain under displacement control, we constrain the end of the chain to be at a desired distance from the substrate and increase the distance at a constant velocity. For displacement control, applied displacement was incremented and we found resulting mean force. In order to capture the effects of a fluctuating AFM cantilever on the system, we applied displacement to an invisible node that was connected to the AFM bead via a spring (of stiffness  $k_{probe}$ ).

The last bead at the opposite end of the chain was adsorbed strongly to the surface, but slid freely in the x-y plane. This bead was assigned a value of  $\phi_{\min}$  much

larger than the rest (150  $k_BT$ ). Such assignment does not affect the response of the chain through most of the peeling process, however, the non-equilibrium event where the entire chain is removed from the surface is no longer allowed.<sup>33</sup> Therefore, we were able to compare numerical results to an analytical equilibrium model based on the same assumptions.<sup>21</sup>

To enforce the condition of constant segment length, b, at all times, we introduced the constraint for each k-th bond (for  $1 \le k \le N$ -1):

$$\sigma_k \equiv (\mathbf{r}_{k+1} - \mathbf{r}_k)^2 - b^2 = 0 \tag{4.6}$$

resulting in a total of N-1 constraint equations:

$$\begin{cases}
\sigma_{1} \\
\sigma_{2} \\
\vdots \\
\sigma_{N-1}
\end{cases} = 0$$
(4.7)

In all the studies discussed in this chapter, we used an FJC with 20 Kuhn links, each with a Kuhn length segment of 0.65 nm to representative of the distance between phosphorus atoms in a phosphodiester backbone.<sup>21</sup> We used the method of Lagrange multipliers to enforce the bond length constraints shown in Equation 4.7, by adding an extra term to the governing equation (Eq. 4.1),

$$0 = -\xi_n \frac{d\mathbf{r}_n}{dt} + \mathbf{f}_n^r(t) - \left\{ \nabla_n \left[ E - \sum_{k=1}^{N-1} \lambda_k \sigma_k \right] \right\}$$
(4.8)

where  $\lambda_k$  is the Lagrange multiplier corresponding to  $\sigma_k$ . To obtain a numerical time-stepping scheme, this system is first discretized in time as

$$\frac{d\mathbf{r}_n}{dt} = \frac{\mathbf{r}_n(t + \Delta t) - \mathbf{r}_n(t)}{\Delta t} \tag{4.9}$$

Given a starting solution  $\mathbf{r}_n(t)$  that satisfies the constraints, the following equation gives us the solution  $\mathbf{r}_n(t+\Delta t)$  at the end of the time step:

$$\boldsymbol{r}_{n}(t+\Delta t) = \boldsymbol{r}_{n}(t) + \frac{\Delta t}{\xi_{n}} \left( \boldsymbol{f}_{n}^{r}(t) - \left\{ \nabla_{n} \left[ E(t) - \sum_{k=1}^{N-1} \lambda_{k} \sigma_{k} \right] \right\} \right)$$

$$(4.10)$$

An appropriately small time step is chosen using the ratio of the mass of each monomer unit, m, to the friction coefficient ( $\Delta t = \frac{m}{\xi}$ ) to capture events slower than this relaxation time. The system of N equations is propagated in time by solving for  $r_n(t + \Delta t)$  at each time step. Each time increment is accomplished in two phases. In the first phase, Equation 4.10 is used without enforcement of the constraints of Equation 4.7 (i.e.,  $\lambda_k$ 's are all set to zero). In the second phase, the nonlinear constraint is enforced iteratively using Newton-Raphson iterations to determine  $\lambda_k$ .<sup>36</sup>

#### 4.3 Results and Discussion

We and others have observed that peeling of a long chain molecule from a surface is resisted by a constant "plateau" force. <sup>21, 37, 38</sup> We have previously reported measurements of the peeling force for removal of ssDNA homopolymers from graphite

by measuring the average magnitude of the last plateau in the force-displacement curve. We argued that the observation of a plateau force represents removal of the chain under quasi-equilibrium conditions. Based on an equilibrium model, in which the molecule was represented as a freely-jointed chain of the Kuhn length (b), we obtained an expression for the binding free energy per unit length in terms of the measured steady state force.  $f:^{21,25}$ 

$$\Gamma = \ln \left[ \frac{\sinh F}{F} \right] + \ln \left[ \frac{w_{3D}}{w_{2D}} \right]$$

$$\Gamma' = \Gamma - \ln \left[ \frac{w_{3D}}{w_{2D}} \right] = \ln \left[ \frac{\sinh F}{F} \right]$$
(4.11)

where  $F=f\,b/k_BT$  and  $\Gamma=\gamma b/k_BT$  are dimensionless force and adhesion free energy, respectively, and  $\ln(w_{3D}/w_{2D})$  is the conformational free energy required to desorb a link from a surface-adsorbed state into a 3D-FJC-state in solution. Here,  $\gamma$ , is the binding free energy of the chain per unit length excluding the contribution due to conformational changes from 2D to 3D,  $\ln(w_{3D}/w_{2D})$ , i.e.,  $\gamma=\phi_{\min}/b$ , where  $\phi_{\min}$  is the binding free energy of a single node in the chain. In practice, what we measure is the force and hence, what can be inferred using Equation 4.11 is the effective binding free energy,  $\gamma'=\gamma-k_bT\ln\left[\frac{w_{3D}}{w_{2D}}\right]$ . Using this method, we found the average binding energy

per base to be between 7.5  $k_BT$  and 11.3  $k_BT$  depending on the sequence of ssDNA homopolymers.<sup>21, 25</sup>

Note that in the simulations, we prescribe  $\gamma$ , not  $\gamma'$ . We first compare, in the next section, simulation and theory for equilibrium peeling under force control. This comparison allows us to determine the unknown factor  $\ln(w_{3D}/w_{2D})$ . Equilibrium in this case means that the peeling is slow-enough that (i) the adsorbed part of the chain has enough time to sample all allowed conformations, (ii) the desorbed part of the chain likewise has enough time to sample all its allowed conformations, and (iii) the process of adsorption and desorption of bases near the peeling junction is also in equilibrium. The event of the final and full removal of the chain from the substrate is not an equilibrium process. Therefore, complete detachment is explicitly excluded from both the analytical and the numerical model by forcing the last bead to remain bound to the surface. The exclusion does not significantly affect the response during peeling, as shall be evident presently.

4.3.1 Equilibrium peeling of a freely jointed chain from a frictionless surface under force control

Although our studies focus on FJCs with strong adsorption ( $\Gamma > I$ ) to the surface, there remain significant differences between low and high limits of adhesion. Figure 4.2 illustrates the evolution of the chain's conformation upon increase of the applied force in the z-direction. Quasi-equilibrium peeling of two molecules, each with 20 Kuhn links and with free energy of binding per node,  $\gamma$ , of 12 k<sub>B</sub>T and 2 k<sub>B</sub>T, was simulated by application of slow-enough forcing rate, 15  $\mu$ N/s. At the beginning of the simulation (left), the FJC with smaller adhesion (chain B) is only partially adsorbed to the surface, while the chain with the stronger adsorption (chain A) starts out with all its beads

adsorbed onto the surface. The second set of conformations (middle) was obtained when the end-to-end distance of the chains was approximately half the chains' contour length and reveals interesting information: the desorbed part of chain A is stretched nearly to full extension while the adsorbed part is fully attached to the surface. On the other hand, although the end-to-end distance of chain B is about the same as that of chain A's, almost all of the links in B have desorbed from the surface, and the ensemble of conformations for the desorbed part of the chain shows a significantly greater degree of variability. The third set of conformations (right) corresponds to the case where the chain is stretched nearly to full extension. For both low and high adhesion, the ensemble of conformations shows little deviation from a stretched straight line.

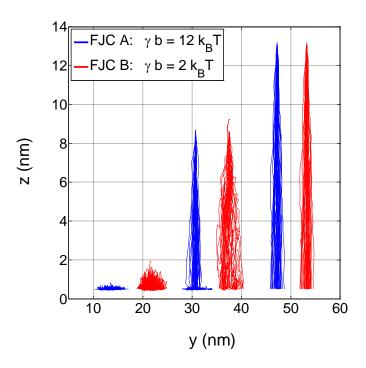


**Figure 4.2.** Clusters of two, 21-node, freely jointed chains with two different binding energies are shown as the applied force in the z-direction increases. Each cluster contains forty conformations. Within one cluster each conformation has been shifted in the x-y plane such that all  $21^{st}$  nodes coincide. (Left) At the beginning of the simulation (t = 0.09 ps), the force is too small to peel the chain off the substrate. Not all nodes of Chain B (moderate binding energy) are adsorbed on the surface, whereas all nodes of chain A (strong surface adhesion) are bound to the surface. (Middle) The physical state of the FJCs when the end-to-end distance of the chains is slightly higher than half their contour length (t = 5.3 μs). (Right) Final conformation obtained near the end of the simulations (t = 9.0 μs) when the FJCs are nearly fully stretched to their contour length.

We conducted simulations of single molecule peeling under both force and displacement control at different peeling rates and adhesion values. To simulate the averaging that occurs automatically during an experiment, we averaged simulated data using small windows, which results in smaller apparent fluctuation (see the Appendix for details). Equation 4.11 gives the plateau peeling force for long chains; for finite chains, it

corresponds to the force when the a chain's average end-to-end distance is half of its contour length.<sup>21</sup> To compare the full simulated and theoretical force-displacement response, we use the complete theoretical equilibrium model (Eq. 4.12) previously derived by Manohar, *et al.* based on the partition function of the system under force control:<sup>21</sup>

$$\langle R_z \rangle = b \left( \coth F - \frac{1}{F} \right) \langle n \rangle$$
 (4.12)

where, 
$$\langle n \rangle = \left(\frac{1}{\exp(\Gamma - X) - 1} - \frac{(N+1)}{\exp((N+1)(\Gamma - X)) - 1}\right)$$
 and  $X = \ln\left[\frac{\sinh F}{F}\right] + \ln\left[\frac{w_{3D}}{w_{2D}}\right]$ .

In deriving this expression, following Rubinstein & Colby<sup>25</sup>, we previously made an arbitrary choice of  $\ln\left[\frac{w_{3D}}{w_{2D}}\right] = \ln[4\pi]$  corresponding to the implicit assumption that the density of states is one per steradian in 3D and one per radian in 2D.<sup>21</sup> In fact, this factor is unknown and, in this work, we extract it by using it as a fitting parameter to minimize the root mean square difference between the theoretical and simulated results.

Figure 4.3A plots force versus mean displacement relationship for a 20 Kuhn link chain that is being removed under force control. Also shown in Figure 4.3A by solid lines is the force-displacement response predicted by the theoretical equilibrium model (Eq. 4.12). We found that, for this 'slow-enough' rate, the analytical equilibrium model and Brownian Dynamics simulation can be brought into very good agreement with a single, binding-energy-dependent, parameter,  $\ln[w_{3D}/w_{2D}]$ .

Since the last node is constrained to the surface, when the surface adhesion is negligible, the force-displacement relationship for the chain is governed by entropic stretching of the FJC and represented well by the Langevin function (see  $\Gamma = 0~k_BT$  case in Figure 4.3A):<sup>39</sup>

$$\frac{R_z}{nb} = \coth(F) - \left(\frac{1}{F}\right) \tag{4.13}$$

Strictly, our conditions are somewhat different from those under which the Langevin function is derived, since the adsorbed end of the chain is free to slide on the surface. However, Manohar, *et al.* have shown that this makes little difference to the force-displacement response.<sup>20</sup>

The value of conformational free energy of desorption,  $\ln(w_{3D}/w_{2D})$ , in units of  $k_BT$ , was extracted from the fits to Eq. 4.12 shown in Figure 4.3A, and plotted in Figure 4.3B as a function of the free energy of adhesion of a chain,  $\gamma$ . We find a systematic increase in  $\ln(w_{3D}/w_{2D})$  with increasing adhesion. Interestingly, for the largest adhesions simulated, its value is very close to the previously assumed (constant) value of  $\ln(4\pi)$ . As expected, since the chain can only sample half of its conformations near a surface, the value of  $\ln(w_{3D}/w_{2D})$  for an adhesion-less chain in the presence of a surface appears to converge to  $\ln(2)=0.69$ . The ratio  $\ln(w_{3D}/w_{2D})$  increases with greater adhesion, i.e., the density of 2D states decreases as increasing adhesion increasingly constrains bead motion away from the surface.

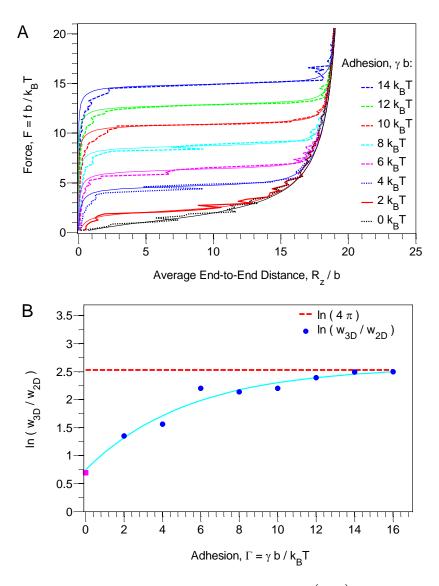


**Figure 4.3.** (A) Effect of dimensionless adhesion,  $\Gamma = \gamma b/(k_B T)$ , on the equilibrium force-displacement relationship in force-controlled peeling. The simulations are shown as thick dashed or solid lines. The equilibrium model is shown by thin solid lines. (B) The conformational free energy required to desorb a link from a 2D-FJC-state on a surface into a 3D-FJC-state in solution,  $\ln(w_{3D}/w_{2D})$ , as a function of adhesion free energy. This quantity was determined by finding the value of  $\ln(w_{3D}/w_{2D})$  that minimizes the normalized root-mean squared difference between the simulated and theoretical force. The normalized root mean squared errors of  $\ln(w_{3D}/w_{2D})$  are comparable to the size of the symbols. The relationship between  $\ln(w_{3D}/w_{2D})$  and  $\Gamma$  is captured, empirically, by fitting the data as  $\ln(w_{3D}/w_{2D}) = a(1 - \exp(-b\Gamma)) + c$  with a = 1.8, b = 0.19, c = 0.75. This fit correctly extrapolates to a value close to  $\ln(w_{3D}/w_{2D}) = \ln(2)$ , as expected, in the absence of adhesion (magenta square).

4.3.2 Peeling of a freely jointed chain from a frictionless surface under displacement control

For short polymers under displacement control, the equilibrium model predicts the occurrence of strong spikes in the peeling force as a result of the removal of individual adsorbed links in a stepwise manner. Approximately, the scaling of spikes in force is given by<sup>20</sup>

$$F_{peak} \approx \exp\left(\frac{\Gamma - \ln\left(\frac{w_{3D}}{w_{2D}}\right)}{n}\right)$$
 (4.14)

where  $F_{peak}$  is the magnitude of the spike in force when n-th bead is removed. Since these spikes, if present, carry the signature of the binding free energy of each base, it is of interest to investigate whether they are present under the more realistic conditions implemented in our simulation.

Figure 4.4 shows the effect of surface adhesion on the force-displacement relationship under displacement control at a peeling rate of 1.44 mm/s, and as we discuss in the next section of this chapter, this removal rate is slow enough to achieve relaxation of relevant molecular motions under force control. For reference, we also show the force-displacement result predicted by the equilibrium model under force control. Consistent with the prediction of the equilibrium model, the amplitude of the force spikes grows with increased adhesion and falls off with the number of bases desorbed. In all the cases shown here, by the time 15 beads have been desorbed, the spikes are no longer

easily distinguishable from fluctuations. Later in the manuscript, we show that when one additionally accounts for the finite spring constant of the AFM probe, its own fluctuations mask these force spikes, explaining why this prediction of the equilibrium theory for peeling under displacement control has not been observed experimentally. In the Appendix, we also show the effect of rate on these force spikes, and compare them to the force-displacement curve obtained from the equilibrium model under displacement control.

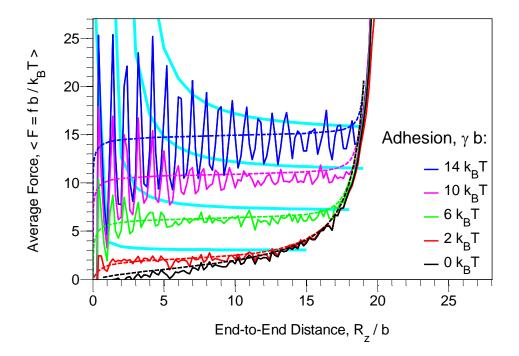


**Figure 4.4.** Effects of surface adhesion on the force-displacement of an FJC under displacement control (solid lines) compared with the theoretical results obtained for the equilibrium rates under force control (dashed lines). The magnitude of the force spikes is represented reasonably well by the behavior predicted by Equation 4.14 (solid lines in cyan) using the values of  $\ln(w_{3D}/w_{2D})$  plotted in Figure 4.3B.

# 4.3.3 Departure from equilibrium

We turn now to the question: what is a sufficiently slow rate to ensure the equilibrium condition, either under force control or displacement control, as assumed in the equilibrium theoretical model.<sup>21, 25</sup> To select a range of peeling rates to study, we considered several processes, any of which could lead to non-equilibrium conditions. These processes include (i) fluctuations in the conformations of the adsorbed part of the chain, (ii) fluctuations in the conformations of the desorbed part of the chain, and (iii) the process of adsorption and desorption of beads.

For these processes, we consider above what characteristic peeling velocity we would expect departure from equilibrium. A summary of our principal results along with a brief description is presented in Table 4.1. The remainder of this section discusses these results in more detail.

**Table 4.1.** Summary of characteristic length scales and peeling velocities associated with processes involving a freely jointed chain interacting with a substrate in fluid. The numbers in parentheses in the third column refer to equation numbers in the text.

Process	Characteristic Length Scale	Characteristic Peeling Velocity	Typical Values <sup>i</sup> (m/s)
Sampling of conformation	$\left\langle L_{c}^{2} \right\rangle^{1/2} = \sqrt{4 \cdot D_{2D} \cdot t_{diffusion}}$	$v_{adsorb}^* = \frac{L_c}{t} \sim \frac{4D_{2D}}{I}$	0.23
space by an		$\mu_{diffusion}$	
adsorbed		(4.16)	
segment			
Sampling of	$\left\langle L_{c}^{2} \right\rangle^{1/2} = \sqrt{6 \cdot D_{3D} \cdot t_{diffusion}}$	$L_c$ $6D_{3D}$	
conformation	$\sqrt{-c}$ / $\sqrt{-3D}$ atylision	$v_{free} - \frac{1}{t_{diffusion}} \sim \frac{1}{L_c}$	0.35
space by a		ayyunon e	
desorbed		(4.17)	
segment	1	, ,	
Desorption from the	b	$v_{barrier}^* \sim \frac{6D_{3D}}{h}$	6.9
surface, no		$b^{umer}$ $b$	
adhesion		(4.18)	
(translocation			
from surface			
into solution by			
a single			
segment)			
Desorption	$\mid b \mid$	$v_{barrier}^* \sim \frac{6D_{3D}}{b} \exp\left(-\frac{E}{k_B T}\right)$	0.51
from the		$V_{barrier} \sim \frac{1}{b} \exp\left(-\frac{1}{k_B T}\right)$	0.01
surface,		, - ,	
overcoming		(4.18)	
energy barrier E	]	(4.10)	0 = 7 +0 -10

*i.* Typical values were calculated for a 20-mer FJC with Kuhn length, b, of 0.65 nm, diffusion coefficient of 7.5.10<sup>-10</sup> m<sup>2</sup>/s, and fluid viscosity of 0.001 Pa.s. The lowered energy barrier, E, was numerically found to be 2.6 k<sub>B</sub>T for removal of a chain (in equilibrium), whose free energy of binding per Kuhn segment is 10 k<sub>B</sub>T.

To estimate the appropriate time scale for process (i) to approach the equilibrium, we estimated the characteristic time scale required for a full chain to diffuse a distance equal to its contour length on the surface.

$$\langle L_c^2 \rangle = 4 \cdot D_{2D} \cdot t_{diffusion}$$
 (4.15)

Therefore, the characteristic peeling velocity for a molecule with contour length of  $\,L_{c}\,$  to equilibrate on the surface is:

$$v_{adsorb}^* = \frac{L_c}{t_{diffusion}} \sim \frac{4D_{2D}}{L_c}$$
(4.16)

The diffusion coefficient of a single nucleotide adsorbed onto graphite that is free to diffuse on the surface was estimated from molecular dynamics to be 7.5·10<sup>-10</sup> m<sup>2</sup>/s.<sup>21</sup> Setting the contour length at 13 nm, we estimated the equilibration time and velocity to be 56 ns and 0.23 m/s, respectively. In other words, if a polymer is removed at rate less than 0.23 m/s and the diffusion coefficient of the molecule is 7.5·10<sup>-10</sup> m<sup>2</sup>/s or greater, equilibrium of the adsorbed part of the chain is maintained. The typical experimental tip velocities used for removal of DNA from a surface are on the order of 100 nm/s, which is many orders of magnitude slower. Therefore, for any reasonable removal rate, one should expect the adsorbed molecules to be in equilibrium.

Similar consideration can be made in evaluating the characteristic velocity for the free (desorbed) part of the chain to equilibrate, process (ii). The free part of the chain is generally fully extended, therefore, in order to be in equilibrium, a very conservative estimate can be made: the peeling rate is slow enough that a bead would have enough time to diffuse the entire contour length  $L_c = Nb$  leading to Equation 4.17 and an estimate of 0.35 m/s for the characteristic velocity,  $v_{free}^*$ .

$$\left\langle L_{c}^{2} \right\rangle = 6 \cdot D_{3D} \cdot t_{diffusion}$$

$$v_{free}^{*} \sim \frac{6D_{3D}}{L_{c}} \tag{4.17}$$

Let us now consider the peeling rate at which the nodes in the peeling junction maintain equilibrium between their bound and unbound states, process (iii). Figure 4.5 shows schematically the potential energy profile under force control when the applied force is smaller than, equal to, or larger than that required for steady-state peeling (see the Appendix for detailed derivation of the potential energy profile).

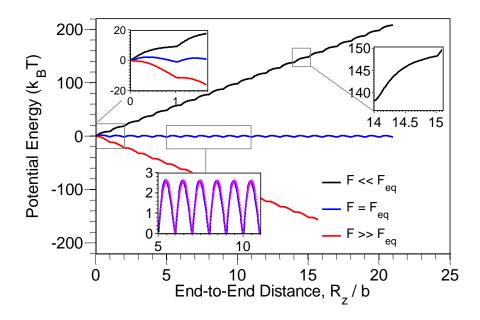


**Figure 4.5.** Comparison of the potential energy of a chain interacting with an ideal surface when the applied force is much smaller than, equal to, and much larger than the force needed to obtain a steady state peeling plateau. Shown in the lower inset, the behavior of the potential energy of the chain (solid blue) is reproduced by a simple periodic function (dotted pink) as described in Equation 4.28.

When negligible or no force is applied to the chain, each link needs to acquire or release an energy of  $\gamma b$  during adsorption-desorption events. During steady-state peeling, bases hop in and out of the adsorbed state, each time crossing a potential barrier whose height is now lower than  $\gamma b$ . For equilibrium peeling, one would need to apply a large enough force so that these states have the same energy. The magnitude of this force depends on the depth of the potential well for each link and the Kuhn length of the FJC:  $f_{eq} \cong \phi_{\min} / b$ . Once  $f_{eq}$  is applied to the chain, one can then numerically find the lowered energy barrier for the equilibrium condition, E. (See section 4.5.3 of the Appendix.) For example, for a chain whose free energy of binding per Kuhn segment (potential well depth) is  $10 \text{ k}_B \text{T}$ , the energy barrier height corresponding to  $f_{eq}$  is reduced to 2.6 k<sub>B</sub>T. The characteristic velocity absent this barrier is governed by relaxation time as  $v \sim 6D_{3D}/b$ . The characteristic velocity of a freely diffusing base which crosses the barrier due to desorption from the surface is reduced by a Boltzmann factor in the energy barrier:

$$v_{barrier}^* \sim \frac{6D_{3D}}{b} \exp\left(-\frac{E}{k_B T}\right) \tag{4.18}$$

According to Equation 4.18, the equilibrium rate for the nodes going in and out of contact with the surface is expected to decrease exponentially with the increase in the monomers' binding energy. Comparing Equations 4.16, 4.17, and 4.18, it is apparent that for long chains, the equilibration of the chain itself controls the critical peeling velocity for equilibrium. On the other hand, for short chains with high adhesion energy, such as the polymers studied in this chapter, equilibration is governed by the kinetics of

transitions between bound and desorbed states. In particular, the equilibration time for the links to overcome the energy barriers will be smaller than the equilibration time for them to sample all the conformations in the adsorbed state ( $v_{barrier}^* > v_{adsorb}^*$ ) if

$$\frac{3L_c}{2b} \exp\left(-\frac{E}{k_B T}\right) > 1 \tag{4.19}$$

When the removal of the chain is sufficiently rapid to be out of equilibrium, we need to supply additional force. One contribution is due to viscous drag. A natural assumption is that if  $\langle n \rangle$  links are desorbed on average, then each will contribute a drag force proportional to velocity, so that the total force due to viscous drag is:

$$F_{drag} = 6\pi \eta \, a \, v \langle n \rangle \tag{4.20}$$

where  $F_{drag}$ ,  $\eta$ , a, and v are the total viscous force, fluid viscosity, hydrodynamic radius of each bead, and velocity of the molecule in the fluid, approximated as its peeling rate. Under force control, peeling rate is not constant, however, and reaches a maximum at a certain extension before it drops back down to zero. Instead, the rate of force application is constant:

$$f = f|_{t=0} + \dot{f} \ t = \dot{f} \ t \tag{4.21}$$

Assume also that the chain is extended so that the end-to-end distance, R, is

$$R = \langle n \rangle b \tag{4.22}$$

Then, combining (20), (21), and (22),

$$\dot{f} t = 6\pi \eta a \left(\frac{dR}{dt}\right) \frac{R}{b} \tag{4.23}$$

Here, we have assumed that the chain is removed from the substrate link-by-link and it is fully stretched in the desorbed state so that end-to-end distance is proportional to n. With the initial condition  $R|_{r=0} = 0$ , Eq. 4.23 is easily integrated to obtain

$$f = \sqrt{\frac{6\pi\eta a \dot{f}}{b}} R \tag{4.24}$$

Equation 4.24 suggests a natural expression for a dimensionless forcing rate,  $\dot{F}_{drag}$ :

$$F = \frac{f b}{k_{\scriptscriptstyle R} T} = \frac{b}{k_{\scriptscriptstyle R} T} \sqrt{\frac{6\pi \eta a \dot{f}}{b}} b \frac{R}{b} = \dot{F}_{drag} \langle n \rangle$$
 (4.25)

where

$$\dot{F}_{drag} = \frac{\sqrt{6\pi\eta a \,\dot{f} \,b^3}}{k_B T} \tag{4.26}$$

A second contribution to the applied force is that needed to break the interaction of the links with a substrate. We next derive the dependence of this desorbing force on forcing rate. To reproduce the potential energy profile of the chain,  $\phi(R,t)$ , seen in Figure 4.5, we first represent the potential profile corresponding to the equilibrium peeling force by a periodic function that repeats every Kuhn link b,  $\left|a\cos\left(\pi\left[\frac{R}{b}-\frac{1}{2}\right]\right)\right|$ , having maxima when an n-th link is half-way in its transition from a fully-adsorbed to a fully-desorbed state. The overlapping of this function (dotted pink) on the potential energy of the chain (solid blue) confirms that this expression closely resembles the

chain's potential energy profile. We then included two terms for the linear dependency

of the total potential energy of the chain on the free energy per unit length,  $\gamma$ , and the applied force,  $f = \dot{f} t$ , resulting in:

$$\phi(R,t) = \left| a \cos\left(\pi \left[\frac{R}{b} - \frac{1}{2}\right]\right) + \gamma R - \dot{f} t R \right|$$
 (4.27)

or, equivalently:

$$\phi(\langle n \rangle, t) = \left| a \cos \left( \pi \left[ \langle n \rangle - \frac{1}{2} \right] \right) \right| + \gamma \langle n \rangle b - \dot{f} t \langle n \rangle b$$
 (4.28)

For the sake of simplicity, we henceforth replace  $\langle n \rangle$ , by n, with the understanding that it is an average of a fluctuating quantity. The potential energy barrier for transition between n and (n+1) desorbed bases with the transition state at (n+1/2) can be approximated as:

$$E_{+} = \phi \left( n + \frac{1}{2}, t \right) - \phi (n, t) = a + \left( \gamma - \dot{f} \ t \right) \frac{b}{2}$$
 (4.29a)

$$E_{-} = \phi \left( n + \frac{1}{2}, t \right) - \phi \left( n + 1, t \right) = a - \left( \gamma - \dot{f} \ t \right) \frac{b}{2}$$
 (4.29b)

To find the net flux,  $\frac{dn}{dt}$  , we considered the backward and forward hopping rates,  $J_{\scriptscriptstyle \pm}$  ,

expected for this potential energy barrier with an attempt frequency, q:

$$J_{\pm} = q \exp\left(-\frac{a \pm \left(\gamma - \dot{f} t\right) \frac{b}{2}}{k_B T}\right) \tag{4.30}$$

$$\frac{dn}{dt} = J_{+} - J_{-} = J_{0} \sinh\left(\frac{(\dot{f}t - \gamma)b}{2k_{B}T}\right) \tag{4.31}$$

where,

$$J_0 = 2q \exp\left(-\frac{a}{k_B T}\right). \tag{4.31a}$$

By integrating Equation 4.31 and rearranging it (see section 4.5.5 in the Appendix), we obtained an expression for peeling force as a function of forcing rate and the free energy of binding:

$$f = \frac{2k_B T}{b} \operatorname{arccosh}\left(\frac{nb \dot{f}}{2J_0 k_B T} + 1\right) + \gamma \tag{4.32}$$

This expression was normalized by multiplying all terms with  $\left(\frac{b}{k_{B}T}\right)$  and setting

dimensionless desorption forcing rate  $\dot{F}_{desorb} = \frac{b \dot{f}}{2 J_{o} k_{B} T}$  to obtain:

$$F_{desorb} = \frac{f b}{k_B T} = 2 \operatorname{arccosh} \left( n \ \dot{F}_{desorb} + 1 \right) + \Gamma \tag{4.33}$$

By adding rate-dependent drag and desorption forces (Eq. 4.25 and 4.33), we arrive at an expression for non-equilibrium peeling force as a function of forcing rate under force control:

$$F = \dot{F}_{drag}n + 2 \operatorname{arccosh}(n\dot{F}_{desorb} + 1) + \Gamma$$
(4.34)

The expression describing the rate dependence of peeling forces under displacement control is discussed later in the Appendix of this chapter.

To separate the equilibration of the chain itself from the bead adsorption-desorption process, we first studied the stretching of an FJC (zero surface adhesion) under a range of forcing rates between 15  $\mu$ N/s and 65 mN/s (Figure 4.6A). For

sufficiently high loading rate, the chain is no longer in equilibrium and viscous drag dominates the pull-off force. The number of desorbed bases as well as the total viscous force acting on the molecule increase linearly with end-to-end distance, consistent with Equation 4.25. Figure 4.6A shows this result for a 20-mer chain with the diffusion coefficient of  $7.5 \cdot 10^{-10}$  m<sup>2</sup>/s, bead radius of 0.29 nm, and viscosity of 0.001 Pa-s. The simulation results are in close agreement with Stokes relationship, Equation 4.25 under fast forcing rates (e.g. for the dimensionless forcing rate  $\dot{F}_{drag}$  of 2.4 and 0.93). We interpret the slight mismatch between the two to be due to the assumption used to derive the Stokes relationship that the links are removed one by one.

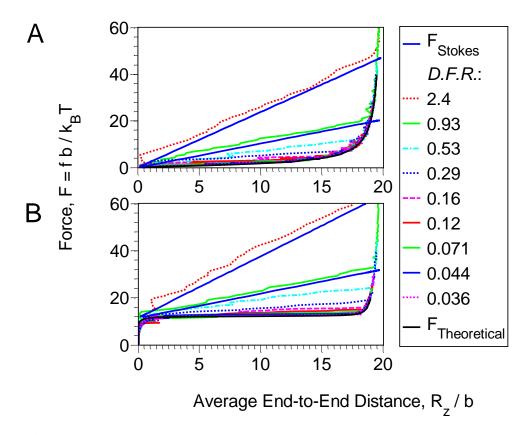


**Figure 4.6.** (A) Stretching of an FJC with 20 Kuhn links and no binding energy peeled at different forcing rates. The dimensionless forcing rates (D.F.R.) were calculated using Equation 4.26. The chain's stretching follows the Langevin function ( $F_{theoretical}$ ) at slow rates as the chain is stretched nearly in equilibrium. As the rates of removal increase, force increases linearly with end-to-end distance, which is captured well by Equations 4.24 and 4.25 and is labeled " $F_{Stokes}$ " in the figure. (B) Effect of forcing rate on force-displacement curve of an FJC with binding energy per Kuhn segment of 11.5 k<sub>B</sub>T under force control.

Figure 4.6B shows the effect of rate on peeling of a chain with 20-Kuhn links and surface binding energy per base of  $11.5 \text{ k}_B\text{T}$ , representative of the poly(dT) ssDNA sequence.<sup>21</sup> As expected, for sufficiently slow rates, the equilibrium force-displacement behavior is retrieved. Note that this expression for the force-displacement behavior also

retrieves the equilibrium result (in the limit of high adhesion, which is implied by the assumption that the desorbed part of the chain is fully stretched).

Figure 4.7 shows the force-rate relationship for different values of binding free energy when the average end-to-end distance of the chain is a half of its contour length. The force-rate curves shift up with an increase in the surface adhesion. For example, the low-rate asymptote (see Equation 4.34) is  $F=\Gamma$ . There appear to be two separate processes that govern how force at fixed n increases with forcing rate. We identify these as the first two terms of Equation 4.34. Because the "arccosh" function grows faster than the first term for small arguments, it governs the first phase of increase in force with forcing rate. For larger values of forcing rate, the first Stokes drag term in Equation 4.34 dominates. The two lines in Figure 4.7 are the prediction of force given by Equation 4.34, in good agreement with simulation results.

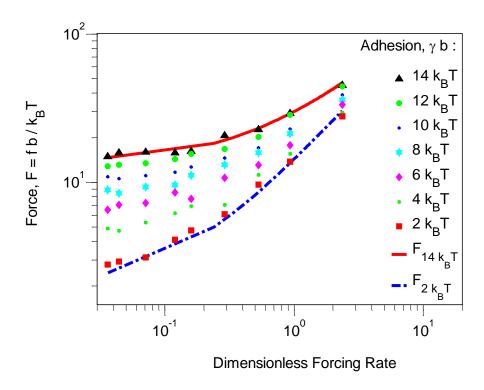


**Figure 4.7.** The relationship between the dimensionless force,  $F = f b/(k_B T)$ , and the dimensionless forcing rate,  $\dot{F} = \frac{\sqrt{6\pi \eta a \dot{f} b^3}}{k_z T}$ , captured at  $R_z = L_c/2$  for removing an

FJC with 20 Kuhn links with different surface adhesion. The lines are predicted by Equation 4.34 for  $\Gamma=14~\rm k_BT$  (solid) and  $\Gamma=2~\rm k_BT$  (dashed). The height of the reduced energy barrier, a, for the chains with free energy of binding of 14 k<sub>B</sub>T and 2 k<sub>B</sub>T per Kuhn segment were numerically found to be 4.0 k<sub>B</sub>T and 0.6 k<sub>B</sub>T using the potential energy profile of these chains as they are being removed at equilibrium peeling as plotted in Figure 4.5. The unknown parameters  $J_{0,14~k_BT}=1.0\cdot10^9~\rm s^{-1}$ ,  $J_{0,2k_BT}=1.2\cdot10^{10}~\rm s^{-1}$  and  $q=1.1\cdot10^{10}~\rm s^{-1}$  were estimated using Equation 4.31.a. with frequency  $q=\frac{6D}{b^2}$  obtained using the diffusion coefficient.

# 4.3.4 Effect of AFM probe fluctuations

The SMFS technique is associated with limitations that mask or alter certain characteristics of single molecule peeling. Some of the limitations include variability in probe spring constants and accuracy issues associated with the calibration of the AFM cantilever. 40 For example, one expects to find the same binding energy per base in a DNA homopolymer upon repeating the experiment multiple times; however, in the actual experiments, one observes a distribution for a given AFM probe and distribution of mean force for different AFM probes.<sup>21</sup> An important source of fluctuation in a given forcedistance experiment is the thermal noise associated with the AFM probe itself. Single molecule peeling experiments have typically been carried out with probe spring constants of 0.1 - 0.3 N/m. As shown in Figure 4.8, the use of a soft spring completely removes the regular and periodic spikes observed in the force-displacement response under displacement control (Figure 4.4). Employing probes of finite stiffness, on the one hand, places the peeling process in the regime intermediate between displacement and force control, thus, reducing  $F_{peak}$  values from their maximum given by Equation 4.14 and, on the other hand, introduces a dominant source of random noise that overwhelms the distinct peaks. This result indicates why the regular spikes in force are not observed in peeling experiments: direct attachment of the molecule to the tip results in the initial region being masked due to large tip-surface adhesion; thus, one misses the critical region of high amplitude force spikes. Alternative attachment of the molecule having high surface affinity via non-adsorbing tether molecules is equivalent to introduction of a soft

spring, thus, producing the force-distance curve of the type with spring constant of 0.1 - 0.3 N/m as shown in Figure 4.8.

The equilibrium analytical model, <sup>20</sup> also predicts that one should be able to distinguish between blocks of different sequence on the same strand. Considering the similarity in the binding energy of homopolymer sequences, the ability to carry out SMFS on block-co-polymers is important, as it would enable one to identify accurately the binding forces of different sequences relative to each other or to one standard baseline sequence. We used adhesion energy of 11.5 k<sub>B</sub>T and 8.3 k<sub>B</sub>T per link, corresponding to poly(dT) and poly(dC), respectively, to simulate the peeling of poly(dT)<sub>10</sub>poly(dC)<sub>10</sub> in equilibrium conditions to investigate whether block-co-polymers display two distinct force plateaus in the presence of the thermal fluctuations due to the AFM probe. Figure 4.8 shows that one should be able to observe the force plateaus of block-co-polymers even in the presence of added force probe noise. Varying the spring constant values proved not to affect the simulated force plateaus. The polymer binding energies obtained from the simulations at spring constants 0.1, 0.2, and 0.3 N/m were found to be  $8.48 \pm$  $0.12~k_BT$  (mean  $\pm$  standard error) and  $12.19\pm0.04~k_BT$  (mean  $\pm$  standard error) for poly $(dC)_{10}$  and poly  $(dT)_{10}$ , respectively. The number of monomeric units involved in the transition of peeling forces between two consecutive homopolymers appears to increase with the softness of the spring.

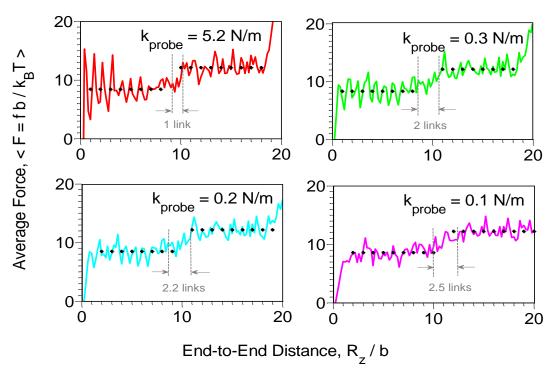


**Figure 4.8.** Effect of thermal fluctuations of a force probe on peeling forces in block-copolymer  $poly(dT)_{10}poly(dC_{10})$  with adhesion energy of  $11.5 k_BT$  and  $8.3 k_BT$  per link corresponding to poly(dT) and poly(dC). Despite the added noise from the AFM probe, the force plateaus associated with block-co-polymers remain distinguishable. Varying the AFM tip spring constant has a minor effects of the peeling forces although it smoothes out the sudden jump between the force plateaus (from one monomer unit to 2.5 bases monomeric units).

### 4.4 Conclusions

Brownian dynamics simulations model the removal of polymeric molecules from surfaces, for example the peeling of ssDNA from graphite, more realistically than analytical models. In the limit of slow peeling, the Brownian dynamics model replicates the results of an equilibrium statistical thermodynamic model under both force control and displacement control. The main new findings reported in this manuscript are the following:

- In Table 4.1, we listed the characteristic length scales and peeling velocities associated with a freely jointed chain that is interacting with a surface in fluid.
- We showed (Equation 4.34 and Figure 4.7) that the force for desorption depends on free energy of binding, the energy barrier for desorption, and Stokes drag. The rate dependence due to hopping over the barrier dominates the process for short chains, while viscous drag dominates for long chains. Our simulation and theory indicate that desorption rate effects can be neglected at typical peeling rates achieved in SFMS setups.
- Since Brownian dynamics simulations are representative of details of molecular conformations, we were also able to observe the effect of the reduced number of surface states for chains with high adhesion. Quantitative comparison of simulation and analytical results yielded the ratio of density of states in the adsorbed and free states, a parameter that is undetermined in the analytical model. We verified implicit assumptions about the density of states in 2D and 3D FJC models used in the derivation of theoretical models. The empirical dependence on binding energy can be used in the interpretation of the experimental data for an accurate calculation of the binding energy per monomer.
- We show that force spikes predicted by the equilibrium model under displacement control are significantly attenuated by non-equilibrium conditions and by fluctuations of the AFM tip. Although with a sufficiently stiff cantilever it may be possible to measure the magnitude of these force spikes and thus to infer individual base adhesive energy, we find that under most practical conditions the force response loses sequence specific information with the disappearance of the decaying and periodic force spikes, and the step jump in force plateaus between blocks is broadened. This makes it difficult to identify individual block-polymers in a chain when the length of the block-polymer is

short (~five segments). Therefore, sequence information for block-co-polymers is not easily detectable using the experimental single molecule peeling technique.

Considering that an ideal surface was employed in our Brownian dynamics simulations, it is important to repeat the studies reported here in the presence of surface friction and to investigate the effect of lateral interactions of the chain with the surface on the equilibrium of polymer peeling. Similarly, the role of intrachain interactions in the peeling process, while critical to actual DNA-surface interactions, remains un-illuminated with models that rely on an idealization such as an FJC model. For future studies, we aim to further modify our system to account for these conceptually important non-ideal features of both the surface and the polymer. Furthermore, various experimental modalities of peeling biopolymers from true nanostructures can be approached with our simulation approach.

# 4.5 Appendix

# 4.5.1 Brownian Dynamics

Brownian dynamics is the Langevin dynamics in limit of negligible inertia. In order to identify whether the use of Brownian dynamics limit of the Langevin dynamics is appropriate for our studies, both position and velocity relaxation times of this system were considered. A simplified version of the equation of motion governing this system was used:

$$\ddot{\mathbf{r}} + \frac{\xi}{m}\dot{\mathbf{r}} + \frac{k_{sp}}{m}\mathbf{r} = 0 \tag{4.35}$$

Here,  $\mathbf{r} = \mathbf{r}(t)$  is the coordinates of each monomer,  $\xi = \gamma m$  is the drag coefficient,  $\gamma$  is the damping constant, m is the mass of a monomer, and  $k_{sp}$  is the gradient of the potential between each monomer and the surface (effective spring constant). This equation neglects the interactions due to presence of rigid bonds neighboring monomers. When the friction coefficient is very small in comparison to the inertial term, we can neglect the friction coefficient term. Hence, the velocity relaxation time,  $\tau_{\nu}$ , becomes:

$$\tau_{v} = \sqrt{\frac{m}{k_{sp}}} \tag{4.36}$$

To estimate the position relaxation time, we ignore the inertial term, making Equation 4.35 independent of the mass of the molecule:

$$\dot{\boldsymbol{r}} + \frac{k_{sp}}{\xi} \boldsymbol{r} = 0 \tag{4.37}$$

The position relaxation time,  $\tau_{p}$ , of the system was then estimated to be:

$$\tau_p = \frac{\xi}{k_{sp}} \tag{4.38}$$

Given that the mass and diffusion coefficient of each thymine base is  $5 \times 10^{-25}$  kg and  $7.5 \times 10^{-10}$  m<sup>2</sup>/s (obtained from simulations),<sup>21</sup> while the spring constant obtained from the Lennard Jones potential is 5.2 N/m, the position and velocity relaxation times are 1.0 and 0.3 picoseconds, respectively. In this system, there is a large difference between the time scales of the rapidly moving solvent molecules (water) and the slow-moving solute (ssDNA or any other molecule that can be modeled as a FJC). Since the velocity relaxation time is faster than position relaxation time by a factor of three, the system can be modeled using the Brownian limit of Langevin dynamics. Therefore, Langevin

dynamics was reduced to Brownian dynamics by neglecting the inertia (mass) of the DNA bases. Although neglecting the inertial contributions may result in losing information about the coupling mode of DNA and its kinetics process, it is expected that this modification to the Langevin dynamics will not reduce the accuracy of our simulation results as our process times are short.

### 4.5.2 Relating the Variance of Random Force to the Viscous Term

Despite the absence of correlation between the noise acting on a system from one point in time to another point in time, there is a relationship between this uncorrelated random force and the viscous drag from the fluid surrounding the molecule. Using this relationship along with a known diffusion coefficient of the molecule in the surrounding liquid, we can compute the magnitude of the random force. In obtaining a definition that correctly relates the random force acting on a molecule to the its viscous drag in fluid, we considered the Langevin Dynamics equation for a single particle under random forces,  $\mathbf{f}_n(t)$ .

$$m\frac{d\mathbf{v}}{dt} = -\xi \mathbf{v} + \mathbf{f}_n(t) \tag{4.39}$$

The friction coefficient for a spherical particle is defined by Stoke's law as  $\xi = 6\pi\eta a$  with  $\eta$  being the viscosity of the liquid and a being the radius of the particle. For the purpose of obtaining a solution to Equation 4.39, we redefine the friction coefficient as:

$$\xi = m\gamma \tag{4.40}$$

where m is the mass of the particle and  $\gamma$  is the damping constant. Equation 4.39 can now

be rewritten as  $\frac{d\mathbf{v}}{dt} = -\gamma \mathbf{v} + \frac{\mathbf{f}_n(t)}{m}$ . Therefore the homogeneous solution to to this

equation becomes  $\mathbf{v}_h = \mathbf{v}_0 \ e^{-\gamma t}$ , while the particular solution can be found by considering a function multiplied by the homogeneous solution to the Langevin function.

$$\mathbf{V}_{p} = e^{-\gamma t} \,\mathbf{W}(t) \tag{4.41}$$

By substituting the particular solution back into Equation 4.39,

$$-\gamma e^{-\gamma t} \mathbf{w}(t) + e^{-\gamma t} \frac{d\mathbf{w}(t)}{dt} = -\gamma e^{-\gamma t} \mathbf{w}(t) + \frac{\mathbf{f}_n}{m}(t)$$
(4.42)

then  $\mathbf{w}(t)$  was expressed as:

$$\mathbf{w}\left(t\right) = \int_{0}^{t} \frac{e^{\gamma t}}{m} \mathbf{f}_{n}\left(\tau\right) d\tau \tag{4.43}$$

And, the total solution was written as:

$$\mathbf{V} = \mathbf{V}_h + \mathbf{V}_p = \mathbf{V}_0 e^{-\gamma t} + e^{-\gamma t} \int_0^t \frac{e^{\gamma t}}{m} \mathbf{f}_n(\tau) d\tau$$
 (4.44)

In equilibrium conditions, the kinetic energy of the system is defined by

 $K.E. = \frac{1}{2}m\mathbf{v}^2 = \frac{3}{2}k_BT$ ; therefore, Equation 4.44 was utilized to find an expression for

 $\boldsymbol{V}^2$ :

$$\langle \mathbf{v}(t) \cdot \mathbf{v}(t) \rangle = \left\langle \left( \mathbf{v}_{0} e^{-\gamma t} + e^{-\gamma t} \int_{0}^{t} \frac{e^{\gamma t}}{m} \mathbf{f}_{n}(\tau) d\tau \right) \cdot \left( \mathbf{v}_{0} e^{-\gamma t} + e^{-\gamma t} \int_{0}^{t} \frac{e^{\gamma t}}{m} \mathbf{f}_{n}(\tau) d\tau \right) \right\rangle$$

$$= \left\langle \mathbf{v}_{0}^{2} e^{-2\gamma t} + 2 e^{-2\gamma t} \int_{0}^{t} \frac{e^{\gamma \tau}}{m} \mathbf{v}_{0} \mathbf{f}_{n}(\tau) d\tau + e^{-2\gamma t} \int_{0}^{t} \frac{e^{\gamma q} e^{\gamma p}}{m^{2}} \mathbf{f}_{n}(p) \mathbf{f}_{n}(q) dp dq \right\rangle$$

$$= \mathbf{v}_{0}^{2} e^{-2\gamma t} + 2 e^{-2\gamma t} \int_{0}^{t} \frac{e^{\gamma \tau}}{m} \mathbf{v}_{0} \left\langle \mathbf{f}_{n}(\tau) \right\rangle d\tau + e^{-2\gamma t} \int_{0}^{t} \frac{e^{\gamma (p+q)}}{m^{2}} \left\langle \mathbf{f}_{n}(p) \cdot \mathbf{f}_{n}(q) \right\rangle dp dq$$

$$(4.45)$$

Since the average unbiased random force is zero and the mean square of this uncorrelated noise is given by a constant,

$$\langle \mathbf{f}_{n}(t) \rangle = 0$$

$$\langle \mathbf{f}_{n}(t) \cdot \mathbf{f}_{n}(t') \rangle = g \delta(t - t')$$
(4.46)

Equation 4.45 was simplified to:

$$\langle \mathbf{v}(t) \cdot \mathbf{v}(t) \rangle = \mathbf{v}_0^2 e^{-2\gamma t} + e^{-2\gamma t} a \int_0^t \frac{e^{2\gamma q}}{m^2} dq = \mathbf{v}_0^2 e^{-2\gamma t} - \frac{g}{2\gamma m^2} e^{-2\gamma t} \left(1 - e^{2\gamma t}\right)$$
(4.47)

To apply the expression for  $\langle \mathbf{v}(t) \cdot \mathbf{v}(t) \rangle$  to equilibrium conditions and use it in the kinetic energy equation, we considered very large time and solved for the constant term, g:

$$\frac{1}{2}m\mathbf{v}^2 = \frac{3}{2}k_B T$$

$$\frac{1}{2}m\frac{g}{2\gamma m^2} = \frac{3}{2}k_B T$$

$$\therefore g = 6k_B T \xi$$
(4.48)

And in a one-dimensional problem, this constant is defined as  $g = 2 k_B T \xi$ .

Using the relationship derived for the uncorrelated random force in terms of the damping coefficient of the surrounding fluid, the next step was to find the magnitude of this noise by obtaining its standard deviation. We considered the Brownian Dynamics equation for a single particle under random forces,  $\mathbf{f}_n(t)$ , such that:

$$\xi \mathbf{V} = \mathbf{f}_n \left( t \right) \tag{4.49}$$

The velocity,  $\mathbf{v}$ , and random force,  $\mathbf{f}_n(t)$ , in Equation 4.49 are vectors.

Therefore,  $\mathbf{f}_n(t)$  was defined as:

$$\mathbf{f}_{n,i}(t) = c_i \, \mathbf{e_i} \tag{4.50}$$

where  $c_i$  is a random amplitude and  $e_i$  is a random unit vector. In step i, the velocity is

$$\mathbf{v_i} = \frac{c_i \mathbf{e_i}}{\xi} \tag{4.51}$$

During a time step,  $\Delta t$ , the particle appears to move by a vector:

$$\mathbf{r}_{\mathbf{i}} = \frac{c_i \, \mathbf{e}_{\mathbf{i}} \, \Delta t}{\xi} \tag{4.52}$$

Therefore, the total distance traveled after *N* steps is:

$$\mathbf{r_{Total}} = \sum_{i=1}^{N} \mathbf{r_i} = \frac{\Delta t}{\xi} \sum_{i=1}^{N} c_i \mathbf{e_i}$$
 (4.53)

Without a constraining potential, the particle diffuses and its mean square displacement increases with time as shown below.<sup>41</sup>

$$\left\langle r_{Total}(t)^2 \right\rangle = 6Dt$$
 (4.54)

Computing that average for Equation 4.53, gave us:

$$\left\langle r_{Total}(t)^{2} \right\rangle = \left(\frac{\Delta t}{\xi}\right)^{2} \left(\sum_{i=1}^{N} c_{i} \mathbf{e}_{i}\right) \cdot \left(\sum_{j=1}^{N} c_{j} \mathbf{e}_{j}\right) = \left(\frac{\Delta t}{\xi}\right)^{2} \left(\sum_{i=1}^{N} c_{i}^{2} \mathbf{e}_{i} \cdot \mathbf{e}_{i} + \sum_{\substack{i=1\\i\neq j}}^{N} \sum_{j=1}^{N} c_{i} c_{j} \mathbf{e}_{j} \cdot \mathbf{e}_{i}\right)$$

$$(4.55)$$

The second summation vanishes for large N because for two randomly oriented vectors, there is equal probability of their dot product being positive and negative.

Therefore Equation 4.55 reduces to:

$$\left\langle r_{Total}(t)^{2}\right\rangle = \left(\frac{\Delta t}{\xi}\right)^{2} \sum_{i=1}^{N} c_{i}^{2} \mathbf{e}_{i} \cdot \mathbf{e}_{i} = \left(\frac{\Delta t}{\xi}\right)^{2} \sum_{i=1}^{N} c_{i}^{2} = \left(\frac{\Delta t}{\xi}\right)^{2} N \left\langle c^{2}\right\rangle = \frac{t \Delta t \left\langle c^{2}\right\rangle}{\xi^{2}}$$
(4.56)

Next, Equation 4.54 and 4.56 were combined to obtain

$$t \Delta t \frac{\langle c^2 \rangle}{\xi^2} = 6Dt \tag{4.57}$$

which can be rearranged to obtain the variance of the forcing noise:

$$\left\langle c^2 \right\rangle = \xi^2 \left( \frac{6D}{\Delta t} \right) \tag{4.58}$$

To express the fluctuations in the uncorrelated force in terms of a damping coefficient, the Einstein relation can be used to substitute for the diffusion coefficient.

$$D = \frac{k_B T}{\xi} \tag{4.59}$$

From Equation 4.59, the standard deviation of random noise was found to be:

$$\left\langle c^2 \right\rangle = \left( \frac{6\xi k_B T}{\Delta t} \right) \tag{4.60}$$

And correspondingly, for each of the three spatial components of the force vector:

$$\left\langle c_x^2 \right\rangle = \left\langle c_y^2 \right\rangle = \left\langle c_z^2 \right\rangle = \left( \frac{2\xi k_B T}{\Delta t} \right) \tag{4.61}$$

# 4.5.3. Bond Length Constraint in the Freely Jointed Chain Model

The governing equation of the Brownian Dynamics describes the motion of free particles:

$$0 = -\xi_n \frac{d\mathbf{r}_n}{dt} + \mathbf{f}_n^r(t) - \nabla E(\mathbf{r}_n)$$
(4.62)

Therefore, one must apply a constraint to bind the DNA bases to one another to create a chain. This constraint was added to the potential energy term,  $E(\mathbf{r}_n)$ , whose gradient gives the forces acting on each bead.

$$0 = -\xi_n \frac{d\mathbf{r}_n}{dt} + \mathbf{f}_n^r(t) - \left\{ \nabla \left[ E(\mathbf{r}_n) - \sum_{k=1}^{N-1} \lambda_k \sigma_k \right] \right\}$$
(4.63)

To simplify the governing equation for the purpose of constructing a code, the equation describing the change in the position of particles was divided into two parts. In the first part, the position of each particle is obtained based on both random force,  $\mathbf{f}_n^r(t)$ , and applied forces,  $\mathbf{f}_n = -\nabla E(\mathbf{r}_n)$ , at the end of each time step,  $\Delta t$ , using Euler's method and without enforcement of the constraint as shown in Equation 4.64:

$$\boldsymbol{\Gamma}_{n}^{t+\Delta t} = \boldsymbol{\Gamma}_{n}^{t} + \frac{\Delta t}{\xi_{n}} (\boldsymbol{f}_{n}^{r}(t) + \boldsymbol{f}_{n})$$
(4.64)

In the second part, the necessary constraint is applied to all beads in order to conserve their bond length.

$$\mathbf{r}_{n,\sigma_{k}=0}^{t+\Delta t} = \mathbf{r}_{n}^{t+\Delta t} + \frac{\Delta t}{\xi_{n}} \left( \nabla \left[ \sum_{k=1}^{N-1} \lambda_{k} \sigma_{k} \right] \right)$$

$$(4.65)$$

To find Lagrange multipliers,  $(\lambda_k)$ , the second term is expanded using the basic constraint equation

$$\sigma_k \equiv (\mathbf{r}_{k+1} - \mathbf{r}_k) \cdot (\mathbf{r}_{k+1} - \mathbf{r}_k) - b^2 = 0 \tag{4.66}$$

to obtain a complete constraint equation for links 1 < n < N-1.

$$\sigma_{n} = \sum_{i=x,y,z} \left( \frac{\mathbf{r}_{i,n+1} - \mathbf{r}_{i,n} - \frac{2\lambda_{i,n+1}(\mathbf{r}_{i,n+2} - \mathbf{r}_{i,n+1})\Delta t}{\xi_{n+1}} + \frac{2\lambda_{i,n}(\mathbf{r}_{i,n+1} - \mathbf{r}_{i,n})\Delta t}{\xi_{n+1}} + \frac{2\lambda_{i,n}(\mathbf{r}_{i,n+1} - \mathbf{r}_{i,n})\Delta t}{\xi_{n+1}} + \frac{2\lambda_{i,n}(\mathbf{r}_{i,n+1} - \mathbf{r}_{i,n})\Delta t}{\xi_{n}} + \frac{2\lambda_{i,n}(\mathbf{r}_{i,n} - \mathbf{r}_{i,n})\Delta t}{\xi_{n}} + \frac{2\lambda_{$$

Similarly, the constraint equations describing the force applied on links 1 and N-1 were obtained as follows.

$$\sigma_{1} = \sum_{i=x,y,z} \left( \mathbf{r}_{i,2} - \mathbf{r}_{i,1} - \frac{2\lambda_{i,2} (\mathbf{r}_{i,3} - \mathbf{r}_{i,2}) \Delta t}{\xi_{2}} + \frac{2\lambda_{i,1} (\mathbf{r}_{i,2} - \mathbf{r}_{i,1}) \Delta t}{\xi_{2}} + \frac{2\lambda_{i,1} (\mathbf{r}_{i,2} - \mathbf{r}_{i,1}) \Delta t}{\xi_{2}} \right)^{2} - b^{2}$$

$$(4.68)$$

$$\sigma_{N-1} = \sum_{i=x,y,z} \left( \mathbf{r}_{i,N} - \mathbf{r}_{i,N-1} + \frac{2\lambda_{i,N-1} (\mathbf{r}_{i,N} - \mathbf{r}_{i,N-1}) \Delta t}{\xi_{N}} + \frac{2\lambda_{i,N-1} (\mathbf{r}_{i,N} - \mathbf{r}_{i,N-1}) \Delta t}{\xi_{N-1}} - \frac{2\lambda_{i,N-2} (\mathbf{r}_{i,N-1} - \mathbf{r}_{i,N-2}) \Delta t}{\xi_{N-1}} \right)^{2} - b^{2}$$

$$(4.69)$$

Using standard Newton-Raphson method, if we have a guess for  $(\lambda_i)$  at a given iteration (starting with  $\lambda_i=0$ ), then a new guess was found by

$$\{\Delta\lambda\} = -[J]^{-1}\{\sigma\} \tag{4.70}$$

where  $\Delta \lambda = \lambda_{i+1} - \lambda_i [J]$  is the Jacobian matrix,

$$J_{\sigma} = \begin{pmatrix} \frac{\partial \sigma_{1}}{\partial \lambda_{1}} & \cdots & \frac{\partial \sigma_{1}}{\partial \lambda_{N-1}} \\ \vdots & \ddots & \vdots \\ \frac{\partial \sigma_{N-1}}{\partial \lambda_{1}} & \cdots & \frac{\partial \sigma_{N-1}}{\partial \lambda_{N-1}} \end{pmatrix}$$

$$(4.71)$$

By running iterations using Newton Raphson method, we ensured that the constraint equations were satisfied.

#### 4.5.3 Potential between a monomer in the FJC and the surface

To derive the potential that describes the interaction between a monomer and the surface, we represented the monomer by a single point, as done in the Brownian dynamics simulation. We then integrated Lennard-Jones potential,

$$\phi_{LJP}(r) = \frac{A}{r^{12}} - \frac{B}{r^6} \tag{4.72}$$

which describes atom-atom or molecule-molecule interactions (Equation 4.72), over a half-space (representing the semi-infinite substrate).

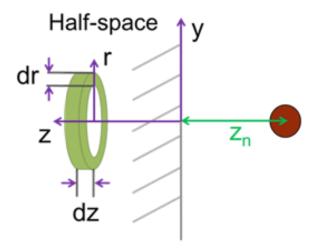


**Figure 4.9.** Schematic of the domain over which the Lennrad Jones potential was integrated. The distance between the monomer and the half-space is denoted by  $z_n$ .

As shown in Figure 4.9, for an annulus or radius r at a distance z from the surface, the potential energy describing the interaction between a monomer and volume element of dV of a solid is a function of  $\sqrt{(z+z_n)^2+r^2}$ , where  $z_n$  is the distance between the location of the monomer and the surface of the half-space with which the monomer is interacting. Integrating the potential energy with respect to z and r:

$$\phi_{n}(z_{n}) = \int_{0}^{\infty} \int_{0}^{\infty} \left\{ 2 \cdot \pi \cdot r \cdot \rho \cdot \phi_{LJP} \left( \sqrt{(z+z_{n})^{2} + r^{2}} \right) \right\} dr dz$$

$$= \int_{0}^{\infty} \int_{0}^{\infty} 2\pi r \rho \left\{ \frac{A}{\left( \sqrt{(z+z_{n})^{2} + r^{2}} \right)^{12}} - \frac{B}{\left( \sqrt{(z+z_{n})^{2} + r^{2}} \right)^{6}} \right\} dr dz$$

$$= \int_{0}^{\infty} \int_{0}^{\infty} 2\pi r \rho \left\{ \frac{A}{\left( (z+z_{n})^{2} + r^{2} \right)^{6}} - \frac{B}{\left( (z+z_{n})^{2} + r^{2} \right)^{3}} \right\} dr dz$$

$$(4.73)$$

Integrating the attractive and repulsive terms separately, the following expressions were obtained:

$$\int_{0}^{\infty} \int_{0}^{\infty} 2\pi r \rho \cdot \frac{A}{\left(\left(z+z_{n}\right)^{2}+r^{2}\right)^{6}} dr dr z = \int_{0}^{\infty} \left[-\frac{1}{5} \frac{A\rho\pi}{\left(\left(z+z_{n}\right)^{2}+r^{2}\right)^{5}}\right]_{r=0}^{r=\infty} dz$$

$$= \int_{0}^{\infty} \left[0+\frac{1}{5} \frac{A\rho\pi}{\left(\left(z+z_{n}\right)^{2}\right)^{5}}\right] dz = \left[-\frac{1}{45} \frac{A\rho\pi}{\left(z+z_{n}\right)^{9}}\right]_{z=0}^{z=\infty} = 0 + \frac{1}{45} \frac{A\rho\pi}{z_{n}^{9}}$$
(4.74.a)

$$\int_{0}^{\infty} \int_{0}^{\infty} -2\pi r \rho \cdot \frac{B}{\left(\left(z+z_{n}\right)^{2}+r^{2}\right)^{3}} dr dr z = \int_{0}^{\infty} \left[\frac{1}{2} \frac{B\rho \pi}{\left(\left(z+z_{n}\right)^{2}+r^{2}\right)^{2}}\right]_{r=0}^{r=\infty} dz$$

$$= \int_{0}^{\infty} \left[0 - \frac{1}{2} \frac{B\rho \pi}{\left(\left(z+z_{n}\right)^{2}\right)^{2}}\right] dz = \left[\frac{1}{6} \frac{B\rho \pi}{\left(z+z_{n}\right)^{3}}\right]_{z=0}^{z=\infty} = 0 - \frac{1}{6} \frac{B\rho \pi}{z_{n}^{3}}$$
(4.74.b)

By recombining the two terms, we arrive at the full expression for the energy potential of the bead at position  $(z + z_n, r)$  from the surface:

$$\phi_n(z_n) = \frac{1}{45} \frac{A \rho \pi}{z_n^9} - \frac{1}{6} \frac{B \rho \pi}{z_n^3}$$
 (4.75)

A compact form can be found in terms of  $z_{min}$ , which is the distance at which the energy assumes its minimum value,  $\phi_{min}$ . To find these parameters, we set the first order derivative to zero:

$$\frac{d\phi_n}{dz_n}\bigg|_{z_n = z_{\min}} = 0 = -\frac{1}{5} \frac{A \rho \pi}{z_{\min}^{10}} + \frac{1}{2} \frac{B \rho \pi}{z_{\min}^4}$$

$$\frac{1}{5} \frac{A}{z_{\min}^6} = \frac{1}{2} B$$
(4.76)

$$z_{\min} = \left(\frac{2A}{5B}\right)^{\frac{1}{6}} \tag{4.77}$$

which can also be written as:

$$A = \frac{5}{2} z_{\min}^{6} B \tag{4.78}$$

With these two Equations 4.75 and 4.78 and two unknowns, we solved for A and B:

$$\phi_{\min} = \rho \pi \left( \frac{1}{18} \frac{z_{\min}^{6} B}{z_{n}^{9}} - \frac{1}{6} \frac{B}{z_{n}^{3}} \right) = -\frac{\rho \pi B}{9 z_{\min}^{3}}$$

$$\therefore B = -\frac{9 \phi_{\min} z_{\min}^{3}}{\rho \pi}$$
(4.79)

$$A = -\frac{45}{2} \frac{\phi_{\min} z_{\min}^9}{\rho \pi}$$
 (4.80)

Therefore, the energy potential for interaction of a bead with a half space can be written as:

$$\phi_{n}(z_{n}) = \frac{\rho \pi A}{45 z_{n}^{9}} - \frac{\rho \pi B}{6 z_{n}^{3}} = -\frac{\rho \pi}{45 z_{n}^{9}} + \frac{45 \phi_{\min} z_{\min}^{9}}{2 \rho \pi} + \frac{\rho \pi}{6 z_{n}^{3}} + \frac{9 \phi_{\min} z_{\min}^{3}}{\rho \pi}$$

$$= -\frac{z_{\min}^{9} \phi_{\min}}{2 z_{n}^{9}} + \frac{3 \phi_{\min} z_{\min}^{3}}{2 z_{n}^{3}} = \phi_{\min} \left( -\frac{z_{\min}^{9}}{2 z_{n}^{9}} + \frac{3 z_{\min}^{3}}{2 z_{n}^{3}} \right)$$

$$(4.81)$$

As expected, for  $z_n = z_{min}$ , one finds that:

$$\phi_n(z_{\min}) = \phi_{\min}\left(-\frac{1}{2} + \frac{3}{2}\right) = \phi_{\min}$$
(4.82)

Therefore,

$$\phi_n(z_n) = \frac{\phi_{\min}}{2} \left( \left( \frac{z_{\min}}{z_n} \right)^9 - 3 \left( \frac{z_{\min}}{z_n} \right)^3 \right)$$
(4.83)

In the last expression, we have switched the sign of  $\phi_{\min}$ , so that it is a positive number, as is done conventionally. The expression that defines the surface force acting on each molecule was obtained by taking the derivative of the potential energy with respect to  $z_n$ :

$$f_n(z_n) = \frac{d\phi_n(z_n)}{dz_n} = \frac{\phi_{\min}}{2} \left( -\frac{9z_{\min}^9}{z_n^{10}} + \frac{9z_{\min}^3}{z_n^4} \right)$$
(4.84)

We used the second order derivative of the potential energy Equation 4.83 and obtained a reference quantity to choose a sufficiently stiff spring constant needed to attach the molecule to the point to which displacement is applied.

$$k = \frac{df_n(z_n)}{dz_n} = \frac{\phi_{\min}}{2} \left( \frac{90z_{\min}^9}{z_n^{11}} - \frac{36z_{\min}^3}{z_n^5} \right)$$
(4.85)

At  $z_n = z_{\min}$ ,

$$k = \frac{\phi_{\min}}{2} \left( \frac{90}{z_{\min}^{2}} - \frac{36}{z_{\min}^{2}} \right) = \frac{27\phi_{\min}}{z_{\min}^{2}}$$
 (4.86)

4.5.4 The desorption energy barrier of a freely jointed chain that needs to be overcome for peeling from a surface

The potential energy profile of a single bead interacting with a surface was derived in the previous section and is shown in Equation 4.87:

$$\phi(z_n) = \frac{\phi_{\min}}{2} \left( \left( \frac{z_{\min}}{z_n} \right)^9 - 3 \cdot \left( \frac{z_{\min}}{z_n} \right)^3 \right)$$
(4.87)

Using Equation 4.87 and assuming step-wise removal of the FJC as depicted in Figure 4.10, we derive the energy potential profile for a chain of beads interacting with an ideal surface as a function of the position of the first bead  $R_z$ .

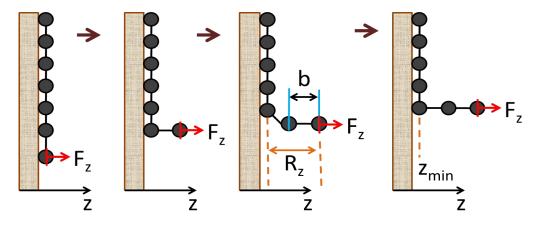


**Figure 4.10.** A schematic diagram of step-wise removal of a FJC from a surface, where  $R_z$  represents the displacement and  $F_z$  represents the applied force in the z-direction.

For this derivation, we assume that beads on the surface are always in their potential energy minimum, while the n beads in solution are always in their fully stretched state. Then, the contribution of each bead to total potential energy of the chain is:

- For the  $i^{\text{th}}$  bead in solution,  $\phi_{\text{solution}}(R_z) = \phi(R_z (i-1)b + z_{\min});$   $1 \le i \le n$
- For the (*N-n*) adsorbed beads,  $\phi(z_{\min})$

To get the total potential energy of the chain, we add the potential of the force,  $-fR_z$ . Summing all the contributions described above results in the total energy of the chain:

$$\phi_{chain}(R_z) = (N - n)\phi(z_{\min}) + \sum_{i=1}^{n} \phi(R_z - (i - 1)b + z_{\min}) - fR_z$$
(4.88)

where 
$$n = \sum_{i=1}^{N} H(R_z - (i-1)b)$$

Here, we used Heaviside step function  $H(R_z - (i-1)b)$  to count the desorbed beads (effectively switching on the potential energy function for each bead in solution). This chain potential energy is plotted in Figure 4.5 of this chapter for three different values of force.

As discussed earlier in this chapter, under the equilibrium condition,  $\phi_{chain}(R_z) = \phi_{chain}(R_z + b) \text{ , the energy barrier is smaller than } \phi_{\min} \text{ . We obtained it}$  numerically; for example, when  $\phi_{\min} = 14 \, k_B T$  , the energy barrier during equilibrium peeling is only  $(4 \, \text{k}_B T)$ .

## 4.5.5 Derivation of the Force Required for Equilibrium Peeling

The potential energy profile for removing monomers of a FJC in a step-wise fashion can be obtained by adding the attractive part of the potential energy for interaction of each respective bead with the surface (Figure 4.11).

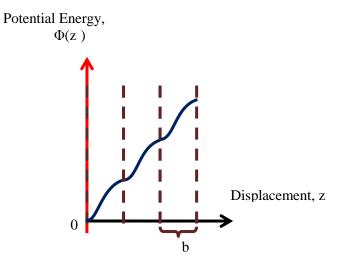


**Figure 4.11.** A schematic diagram of the potential energy profile for removing of a FJC from a surface.

In order to reach the equilibrium peeling conditions in force control, the constant force applied to the freely jointed chain has to be high enough to result in a peeling force-distance curve that oscillates about a constant force, i.e.

$$\phi + f z = 0$$

$$\phi_{n=1} = -f b \tag{4.89}$$

As shown in Figure 4.12, the energy barrier,  $E_{barrier}$ , for peeling an individual base from an ideal surface in the absence of any applied force can be estimated from  $E_{barrier} = \phi_{\min} = slope \cdot b \; . \; \text{The term 'slope' refers to the slope of the energy potential}$  profile as depicted in Figure 4.12.

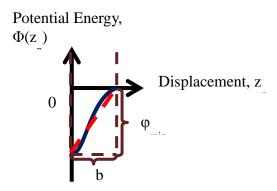


**Figure 4.12.** The energy barrier for removing an individual monomer from an ideal surface is obtainable from the Kuhn segment length, b = 0.65 nm, of the freely jointed chain and the slope was of potential energy profile for peeling a chain ( $z_{\min} = 0.5$  nm,  $\phi_{\min} = \gamma b$ ).

Since a flat peeling force curve is observed in equilibrium, an equal but opposite quantity of force obtained from the slope of the potential energy profile must be applied in order to peel off the chain.

$$slope = -f_{total} = \frac{\phi_{\min}}{b} \tag{4.90}$$

This force can also be approximated by  $f_{total} = \gamma_{total}$  when operating under large peeling forces (F>>1).<sup>21</sup>

As discussed earlier in this chapter, the addition of this force to the system resulted in an energy barrier that is smaller than  $\phi_{\min}$ . In order to make use of the previously derived expressions for the hopping rate of the bases, we had to quantify the values of the attempt frequency and the amplitude of the periodic function representing the energy barrier. To obtain the exact height of the energy barrier analytically, we derived an expression to find the height of the energy barrier when equilibrium peeling

conditions are applied. The energy profile for removing a chain that is interacting with a substrate under force control is written as:

$$g(z) = \phi_{\min} - \phi(z) - f z \tag{4.91}$$

When the peeling of the chain occurs under equilibrium conditions, the total energy, g(z), is zero. Using this condition, one can write an expression for the applied force,

 $f = \frac{\phi_{\min} - \phi(b)}{b}$ , in terms of the free energy of binding of the chain to the substrate,  $\phi_{\min}$ ,

and hence express Equation 4.91 as:

$$g(z) = \phi_{\min} - \phi(z) - \frac{\phi_{\min} - \phi(b)}{b} z \tag{4.92}$$

To obtain the energy profile of the system under equilibrium conditions, we set the derivative of g(z) to zero:

$$\frac{dg(z)}{dz} = -\frac{d\phi(z)}{dz} - \frac{\phi_{\min} - \phi(b)}{b} = 0 \tag{4.93}$$

Therefore,

$$\frac{d\phi(z)}{dz} = \frac{\phi(b) - \phi_{\min}}{b} \tag{4.94}$$

Using the attractive portion of Equation 4.83 and approximating  $\frac{d\phi(z)}{dz}$  by only

considering of this function, we find that:

$$\frac{d\phi(z)}{dz} = -\frac{9\,\phi_{\min}}{2} \left(\frac{z_{\min}}{z}\right)^4 = \frac{\phi(b) - \phi_{\min}}{b} z_{\min} \tag{4.95}$$

$$\left(\frac{z_{\min}}{z}\right)^4 = \frac{2}{9} \frac{\phi_{\min} - \phi(b)}{\phi_{\min}} \frac{z_{\min}}{b} \tag{4.96}$$

At the limit of  $|\phi_{\min}| \gg |\phi(b)|$ ,

$$\left(\frac{z_{\min}}{z}\right)^{4} \approx \frac{2}{9} \frac{z_{\min}}{b}$$

$$\therefore \left(\frac{z}{z_{\min}}\right)^{4} \approx \frac{9}{2} \frac{b}{z_{\min}}$$

$$\therefore z^{*} = \left(\frac{9}{2} \frac{b}{z_{\min}}\right)^{\frac{1}{4}} z_{\min}$$
(4.97)

By substituting this equilibrium displacement (Equation 4.97) into the original total potential energy Equation 4.92 allows us to analytically obtain the energy barrier when  $f_{eq}$  is applied (i.e. the reduced value of this energy barrier):

$$g(z^*) = \phi_{\min} - \phi(z^*) - \frac{\phi_{\min} - \phi(b)}{b} z^*$$

$$= \phi_{\min} - \phi(z^*) - \frac{\phi_{\min}}{b} z^*$$

$$= \phi_{\min} \left[ 1 - \left( \frac{z_{\min}}{b} \right)^{\frac{3}{4}} \left( \frac{9}{2} \right)^{\frac{1}{4}} \right] + \frac{\phi_{\min} z_{\min}}{b}$$
(4.98)

Using Equation 4.98 for a FJC with free energy of binding per base,  $\phi_{\min}$ , of 14 k<sub>B</sub>T, Kuhn segment length, b, of 6.5 nm, and  $z_{\min}$  of 0.5 nm, we estimate the lowered energy barrier to be 8 k<sub>B</sub>T. Comparing this estimated energy required for each Kuhn segment to overcome during equilibrium peeling with those obtained numerically (2 k<sub>B</sub>T) as shown in Figure 4.5 in this chapter, Equation 4.98 appears to overestimate the results.

#### 4.5.6 Estimate of Attempt Frequency

Ultimately, the attempt frequency and hence, the equilibrium peeling rate required to overcome the energy barrier for individual monomers also need to be quantified. This calculation can be executed by either using the energy barrier for removal of each base (Equation 4.99 and 4.100) or by considering the friction and diffusion coefficient of each base in fluid. In the first approach, we used Stokes's law ( $F = 6\pi \eta av$ ), where  $\eta$  is the fluid viscosity (kg/m/s), a is the radius of gyration of the molecule (m), and v is the velocity in fluid (m/s). By rearranging the Stoke's equation, we obtained the equilibrium velocity for a given steady state peeling force.

$$v = \frac{\phi_{\min}}{6\pi \eta a b} \tag{4.99}$$

For a chain with Kuhn length of 0.65 nm, depth of the potential well of  $10 \text{ k}_B\text{T}$ , fluid viscosity of 1 mg/m/s, and radius of gyration of 0.29 nm, we calculated the equilibrium peeling rate for individual monomers to be 11.5 m/s. This is significantly larger than any of the rates that we have considered for studying the rate effects on peeling of a chain from the surface. The attempt frequency (s<sup>-1</sup>), q, was then calculated based on the time it takes to transverse length b separating the two states (adsorbed/desorbed) at velocity v:

$$q = \frac{1}{t_b} = \frac{1}{b/v} \tag{4.100}$$

In a different approach, the attempt frequency for equilibrium peeling is estimated based on the total number of Kuhn segments N in the FJC and the total time it takes for the chain to be removed, t:

$$N = q \cdot t \tag{4.101}$$

Using the relationship between the end-to-end distance of the chain, which is also estimated as  $\langle r^2 \rangle = N b^2$ , and the diffusivity of the chain as well as the elapsed time,  $\langle r^2 \rangle = 6Dt$ , the attempt frequency is estimated in the following way:

$$\langle r^{2} \rangle = 6Dt$$

$$\langle r^{2} \rangle = Nb^{2} = qtb^{2}$$

$$6Dt = qtb^{2}$$

$$q = \frac{6D}{b^{2}}$$
(4.102)

The attempt frequencies were computed to be  $1.8 \cdot 10^{10} \, \mathrm{s}^{-1}$  from Equation 101 and  $1.1 \cdot 10^{10} \, \mathrm{s}^{-1}$  from Equation 102, and are on the same order of magnitude. Note that since the hopping for this system occurs in a three-dimensional setting, we used 6Dt instead of 4Dt. Moreover, we were interested in the hopping rate of each individual base; therefore, the diffusion constant was divided by the Kuhn length instead of the chain's contour length. In cases where the movement in a two-dimensional setting is of interest, 4Dt should be applied instead of 6Dt in the calculations discussed above. The diffusion of individual links of a freely-jointed chain on a planar surface is an example of this two-dimensional setting.

# 4.5.7 Number of Links Going In and Out of Contact with a Surface in Equilibrium

Assuming that we have a FJC that is weakly bound to a surface and is being peeled off under non-equilibrium conditions, we related the thermally activated crossing of the energy barrier to the equilibrium number of links going in and out of contact with the surface. Here, we considered a partially adsorbed chain under the displacement control model.

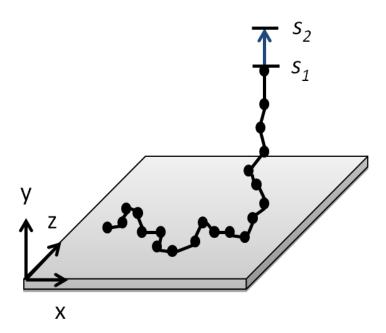


Figure 4.13. A schematic diagram of FJC removal under displacement control

The energy for this system is given by:

$$G = G_{stb} + G_{adh} + G_{stretching} \tag{4.103}$$

The first term represents the entropy gain that comes from the desorption of the links from the surface (2D state) into the bulk fluid (3D state).<sup>25</sup>

$$G_{stb} = -k_B T n \left\{ \ln \left( \frac{w_{3D} \sinh F}{w_{2D} F} \right) \right\} = -k_B T n \ln \left( \left( \frac{w_{3D}}{w_{2D}} \right) \left( 1 + \frac{F^2}{3!} + \dots \right) \right)$$
(4.104)

Here, n is the number of desorbed links,  $w_{3D}$  is the number of microstates of a single link in a free chain in solution while  $w_{2D}$  is the number of microstates in an adsorbed chain, and F is the dimensionsless force applied,  $F = f b/(k_B T)$ . For the links to desorb from the surface into the bulk, we assumed that they are weakly adsorbed to the surface. Therefore, at the limit of small forces, Equation 4.104 becomes:<sup>25</sup>

$$G_{stb} = -k_B T n \ln \left( \frac{w_{3D}}{w_{2D}} \right)$$
 (4.105)

The second term,  $G_{\text{adh}}$ , represents the energy reduction due to the adsorption of the links onto the surface:

$$G_{adh} = -b\gamma(N-n) \tag{4.106}$$

 $\gamma$  is the free energy of adhesion per link, b the Kuhn length of each link, and N is the total number of links. The third term represents the stretching entropy of a Gaussian chain (GC) (in low force limit):

$$G_{stretching} = \int_{0}^{R} f dZ = \int_{0}^{R} (k_{FJC} \cdot Z) dZ = \frac{1}{2} k_{FJC} R^{2}$$
 (4.101)

Where R is the displacement and  $k_{FJC}$  is the spring constant for a 3-D spring is obtained from the length of the desorbed chain ( $l_d = nb$ ) as follows:

$$k_{FJC} = \frac{3k_B T}{l_d b} = \frac{3k_B T}{nb^2}$$
 (4.102)

Therefore, the free energy of the system can be written as:

$$G = -k_B T n \ln \left(\frac{w_{3D}}{w_{2D}}\right) - b\gamma (N - n) + \frac{3k_B T}{2nb^2} R^2$$
 (4.103)

To simulate the energy barrier that individual monomer units have to overcome in order to desorb from the surface, we added a sinusoidal variation to the free energy, where 'a' is the height of this energy barrier.

$$G_{t} = -k_{B} T n \ln \left(\frac{w_{3D}}{w_{2D}}\right) - b\gamma (N - n) + \frac{3k_{B} T}{2nb^{2}} R^{2} + a\sin(2\pi n)$$
 (4.104)

$$G_t = G + a \sin(2\pi n)$$

The potential energy barrier is both dependent on the minimized sinusoidal function,

 $2a\pi \cdot \cos(2\pi n)$ , and the slope of the free energy of the system,  $\frac{dG}{dn}$ . Therefore, we

minimize the total free energy of the system

$$\frac{dG_t}{dn} = \frac{dG}{dn} + 2a\pi \cdot \cos(2\pi n) \tag{4.105}$$

and define the expression for the thermal energy barrier.

$$E_{barrier} = a \pm \frac{1}{2\pi} \frac{dG}{dn} \tag{4.106}$$

The  $\pm$  represent the forward and the backward energy barriers. Therefore, the hopping rate,  $J_{\pm}$ , based on this thermal energy barrier and the attempt frequency, q, is:

$$J_{\pm} = q \cdot \exp\left(-\frac{a \pm \left(\frac{1}{2\pi}\right) \frac{dG}{dn}}{k_{B}T}\right) \tag{4.107}$$

From this, the net flux was obtained:

$$\frac{dn}{dt} = J_{+} - J_{-} = q \cdot \exp\left(-\frac{a + \left(\frac{1}{2\pi}\right)\frac{dG}{dn}}{k_{B}T}\right) - q \cdot \exp\left(-\frac{a - \left(\frac{1}{2\pi}\right)\frac{dG}{dn}}{k_{B}T}\right)$$
(4.108)

$$= q \cdot \exp\left(-\frac{a}{k_{B}T}\right) \cdot \left\{ \exp\left(-\frac{\left(\frac{1}{2\pi}\right)\frac{dG}{dn}}{k_{B}T}\right) - \exp\left(\frac{\left(\frac{1}{2\pi}\right)\frac{dG}{dn}}{k_{B}T}\right) \right\} \cdot \frac{2}{2}$$

Since  $\sinh(x) = (\exp(x) - \exp(-x))/2$ , we let  $x = -(dG/dn)/(2\pi k_B T)$  and obtained the following expression by applying the Taylor series expansion of  $\sinh(x) = x + x^3/3! + ...$ :

$$\frac{dn}{dt} = q \cdot \exp\left(-\frac{a}{k_B T}\right) \cdot 2 \cdot \sinh\left(-\frac{\frac{dG}{dn}}{2\pi k_B T}\right) = J_0 \cdot \sinh\left(-\frac{\frac{dG}{dn}}{2\pi k_B T}\right) \approx J_0 \cdot \left(-\frac{\frac{dG}{dn}}{2\pi k_B T}\right)$$

$$(4.109)$$

The derivative of free energies (Equation 4.107) was taken with respect to the desorbed number of monomers to obtain the following expression:

$$G = -k_B T n \ln \left( \frac{w_{3D}}{w_{2D}} \right) - b \gamma (N - n) + \frac{3k_B T}{2nb^2} R^2$$
(4.110)

$$\frac{dG}{dn} = \frac{d}{dn} \left\{ -k_B T n \ln \left( \frac{w_{3D}}{w_{2D}} \right) - b\gamma (N - n) + \frac{3k_B T}{2nb^2} R^2 \right\} 
= -k_B T \ln \left( \frac{w_{3D}}{w_{2D}} \right) + b\gamma - \frac{3k_B T}{2n^2b^2} R^2$$
(4.111)

Substituting this expression into the flux equations,

$$\frac{dn}{dt} = -\frac{J_0}{2\pi k_B T} \left( -k_B T \ln \left( \frac{w_{3D}}{w_{2D}} \right) + b\gamma - \frac{3k_B T}{2n^2 b^2} R^2 \right)$$
(4.112)

$$\frac{dn}{dt} = -\frac{J_0}{2\pi} \left( \Gamma' - \frac{3}{2n^2b^2} R^2 \right)$$
 (4.113)

where  $\Gamma' = \Gamma - \ln\left(\frac{w_{3D}}{w_{2D}}\right)$  and  $\Gamma = \gamma b/(k_B T)$  is dimensionless free energy of binding.

Setting the flux term to zero, we obtained the equilibrium expression and hence solved for the equilibrium number of bases at a fixed displacement, R:

$$\frac{dn}{dt} = -\frac{J_0}{2\pi} \left( \Gamma - \frac{3}{2n^2 b^2} R^2 \right) = 0 \tag{4.114a}$$

$$\Gamma' = \frac{3}{2n^2b^2}R^2 \tag{4.114b}$$

$$n^2 = \frac{3}{2\Gamma'} \cdot \left(\frac{R}{b}\right)^2 \tag{4.114c}$$

$$n = \left(\frac{3}{2\Gamma'}\right)^{\frac{1}{2}} \cdot \frac{R}{b} \tag{4.115}$$

To consider the applied force, we used the Gaussian chain (GC) in the limit of small dimensionless forces:

$$f = k_{GC}R \tag{4.116}$$

where  $k_{GC} = \frac{3k_BT}{nb^2}$  for a 3-D system

Therefore,

$$\frac{R}{b} = \frac{f \, nb}{3k_B T} = \frac{F \, n}{3} \tag{4.117}$$

where  $F = f b/(k_B T)$  is the dimensionless force. This expression value was substituted into the equilibrium Equation 4.115 for the number of bases

$$n = \left(\frac{1}{6\Gamma'}\right)^{\frac{1}{2}} \cdot F n \tag{4.118}$$

Simplifying Equation 4.118 deduces to the following expression:

$$\Gamma' = \frac{F^2}{6}$$

$$= \Gamma - \ln\left(\frac{w_{3D}}{w_{2D}}\right) \tag{4.119}$$

which is expected from the equilibrium model for Gaussian chain. Given that

 $R(t) = v \cdot t = n(t) \cdot b$ , then dn/dt = v/b. Therefore, Equation 4.114.a. can be rewritten

as:

$$\frac{v}{b} = \frac{J_0}{2\pi} \left( -\Gamma' + \frac{3}{2n^2} \left( \frac{R}{b} \right)^2 \right) 
= -\frac{J_0 \Gamma'}{2\pi} + \frac{3J_0}{4\pi n^2} \left( \frac{R}{b} \right)^2$$
(4.120a)

$$\frac{2\pi v}{J_0 b} + \Gamma' = \frac{3}{2n^2} \left(\frac{R}{b}\right)^2$$

$$n = \sqrt{\frac{3J_0b}{4\pi v + 2J_0b\Gamma}} \cdot \frac{R}{b} \tag{4.120b}$$

By design, as mentioned previously, 
$$\frac{R}{b} = \frac{F}{3}n = \sqrt{\frac{4\pi v + 2J_0b\Gamma'}{3J_0b}}n$$

Therefore, by rearranging and substituting the expression for equilibrium number of links under displacement control and applied Gaussian force, we found that

$$F = \sqrt{\frac{12\pi v + 6J_0b\Gamma'}{J_0b}}$$
 (4.121)

To consider the equilibrium number of FJC monomers desorbed from a surface under displacement control, we also used the Langevin function:

$$R = nb \left( \coth \left( \frac{fb}{k_B T} \right) - \left( \frac{k_B T}{fb} \right) \right) = nbL \left( \frac{fb}{k_B T} \right)$$
(4.122)

We then repeated the same argument outlined above for the Langevin function instead of the Gaussian spring (Equation 4.103 through Equation 4.120.b.). Therefore,

$$G = -nk_B T \ln\left(\frac{w_{3D}}{w_{2D}}\right) - \left(N - n\right)b\gamma + \int_0^{\delta} f \, dR \tag{4.123}$$

The force term, 'f', is the inverse Langevin function,  $f = \frac{k_B T}{b} L^{-1} \left( \frac{R}{nb} \right)$ , and can be

approximated using  $L^{-1}(x) \cong x \cdot \frac{3-x^2}{1-x^2}$ . In lumping parameters together, we set

 $F = fb/(k_B T)$  and u = R/(nb). The force term was simplified and integrated to obtain the entropic stretching of a chain.

$$F = L^{-1}(u) \cong u \cdot \frac{3 - u^2}{1 - u^2} = u \cdot \frac{2 + 1 - u^2}{1 - u^2} = \frac{2u}{1 - u^2} + u \cdot \frac{1 - u^2}{1 - u^2}$$
(4.124)

$$\int_{0}^{u} F \, du = \int_{0}^{u} u \, du + \int_{0}^{u} \frac{2u}{1 - u^{2}} \, du$$

$$= \frac{u^{2}}{2} + 2 \cdot \left( -\frac{\ln(1 - u^{2})}{2} \right)$$

$$= \frac{u^{2}}{2} - \ln(1 - u^{2})$$
(4.125)

Using this expression, we defined the dimensionless free energy of stretching or the strain energy under the force-displacement curve as:

$$\Gamma_{stretching} = \left\{ \frac{1}{2} \left( \frac{R}{nb} \right)^2 - \ln \left( 1 - \left( \frac{R}{nb} \right)^2 \right) \right\}$$
 (4.126)

As shown in Equation 4.111, the derivative of all energy terms is needed in order to obtain the minima as well as the equilibrium number of bases as they go in and out of contact with the surface. The derivative of the first term of  $\Gamma_{stretching}$  is obtainable through the conventional derivation technique; however, chain rule was applied to take the first order derivative of the second term. We let  $y = \ln\left(1 - \left(\frac{R}{nb}\right)^2\right)$ .

$$\frac{dy}{dn} = \frac{dy}{du} \cdot \frac{du}{dw} \cdot \frac{dw}{dn}$$

$$y = \ln(u) \qquad \rightarrow \qquad \frac{dy}{du} = \frac{1}{u}$$

$$u = 1 - w^2 \qquad \rightarrow \qquad \frac{du}{dw} = -2w$$

$$w = \frac{R}{nb} \qquad \rightarrow \qquad \frac{dw}{dn} = -\frac{R}{n^2b}$$

$$\therefore \frac{dy}{dn} = \frac{2R^2}{n^3b^2 - nR^2}$$
(4.127)

To obtain an expression for the change in the number of desorbed monomers with time, we first placed together the derivative of all the terms that describe contributions to the total free energy back.

$$G = -k_B T n \ln\left(\frac{w_{3D}}{w_{2D}}\right) - b\gamma(N - n) + k_B T \left\{ \frac{1}{2} \left(\frac{R}{nb}\right)^2 - \ln\left(1 - \left(\frac{R}{nb}\right)^2\right) \right\}$$

$$(4.128)$$

$$\frac{dG}{dn} = -k_B T \ln\left(\frac{w_{3D}}{w_{2D}}\right) + b\gamma - \frac{k_B T}{2} \cdot \frac{2R^2}{n^3 b^2} - k_B T \cdot \frac{2R^2}{n^3 b^2 - nR^2}$$
(4.129)

$$\frac{dn}{dt} \approx \frac{J_0}{2\pi k_B T} \left( -\frac{dG}{dn} \right)$$

$$= \frac{J_0}{2\pi k_B T} \left( k_B T \ln \left( \frac{w_{3D}}{w_{2D}} \right) - b\gamma + \frac{k_B T}{2} \cdot \frac{2R^2}{n^3 b^2} + k_B T \cdot \frac{2R^2}{n^3 b^2 - nR^2} \right)$$

$$= 0 \qquad \left( \text{at equilibrium} \right)$$

$$(4.130)$$

$$\therefore \frac{k_B T}{b} \ln \left( \frac{w_{3D}}{w_{2D}} \right) - \gamma + k_B T \cdot \frac{R^2}{n^3 b^3} + k_B T \cdot \frac{2R^2}{n^3 b^3 - nbR^2} = 0$$
 (4.131.a)

$$\therefore -\Gamma' + b \cdot \frac{R^2}{n^3 b^3} + b \cdot \frac{2R^2}{n^3 b^3 - nbR^2} = 0$$
 (4.131.b)

To solve for the equilibrium number of bases going in and out of contact with the surface for a given displacement, Equation 4.131 needed to be solved for 'n'; however, this is not a simple task given that this equation is implicit. Therefore, we simplified Equation 4.131.b by considering a chain in the limit of long contour lengths.

$$\therefore -\Gamma' + b \cdot \frac{R^2}{n^3 b^3} + b \cdot \frac{2R^2}{n^3 b^3} = 0$$
 (4.132)

Using Equation 4.132 and dimensionless binding energy,  $\Gamma = \gamma b/(k_B T)$ , an expression for the equilibrium number of desorbed bases was derived:

$$\Gamma' = \frac{3bR^2}{n^3b^3} \tag{4.133}$$

$$n = \left\{ \frac{3 R^2}{\Gamma' b^2} \right\}^{\frac{1}{3}} \tag{4.134}$$

As before, we used the definition dn/dt = v/b to derive the expression for the equilibrium number of bases out of contact with the surface as well as the equilibrium peeling forces in terms of peeling rates.

$$\frac{dn}{dt} = \frac{v}{b} \cong \frac{J_0}{2\pi k_B T} \left( k_B T \ln \left( \frac{w_{3D}}{w_{2D}} \right) - b\gamma + k_B T \cdot \frac{3R^2}{n^3 b^2} \right)$$
(4.135)

$$\frac{2\pi v}{J_0 b} = \ln\left(\frac{w_{3D}}{w_{2D}}\right) - \frac{b\gamma}{k_B T} + \frac{3R^2}{n^3 b^2}$$
 (4.136.a)

$$\frac{3R^2}{n^3b^2} = \frac{2\pi v}{J_0b} + \Gamma' \tag{4.136.b}$$

$$n = \left(\frac{3R^2}{b^2 \left(\frac{2\pi v}{J_0 b} + \Gamma'\right)}\right)^{\frac{1}{3}}$$
 (4.137)

And by substituting the expression above into Equation 4.122, we can rewrite the Langevin function as:

$$R = \left(\frac{3bR^2}{\left(\frac{2\pi v}{J_0 b} + \Gamma'\right)}\right)^{\frac{1}{3}} \cdot L\left(\frac{fb}{k_B T}\right)$$

$$R^{\frac{1}{3}} = \left(\frac{3b}{\left(\frac{2\pi v}{J_0 b} + \Gamma'\right)}\right)^{\frac{1}{3}} \cdot L\left(\frac{fb}{k_B T}\right)$$

$$(4.138)$$

To graphically depict this result (Figure 4.14), we compared the potential energy for a FJC interacting with an ideal surface when no force is applied to the chain to the potential energy under equilibrium conditions obtained from the Langevin function. The point at which the number of desorbed monomers from the potential energy corresponding to the interaction of individual bases (black line) with the surface is equal to the number of desorbed bases from the Langevin potential (blue curves) is considered the number of desorbed bases in equilibrium with the surface. Figure 4.14 in particular shows that the bases, of our 20 monomer long chain, going in and out of contact with the surface under displacement control are expected to remain in equilibrium with the surface at all times.

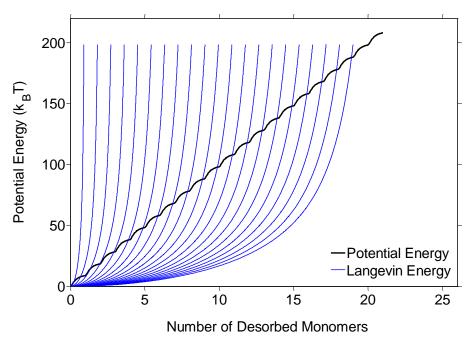


**Figure 4.14.** Comparison of the potential energy of a freely jointed chain interacting with an ideal surface when peeling of the chain is not in equilibrium (black line) against the equilibrium entropic stretching of the chain obtained from the Langevin function.

The expression for the equilibrium number of desorbed bases (Equation 4.134) can then be substituted for 'n' in  $f = \frac{k_B T}{b} L^{-1} \left( \frac{R}{nb} \right) \cong \frac{k_B T}{b} \left( \frac{R}{nb} + \frac{2R/(nb)}{1 - (R/(nb))^2} \right)$  to obtain the equilibrium expression for peeling forces in terms of peeling rates.

#### 4.5.8 Derivation of peeling force at finite forcing rates

In obtaining a complete expression for the non-equilibrium peeling of a chain from a surface, both the viscous and desorption forces are needed to be defined as a function of forcing rate. Starting with Equation 4.31, which defines the rate of desorption of the links as a function of both forcing rate and the free energy of binding of the chain to the surface,

$$\frac{d\langle n\rangle}{dt} = J_0 \sinh\left(\frac{(\dot{f} t - \gamma)b}{2k_B T}\right) \tag{4.31}$$

and integrating this equation,

$$\int d\langle n \rangle = \int J_0 \sinh\left(\frac{(\dot{f} t - \gamma)b}{2k_B T}\right) dt \tag{4.139}$$

we obtain the following:

$$\langle n \rangle = \frac{2J_0 k_B T}{\dot{f} b} \cosh \left( \frac{\left( \dot{f} t - \gamma \right) b}{2k_B T} \right) + C = \frac{2J_0 k_B T}{\dot{f} b} \cosh \left( \frac{\left( f - \gamma \right) b}{2k_B T} \right) + C \tag{4.140}$$

To establish the value of the integration constant, we need to use an initial condition for when  $\langle n \rangle = 0$ . Formally at t = 0,  $\langle n \rangle = 0$ ; however, this is not a good initial condition because  $\frac{d\langle n \rangle}{dt} < 0$  (and, therefore,  $\langle n \rangle$  remains 0) for some time, until f exceeds  $\gamma$ . The appropriate initial condition is therefore  $\langle n \rangle = 0$  at  $f = \gamma$ , applying which we obtain for the integration constant:

$$0 = \frac{2J_0 k_B T}{\dot{f} b} \cosh(0) + C \tag{4.141}$$

$$C = -\frac{2J_0 k_B T}{\dot{f} b} \tag{4.142}$$

Therefore, Equation 4.140 becomes:

$$\langle n \rangle = \frac{2J_0 k_B T}{\dot{f} b} \left[ \cosh \left( \frac{(f - \gamma)b}{2k_B T} \right) - 1 \right]$$
 (4.143)

which we then rearranged to obtain:

$$\operatorname{arcosh}\left(\frac{\dot{f}\,b}{2J_0k_BT}\langle n\rangle + 1\right) = \frac{(f-\gamma)b}{2k_BT} \tag{4.144}$$

or, in dimensionless form:

$$F = \Gamma + 2\operatorname{arcosh}(\dot{F}_{desorb}\langle n \rangle + 1)$$
(4.145)

which is the same as Equation 4.34 of this chapter.

# 4.5.9 Conformation of a FJC as a Function of Forcing Rate

We considered the removal of a chain with 20 Kuhn links in force control for a range of forcing rates (22.2  $\mu$ N/s - 63.5 mN/s). Figure 4.15 shows the effect of forcing rate on the evolution of an FJC's conformation under force control. Although the chain does not interact with a substrate, it is fixed in the z-direction from one end in order to capture only its extension and stretching in fluid. As expected, at the beginning and at the end of the simulation, the FJC is fully coiled and stretched out, correspondingly, for all forcing rates. The second set of conformations was obtained when the end-to-end distance of the chain was close to half of its contour length and it reveals interesting information. For the fastest forcing rate (63.5 mN/s shown in blue), the chain is stretched nearly to full extension from one end to which force is being applied. Meanwhile, the

FJC that is removed at the slowest rate (22.2  $\mu$ N/s shown in green) appears to be fully stretched from the end which is fixed to the surface in the z-direction. This observation suggests that when the chain is pulled fast enough so that it cannot equilibrate, a rapid extension and removal of the links occurs one by one consecutive to the end that is being pulled. Under slow removal rates, force is transferred from the end that is being pulled to to the rest of the chain. The FJC is then given enough time to equilibrate with itself and its surrounding, allowing the entire chain to be lifted in the upward direction.

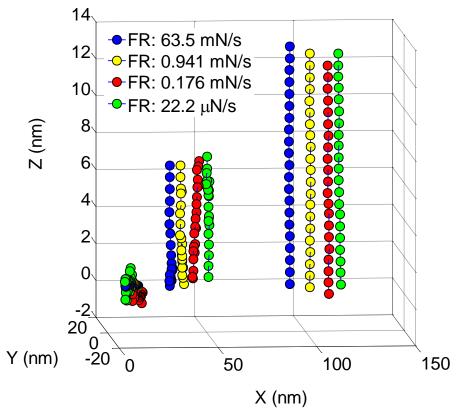


**Figure 4.15.** Snapshots of a freely jointed chain with 20 Kuhn links is shown as the applied force in z-direction increases at different forcing rates. (Left) At the beginning of the simulation, the force is too small to uncoil the chain. (Middle) The second set of conformations illustrates the effect of forcing rate and chain equilibration on the physical state of the FJC when the end-to-end distance of the chain is slightly higher than half of its contour length. (Right) Final conformation was obtained at the very end of the simulations when the FJC is fully stretched to its contour length.

## 4.5.10 Reducing noise from the simulations by means of averaging

Under force control, to plot the resulting average end-to-surface distance, we varied the averaging windows based on the peeling rates so that there would be a total of 100 data points for each plot. For example, for the slowest simulations, where  $10^8$  time steps were used, each averaging window holds  $10^6$  data points. Over the entire duration of this averaging window, a constant force was applied to the chain and the end-to-surface distances of the FJC were collected and averaged. Figure 4.16 plots results with and without averaging for a chain with binding energy of  $14 \text{ k}_B\text{T}$  per base peeled at a forcing rate of  $15 \text{ \mu N/s}$  under force control.

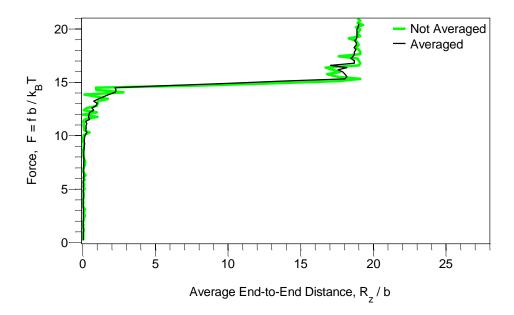


**Figure 4.16.** Comparison between results for a chain with adhesion energy of  $14 k_B T$  per base under force control with and without averaging.

#### 4.5.12. Effect of forcing rate on force-displacement relationship of a free chain

Figure 4.17 shows the force-displacement curves for pulling a free chain in fluid under different forcing rates.

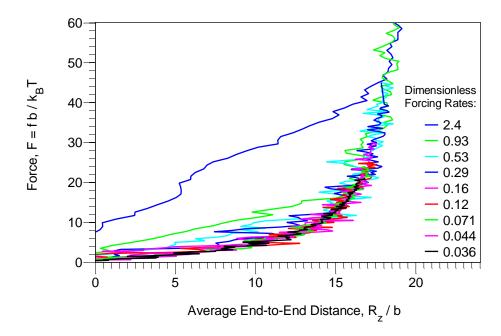


**Figure 4.17.** Pulling a free chain with 20 Kuhn links at different forcing rates in fluid. The dimensionless forcing rates were obtained using  $\dot{F} = \frac{\sqrt{6\pi \eta a \, \dot{f} \, b^3}}{k_B T}$ .

The force-forcing rate relationship of a FJC chain with a free end vs. a chain with end fixed in the z-direction (but free in xy-plane) (Figure 4.7 in this chapter) shows that there is a difference between the peeling forces experienced by the two chains. This difference is highly dependent on removal rates. Operating at or near quasi-equilibrium removal rates result in much larger discrepancies in peeling forces between the two chains in comparison to when lower pulling forces are applied. This observation is due to

removal of a larger number of Kuhn links at once when lower forcing rates are applied to a free chain as opposed to a FJC with a fixed end.

Here, we show that in the absence of the constraint on one end of the chain, the force required to peel a free FJC slowly is twice the magnitude of that required to peel a chain that has a fixed end. The force,  $f = \dot{f} t$ , required to overcome the viscous drag acting on a FJC pulled in a fluid is given by Stokes equation and depends on fluid viscosity ( $\eta$ ), radius of the molecule (a), number of Kuhn links (n), and velocity of peeling ( $v = \frac{dR}{dt}$ ):

$$\dot{f} t = 6\pi \eta \, a \, n \frac{dR}{dt} \tag{4.146}$$

Since in pulling a free FJC, all links will move away from their initial positions at the same time, the expression above was re-written as:

$$\dot{f} t = 6\pi \eta \, a \, N \frac{dR}{dt} \tag{4.147}$$

By integrating and rearranging Equation 4.147, we defined the end-to-end distance of the chain as following:

$$R = \frac{\dot{f} t^2}{12\pi\eta \, a \, N} \tag{4.148}$$

In plotting Figure 4.6 in this chapter, we were interested in the peeling force as a function of the forcing rate when the end-to-end distance of the chain is one-half of its contour length i.e. when  $R = \frac{N}{2}b$ . Therefore,

$$\frac{N}{2}b = \frac{\dot{f}\,t^2}{12\pi\eta\,a\,N}\tag{4.149}$$

which was rearranged to obtain an expression for peeling force, f.

$$f \mid_{free, R = \frac{N}{2}b} = \sqrt{6\pi \eta \, a \, \dot{f} \, b} \, N \tag{4.150}$$

Considering a FJC whose one end is constrained

$$f = \sqrt{\frac{6\pi\eta a \dot{f}}{b}} R$$

$$= \sqrt{6\pi\eta a \dot{f} b} n$$
(4.151)

and has the end-to-end distance of one-half of its contour length,

$$f \mid_{fixed, R = \frac{N}{2}b} = \sqrt{6\pi \eta \, a \, \dot{f} \, b} \, \frac{N}{2}$$
 (4.152)

it is evident that the force required to remove a free chain will be twice as large as that required to peel a chain with a fixed end.

#### 4.5.11 Effect of Removal Rate on Force Spikes in Displacement Control

Figure 4.18 shows the effect of the peeling rate on the force-displacement curve under displacement control for a chain with adhesion of 11.5 k<sub>B</sub>T per Kuhn segment. Observe that even when the slowest peeling rate is applied, the force spikes from the simulated force-displacement results are significantly attenuated and broadened in comparison to those predicted by the equilibrium model.<sup>20</sup> Neither the location, nor the amplitude of the force spikes from the simulations exactly match the equilibrium results. This observation suggests that the system is going out of equilibrium during the sharp

transition in force. Furthermore, at faster peeling rates, fluctuation in the force is disorderly and masks the periodic force spikes predicted under equilibrium.

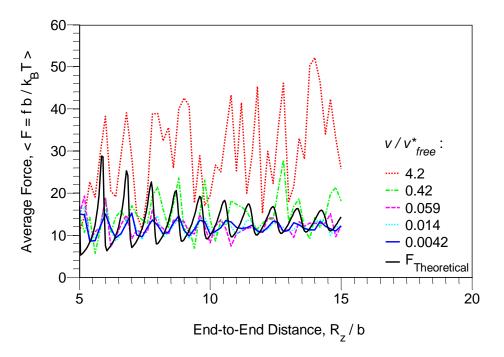


**Figure 4.18.** The effect of rate on the force-displacement relationship for a 20-mer FJC with surface adhesion of  $11.5 \, k_B T$  per link under displacement control. Similar to the force control results, moving away from the equilibrium rate results in deviations from the equilibrium force until the plateau is no longer recognizable.

# 4.5.12 Effect of chain length on force spikes of block-co-polymers in displacement control

We explored the effect of length in block-co-polymers on the shape of the force-displacement curves. The peeling of  $poly(dT_5)poly(C_5)poly(T_5)poly(C_5)$  under displacement control and in the presence of AFM probe ( $k_{sp}=0.2\ N/m$ ) showed that the thermal fluctuations of the AFM probe not only remove the spikes in peeling forces

corresponding to individual bases, but also make it impossible to distinguish between short blocks of different sequences (Figure 4.19). Therefore, it is important to consider sufficiently long blocks to carry out SMFS experiments on block-polymers.

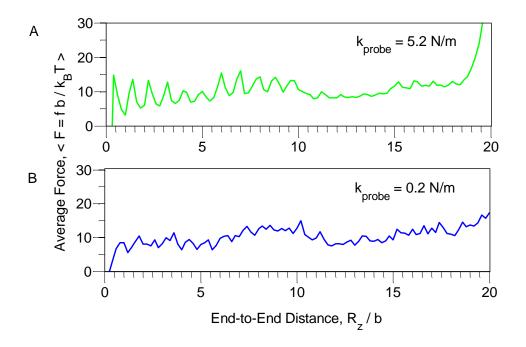


**Figure 4.19.** The effect of the length of homopolymer sequence in block-co-polymers on peeling of the FJC with stiff probes ( $k_{probe} = 5.2 \text{ N/m}$ ) and in the presence of compliant probes ( $k_{probe} = 0.2 \text{ N/m}$ ).

# 4.5.13 Testing Thermal Fluctuation Effects of an Added AFM Probe to the System

By making the last FJC bead very large in comparison to all other beads representing the monomers, we implemented the thermal fluctuation effects of an added AFM probe. To verify that this addition to the system was implemented correctly, we tested the movements of a single particle restricted by a spring. It is expected that by positioning the particle at the origin (x = y = z = 0) and also anchoring the spring to this

location, that the particle should diffuse for short times and not see the spring force. In this limit, the average distance traveled by the particle is obtained from:

$$\langle r^2 \rangle = 6Dt \tag{4.153}$$

As we approach equilibrium in the limit of long times, the average distance traveled by the particle is given by that of a harmonic oscillator and obtained from the equipartition theorem. In this case, there is no longer a dependence on time:

$$\left\langle r^2 \right\rangle = 3 \frac{k_B T}{k_{sp}} \tag{4.154}$$

Figure 4.20 shows that these two limits are indeed satisfied in our simulations. Especially, note that stiffer springs result in shorter times to reach the equilibrium limit described above.

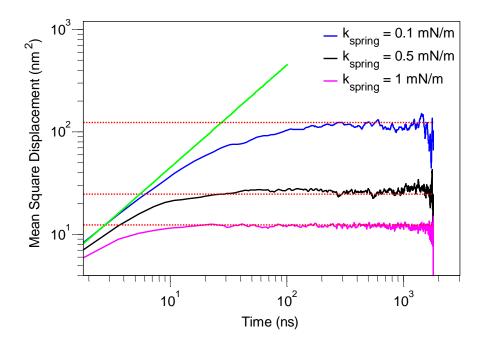


**Figure 4.20.** Mean square distance traveled by a particle as a function of time (log-log plot). The green line shows the diffusive limit of true evolution of mean square

displacement (Equation 4.153), and the red lines are the equilibrium limit for springs of different stiffness described by Equation 4.154.

Figure 4.21 shows the agreement between the cumulative distribution function for the mean square displacement of the simulated particle and the exact result obtained from the spring fluctuations described by a Gaussian distribution (Equation 4.155).

$$c.d.f. = -\sqrt{\frac{2k_{sp} r^2}{\pi k_B T}} \cdot \exp\left(-\frac{k_{sp} \cdot r^2}{2k_B T}\right) + erf\left(\sqrt{\frac{k_{sp} \cdot r^2}{2k_B T}}\right)$$
(4.155)

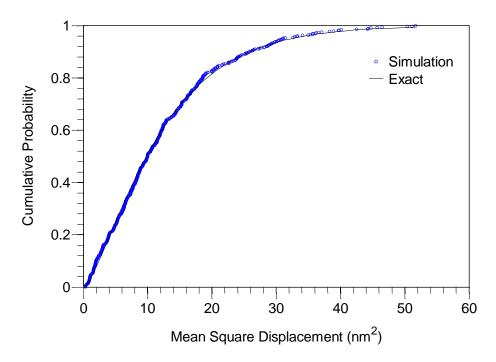


**Figure 4.21.** Cumulative distribution of mean square displacement for  $k_{sp} = 1$  mN/m after 0.72  $\mu$ s compared to the exact results given by Equation 4.155.

To implement an AFM probe in the simulations, the size of the last bead was altered so that its effects on thermal fluctuations were captured through the damping constant,  $\gamma$ . In selecting the size for the AFM probe, one has to ensure that it is large enough in comparison to the beads representing the FJC so that fluctuations of the force probe dominate those of the monomers.

# 4.5.14 Rate Dependence of Peeling Forces under Displacement Control

The Brownian dynamics studies discussed in this chapter that were simulated under displacement control were done so by varying the position of the AFM probe at a constant tip velocity:

$$v = \frac{dz}{dt} = b\frac{dn}{dt} \tag{4.156}$$

As derived previously (Equation 4.31),

$$\frac{dn}{dt} = J_0 \sinh\left(\frac{(f - \gamma)b}{2k_B T}\right) \tag{4.157}$$

By substituting Equation 4.157 into 4.156, and rearranging it, we find that:

$$F = \Gamma + 2\operatorname{arcsinh}\left(\frac{v}{bJ_o}\right) + 6\pi\eta a n v \tag{4.158}$$

where the last term is  $F_{drag}$  as described by Equation 4.20.

## 4.6 References

- (1) Prato, M.; Kostarelos, K.; Bianco, A., Functionalized carbon nanotubes in drug design and discovery. *Acc. Chem. Res.* **2008**, *41*, 60-68.
- (2) Liu, Z.; Tabakman, S. M.; Welsher, K.; Dai, H., Carbon nanotubes in biology and medicine: in vitro and in vivo detection, imaging, and drug delivery. *Nano Research* **2009**, *2*, 85-120.
- (3) Chen, Z.; Tabakman, S. M.; Goodwin, A. P.; Kattah, M. G.; Daranciang, D.; Wang, X.; Zhang, G.; Li, G.; Liu, Z.; Utz, P. J.; Jiang, K.; Fan, S.; Dai, H., Protein microarrays with carbon nanotubes as multicolor Raman labels. *Nature Biotechnology* **2008**, *26*, 1285-1292.
- (4) Liu, Z.; Chen, K.; Davis, C.; Sherlock, S.; Cao, Q.; Chen, X.; Dai, H., Drug delivery with carbon nanotubes for in vivo cancer treatment. *Cancer Res.* **2008**, *68*, 6652-6660.
- (5) Zheng, M.; Jagota, A.; Semke, E. D.; Diner, B. A.; Mclean, S. R. L.; Richardson, R. E.; Tassi, N. G., DNA-assisted dispersion and separation of carbon nanotubes. *Nature Materials* **2003**, *2*, 338-343.
- (6) Liu, Z.; Winters, M.; Holodniy, M.; Dai, H., siRNA delivery into human t cells and primary cells with carbon nanotube transporters. *Angew. Chem.* **2007**, *119*, 2069-2073.
- (7) Kam, N. W. S.; Liu, Z.; Dai, H., Functionalization of carbon nanotubes via cleavable disulfide bonds for efficient intracellular delivery of siRNA and potent gene silencing. *J. Am. Chem. Soc.* **2005**, *127*, 12492-12493.

- (8) Kam, N. W. S.; Liu, Z.; Dai, H., Nanotube molecular transporters: internalization of carbon nanotube-protein conjugates into mammalian cells. *J. Am. Chem. Soc.* **2004**, *126*, 6850-6851.
- (9) Welsher, K.; Liu, Z.; Daranciang, D.; Dai, H., Selective probing and imaging of cells with single walled carbon nanotubes as near-infrared fluorescent molecules. *Nano Letters* **2008**, *8*, 586-590.
- (10) Heller, D. A.; Jin, H.; Martinez, B. M.; Patel, D.; Miller, B. M.; Yeung, T. K.; Jena, P. V.; Hobartner, C.; Ha, T.; Silverman, S. K.; Strano, M. S., Multimodal optical sensing and analyte specificity using single-walled carbon nanotubes. *Nature Nanotechnology* **2008**, *4*, 114-120.
- (11) Strano, M. S.; Jin, H., Where is it heading? single-particle tracking of single-walled carbon nanotubes. *ACS Nano* **2008**, *2*, 1749-1752.
- (12) Liu, Z.; Li, X.; Tabakman, S. M.; Jiang, K.; Fan, S.; Dai, H., Multiplexed multicolor raman imaging of live cells with isotopically modified single walled carbon nanotubes. *J. Am. Chem. Soc.* **2008**, *130*, 13540-13541.
- (13) Zavaleta, C.; Zerda, A.; Keren, S.; Cheng, Z.; Schipper, M.; Chen, X.; Dai, H.; Gambhir, S. S., Noninvasive Raman spectroscopy in living mice for evaluation of tumor targeting with carbon nanotubes. *Nano Letters* **2008**, *8*, 2800-2805.
- (14) Zerda, A.; Zavaleta, C.; Keren, S.; Vaithilingam, S.; Bodapati, S.; Liu, Z.; Levi, J.; Smith, B. R.; Ma, T. J.; Oralkan, O.; Cheng, Z.; Chen, X.; Dai, H.; Khuri-Yakub, B. T.; Gambhir, S. S., Carbon nanotubes as photoacoustic molecular imaging agents in living mice. *Nature Nanotechnology* **2008**, *3*, 557-562.

- (15) Liu, Z.; Davis, C.; Cai, W.; He, L.; Chen, X.; Dai, H., Circulation and long-term fate of functionalized, biocompatible single-walled carbon nanotubes in mice probed by Raman spectroscopy. *PNAS* **2008**, *105*, 1410-1415.
- (16) Liu, Z.; Cai, W.; He, L.; Nakayama, N.; Chem, K.; Sun, X.; Chen, X.; Dai, H., In vivo biodistribution and highly efficient tumour targeting of carbon nanotubes in mice.

  Nature Nanotechnology 2007, 2, 47-52.
- (17) Smith, S. B.; Cui, Y.; Bustamante, C., Overstretching B-DNA: The Elastic Response of Individual Double-Stranded and Single-Stranded DNA Molecules. *Science* **1996**, *271*, 795-799.
- (18) Moy, V.; Florin, E.; Gaub, H., Intermolecular forces and energies between ligands and receptors. *Science* **1994**, *266*, 257-259.
- (19) Florin, E.; Moy, V.; Gaub, H., Adhesion forces between individual ligand-receptor pairs. *Science* **1994**, *264*, 415-417.
- (20) Manohar, S.; Jagota, A., Sequence-dependent force response during peeling of single-stranded DNA from graphite. *Physical Review E* **2010**, *81*, 021805.
- (21) Manohar, S.; Mantz, A. R.; Bancroft, K. E.; Hui, C.-Y.; Jagota, A.; Vezenov, D. V., Peeling Single-Stranded DNA from Graphite Surface to Determine Oligonucleotide Binding Energy by Force Spectroscopy. *Nano Letters* **2008**, *8*, 4365-4372.
- (22) Roxbury, D.; Tu, X.; Zheng, M.; Jagota, A., Recognition Ability of DNA for Carbon Nanotubes Correlates with Their Binding Affinity. *Langmuir* **2011**, *27*, 8282-8293.

- (23) Roxbury, D.; Manohar, S.; Jagota, A., Molecular Simulation of DNA β-Sheet and β-Barrel Structures on Graphite and Carbon Nanotubes. *The Journal of Physical Chemistry C* **2010**, *114*, 13267-13276.
- (24) Roxbury, D.; Jagota, A.; Mittal, J., Sequence-Specific Self-Stitching Motif of Short Single-Stranded DNA on a Single-Walled Carbon Nanotube. *Journal of the American Chemical Society* **2011**, *133*, 13545-13550.
- (25) Iliafar, S.; Wagner, K.; Manohar, S.; Jagota, A.; Vezenov, D., Quantifying Interactions between DNA Oligomers and Graphite Surface Using Single Molecule Force Spectroscopy. *The Journal of Physical Chemistry C* **2012**, *116*, 13896-13903.
- (26) Friedsam, C.; Gaub, H. E.; Netz, R. R., Adsorption energies of single charged polymers. *Europhys. Lett.* **2005**, *72*, 844-850.
- (27) Bhattacharya, S.; Milchev, A.; Rostiashvili, V., G.; Vilgis, T., A., Pulling an adsorbed polymer chain off a solid surface. *Eur. Phys. J. E* **2009**, *29*, 285-297.
- (28) Bhattacharya, S.; Rostiashvili, V. G.; Milchev, A.; Vilgis, T. A., Forced-Induced Desorption of a Polymer Chain Adsorbed on an Attractive Surface: Theory and Computer Experiment. *Macromolecules* **2009**, *42*, 2236-2250.
- (29) Bhattacharya, S.; Rostiashvili, V. G.; Milchev, A.; Vilgis, T. A., Polymer desorption under pulling: A dichotomic phase transition. *Physical Review E* **2009**, *79*, 030802.
- (30) Staple, D. B. G., M.; Hugel, T; Kreplak, L.; and Kreuzer, H. J., Forced desorption of polymers from interfaces. *New J. Phys.* **2011**, *13*.
- (31) Schlick, T., Molecular modeling and simulation: an interdisciplinary guide. In Springer: New York, 2002.

- (32) Kilina, S.; Tretiak, S.; Yarotski, D. A.; Zhu, J.-X.; Modine, N.; Taylor, A.; Balatsky, A. V., Electronic Properties of DNA Base Molecules Adsorbed on a Metallic Surface. *The Journal of Physical Chemistry C* **2007**, *111*, 14541-14551.
- (33) Staple, D. B.; Geisler, M.; Hugel, T.; Kreplak, L.; Kreuzer, H. J., Forced desorption of polymers from interfaces. *New J. Phys.* **2011**, *13*, 013025/1-013025/20.
- (34) Öttinger, H. C., Brownian dynamics of rigid polymer chains with hydrodynamic interactions. *Physical Review E* **1994**, *50*, 2696-2701.
- (35) White, T. O.; Ciccott, G.; Hansen, J.-P., Brownian dynamics with constraints. *Molecular Physics* **2001**, *99*, 2023-2036.
- (36) Greenberg, M. D., Advanced engineering mathematics. In Prentice Hall: 1997.
- (37) Sonnenberg, L.; Billon, L.; Gaub, H. E., Competitive Adhesion Reduces the Effective Bridging Length of Polymers. *Macromolecules* **2008**, *41*, 3688-3691.
- (38) Wagner, K.; Cheng, P.; Vezenov, D., Noncontact Method for Calibration of Lateral Forces in Scanning Force Microscopy. *Langmuir* **2011**, *27*, 4635-4644.
- (39) Pérez-López, B.; Merkoçi, A., Nanomaterials based biosensors for food analysis applications. *Trends in Food Science & Technology* **2011**, 22, 625-639.
- (40) Vezenov, D. V.; Noy, A.; Ashby, P., Chemical force microscopy: probing chemical origin of interfacial forces and adhesion. *Journal of Adhesion Science and Technology* **2005**, *19*, 313-364.
- (41) Bird, R. B., Stewart, W.E. and Lightfoot, E.N., *Transport Phenomena* 2ed.; John Wiley & Sons.: 2001.

# Chapter 5 In-plane force-extension response of a polymer confined to a surface

The work described in this chapter has been titled in "In-plane force-extension response of a polymer confined to a surface" by Sara Iliafar, Dmitri Vezenov, and Anand Jagota, Submitted.

The force-extension response of synthetic polymers and biomolecules governs properties such as bulk elasticity of rubbery materials and the behavior of DNA and several filamentous proteins. In several cases, such as DNA adsorbed on a plasma membrane, or polymers adsorbed onto a hard material, the molecule is confined to two dimensions as it extends under external forces (e.g., due to applied electric field). However, the force response in two dimensions is relatively poorly-studied. In this chapter, we present closed-form analytical expressions for the two-dimensional forceextension response of a freely-jointed chain under force control. Our principal results relate end-to-end distance to total force under two modes of stretching: i) when force is applied only to the free end of the chain, and ii) when the applied force is distributed uniformly throughout the chain. In both cases, we further propose explicit approximate expressions for force in terms of extension. Analytical results have been verified by Brownian dynamics simulation. We also show that the distributed force model agrees well with experimental measurements of stretching surface-adsorbed DNA by an electric field.

## 5.1 Introduction

It is well known that the elastic and viscoelastic behavior of polymers derives from the force-displacement response of individual macromolecules. Systems where elastic stretching of macromolecules occurs in three-dimensional (3D) settings are common and well-studied. Systems where polymer molecules are confined to a surface are important but less frequent and, perhaps for this reason, there are far fewer studies of stretching a molecule in two-dimensions.

For biological macromolecules such as DNA and polypeptides, the mechanical behavior of individual molecules plays an important physiological role. For this reason, numerous experimental studies have examined the 3D stretching of macromolecules via the use of atomic force microscopy and optical or magnetic tweezers, <sup>2-4</sup> electrophoretic stretching of DNA in uniform electric fields or flow, <sup>5,6</sup> stretching of DNA under alternating current field, 7,8 hydrodynamic focusing of multiple streams, and the effect of velocity gradient created by hydrodynamic flow in contracting and expanding channels.<sup>9, 10</sup> To complement the experimental findings that assess the 3D stretching of a polymer, many theoretical models 11-15 have been developed and computer simulations conducted using molecular dynamics and Monte Carlo approaches. 11, 12, 16, 17 Models range in complexity from the simple freely-jointed chain (FJC) and worm-like chain (WLC), 12, 16, 17 to all-atom representations in molecular dynamics. 18 Simpler models, such as the FJC and WLC, are particularly useful for interpretation and quantification of experiments by providing explicit closedform relationships between force and extension of the molecule. For example, it is well-known that the stretching of the freely jointed chain under force control is

governed by the Langevin function, <sup>16, 17</sup> and a similar approximate force-extension relationship is available for the worm-like chain. <sup>12</sup> Similarly, exact expressions relating force required to peel an FJC or a WLC from a substrate have been obtained. <sup>19-21</sup> However, much less work has been conducted on either analytical or the numerical aspects of stretching a chain-like molecule in 2D.

The 2D stretching of polymers occurs in systems such as polymers confined to the air-water interface<sup>22</sup> and combing of molecules via a meniscus alignment technique.<sup>23, 24</sup> In micro and nanofluidic systems, the transport of biopolymers such as DNA, RNA, and peptides has led to advances in gene and restriction mapping. <sup>25-29</sup> The stretching of biopolymers that are strongly adsorbed on a surface with one end fixed is often observed in systems involving separation of biomolecules via nanopillars and nanochannels. <sup>30-32</sup> <sup>33-35</sup> In a study by Mailer, et al., the 2D stretching response of DNA to an external electric field was investigated by tethering one end of the molecule and confining the entire molecule to the surface of a cationic lipid membrane. <sup>36</sup> While there has been a general lack of theoretical models for 2D stretching of chain-like molecules, in a recent study, Manca, et al., reported results for the stretching of a chain-like molecule due to a point and distributed forces both in 2D and 3D. <sup>37, 38</sup>

The principal results we present in this chapter are simple, closed-form expressions, obtained from a direct and transparent derivation, relating extension to force experienced by a freely jointed chain confined to a planar surface. In addition, we provide approximate inverse expressions for the force-stretch relationship that are often needed in practice, complement our analytical results by Brownian dynamics simulations, and validate the 2D results for distributed applied force by comparison to

experimental data. We expect that these results will be helpful to experimentalists for analyzing 2D stretching experiments.

#### 5.2 Methods

To complement and verify our analytical results, we conducted Brownian Dynamics simulations of freely jointed chains in 3D and confined to a flat 2D surface, with and without self-avoidance. We used a program described previously elsewhere; here we provide only a brief account. The freely jointed chain comprises N identical nodes connected by N-1 links. The vector form of the governing Brownian dynamics equation for bead i at position  $\mathbf{f}_i = (x_i, y_i, z_i)$  is written in terms of the viscous damping constant,  $\xi_i$  (kg/s), a random force,  $\mathbf{f}_i^r$ (N), and the potential energy of the system as a function of coordinates of each link E:

$$0 = -\xi_i \frac{d\mathbf{r}_i}{dt} + \mathbf{f}_i^r(t) - \nabla E_i(\mathbf{r}_i)$$
(5.1)

The potential energy includes (i) possible repulsion between beads to model self-avoidance, (ii) attractive interaction with a surface to model adsorption, and (iii) constraints to enforce fixed bond length. One end was immobilized on a surface and force was applied either to the other end or to all other beads. Force was applied either out-of-plane, in a direction normal to the surface, to model 3D stretching, or in-plane, to model 2D stretching.

When modeling 2D stretching, we included an adsorption potential in the model that was sufficiently strong to ensure that all beads were strongly adsorbed and their

motion confined to a frictionless surface. An adhesion free energy of  $12~k_BT$  per Kuhn length of the molecule was chosen based on our previous work representative of single-stranded DNA (ssDNA) as adequate for strong adsorption on a surface such as graphite.  $^{19,\,39}$ 

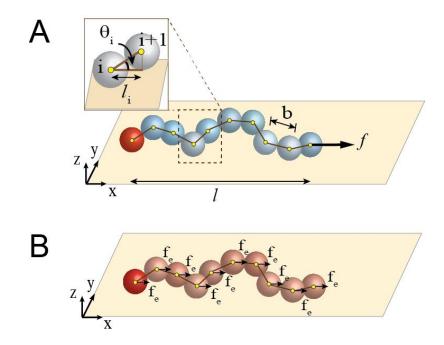


**Figure 5.1.** A schematic diagram of the freely jointed chain adsorbed on a solid substrate. The polymer chain is fixed to a point on the surface at one end (red node) and force is applied to the opposite end (A) or uniformly to each node (B). The molecule is represented by identical nodes, connected by freely jointed links.

## **5.3 Results and Discussions**

# 5.3.1 Force-displacement response of a freely jointed chain in 2D

The Langevin function relates average stretch of a freely jointed chain to applied force,

f. This relationship is derived under constraints of fixed force and temperature. A

similar approach in 2D also yields closed form results. Consider the Helmholtz free energy of the externally loaded FJC:

$$A = U - T S - f l \tag{5.2}$$

where  $l = \sum_{i=1}^{N} l_i = \sum_{i=1}^{N} b \cos \theta_i$  is the end-to-end distance of the chain, with b the Kuhn

length, i.e., the distance between nodes (Figure 5.1). Combining Eq. 5.2 with the fundamental equation for energy:

$$dU = -pdV + TdS + fdl (5.3)$$

we have:

$$dA = -S dT - p dV - l df$$

$$l = -\frac{\partial A}{\partial f}\Big|_{T,V} = -\frac{\partial}{\partial f} \left(-k_B T \ln Z\right)$$
(5.4)

where Z is the partition function for the FJC molecule. We need to consider only the conformational part of the partition function, since it is assumed that only orientation of the segments depends on force. <sup>17</sup> The conformational partition function  $Z_C$  is:

$$Z_C = \int w \exp(f l/k_B T) d\mathbf{q}$$
 (5.5)

where the integral is over all degrees of freedom that define the conformation of the molecule, and w is the density of states. For stretching of a FJC in 3D by a point force (pf) applied at the free end of a molecule, the extension-force relationship, which results from Eqs. 5.4 and 5.5, is well-known:  $^{17}$ 

$$L_{pf,3D} = \coth(F) - \frac{1}{F} \equiv \mathcal{Z}_{pf,3D}(F)$$
(5.6)

where,  $\mathcal{I}_{pf,3D}(F)$  is the Langevin function, and  $L = \frac{l}{Nb}$  and  $F = \frac{fb}{k_BT}$  are dimensionless molecular extension and applied force.

Consider now the stretching of an FJC by a point force, while keeping the other end fixed and confining the entire chain to a planar surface. The conformational partition function for the chain can be found by considering that in 2D each link, i, samples all orientations uniformly by angle,  $\theta_i$ , independently of all other links.

$$Z_{C,2D} = \int w_{2D} \exp(f l/k_B T) \prod_{i=1}^{N} d\theta_i$$
 (5.7)

Here, the integral sign represents N integrals, one for each of the N links in the chain, and  $w_{2D}$  is the density of states. Since the total length of this FJC is

$$l = \sum_{i=1}^{N} l_i = \sum_{i=1}^{N} b \cos \theta_i$$
, Eq. 5.7 can be rewritten as:

$$Z_{C,2D} = \int w_{2D} \exp\left(f \sum_{i=1}^{N} b \cos \theta_i / k_B T\right) \prod_{i=1}^{N} d\theta_i$$

$$= \int \prod_{i=1}^{N} w_{2D} \exp\left(f b \cos \theta_i / k_B T\right) d\theta_i$$
(5.8)

Because each integral is independent of the others, we have:

$$Z_{C,2D} = \left[ \int_{\theta=0}^{2\pi} w_{2D} \exp\left(f b \cos\theta / k_B T\right) d\theta \right]^N$$
 (5.9)

The integral in Eq. 5.9 evaluates as<sup>41</sup>

$$\int_{\theta=0}^{2\pi} w_{2D} \exp(f b \cos\theta / k_B T) d\theta = 2\pi w_{2D} I_o(F),$$
 (5.10)

where  $I_0(F)$  is the modified Bessel function of the first kind of order '0', resulting in:

$$Z_{C,2D} = [2\pi w_{2D} I_o(F)]^N$$
 (5.11)

Using this expression for the partition function, we obtain the free energy of the FJC in 2D:

$$A_{2D} = -k_B T \ln (Z_C) = -N k_B T \ln [2\pi w_{2D} I_o(F)]$$
 (5.12)

Under force control, we find that the end-to-end distance in the 2D case is given by:

$$L_{pf,2D} = \frac{l}{Nb} = \frac{1}{Nb} \left( -\frac{\partial A}{\partial f} \Big|_{T,V} \right) = \frac{I_1(F)}{I_o(F)} \equiv \mathcal{I}_{pf,2D}(F)$$
 (5.13)

where  $I_1(F)$  and  $I_0(F)$  are modified Bessel functions of the first kind, and  $\mathcal{Z}_{pf,2D}(F)$  is defined as the 2D equivalent of the Langevin function under a point force.

For completeness, one can also list the known result for a one-dimensional (1D) case:

$$L_{pf,1D} = \tanh(F) \equiv \mathcal{Z}_{pf,1D}(F) \tag{5.14}$$

Although it is difficult to imagine how this case would be realized experimentally, it is possible that the stretching of a biomolecule such as ssDNA that is tightly confined to a nanochannel may represent a situation that approximates this case.

In Figure 5.2A, we show that the force-displacement response in both the known 3D case (Eq. 5.6) and the 2D case (Eq. 5.13) match the results of Brownian dynamics simulations of a FJC with N=21. Figure 5.2B demonstrates good agreement between the simple analytical results, which neglect self-avoidance, and simulations that include a repulsive potential between beads to model self-avoidance. Not unexpectedly, it appears that the effect of self-avoidance is insignificant for such short polymers. Also, as expected, stretching in 1D requires less force than in 2D, and in 2D less than in 3D.<sup>22</sup>

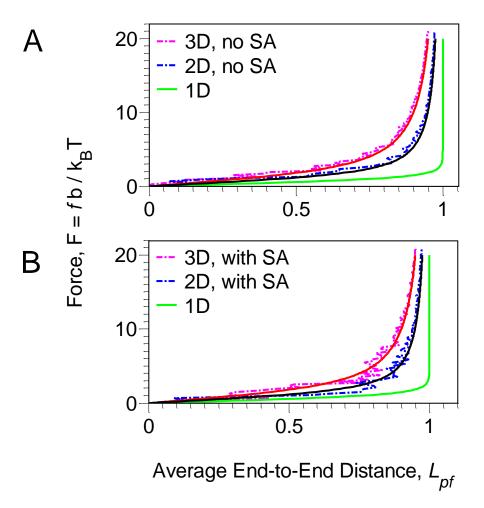


**Figure 5.2.** The force-displacement relationship for a freely jointed chain in 3D, 2D, and 1D under a point force. The solid curves represent the equilibrium results (equations 5.6, 5.13, and 5.14 for 3D, 2D, and 1D, respectively). The dashed lines are

results obtained via Brownian dynamics simulations carried out without (A) and with (B) self-avoidance and at slow-enough rates to occur in equilibrium.

## 5.3.2. Extension under an External Field

Stretching in 3D by force applied at the ends of the molecule is accomplished in numerous experiments that use force spectroscopy based on atomic force microscopy or optical/magnetic tweezers. In 2D, however, it is difficult to apply force only at the ends of the chain. Rather, most experiments employ a field, such as hydrodynamic flow or an electric field that acts on all the beads in the chain. For example, an electric field applied to ssDNA tethered at one end will result in about the same force being applied to each charged (phosphate) group.<sup>36</sup> For quantitative interpretation of such experiments, we extend the results obtained above to the case where force is distributed along the molecule backbone.

Consider an FJC with N beads and N-I total links subjected to a field that provides a force  $f_e$  on each bead. If each bead carries a (net or effective) charge q and the molecule resides in an electric field E, then  $f_e = qE$ ; if the molecule has N mobile beads, the total force is  $f = N f_e$ . Bead '1' is fixed but the remaining beads are free to move. Let  $l_j$  be the distance between bead j and j+1, projected in the direction of field (force) (see Figure 5.1A). Let  $L_i$  be the total distance from the fixed bead (bead '1') to bead 'i', i.e.  $L_i = \sum_{j=1}^i l_j$ . The fundamental energy equation now has work contributions due to the movement of each of the charged beads in the electric field:

$$dU = -pdV + TdS + f_e \sum_{j=1}^{N} dL_i$$

$$= -pdV + TdS + f_e dl_{\Sigma} ; \qquad l_{\Sigma} \equiv \sum_{i=1}^{N} L_i$$
(5.15)

where  $l_{\Sigma}$  is the sum of the projected lengths  $L_i$ 's. Following a Legendre transformation to switch to force control, we obtain:

$$dA = -S dT - p dV - l_{\Sigma} df_{e}$$

$$l_{\Sigma} = -\frac{\partial A}{\partial f_{e}} \Big|_{T,V}$$
(5.16)

To calculate the free energy A, we first need the conformational partition function, which is

$$Z_{C,2D} = \int w_{2D} \exp\left(\sum_{i=1}^{N} \frac{f_e L_i}{k_B T}\right) \prod_{j=1}^{N} d\theta_j .$$
 (5.17)

The argument of the Boltzmann factor, which has contributions from each of the mobile beads, can be written as

$$\sum_{i=1}^{N} \frac{f_{e} L_{i}}{k_{B}T} = \left(\frac{f_{e} L_{1} + f_{e} L_{2} + f_{e} L_{3} + ...}{k_{B}T}\right) = \frac{1}{k_{B}T} \begin{pmatrix} f_{e} b \cos \theta_{1} + \\ f_{e} b [\cos \theta_{1} + \cos \theta_{2}] + \\ f_{e} b [\cos \theta_{1} + \cos \theta_{2} + \cos \theta_{3}] + \\ ...... \end{pmatrix}$$

$$= \frac{1}{k_{B}T} \begin{pmatrix} N f_{e} b \cos \theta_{1} + \\ (N-1) f_{e} b \cos \theta_{2} + \\ (N-2) f_{e} b \cos \theta_{3} + \\ ..... + f_{e} b \cos \theta_{N} \end{pmatrix} = \sum_{i=1}^{N} \frac{(N-i+1) f_{e} b \cos \theta_{i}}{k_{B}T}$$
(5.18)

Substituting Eq. 5.18 into Eq. 5.17, we have:

$$Z_{C,2D} = \int w_{2D} \exp\left(\sum_{i=1}^{N} \frac{(N-i+1)f_{e}b\cos\theta_{i}}{k_{B}T}\right) \prod_{j=1}^{N} d\theta_{j}$$

$$= \prod_{i=1}^{N} w_{2D} \int_{0}^{2\pi} \exp\left(\frac{(N-i+1)f_{e}b\cos\theta_{i}}{k_{B}T}\right) d\theta_{i}$$
(5.19)

Considering that all angles are independent, the last equation can be rewritten as:

$$Z_{C,2D} = \prod_{i=1}^{N} w_{2D} \int_{0}^{2\pi} \exp\left(\frac{i f_e b \cos \theta_i}{k_B T}\right) d\theta_i$$
 (5.20)

By applying the identity of the modified Bessel functions of the first kind of order v

used previously in Eq. 5.10, 
$$^{41}I_{v}(z) = \frac{1}{2\pi} \int_{0}^{2\pi} \exp(z\cos\theta) \cdot \cos(v\theta) d\theta$$
 with  $z = \frac{i f_{e}b}{k_{B}T}$ ,

we find:

$$Z_{C,2D} = (2\pi w_{2D})^N \prod_{i=1}^N I_o(iF_e)$$
 (5.21)

$$F_e = f_e b/k_B T (5.22)$$

Using Eq. 5.16, we obtain for  $l_{\Sigma}$ :

$$A = -k_B T \ln \left( Z_{C,2D} \right) = -k_B T \left[ N \ln \left( 2\pi w_{2D} \right) + \sum_{i=1}^{N} \ln \left( I_o(iF_e) \right) \right]$$
(5.23)

$$l_{\Sigma} = \sum_{i=1}^{N} L_{i} = \sum_{i=1}^{N} \left( \sum_{j=1}^{i} l_{j} \right) = -\frac{\partial A}{\partial f_{e}} \bigg|_{T,V} = \sum_{i=1}^{N} ib \frac{I_{1}(iF_{e})}{I_{o}(iF_{e})}$$
 (5.24)

We can interpret  $l_{\Sigma}$  as:

$$l_{\Sigma} = \sum_{i=1}^{N} L_{i} = L_{N} + L_{N-1} + \dots + L_{2} + L_{1} =$$

$$= (l_{1} + l_{2} + \dots + l_{N-1} + l_{N}) + (l_{1} + l_{2} + \dots + l_{N-1}) + \dots + (l_{1} + l_{2}) + l_{1} =$$

$$= l_{N} + 2l_{N-1} + \dots + (N-1)l_{2} + Nl_{1} = \sum_{j=1}^{N} (N+1-j)l_{j}$$
(5.25)

Comparing Eqs. 5.24 and 5.25, we observe that:

$$l_{j} = b \frac{I_{1}([N+1-j]F_{e})}{I_{o}([N+1-j]F_{e})}$$
(5.26)

The physical interpretation of Eq. 5.26 can be given as follows. Although an equal magnitude of an external force,  $f_e$ , is applied to each bead, the effective force acting on each beads is determined by how far along the FJC each node is located at with respect to the direction of the force applied. In other words, while  $f_e$  is applied to the last bead 'N', twice the magnitude of  $f_e$  is applied to bead 'N-I', bead 'N-I' experiences three times the force  $f_e$ , and so on. The effective applied force on each bead 'f' (i.e. here f0 is obtained by evaluating Eqs. 5.9 through 5.13 and substituting the corresponding multiples of f0 for f1, so that:

$$l_{N} = b \frac{I_{1}(F_{e})}{I_{o}(F_{e})}; l_{N-1} = b \frac{I_{1}(2F_{e})}{I_{o}(2F_{e})} \quad \dots \quad l_{1} = b \frac{I_{1}(NF_{e})}{I_{o}(NF_{e})}$$
(5.27)

Of particular interest is the end-to-end distance of the chain,  $L_N$ , which is the projected distance from bead '1' to bead 'N' given by

$$l = L_{N} = (l_{1} + l_{2} + \dots l_{N}) = \sum_{i=1}^{N} b \frac{I_{1}(iF_{e})}{I_{o}(iF_{e})}$$

$$L_{ff,2D} = \frac{l}{Nb} = \frac{1}{N} \sum_{i=1}^{N} \frac{I_{1}(iF_{e})}{I_{o}(iF_{e})}$$
(5.28)

To compare the case where the force is distributed along the chain ( $f_e$  applied to each node) with the case where the force is applied only to the end (force f), let the total force in each case be the same, i.e. set  $f_e = f/N$ . In Figure 5.3, we show the force-displacement relationship obtained from Eqs. 5.13 and 5.28 is in close agreement with results of the corresponding Brownian dynamics simulations. As might be expected, for the same magnitude of the total force applied, the molecule will always be more extended when force is applied only to one end of the chain.

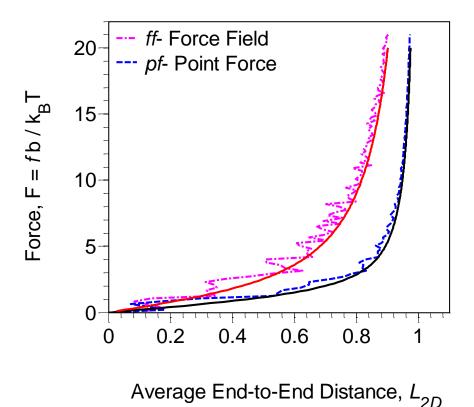


**Figure 5.3.** The force-displacement relationship for a non-self-avoiding freely jointed chain presenting the elastic response of the chain when it is stretched in 2D due to i) force applied to one end of the chain, *i.e.* point force (dashed blue line), and ii) a force field applied to the entire chain (dashed magenta line). The total force is the same in both cases. The stretching behavior of the chain is correctly predicted by I(E) = I(E/N)

 $L_{pf,2D} = \frac{I_1(F)}{I_o(F)} \text{ and } L_{ff,2D} = \frac{1}{N} \sum_{i=1}^N \frac{I_1(iF/N)}{I_o(iF/N)} \text{ as shown by the solid black and red lines, respectively.}$ 

In the limit of long chains, the force is distributed in very small quanta  $(F_e = F/N)$  as the number of Kuhn segments, N, increases to a large value. Then the summation in Eq. 5.28 can be converted to an integral:

$$l = b \sum_{i=1}^{N} \frac{I_1(iF_e)}{I_o(iF_e)} = b \int_{i=1}^{i=N} \frac{I_1(iF_e)}{I_o(iF_e)} di = \frac{b \ln(I_o(iF_e))}{F_e} \bigg|_{i=1}^{i=N}$$
 (5.29)

Therefore, the end-to-end distance of the chain becomes:

$$L_{ff,2D}(F) = \frac{l}{Nb} \to \frac{\ln(I_o(F))}{F} \equiv \mathcal{Z}_{ff,2D}(F)$$
(5.30)

Here,  $\mathcal{I}_{ff,2D}(F)$  is the equivalent of the Langevin function for the 2D case under a force field.

Maier, et al. measured the elastic response of  $\lambda$ -DNA confined to the surface of a cationic lipid membrane. The DNA was tethered at one end to an immobilized bead and subjected to external electric field of varying strength. The extension of the molecule in the direction of the field was measured. Numerical values extracted from their Figure 5.3 are compared with equation 30 in Figure 5.4. The experimental data were reported as the extension of the biopolymer,  $l = L_{ff,2D}Nb$  ( $\mu$ m) vs. electric field, E (V/cm). The molecule used in this experiment is double stranded DNA (dsDNA) with contour length,  $L_c = Nb$ , of  $20 \pm 1~\mu$ m (48502 base pairs, where each base pair has elongation length of 0.44 nm). Typically, dsDNA is modeled as a worm-like chain. However, by taking the Kuhn length, b, of this chain to be twice its persistence length ( $l_p = 65~\text{nm}^{36}$ ), one can treat the  $\lambda$ -DNA as a freely jointed chain. The applied force,  $f = Nf_e$  is defined in terms of electric field, E, as follows:

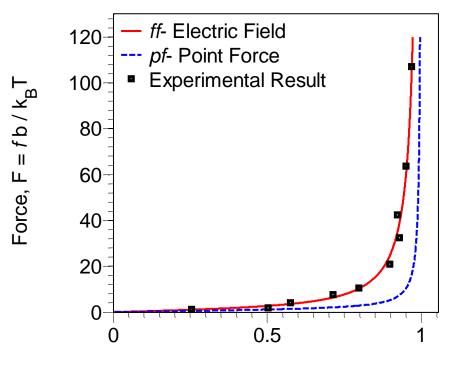
$$f = L_c q E \tag{5.31}$$

where, q is the effective electrophoretic line charge density reported to be  $0.6 \pm 0.1~e$  per Kuhn length in this experiment.<sup>36</sup> The experimentally reported electric field

strength values were converted into applied force, which was then non-dimensionalized

as  $F = \frac{f b}{k_B T}$ . It is apparent from Figure 5.4 that our analytical result for distributed

force, Eq. 5.30, is in excellent agreement with experiments with no adjustable parameters.



Average End-to-End Distance,  $L_{2D}$ 

**Figure 5.4.** The elastic response of a long freely jointed chain when it is stretched in 2D due to i) a force field applied to the entire chain e.g. under an electric field (solid line) predicted by  $L_{ff,2D} = \frac{\ln \left(I_o(F)\right)}{F}$ , and ii) force applied to one end of the chain, i.e. point force (dashed line) predicted by  $L_{pf,2D} = \frac{I_1(F)}{I_o(F)}$ . The experimental data<sup>36</sup>

(squares) for stretching  $\lambda$ -DNA confined to a surface and under an electric field closely follow the predicted results for the distributed force mode of stretching.

The stretching of molecules due to a distributed force is also important in applications where the molecule is permitted to adopt 3D conformations, as in gel electrophoresis and translocation of molecules through pores. For this reason, we used an approach similar to the 2D case above, to derive an expression for the 3D stretching of an FJC under a uniformly distributed force. We start with the general expression for the conformational partition function:

$$Z_{C,3D} = \int_{\phi=0}^{\phi=2\pi} \int_{\theta=0}^{\theta=\pi} \exp\left(\sum_{i=1}^{N} \frac{f_e L_i}{k_B T}\right) \prod_{i=1}^{N} w_{3D} \sin \theta_i d\theta_i d\phi_i$$
 (5.32)

which, using equation 5.18, 
$$\sum_{i=1}^{N} \frac{f_e L_i}{k_B T} = \sum_{i=1}^{N} \frac{\left(N - i + 1\right) f_e b \cos \theta_i}{k_B T} = \sum_{i=1}^{N} \frac{i f_e b \cos \theta_i}{k_B T}$$
, can

be transformed into:

$$Z_{C,3D} = -(w_{3D})^N \prod_{i=1}^N \int_{\theta=0}^{\theta=\pi} \exp\left(\frac{i f_e b \cos \theta_i}{k_B T}\right) \frac{d(\cos \theta_i)}{2}$$

$$Z_{C,3D} = (w_{3D})^N \prod_{i=1}^N \left(\frac{\sinh(iF_e)}{iF_e}\right) \qquad F_e = \frac{f_e b}{k_B T}$$
(5.33)

As before, conformational partition function defines the free energy of the FJC:

$$A = -k_B T \ln \left( Z_{C,3D} \right) = -k_B T N \ln \left( w_{3D} \right) - k_B T \sum_{i=1}^{i=N} \ln \left( \frac{\sinh \left( i F_e \right)}{i F_e} \right)$$
 (5.34)

Using Eq. 5.16, the sum of the total projected lengths,  $l_{\Sigma} \equiv \sum_{i=1}^{N} L_i = -\frac{\partial A}{\partial f_e}\Big|_{T,V}$ , can be calculated as:

$$l_{\Sigma} = \sum_{i=1}^{N} ib \left\{ \coth(iF_e) - \frac{1}{iF_e} \right\}$$
 (5.35)

To extract the experimentally measured end-to-end extension of the molecule, we use the same interpretation of changes in the effective force with bead position in a chain as described earlier for 2D stretching under a force field (Eqs. 5.26 and 5.27) and find (since  $l_i = b \left\{ \coth(iF_e) - \frac{1}{iF_e} \right\}$ ) that the projected length of the chain is:

$$L_{ff,3D} = \frac{l}{Nb} = \frac{1}{N} \sum_{i=1}^{N} \left\{ \coth(iF_e) - \frac{1}{iF_e} \right\}$$
 (5.36)

For very long molecules, the summation in Eq. 5.36 can again be converted into an integral:

$$L_{ff,3D} = \frac{1}{N} \int_{i=1}^{N} \left\{ \coth(iF_e) - \frac{1}{iF_e} \right\} di = \frac{1}{NF_e} \ln\left(\frac{\sinh(NF_e)}{N \cdot \sinh(F_e)}\right)$$

$$L_{ff,3D} = \frac{1}{F} \ln\left(\frac{\sinh(F)}{N \cdot \sinh(F/N)}\right)$$
(5.37)

For large molecules,  $\sinh(F/N) \rightarrow F/N$ , and Eq. 5.37 becomes:

$$L_{ff,3D} = \frac{1}{F} \ln \left( \frac{\sinh(F)}{F} \right) = \mathcal{Z}_{ff,3D}(F)$$
 (5.38)

where,  $\mathcal{I}_{ff,3D}(F)$  is the equivalent of the Langevin function for the 3D case under a force field.

# 5.3.2 Approximations to Explicit Force-Extension Relationships

The expressions that we have reported so far for the stretching of a chain are explicit in terms of force. However, it is often useful to know the force explicitly in terms of the normalized extension,  $L = \frac{l}{Nb}$ . An approximation for the inverse

Langevin function for point force stretching in 3D has been reported in the literature, 42

$$F_{pf,3D} = \mathcal{Z}_{3D}^{-1} \left( L_{pf,3D} \right) \approx L_{pf,3D} \cdot \left( \frac{3 - L_{pf,3D}^2}{1 - L_{pf,3D}^2} \right)$$
 (5.39)

Consider first the stretching behavior of the chain at the limits of small and large extensions. For small arguments in the 3D case under a point force, Eq. 5.6 can be approximated by using  $\coth(F) \approx \frac{1}{F} + \frac{F}{3}$ , and

$$F_{pf,3D} = 3L_{pf,3D}$$
 for  $F << 1$  (5.40)

Similarly, for small arguments in the 2D case under a point force (Eq. 5.14),

$$I_1(F) \approx F/2$$
;  $I_o(F) \approx 1$ . Therefore,

$$F_{pf,2D} = 2L_{pf,2D}$$
 for  $F \ll 1$  (5.41)

and, in the limit of low force, the 1D stretching relationship is approximated as:

$$F_{pf,1D} = L_{pf,1D}$$
 for  $F << 1$  (5.42)

Eqs. 5.40-5.42 show, as expected for Gaussian chains, that for small lengths the force-displacement relationship is governed by the system's dimensionality.<sup>43</sup> For small force, the force-extension relationship under a uniformly distributed force field is twice as large as that under a point force:

$$F_{ff,3D} = 6 L_{ff,3D}$$
 for  $F << 1$  (5.43)

$$F_{ff,2D} = 4 L_{ff,2D}$$
 for  $F << 1$  (5.44)

Using the asymptotic expression for the modified Bessel's functions of order  $\nu$  for large arguments:<sup>41</sup>

$$I_{\nu}(z) \approx \frac{e^{z}}{\sqrt{2\pi z}} \left( 1 + \frac{(1 - 2\nu) \cdot (1 + 2\nu)}{8z} \right)$$
 (5.45)

the 2D case under a point force (Eq. 5.13) for large forces can be expressed as:

$$L_{pf,2D}(F) = \frac{I_1(F)}{I_o(F)} \approx \frac{8F - 3}{8F + 1} \qquad \text{for } F >> 1$$
or
$$F_{pf,2D} = \frac{\left(3 + L_{pf,2D}\right)}{8\left(1 - L_{pf,2D}\right)} \qquad \text{for } F >> 1$$

A good approximation for the inverse 2D function that satisfies both limits (Eqs. 5.41 and 5.46) is:

$$F_{pf,2D} = \mathcal{Z}_{pf,2D}^{-1} \left( L_{pf,2D} \right) \approx \frac{L_{pf,2D} \left( 8 - L_{pf,2D} - 3L_{pf,2D}^2 \right)}{4 \left( 1 - L_{pf,2D}^2 \right)}$$
 (5.47)

However, the distributed force results, equations 5.30 and 5.38, do not have large-force limits that can be written as simple rational functions. Using Eq. 5.45 in 5.38 shows that, in the limit of large force,

$$L_{ff,3D} = \frac{1}{F} \ln \left( \frac{\sinh(F)}{F} \right) \rightarrow \frac{1}{F} \ln \left( \frac{\exp(F)}{F} \right) = 1 - \ln(F) / F;$$

$$1 - L \approx \ln(F) / F;$$

$$F \approx \frac{\ln(1/(1-L))}{(1-L)}$$
(5.48)

Using Eq. 5.48 in 5.30 shows that the force in the 2D distributed-force case also diverges as  $F \sim \frac{\ln(1/(1-L))}{(1-L)}$  as L approaches unity. However, this converges slowly to the exact result, and is not very useful as a guide to obtain an approximate inverse function that satisfies the limits of both small and large forces. Therefore, we adopt empirically the general form:

$$F = \frac{a L(b - L^2)}{(1 - L^2)}$$
 (5.49)

To ensure that the force-extension behavior of the chain for small arguments is satisfied, we set the limit of Eq. 5.49 for small arguments, i.e.  $F \approx ab L$ , equal to those limits given by Eqs. 5.43 and 5.44. By fitting Eq. 5.49 to the exact result in the range F < 50, we find values of a and b.

Figure 5.5 shows the exact and approximate inverse force-distance relationships obtained from both the Langevin functions and their inverse functions in 2D and 3D. We have collected all the results in Table 5.1 and indicated the maximum error of the inverse functions.

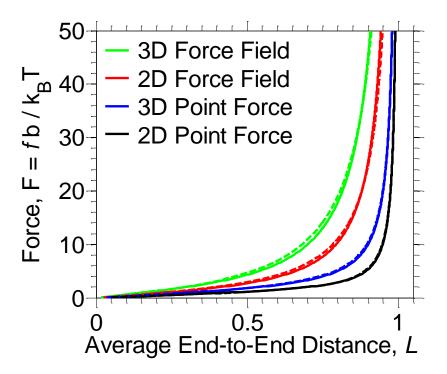


**Figure 5.5.** The force-displacement relationship for 3D and 2D elastic responses of a freely jointed chain. The solid curves represent the exact results; the dashed lines show the approximate inverse functions.

**Table 5.1.** Exact extension-force relations and approximations for inverse force-extension relations for a freely jointed chain in 2D & 3D, under point or distributed force.

		2D	3D
Point Force	L(F)	$L = \frac{I_1(F)}{I_o(F)}$ (Eq. 5.14)	$L = \coth(F) - \frac{1}{F}$ (Eq. 5.7)
		(Eq. 5.14) $F \approx \frac{L(8-L-3L^2)}{4(1-L^2)}$ (Eq. 5.50) $\varepsilon = 4.3 \%$ $F = 2 L$	$F \approx L \cdot \left(\frac{3 - L^2}{1 - L^2}\right)$ (Eq. 5.42) $\epsilon = 4.9 \%$
		for $L \to 0$ $F \approx \frac{(3+L)}{8(1-L)}$ for $L \to 1$	$F = 3L$ for $L \to 0$ $F \approx \frac{1}{1-L}$ for $L \to 1$
	L(F)	$L = \frac{\ln\left(I_o(F)\right)}{F}$ (Eq. 5.31)	$L = \frac{1}{F} \ln \left( \frac{\sinh(F)}{F} \right)$ (Eq. 5.40)
Force Field	F(L)	(Eq. 5.31) $F \approx \frac{3L(8/3 + L^2)}{2(1 - L^2)}$ (Eq. 5.52) $\varepsilon = 9.9 \%$ $F = 4 L$ for $L \rightarrow 0$	$F \approx \frac{4L(3/2 + L^2)}{(1 - L^2)}$ (Eq. 5.52) $\varepsilon = 9.9 \%$ $F = 6 L$ for $L \rightarrow 0$

# **5.4 Conclusions**

The 2D stretching of polymers and biomolecules often occurs during processes such as molecular combing (or meniscus alignment) and in separation techniques that use nanofluidic systems. In some cases, as in molecular combing, the applied force acts on

the chain at a single point at the air-water interface. On the contrary, when molecules are transported and separated in nanofluidic systems, often an electric field is applied across the sample. In this case, the total force is distributed over the entire molecule. To aid the quantitative analysis of such experiments, in this chapter, we have presented analytical expressions to describe the 2D and 3D stretching of a freely jointed chain under two modes of stretching: i) when force is applied only to one end of the chain, and ii) when the applied force is distributed uniformly throughout the chain. We have provided expressions that describe the force-extension relationship as force as a function of extension, as well as extension explicitly in terms of force. These formulas agree closely with results of the Brownian dynamics simulations and, in the case of stretching in 2D by distributed force, correctly describe experimental results.

## **5.5 References**

- (1) Treloar, L. R. G., *The Physics of Rubber Elasticity*. Oxford University Press: 2005.
- (2) Smith, S. B.; Cui, Y.; Bustamante, C., Overstretching B-DNA: the elastic response of individual double-stranded and single-stranded DNA molecules. *Science* **1996**, *271*, 795-9.
- (3) Simmons, R. M.; Finer, J. T.; Chu, S.; Spudich, J. A., Quantitative measurements of force and displacement using an optical trap. *Biophys. J.* **1996**, *70*, 1813-1822.
- (4) Cluzel, P.; Lebrun, A.; Heller, C.; Lavery, R.; Viovy, J.-L.; Chatenay, D.; Caron, F., DNA: an extensible molecule. *Science* **1996**, *271*, 792-4.
- (5) Perkins, T. T.; Smith, D. E.; Larson, R. G.; Chu, S., Stretching of a single tethered polymer in a uniform flow. *Science* **1995**, *268*, 83-7.
- (6) Ferree, S.; Blanch, H. W., Electrokinetic stretching of tethered DNA. *Biophys. J.* **2003**, *85*, 2539-2546.
- (7) Ueda, M., Dynamics of long DNA confined by linear polymers. *J. Biochem. Biophys. Methods* **1999**, *41*, 153-165.
- (8) Kaji, N.; Ueda, M.; Baba, Y., Stretching of megabase-sized deoxyribonucleic acid molecules by tuning electric-field frequency. *Appl. Phys. Lett.* **2003**, *83*, 3413-3415.
- (9) Wong, P. K.; Lee, Y.-K.; Ho, C.-M., Deformation of DNA molecules by hydrodynamic focusing. *J. Fluid Mech.* **2003**, *497*, 55-65.
- (10) Tegenfeldt, J. O.; Bakajin, O.; Chou, C.-F.; Chan, S. S.; Austin, R.; Fann, W.; Liou, L.; Chan, E.; Duke, T.; Cox, E. C., Near-field scanner for moving molecules. *Phys. Rev. Lett.* **2001,** *86*, 1378-1381.

- (11) Phillips, R.; Kondev, J.; Theriot, J., *Physical Biology of the Cell*. Garland Science: 2008.
- (12) Marko, J. F.; Siggia, E. D., Stretching DNA. *Macromolecules* **1995**, 28 8759-8770.
- (13) Hofmann, T.; Winkler, R. G.; Reineker, P., Dynamics of a polymer chain in an elongational flow. *Phys. Rev. E: Stat. Phys.*, *Plasmas, Fluids, Relat. Interdiscip. Top.* **2000,** *61*, 2840-2847.
- (14) Gross, P.; Laurens, N.; Oddershede, L. B.; Bockelmann, U.; Peterman, E. J. G.; Wuite, G. J. L., Quantifying how DNA stretches, melts and changes twist under tension. *Nat. Phys.* **2011**, *7*, 731-736.
- (15) Dai, L.; Liu, F.; Ou-Yang, Z.-C., Maximum-entropy calculation of the end-to-end distance distribution of force-stretched chains. *J. Chem. Phys.* **2003**, *119*, 8124-8132.
- (16) Flory, P. J., *Statistical mechanics of chain molecules*. Butterworth-Heinemann Ltd: 1969.
- (17) Rubinstein, M.; Colby, R. H., *Polymer Physics*. Oxford University Press New York, 2003.
- (18) MacKerell Jr., A. D.; Banavali, N. K., All-atom empirical force field for nucleic acids: II. application to molecular dynamics simulations of DNA and RNA in solution. *J. Comput. Chem.* **2000**, *21*, 105-120.
- (19) Iliafar, S.; Wagner, K.; Manohar, S.; Jagota, A.; Vezenov, D., Quantifying Interactions between DNA Oligomers and Graphite Surface Using Single Molecule Force Spectroscopy. *The Journal of Physical Chemistry C* **2012**, *116*, 13896-13903.

- (20) Manohar, S.; Jagota, A., Sequence-dependent force response during peeling of single-stranded DNA from graphite. *Physical Review E* **2010**, *81*, 021805.
- (21) Manohar, S.; Mantz, A. R.; Bancroft, K. E.; Hui, C.-Y.; Jagota, A.; Vezenov, D. V., Peeling Single-Stranded DNA from Graphite Surface to Determine Oligonucleotide Binding Energy by Force Spectroscopy. *Nano Letters* **2008**, *8*, 4365-4372.
- (22) Ramírez, P.; Stocco, A.; Muñoz, J.; Miller, R., Interfacial rheology and conformations of triblock copolymers adsorbed onto the water–oil interface. *Journal of Colloid and Interface Science* **2012**, *378*, 135-143.
- (23) Petit, C. A. P.; Carbeck, J. D., Combing of Molecules in Microchannels (COMMIC): A Method for Micropatterning and Orienting Stretched Molecules of DNA on a Surface. *Nano Letters* **2003**, *3*, 1141-1146.
- (24) Bensimon, D.; Simon, A. J.; Croquette, V.; Bensimon, A., Stretching DNA with a Receding Meniscus: Experiments and Models. *Physical Review Letters* **1995**, *74*, 4754-4757.
- (25) Reisner, W.; Larsen, N. B.; Silahtaroglu, A.; Kristensen, A.; Tommerup, N.; Tegenfeldt, J. O.; Flyvbjerg, H., Single-molecule denaturation mapping of DNA in nanofluidic channels. *Proc. Natl. Acad. Sci. U. S. A.* **2010,** *107*, 13294-13299.
- (26) Randall, G. C.; Schultz, K. M.; Doyle, P. S., Methods to electrophoretically stretch DNA: microcontractions, gels, and hybrid gel-microcontraction devices. *Lab Chip* **2006**, *6*, 516-525.
- (27) Mueller, O.; Hahnenberger, K.; Dittmann, M.; Yee, H.; Dubrow, R.; Nagle, R.; Ilsley, D., A microfluidic system for high-speed reproducible DNA sizing and quantitation. *Electrophoresis* **2000**, *21*, 128-134.

- (28) Riehn, R.; Lu, M.; Wang, Y.-M.; Lim, S. F.; Cox, E. C.; Austin, R. H., Restriction mapping in nanofluidic devices. *Proc. Natl. Acad. Sci. U. S. A.* **2005**, *102*, 10012-10016.
- (29) Ueberfeld, J.; McKenna, B.; Rubin-Bejerano, I.; Verstrepen, K.; Ehrlich, D. J., Reaction-Mapped Quantitative Multiplexed Polymerase Chain Reaction on a Microfluidic Device. *Anal. Chem.* **2008**, *80*, 7430-7436.
- (30) Kim, Y.; Kim, K. S.; Kounovsky, K. L.; Chang, R.; Jung, G. Y.; de, P. J. J.; Jo, K.; Schwartz, D. C., Nanochannel confinement: DNA stretch approaching full contour length. *Lab Chip* **2011**, *11*, 1721-1729.
- (31) Wang, G. M.; Sandberg, W. C., Non-equilibrium all-atom molecular dynamics simulations of free and tethered DNA molecules in nanochannel shear flows.

  Nanotechnology 2007, 18, 135702/1-135702/9.
- (32) Reisner, W.; Pedersen, J. N.; Austin, R. H., DNA confinement in nanochannels: physics and biological applications. *Rep. Prog. Phys.* **2012**, *75*, 106601/1-106601/34.
- (33) Lin, P.-K.; Lin, K.-h.; Fu, C.-C.; Lee, K. C.; Wei, P.-K.; Pai, W.-W.; Tsao, P.-H.; Chen, Y. L.; Fann, W. S., One-dimensional dynamics and transport of DNA molecules in a quasi-two-dimensional nanoslit. *Macromolecules* **2009**, *42*, 1770-1774.
- (34) Yasui, T.; Kaji, N.; Ogawa, R.; Hashioka, S.; Tokeshi, M.; Horiike, Y.; Baba, Y., DNA Separation in Nanowall Array Chips. *Anal. Chem.* **2011**, *83*, 6635-6640.
- (35) Krishnan, M.; Mönch, I.; Schwille, P., Spontaneous Stretching of DNA in a Two-Dimensional Nanoslit. *Nano Letters* **2007**, *7*, 1270-1275.
- (36) Maier, B.; Seifert, U.; Radler, J. O., Elastic response of DNA to external electric fields in two dimensions. *Europhys. Lett.* **2002**, *60*, 622-628.

- (37) Kierfeld, J.; Niamploy, O.; Sa-yakanit, V.; Lipowsky, R., Stretching of semiflexible polymers with elastic bonds. *Eur. Phys. J. E* **2004**, *14*, 17-34.
- (38) Manca, F.; Giordano, S.; Palla, P. L.; Cleri, F.; Colombo, L., Theory and Monte Carlo simulations for the stretching of flexible and semiflexible single polymer chains under external fields. *J. Chem. Phys.* **2012**, *137*, 244907/1-244907/12.
- (39) Iliafar, S.; Vezenov, D.; Jagota, A., Brownian Dynamics Simulation of Peeling a Strongly-Adsorbed Polymer Molecule from a Frictionless Substrate. *Langmuir* **2013**, *29*, 1435-1445.
- (40) Huang, J.; Schlick, T., Macroscopic modeling and simulations of supercoiled DNA with bound proteins. *Journal of Chemical Physics* **2002**, *117*, 8573-8586.
- (41) Abramowitz, M. S., I. A., *Handbook of Mathematical Functions*. Courier Dover Publications: 1954
- (42) Cohen, A., A Pade approximant to the inverse Langevin function. *Rheologica Acta* **1991**, *273*, 270-273.
- (43) Boal, D., Mechanics of the Cell. Cambridge University Press: 2001.

Chapter 6 Future Work: Exploratory Studies on the Effect of Surface Friction on the Removal Dynamics of a Polymeric Chain from a Graphitic Surface

#### 6.1 Introduction

In developing micro- and nano-electromechanical systems, the size of electronic and mechanical devices has been shrinking down to the nanometer scale, where the performance of these systems begins to be dominated by surface forces. Despite extensive studies on the impact of friction, wear, and lubrication at the macroscopic scale, atomic scale tribology is a relatively new field. Recent advances in experimental techniques such as quartz crystal microbalance (QCM)<sup>1</sup> and friction force microscopy (FFM)<sup>2</sup> have enabled nanotribological research. Analogus to our interest and justification in the studies described in this dissertation, the paradigm of the nanotribological field is based on the notion that it is necessary to investigate the frictional behavior of a single asperity contact in order to gain insight into the macroscopic frictional behavior of systems. Although most nanotribological studies have been conducted on atomically flat substrates and using FFM.<sup>3-6</sup> there have been some experiments in which the tip apex consisting of only a few atoms is dragged across atomic-scale surface steps. <sup>7-9</sup> The collection of these frictional studies have shown dependence on temperature, surface composition and roughness, applied force, tip velocity, and even the direction of movement of the tip.

Friction, or the total dissipated energy from all the micro- and nano-contacts that occur due to sliding of two macroscopic surfaces over one other, is characterized

by a multitude of phenomena including the stick—slip behavior, <sup>10</sup> surface roughness, <sup>11</sup>, <sup>12</sup> geometric interlocking and interlocking mediated by so-called third bodies, <sup>13</sup> and rupture of bonds, <sup>14</sup> etc. Although these phenomena are regularly observed on most surfaces, even on those covered with alkylsilane self-assembled monolayer (SAM) lubricants, <sup>15, 16</sup> frictional forces on the atomically flat graphite and mica are known to be quite small. <sup>2</sup> Frictional interaction between individual molecules and surfaces is another area of interest. To probe these interactions, scientists can modify the FFM technique by the covalent attachment of single molecules to the AFM probe. Similar to lateral forces of an AFM probe on graphite, the frictional barrier for the lateral movement of molecules such as DNA oligomers on graphite has been shown to be quite small (< 2 k<sub>B</sub>T per base). <sup>17-19</sup> For this reason, in our single molecule force spectroscopy (SMFS) studies and models, we have always assumed these interactions to be sufficiently weaker than binding strength to be negligible.

Interestingly, however, the peeling of polythymine on 3aminopropyltriethoxysilane (APTES)-modified silicon wafer and polyguanine on
graphite have shown a stretching behavior in our SMFS experiments. Assuming the
lateral friction to be negligible, we have previously attributed this stretching behavior to
be due to fixation of the molecule on the substrate. Upon increasing the applied force,
the portion of the molecule connecting the AFM probe to the fixed point on the surface
becomes completely stretched out until it eventually retracts spontaneously. Motivated
by this observation, we became interested in studying the effect of surface friction on
the peeling behavior of molecules by asking the following questions: what if the source
of this stretching behavior is analogous to that in the stick-slip phenomena? Could the

vertical interactions between the molecule and the substrate result in strong contacts that would fixate the molecule on the surface? We used Brownian dynamics simulations to address these questions. The details of our theoretical approach this problem are discussed in the following sections.

## 6.2 Methods

In previous studies, we explored 3D and 2D Brownian dynamics simulations for stretching a freely jointed chain strongly adsorbed to a flat surface.<sup>20</sup> These simulations shed light on effects of tip velocity, peeling mode and dimensionality, thermal noise and spring constant contributions, etc. on the elastic response of the molecule. In this new work, we use the same program with a few modifications to introduce graphitic surface corrugations. To briefly describe the structure of our model, the freely jointed chain is made of N identical nodes linked by N-1 links. The Brownian dynamics equation governing this system in vector is given by:

$$0 = -\xi_i \frac{d \mathbf{r}_i}{dt} + \mathbf{f}_i^r(t) - \nabla E_i \left( \mathbf{r}_i \right)$$
(6.1)

where i is the bead number,  $\mathbf{f}_i = (x_i, y_i, z_i)$  the bead position,  $\xi_i$  (kg/s) the viscous damping constant,  $\mathbf{f}_i^r$  (N) a random force, and E the potential energy of the system as a function of coordinates of each link.<sup>20</sup> The segment length for each link, b, was then forced to remain constant throughout the progression of the simulation in time.

The interactions of bead n with the flat substrate was based on the Lennard Jones potential and obtained to be:

$$\phi_n(z_n) = \frac{\phi_{\min}}{2} \left( \frac{z_{\min}^9}{z_n^9} - \frac{3z_{\min}^3}{z_n^3} \right)$$
 (6.2)

with  $\phi_{\min}$  being the depth of, and  $z_{\min}$  the location of the potential well. The magnitude of  $z_{\min}$  (5Å) and  $\phi_{\min}$  were chosen based on typical values for DNA nucleotides adsorbed on graphite. <sup>21-23</sup>

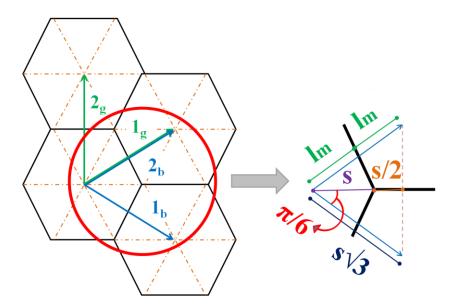


**Figure 6.1.** Pictorial presentation of a graphene-like surface, divided into subunits to create two new frames of reference, labeled in subscripts g and b.

To introduce graphitic surface corrugations, we modify the expression defining the surface potential energy (Eq. 6.2) to include dependencies in the x-y directions as well. Here, the x- and the y-axis refer to the horizontal and the vertical axis of a two-dimensional Cartesian coordinate system, respectively. Since a graphene-like surface has hexagonal periodicity, which itself is made of axisymmetric, identical inner triangles (Figure 6.1), we must first define new axes for our new frame of reference. Marked in numbers one through four on Figure 1, we identify the new axes of our plane. Note that for the purpose of simplicity, we use two sets of codirectional vectors, where vectors two and three are identical. Given that each side of any given hexagon has the length s, then the sides of each inner triangle is also going to be s long. Physically, the parameter s is the carbon-carbon bond length in a graphene sheet, which is smaller than or on the order of 1.42 Å.  $^{24-27}$  Assuming that the length of the unit vector that bisects each inner triangle is  $l_m$ , we can obtain comparative length information using simple trigonometric relations. Therefore, we find that the length of each unit vector is:

$$2l_m = 2s\cos\left(\frac{\pi}{6}\right) = s\sqrt{3} \tag{6.1}$$

The Cartesian components of these unit vectors (i.e. the x and y dependencies  $\hat{i}$  and  $\hat{j}$ ) are then normalized through division by  $s\sqrt{3}$ . We define each unit vector with  $\hat{e}_{n,r}$ , where n identifies the vector number and r identifies the frame of reference. As an example, let us consider unit vector  $1_b$ ,  $\hat{e}_{1b}$ , where the x-component is defined as  $\hat{e}_{1b,x}$  and the y-component as  $\hat{e}_{1b,y}$ :

$$\hat{e}_{1b,x} = \frac{3}{2}s \xrightarrow{Normalized} \hat{e}_{1b,x} = \frac{\sqrt{3}}{2}\hat{i}$$

$$239$$

$$(6.2 a)$$

$$\hat{e}_{1b,y} = -\frac{\sqrt{3}}{2}s \xrightarrow{Normalized} \hat{e}_{1b,y} = -\frac{1}{2}\hat{j}$$
 (6.2 b)

Similarly, unit vector  $2_b$  (identical to unit vector  $1_g$ ) can be described by:

$$\hat{e}_{2b,x} = \frac{3}{2}s \quad \xrightarrow{Normalized} \quad \hat{e}_{2b,x} = \frac{\sqrt{3}}{2}\hat{i}$$
 (6.3 a)

$$\hat{e}_{2b,y} = \frac{\sqrt{3}}{2} s \xrightarrow{Normalized} \hat{e}_{2b,y} = \frac{1}{2} \hat{j}$$
 (6.3 b)

And, unit vector 2<sub>g</sub> becomes:

$$\hat{e}_{2g,x} = 0 \xrightarrow{Normalized} \hat{e}_{2g,x} = 0\hat{i}$$
 (6.4 a)

$$\hat{e}_{2g,y} = \sqrt{3}s \xrightarrow{Normalized} \hat{e}_{2g,y} = 1\hat{j}$$
 (6.4 b)

To define new non-Cartesian axes, identifying the covariant and contravariant components are essential. Covariant components,  $P_{n,r}$ , are obtained from the general expression:

$$P_{n,r}(x,y) = \overline{P}(x,y) \cdot \hat{e}_{n,r} \tag{6.5}$$

As before, n identifies the vector number and r identifies the frame of reference.

 $\overline{P}(x, y)$  is any given point on the plane defined by the Cartesian coordinate system. The contravariant components,  $P_r^n$ , are then defined as:

$$P_r^n(x,y) = [g^{ij}] \{P_{n,r}(x,y)\}$$
(6.5)

where  $[g^{ij}]$  is the inverse metric tensor  $[g_{ij}]$ :

$$[g^{ij}] = [g_{ij}]^{-1} = [\hat{e}_i \cdot \hat{e}_j]^{-1}$$

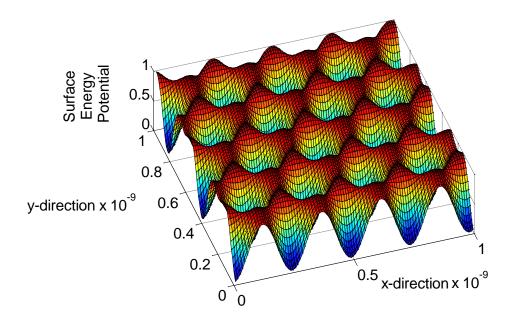
$$\therefore [g^{ij}] = \begin{bmatrix} 1 & \frac{1}{2} \\ \frac{1}{2} & 1 \end{bmatrix}^{-1} = \begin{bmatrix} \frac{4}{3} & -\frac{2}{3} \\ -\frac{2}{3} & \frac{4}{3} \end{bmatrix}$$

$$(6.6)$$

As presented in Figure 6.2, the potential energy of a two dimensional graphitic surface,  $\phi(x, y)$ , in terms of the new unit vectors becomes:

$$\phi(x,y) = \left(1 - \cos\left(\frac{2\pi P_b^1(x,y)}{2l_m}\right)\right) + 2\left(2 - \cos\left(\frac{2\pi P_b^2(x,y)}{2l_m}\right) - \cos\left(\frac{2\pi P_g^1(x,y)}{2l_m}\right)\right) + \left(1 - \cos\left(\frac{2\pi P_g^2(x,y)}{2l_m}\right)\right)$$

(6.7)



(a)

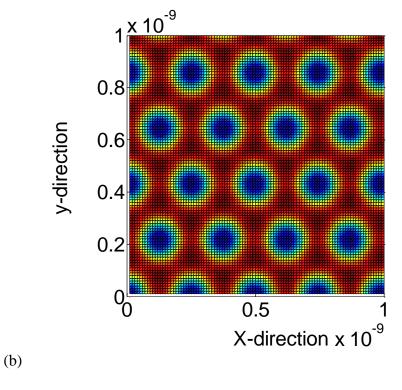


**Figure 6.2.** The normalized corrugated surface potential of a graphitic surface, with hexagonal repeating unit cells, over the planar surface (in the x-y directions) viewed from an angle (a) and directly from the top (b). A Carbon-Carbon bond length of 1.42 Å was used.

By combining the planar surface energy potential,  $\phi(x, y)$ , with our previously-derived expression for the vertical interactions of a bead with a flat surface,  $\phi(z)$ , (Eq. 6.2), the total potential energy of any given bead for the FJC interacting with this corrugated surface (Figure 6.3), can be written as:

$$\phi_{total}(x, y, z) = \phi(z) \{1 - \alpha \phi(x, y)\}$$
(6.8)

where  $\alpha$  is a surface undulation parameter through which the energy barrier height can be adjusted.

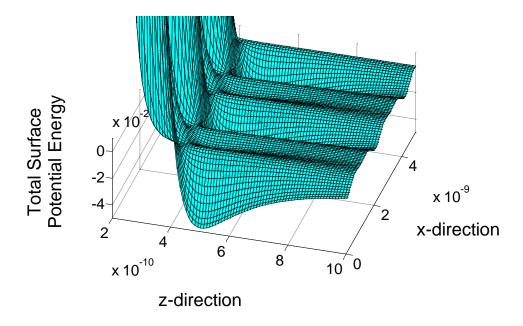


**Figure 6.3.** The total surface energy potential for a bead interacting with a corrugated surface such as graphene shown as a function of x- and z-. In this schematic presentation of the surface potential energy,  $\alpha$  was set to 1,  $\phi_{\min}$  to 12 k<sub>B</sub>T, and  $z_{\min}$  to 0.25 nm.

As shown in Figure 6.3, the effects of surface corrugations are expected to be maximized when the molecule is closest to the minima and to disappear at distances far from the surface. Furthermore, when the modification parameter is at zero value, the Brownian dynamics simulations should reproduce the equilibrium results predicted by the statistical model and confirmed by our previous theoretical work. To make this comparison possible, the freely jointed chain used in our new studies was 20 monomeric units long, with the first bead fixed on the by a stiff spring. All removal events were conducted under force control and in the vertical direction, away from the

surface, unless specified otherwise. In the next section, we discuss our specific studies of interest and our work completed so far.

#### **6.3 Results and Discussions**

Single molecule force spectroscopy experiments on single stranded DNA molecules are performed by applying an external force to one end of the molecule in the vertical direction and away from the sample surface. These experiments typically show flat peeling force plateaus, which have been interpreted as the removal of an individual molecule from the surface in equilibrium conditions. Although all experiments are conducted under the same peeling velocities, some sequences such as polyguanine show stretching as well as peeling behavior, which is indicative of fixation of the molecule at some contact points on the surface. Such fixations, as a result, move the peeling process out of equilibrium and result in higher pull-off forces for the same sequence.

In the simulations described in this chapter, we are interested to explore the role of surface friction in the SMFS experiments. For example, could surface friction result in stretching behavior in a peeling molecule similar to that observed often for polyguanine? To address this main question, we propose multiple studies by posing the following questions: 1) How do graphitic surface corrugations affect the equilibrium peeling of a polymeric molecule from the substrate? 2) At high surface corrugations, does the effective binding of the molecule to the surface enhance, reduce, or remain unaffected? And lastly, 3) are the SMFS peeling experiments in which a molecule is

pulled out of the plane of the substrate a reliable method for identifying the true binding strength of the molecule to that substrate?

To begin our studies, it is important to first equilibrate the molecular conformation of the FJC on a flat surface. This process is critical for obtaining accurate peeling behavior as well as improving the performance and speed of the Brownian dynamics simulations. The planar- as well as the side- view of one of the equilibrium conformations after 0.903 microseconds for a 20-mer long FJC with a low binding strength to a flat surface (2 k<sub>B</sub>T per Kuhn link) is shown in Figure 6.4 (a-b). To confirm that 0.903 microseconds was long enough to reach equilibrium, we considered the average dimensionless end-to-end distance of this chain over time and compared its mean value with the expected mean end-to-end distances of a 3D Gaussian chain in equilibrium (Figure 6.4 c). This expected dimensionless mean value was estimated to  $be\left(\frac{R_{ee} \cdot R_{ee}}{b^2}\right)^{\frac{1}{2}} = \sqrt{N} = 4.5$ , which, not surprisingly, is slightly different than the actual mean of the ensemble, given that this short chain is interacting with a surface and

may not be completely in its 3D conformation.

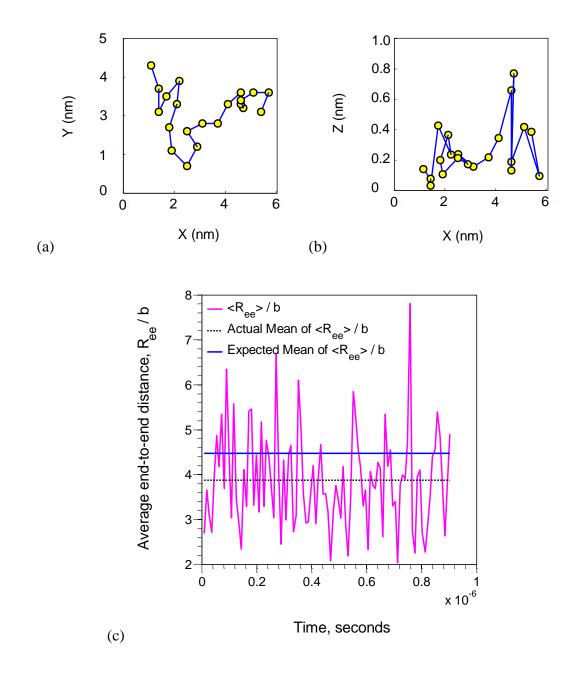


**Figure 6.4.** (a-b) Molecular conformation of a 20-mer long FJC, interacting with a flat surface with a binding strength of 2 kBT per Kuhn link, equilibrated for 0.903 microseconds shown from above as well as the side. (c) The dimensionless average end-to-end distance,  $R_{ee}/b$ , of this molecule over time shows that equilibrium was reached quickly.

As mentioned earlier, the frictional barrier for ssDNA nucleobases on graphite are known to be quite small, and graphite is typically identified as a frictionless substrate. Therefore, we simulated the equilibrium peeling (1.44 mm/s) of a polymeric chain with a binding strength comparative to the experimentally obtained measurements for polythymine (11.3  $k_BT$  per nucleotides), from our newly-modeled graphitic surface. The term 'binding strength' here refers to the free energy required to desorb a link in a 2D-FJC-state from a flat surface, i.e. in the absence of surface undulations, into a 3D-FJC-state in solution. In our simulations, the magnitude of this binding strength is implemented through  $\phi_{min}$ .

In this first study, the surface undulation parameter,  $\alpha$ , was adjusted from 0 to 0.5 to 1 to vary the height of the surface energy barriers. At  $\alpha=0$ , the surface undulations are absent and, therefore, the surface is (energetically) flat. For this reason, the molecule is expected to have the same peeling behavior as our previously published result for peeling a molecule of the same length and binding energy from a flat surface. The overlapping of the force-distance curves, shown in Figure 6.5, for peeling the molecule from a flat surface versus an undulated surface with  $\alpha=0$ , compared to the analytically predicted results confirms this expectation.

Interestingly, increasing the surface undulations result in 1) an increase in the mean surface potential energy, and 2) appearance of small steps in the flat region of the peeling plateaus. Note that neither of these changes may be detectable experimentally. Specifically, the appearance of small steps in the flat peeling plateaus may be masked due to the low spring constant of the soft contact mode cantilevers, the AFM probe

thermal fluctuations, and the averaging of data in SMFS experiments. In other words, surface undulations or surface friction might not necessary result in appearance of new features in the experimental force plateaus, a behavior we have expected to observe. Therefore, it is not surprising that most ssDNA homopolymers appear to only show flat peeling plateaus upon their removal from *graphite*. Instead, these physical features may shift the force up or down in comparison to those obtained from flat surfaces i.e. in the absence of surface undulations. However, since an undulating surface has a different mean potential energy in comparison to a flat surface, a correct comparison should be made by considering the Boltzmann weighted mean potential energy of the system averaged over the entire surface.

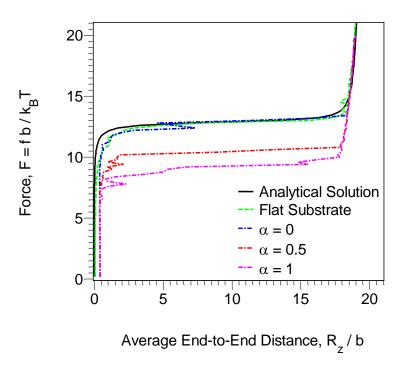


**Figure 6.5.** Effect of surface undulations,  $\alpha$ , on the equilibrium force—displacement relationship in force-controlled peeling. Simulations at  $\phi_{\min} = 12 \ k_B T$  are shown as dashed lines lines, and the analytically predicated result for a flat surface  $(\alpha = 0)$  as a solid black line.

In our next study, we were interested to investigate the effect of maximum surface undulation  $(\alpha=1)$  on the surface effective or mean binding strength for molecules with different free energy of binding per nucleotide  $(\phi_{\min})$ . In Figure 6.6, we compare the results of this study (dashed lines) with those obtained from the interactions of the same molecule with a flat surface  $(\alpha=0)$  (solid lines). At maximum surface undulations, increasing the adhesiveness of the molecule to the surface increases the peeling forces, until they eventually become much larger than the forces required to remove the molecule from a flat surface. Note that the presence of surface undulations alter the binding energy of the molecule to the surface. Therefore, as mentioned before, a more accurate comparison for this result would be to consider the data shown in Figure 6.6 with the corresponding Boltzmann weighted mean potential energy of the system averaged over the entire surface.

A second interesting observation is the magnification of the steps that appear in the peeling plateaus for stickier molecules. As before, it is not surprising if these features are not experimentally detectable.

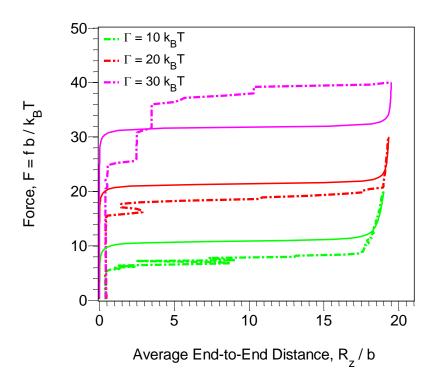


**Figure 6.6.** Effect of surface adhesion,  $\Gamma$ , on the equilibrium force—displacement relationship in force-controlled peeling in the presence of maximum surface undulations (dotted lines) compared to those from a flat surface (solid lines).

The non-equilibrium removal dynamics of a polymeric molecule from a flat surface was previously established to be highly dependent on stokes drag as well as desorption rate of individual bases, resulting in higher peeling forces than expected from the equilibrium model. To investigate whether the higher forces observed for removing stickier molecules from a highly undulated surface (Figure 6.6) are a direct consequence of interactions with these surface undulations or indirectly caused by deviations from equilibrium, we next simulated the peeling of a molecule with the free energy of binding of  $12 \, k_B T$  per nucleotide from a highly undulated surface, but this

time at different removal rates. We then compared the results of this study with those previously obtained from peeling the same molecule from a flat surface at these same removal rates (Figure 6.7). This comparison clarifies two points: 1) the peeling forces increase with an increase in tip velocity in both the absence and presence of surface undulations, and 2) regardless of the tip velocity, the forces are consistently lower in the presence of maximum surface undulations (dashed lines) than in their absence (solid lines). Comparing the results from Figure 6.6 and Figure 6.7, it is likely that the increase in peeling forces of stickier molecules from a highly undulated surface is a direct outcome of the present surface features, and not deviations from equilibrium. This conclusion will need to be more completely analyzed by accounting for the adjusted mean potential energy of the system in the presence of surface undulations.

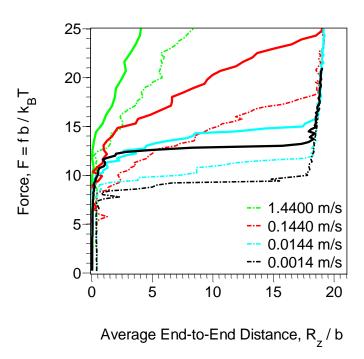


**Figure 6.7.** Effect of peeling rate on the force–displacement curve of an FJC with binding energy per Kuhn segment of 12 k<sub>B</sub>T under force control, when surface undulations are maximized ( $\alpha = 1$ ) (dashed lines) vs. absent (solid lines).

So far, our Brownian dynamics simulations from studies on the effect of surface undulations, free energy of binding to the surface and removal rates in the presence of maximum surface undulations, all suggest that 1) surface features affect the peeling behavior of a molecule from the substrate, and 2) these effects are difficult to distinguish by only considering the forces measured from the vertical peeling experiments. As a result, one should also consider the elastic response of the molecule, when dragged on a surface. Our dynamics simulations for the lateral peeling a 20-mer FJC in the presence of maximum surface undulation ( $\alpha = 1$ ) for a molecule with a free energy of binding of 12 k<sub>B</sub>T per Kuhn link, show a high peeling dimensionality dependence on the removal forces (Figure 6.8).

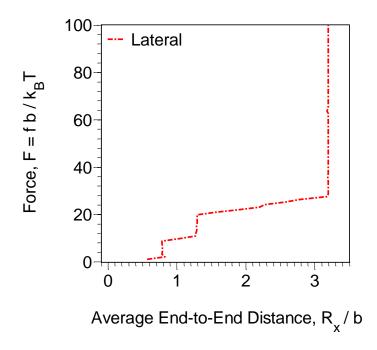


**Figure 6.8.** The equilibrium lateral peeling behavior of 20-mer FJC with binding energy per Kuhn segment of  $12 \text{ k}_B\text{T}$  under force control from a highly undulated surface ( $\alpha = 1$ ).

Since the lateral removal forces are high enough to be detectable in peeling experiments, as our future work, we would like develop analytical models to 1) extract information regarding the height of surface undulations from the lateral peeling experiments, and 2) separate out the surface undulation contributions to the vertical peeling forces by estimating the expected mean surface potential energy for a given surface energy undulation height barrier. This information can then be used by experimentalists to more accurately report measurements for the binding strength of molecules to surfaces.

## **6.4 Conclusions**

In summary, we established that surface features not only change the magnitude of forces required to remove a molecule from a surface, but also they modify the peeling behavior by introducing steps to the otherwise typically flat, equilibrium, force plateaus. Identifying any such changes in the experimentally obtained peeling force curves will be a difficult task to accomplish. For this reason, we suggest that experimentalists carry out lateral peeling experiments in addition to the traditional SMFS studies in order to separate out any contributions from surface features to the peeling forces.

#### 6.5 References

- (1) Krim, J.; Solina, D. H.; Chiarello, R., Nanotribology of a krypton monolayer: a quartz-crystal microbalance study of atomic-scale friction. *Phys. Rev. Lett.* **1991,** *66*, 181-4.
- (2) Mate, C. M.; McClelland, G. M.; Erlandsson, R.; Chiang, S., Atomic-scale friction of a tungsten tip on a graphite surface. *Phys. Rev. Lett.* **1987,** *59*, 1942-5.
- (3) Morita, S.; Fujisawa, S.; Sugawara, Y., Spatially quantized friction with a lattice periodicity. *Surf. Sci. Rep.* **1996**, *23*, 1-41.
- (4) Kerssemakers, J.; De, H. J. T. M., Atomic force microscopy imaging of transition metal layered compounds: a two-dimensional stick-slip system. *Appl. Phys. Lett.* **1995**, 67, 347-9.
- (5) Holscher, H.; Schwarz, U. D.; Zworner, O.; Wiesendanger, R., Consequences of the stick-slip movement for the scanning force microscopy imaging of graphite. *Phys. Rev. B: Condens. Matter Mater. Phys.* **1998,** *57*, 2477-2481.
- (6) Socoliuc, A.; Bennewitz, R.; Gnecco, E.; Meyer, E., Transition from stick-slip to continuous sliding in atomic friction: entering a new regime of ultralow friction. *Phys Rev Lett* **2004**, *92*, 134301.
- (7) Sung, I.-H.; Lee, H.-S.; Kim, D.-E., Effect of surface topography on the frictional behavior at the micro/nano-scale. *Wear* **2003**, *254*, 1019-1031.
- (8) Sundararajan, S.; Bhushan, B., Topography-induced contributions to friction forces measured using an atomic force/friction force microscope. *J. Appl. Phys.* **2000**, 88, 4825-4831.

- (9) Muller, T.; Lohrmann, M.; Kasser, T.; Marti, O.; Mlynek, J.; Krausch, G., Frictional Force between a Sharp Asperity and a Surface Step. *Phys. Rev. Lett.* **1997**, *79*, 5066-5069.
- (10) Li, B.; Clapp, P. C.; Rifkin, J. A.; Zhang, X. M., Molecular dynamics simulation of stick-slip. *J. Appl. Phys.* **2001**, *90*, 3090-3094.
- (11) Qi, Y.; Cheng, Y.-T.; Çağin, T.; Goddard, W. A., III, Friction anisotropy at Ni(100)/(100) interfaces: Molecular dynamics studies. *Physical Review B* **2002**, *66*, 085420.
- (12) Zhang, Q.; Qi, Y.; Hector, L. G., Jr.; Çağın, T.; Goddard, W. A., III, Atomic simulations of kinetic friction and its velocity dependence at interfaces. *Physical Review B* **2005**, 72, 045406.
- (13) Perry, M. D.; Harrison, J. A., Molecular Dynamics Studies of the Frictional Properties of Hydrocarbon Materials. *Langmuir* **1996**, *12*, 4552-4556.
- (14) Raviv, U.; Giasson, S.; Frey, J.; Klein, J., Viscosity of ultra-thin water films confined between hydrophobic or hydrophilic surfaces. *J. Phys.: Condens. Matter* **2002**, *14*, 9275-9283.
- (15) Harrison, J.; Woodhouse, J.; Dowson, A. J., The management of occupational health by NHS Trusts in the north of England. *Occup Med (Lond)* **1999**, *49*, 525-33.
- (16) Tupper, K. J.; Brenner, D. W., Molecular dynamics simulations of friction in self-assembled monolayers. *Thin Solid Films* **1994**, *253*, 185-9.
- (17) Manohar, S.; Tang, T.; Jagota, A., Structure of Homopolymer DNA-CNT Hybrids. *J. Phys. Chem. C* **2007**, *111*, 17835-17845.

- (18) Johnson, R. R.; Johnson, A. T. C.; Klein, M. L., Probing the Structure of DNA-Carbon Nanotube Hybrids with Molecular Dynamics. *Nano Lett.* **2008**, *8*, 69-75.
- (19) Gowtham, S.; Scheicher, R. H.; Ahuja, R.; Pandey, R.; Karna, S. P., Physisorption of nucleobases on graphene: Density-functional calculations. *Phys. Rev. B: Condens.*Matter Mater. Phys. **2007**, 76, 033401/1-033401/4.
- (20) Iliafar, S.; Vezenov, D.; Jagota, A., Brownian Dynamics Simulation of Peeling a Strongly-Adsorbed Polymer Molecule from a Frictionless Substrate. *Langmuir* **2013**, 29, 1435-1445.
- (21) Roxbury, D.; Manohar, S.; Jagota, A., Molecular Simulation of DNA β-Sheet and β-Barrel Structures on Graphite and Carbon Nanotubes. *The Journal of Physical Chemistry C* **2010**, *114*, 13267-13276.
- (22) Kilina, S.; Tretiak, S.; Yarotski, D. A.; Zhu, J.-X.; Modine, N.; Taylor, A.; Balatsky, A. V., Electronic Properties of DNA Base Molecules Adsorbed on a Metallic Surface. *The Journal of Physical Chemistry C* **2007**, *111*, 14541-14551.
- (23) Roxbury, D.; Jagota, A.; Mittal, J., Sequence-Specific Self-Stitching Motif of Short Single-Stranded DNA on a Single-Walled Carbon Nanotube. *Journal of the American Chemical Society* **2011,** *133*, 13545-13550.
- (24) Mizes, H. A.; Foster, J. S., Long-range electronic perturbations caused by defects using scanning tunneling microscopy. *Science (Washington, D. C., 1883-)* **1989,** 244, 559-62.
- (25) Wehling, T. O.; Balatsky, A. V.; Katsnelson, M. I.; Lichtenstein, A. I.; Scharnberg, K.; Wiesendanger, R., Local electronic signatures of impurity states in graphene. *Phys. Rev. B: Condens. Matter Mater. Phys.* **2007**, *75*, 125425/1-125425/5.

- (26) Bena, C., Effect of a Single Localized Impurity on the Local Density of States in Monolayer and Bilayer Graphene. *Phys. Rev. Lett.* **2008**, *100*, 076601/1-076601/4.
- (27) Basko, D. M., Resonant low-energy electron scattering on short-range impurities in graphene. *Physical Review B* **2008**, *78*, 115432.

## Curriculum Vitae

## Sara Cook

422 Main Street, Apt. 124, Harleysville, PA 19438 (484) 252-6020 siliafar@gmail.com

## **Summary**

**Surface Characterization:** Atomic/Chemical Force Spectroscopy, Single Molecule Force Microscopy, Total Internal Reflection Fluorescence (TIRF) Microscopy, Scanning Tunneling Microscopy, Transmission Electron Microscopy, Ellipsometry, Optical Microscopy, Contact angle

**Surface Modification:** Nanofabrication, Photolithography and lift-off, Spin Coating, Plasma treatment, Self-assembled monolayers

**Simulations and Theory:** Writing of computer codes for example to simulate 3D molecular interactions (based on Brownian dynamics), and analyze outsized data sets, Derivation of mathematical expressions to model experimental systems

**Additional Techniques:** Coatings formulation and testing, High Performance Liquid Chromatography, UV/Vis/NIR Spectroscopy, Thermogravimetric Analysis, Polymer formation and characterization via Instron

**Software:** Matlab, Igor/MFP3-D, V720, Visualization software (VMD, Materials Studio), COMSOL, HYSYS, ASPEN, Cap Cost, Maple, Mobius, Lotus Notes, LabView, AutoCAD, Fortran, Microsoft Office

**Management and Leadership:** Elected Vice President of Graduate Student Senate as well as Chemical Engineering Graduate Association at Lehigh University

#### Education

Lehigh University	<b>B</b> ethlehem, PA
Doctor of Philosophy in Chemical Engineering	September 2009 - December 2013

# **Drexel University**Master of Science in Chemical Engineering Concentration in *Engineering Management*Philadelphia, PA June 2007 - June 2009

<b>Drexel University</b>	Philadelphia, PA
Bachelor of Science in Chemical Engineering	September 2005 - June <b>2009</b>
Concentration in <i>Bioscience and Biotechnology</i>	

## **Research and Work Experience**

## Lehigh University

Bethlehem, PA

## **Graduate Research Assistant**

August 2009 - Present

Advanced understanding of biopolymer-nanomaterials interactions with applications in and nanotubes separation technology as well as in targeted drug delivery and cancer therapy. Research was focused on developing biofunctional nanomaterials and characterizing the adhesion parameters to synthesize stable dispersions of such hybrids in solution.

## **Lehigh University**

Bethlehem, PA

**Teaching Assistant** 

January 2011- December 2013

Biomechanics - Instructed an undergraduate Biomechanics laboratory course.

*Chemical Reactor Design* - Provided assistance to the instructor for the undergraduate Kinetics and Chemical Reaction Engineering course.

## **Drexel University**

Philadelphia, PA

**Senior Design Project** 

October 2008 - June 2009

Designed production plants for the synthesis of industrial chemicals: Cyclohexane and Hydroquinone.

## E. I. Dupont De Nemours & Co.

Philadelphia, PA

Dispersion Engineer- Fulltime Co-Op position

September 2007 - March 2008

Performed coating formulation research with pigments to yield improved product cost position for automotive refinish business.

## **Drexel University**

Philadelphia, PA

## **Undergraduate Research Assistant**

April 2007 - August 2008

Performed research which resulted in improvements to an insulin delivery system for potential medical applications.

## **MAB Paints**

Philadelphia, PA

## **Chemist - Fulltime Co-Op position**

September 2006 - March 2007

Performed research to develop new competitive architectural and decorative coatings with improved performance characteristics.

## **Drexel University**

Philadelphia, PA

#### **Engineering Design Project**

January 2006

Designed more effective insulating paints using various sizes of hollow microspheres.

#### **Publications and Presentations**

- 1. <u>Iliafar, S.</u>; Vezenov, D.; Jagota, A., Interaction of Single-Stranded DNA with Curved Carbon Nanotube is Much Stronger than with Flat Graphite. (submitted)
- 2. <u>Iliafar, S.</u>; Vezenov, D.; Jagota, A., Stretching of a Freely Jointed Chain in Two-Dimensions. (submitted)

- 3. <u>Iliafar, S.</u>; Vezenov, D.; Jagota, A., Brownian Dynamics Simulation of Peeling a Strongly-Adsorbed Polymer Molecule from a Frictionless Substrate. *Langmuir* **2013**, 29 (5), 1435-1445.
- 4. <u>Iliafar, S.</u>; Wagner, K.; Manohar, S.; Jagota, A.; Vezenov, D., Quantifying Interactions between DNA Oligomers and Graphite Surface Using Single Molecule Force Spectroscopy. *The Journal of Physical Chemistry C* **2012**, *116* (26), 13896-13903.
- 5. Vezenov, D.; <u>Iliafar, S.</u>; Manohar, S.; Jagota, A. Single Molecule Peel Test: Adhesion between Single-Stranded DNA and Graphite. *Proc. Annu. Meet. Adhes. Soc.* **2011**, 34th.

#### **Selected Conferences and Poster Sessions:**

## **Materials Research Society**

Boston, MA

## Synthesis, Characterization, and Modeling Methods

November 2012

 Presentation Title: "Quantifying the Interactions Between a single-stranded DNA and Graphite by Single Molecule Force Spectroscopy and Brownian Dynamics Simulations"

## **Lehigh University**

Bethlehem, PA

## **Biophysical Society Pennsylvania Network Meeting**

September 2012

■ Poster Title: "Quantifying the Interactions Between a single-stranded DNA and Graphite by Single Molecule Force Spectroscopy and Brownian Dynamics Simulations"

## **Lehigh University**

Bethlehem, PA

## A Unique Surface Analysis Symposium

March 2011

• Poster Title: "Peeling DNA from a Rigid Substrate"

## **Honors and Awards**

- Accepted into the Rossin Doctoral Fellows program, Lehigh University (2013)
- Received University Fellowship, Lehigh University (2009)
- Graduated with Honors Distinction, Drexel University (2009)
- Awarded with Professional Development and Career Management Certificate of Merit, Drexel University (2006)
- Selected as a member of Pennoni Honors College, Drexel University (2005 2009)
- Awarded with Dean's Scholarship, Drexel University (2005-2009)
- Received Dr. Martin Science Award, New College, Swindon, England (June 2005)

## **Leadership and Professional Affiliations**

- Member of American Chemical Society (2010-Present)
- Elected Vice President of the Chemical Engineering Graduate Association, Lehigh University (2010-2012)
- Elected Vice President of the Graduate Student Senate, Lehigh University (2011-2012)
- Elected Secretary of the Graduate Student Senate, Lehigh University (2010-2011)
- The Graduate Student Representative to the Council of Student Presidents (2011-2012)
- The Graduate Student Representative to the Lehigh University Transportation Committee (2011)